ACOUSTIC EMISSION TECHNIQUES FOR THE DAMAGE ASSESSMENT OF REINFORCED CONCRETE STRUCTURES

NORAZURA MUHAMAD BUNNORI

Ph.D. MARCH 2008

DECLARATION

This work has not previously been accepted in substance for any degree and not being concurrently submitted in candidature for any degree.

Singed ______________________ (candidate)

Date 14/03/2008

STATEMENT 1

This thesis is the result of my own investigations, except where otherwise stated.

Other sources are acknowledged by explicit references.

Singed ______________________ (candidate)

Date 14/03/2008

STATEMENT 2

I hereby give consent for my thesis, if accepted, to be available for photocopying and the inter-library loan, and for the title and summary to be made available to outside organizations.

Singed ______________________ (candidate)

Date 14/03/2008

ACOUSTIC EMISSION TECHNIQUES FOR THE DAMAGE ASSESSMENT OF REINFORCED CONCRETE STRUCTURES

PhD Thesis

Norazura Muhamad Bunnori (BEng (Hons), MSc)

School of Engineering
Cardiff University, Cardiff
UK
March 2008

Prifysgol Caerdydd **SUMMARY OF THESIS** **Cardiff University**

Candidate's Surname: Muhamad Bunnori

Candidate's Forenames: Norazura

Candidate for the Degree of: PhD

Institution at which study pursued: Cardiff University, Wales, UK

Full Title of Thesis: Acoustic Emission Techniques for the Damage Assessment of Reinforced Concrete Structures

Summary:

This thesis examines the role of Acoustic Emission (AE) techniques as a non-destructive testing (NDT) technique for reinforced concrete structures. The work focuses on the development of experimental techniques and data analysis methods for the detection, location and assessment of AE from the reinforced concrete specimens. Three key topics are investigated:

1. **Method of analysis for laboratory-based pre-corroded and post-corroded reinforced concrete specimens tested in flexure.**

Experimental results from a series of laboratory studies are presented. The work investigates the changing behaviour of the reinforced concrete beams due to chloride-induced reinforcement corrosion by using a parameter-based approach to detect, locate and follow the progression of cracks. The use of AE absolute energy as an indication of concrete cracking is also explored.

2. **A practical investigation into acoustic wave propagation in reinforced concrete structures.**

Experimental results from acoustic wave propagation of two source modes (parallel and normal to sensor face) are presented. The work investigates the wave velocity in concrete structures over a variety of source-to-sensor distances with the influence of pre-set threshold levels. Specimen geometry, specimen conditions and source orientation is explained. The application of modal behaviour on the AE from both artificial and real sources is examined. Experimental data describing signal attenuation is also presented.

3. **The detection of damage within an in-service concrete crosshead.**

Further analysis of a commercial bridge inspection is given. A comparison of results from both clustered and non-clustered events, with laboratory based results is made. Apart from being interested with clustered events, non-clustered events are also an important contribution to damage detection in structural monitoring.

Key Words: Acoustic Emission, Corrosion, Reinforced Concrete, Concrete Cracks, Source Location, Wave Propagation, Damage Assessment, Bridge Monitoring.

ACKNOWLEDGEMENTS

I take this opportunity to express my great debt of gratitude to Professor R. J. Lark and Professor K. M. Holford for their excellent guidance, support and invaluable patience throughout this work. I thank Dr. Rhys Pullin (Cardiff University), Tim Bradshaw (PAL) and Jon Watson (PAL) for three years provided great support and technical assistance.

I would like to thank to Universiti Sains Malaysia (USM) and Ministry of Higher Education, Malaysia for giving me an opportunity in pursuing a PhD study. My thanks also to the technical staff of the Cardiff University School of Engineering, particularly to Carl Wadsworth, Brian Hooper, Des Sanford, Len Czekaj and Andrew Sweeney.

Finally I would like to thank my family, especially my parents Muhamad Bunnori Kardi and Sadiah Jamali and my husband Mohamed Johari Hashim for their emotional and financial support and prayer.

GLOSSARY OF TERMS FOR AE TESTING

Acoustic Emission (AE): Elastic waves generated by the rapid release of energy from sources within a material.

Absolute Energy: This is a true energy measure of an AE hit whose units are measured in attoJoule (aJ). Absolute energy is derived from the integral of the squared voltage signal divided by the reference resistance over the duration of the AE waveform packet.

AE Count: The number of times the signal amplitude exceeds the pre-set reference threshold.

Array: A group of sensors used for source location.

Attenuation: Loss of amplitude with distance as the wave travels through the test structures.

Broad Band Sensors: High sensitivity over a wide frequency range.

Burst Emission: A qualitative term applied to AE when bursts are observed.

Channel: A single sensor and the related instrumentation for transmitting, conditioning, detection and measuring a signal.

Cluster Location: An area of predefined size on a structure that contains an AE source of such significance that it crosses predefined signal thresholds. This allows ranking of sources found using location monitoring.

Continuous Emission: A qualitative term applied to AE when bursts or pulses are not discernible.

Couplant: A substance providing an acoustic link between the propagation medium and sensor.

Duration: The interval between the first and last time the threshold has been exceeded by the signal.

Energy (MARSE): MARSE (**M**easured **A**rea under the **R**ectified **S**ignal **E**nvelope) energy is relative value proportional to the true energy of the source event.

Event: A single AE source produces a transient mechanical wave that propagates in all directions in a medium. The AE wave is detected in the form of hits on one or more channels. An event therefore, is the group of AE hits that was received from a single source.

Felicity Ratio: The measurement of the felicity effect. Defined as the ratio between the applied load at which the AE appears during the next application of loading and the previous maximum applied load.

Global Monitoring: Large scale monitoring of a structure when no specific flaws are known.

Hit: A hit is the term used to indicate that a given AE channel has detected and processed an AE transient.

H-N Source: Also known as Hsu-Neilson or lead break; the industry standard calibration method, which involves fracturing a 0.5 diameter, 3mm long, 2h propelling pencil lead at 30° orientation.

Kaiser Effect: The absence of detectable AE until the previous maximum applied stress level has been exceeded.

Lamb Wave: In a medium bounded by two surfaces, i.e. a plate, at distances greater than a few centimetres from AE source surface waves can couple to produce Lamb waves.

Location Group: An array of AE sensors (based on known placement between one another) for the purpose of determining the general or exact location of an event occurring near or within the detection area.

Local Monitoring: A source location examination of a known flaw.

Location Plot: Representation of sources of AE computed using an array of sensors.

Lockout Time: The minimum time following the detection of an event before the analysis software resumes event processing within a location group. This is typically set to the period of time taken for an AE signal to propagate from one sensor in a group to the most distant sensor in the given group. Use of lockout time is intended to prevent reflections from a single source event being incorrectly identified as new events by the source location algorithm.

Measure Amplitude Ratio (MAR): MAR expressed as a percentage that is the ratio of the first wave peak amplitude to the second wave peak amplitude.

Noise: The signal obtained in the absence of any AE, the signal has electrical and mechanical background.

Parametric Inputs: Environmental variables (e.g. load, pressure, temperature) that can be measured and stored as part of the signal description.

Peak Amplitude: Maximum signal amplitude within the duration of the signal.

Pencil Source: An artificial source using the fracture of a brittle graphite lead in a suitable fitting to simulate an AE event (also known as an Hsu-Neilson source).

Rayleigh Wave: Rayleigh waves are longitudinal and transverse waves which propagate in the bulk of the material combine in the region close to the surface.

Reference Threshold: A pre-set voltage level that has to be exceeded before an AE signal is detected and processed.

Resonant Sensor: A sensor that uses the mechanical amplification due to a resonant frequency to give high sensitivity in a narrow band.

Rise-time: The interval between the first threshold crossing and the maximum amplitude of the signal.

Sensor: A device that converts the physical parameters of a wave into an electrical signal.

Signal Features: Measurable characteristic of AE signal, such as amplitude, AE energy, duration, counts, rise-time, that can be stored as a part of AE hit decription.

Source: The place where an event takes place.

Source Location: The computed origin of AE signal.

Velocity: The speed at which an AE wave propagates from one sensor to another.

INDEX OF CONTENTS

CHAPTER 1: THE ASSESSMENT OF CONCRETE STRUCTURE DUE TO CHLORIDE-INDUCED REINFORCEMENT CORROSSION

CHAPTER 2: ACOUSTIC EMISSION THEORY AND ITS APPLICATION IN CONCRETE MONITORING

CHAPTER 3: EXPERIMENTAL INSTRUMENTATION AND TECHNIQUES

CHAPTER 4: LABORATORY FLEXURAL TESTING ON REINFORCED CONCRETE BEAM WITH PRE-CORRODED AND POST-CORRODED REINFORCING BARS

4.4 HARDENED CONCRETE TEST

CHAPTER 5: A PRACTICAL INVESTIGATION INTO ACOUSTIC WAVE PROPAGATION IN CONCRETE STRUCTURE

5.4 RESULTS

5.4.1 Artificial Source from H-N Source

CHAPTER 6: ACOUSTIC EMISSION ASSESSMENT OF M4 ELEVATED CROSSHEAD

6.3 EXPERIMENTAL PROCEDURE

6.4 FURTHER INVESTIGATION

CHAPTER 7: CONCLUSIONS AND RECOMMENDATIONS FOR FURTHER WORK

APPENDIX A: SENSOR CALIBRATION CERTIFICATES

APPENDIX B: RESULTS FOR PRE-CORRODED (PR) SPECIMENS

APPENDIX C: RESULTS FOR POST-CORRODED (PS) SPECIMENS

APPENDIX D: PUBLISHED PAPERS

CHAPTER 1: THE ASSESSMENT OF THE DETERIORATION CONCRETE STRUCTURES DUE TO CHLORIDE-INDUCED REINFORCEMENT CORROSION

1.1 INTRODUCTION

The aim of this chapter is to investigate the use of structural health monitoring to assess the deterioration of concrete structures due to chloride-induced reinforcement corrosion. Non-Destructive Testing (NDT) methods for doing this are reviewed and the influence of the corrosion process within concrete structures on these techniques is considered.

Deterioration of concrete bridges and other concrete structures caused by environmental exposure is a severe global problem. One of the most serious matters with major economic implications is the degradation due to chloride-induced reinforcement corrosion. Serious deterioration of the civil engineering infrastructure has encouraged structural monitoring of the integrity of structural systems.

Monitoring the structural health condition at regular intervals can:

i. Enable the detection and location of damage or degradation of structural components and provide this information to the operators and users of the structure quickly and comprehensibly.
ii. Allow structural degradation to be identified early prior to local failure.
iii. Prevent system failure.
iv. Help reduce maintenance costs.

Park (2002) suggests that an ideal structural health monitoring system should be capable of:

i. detecting existing damage,
ii. locating the damage,
iii. sizing the damage, and
iv. determining the impact of the damage on the performance of the structure.

A recent example of where structural health monitoring of a structure is now required is as a result of problems that have been identified in 2004 with the Lumpur Middle Ring Road 2, known as the MRR2 in Malaysia. The government carried out investigations of a 1.7km flyover, which forms part of the MRR2, and it was reported as being faulty because 31 of the 33 pillars supporting the flyover were identified as having active cracks. As a result the flyover was closed to traffic and only reopened with traffic restricted to 4 out of 6 lanes. To ensure that the MRR2 flyover does not become a threat to public safety less than two years after its completion and to identify what remedial action needs to be undertaken to end the daily hardship and inconvenience to tens of thousands of commuters an NDT method is needed to monitor the whole structure. Early detection of the growth of this damage prior to local failure is needed to prevent disastrous failures of the whole system.

As well as detecting and locating corrosion damage in structures, further investigation is required by observing the behaviour of concrete structures which have been affected by chloride induced reinforcement corrosion. This can be considered as an early warning sign indicating that deterioration has occurred inside the structure. Steel corrosion in reinforced concrete (RC) leads to cracking, reduction of bond strength and steel cross section, loss of concrete cover and, in extreme cases, a loss of structural integrity. The effects of these phenomena on the changing behaviour of RC structures, for example as caused by de-icing chemicals, must detected early and studied in detail.

It is possible to use the acoustic emission (AE) signal resulting from damage, to clarify the location of such damage. Experiments have been performed on steel-reinforced concrete specimens to determine the feasibility of using AE monitoring to detect the effect of corrosion on the behaviour of RC structures. The evaluation on the performance of AE, with regards to the structural effects of corrosion-damage, is highly significant in order to help monitor large structures.

1.2 AIMS, OBJECTIVES AND THESIS ORGANISATION

The aims of this study are to investigate the AE technique further for use in global structural monitoring; study the effect and changing behaviour caused by chloride-induced reinforcement corrosion in concrete bridges and provide a practical technique for the non-destructive testing of concrete bridges. Regarding smart bridges, this study conveys the effect of corrosion on RC structures and the AE output in order to develop a tool that could be used to determine damage and/or deterioration in generic RC structures.

The objectives are to evaluate and enhance existing assessment methods using AE in order to monitor the behaviour of RC bridges due to corrosion and to improve traditional methods of source location. Studies will include:

i. Laboratory based stepwise static loading tests monitored using AE of corroded and uncorroded RC beams.
ii. Source location trials of AE to determine deterioration/crack location.
iii. Investigation into acoustic wave propagation in concrete structures.
iv. Further investigation of bridge monitoring data.

Chapters 1 and 2 present and critically review background research and reference works. Chapter 3 details the instrumentation and experimental techniques common to all conducted experimental work. Chapters 4, 5 and 6 report all the experimental and analytical work undertaken. Each chapter examines the results and discussion relevant to each group of experiments with conclusions presented separately at the end of each chapter. Chapter 7 draws together all chapters with recommendations for future work. All references are presented in Chapter 8.

1.3 PROPERTIES OF STEEL REINFORCED CONCRETE (RC)

Generally, RC is a composite material made up of concrete and some form of reinforcement such as steel rods, bars or wires; these materials combine to provide a versatile construction material.

Concrete has a high compressive but a low tensile strength. Steel, on the other hand, has a very high tensile and compressive strength. Due to the high cost of steel, it is cost effective to combine steel and concrete into a composite material, making use of both, the high strength of steel and the relatively low-cost compressive strength of concrete.

Corrosion of the reinforcement is a major durability problem. This largely due to when the rebar in the concrete is exposed to chlorides, either from the concrete's ingredients or from the surrounding chloride-bearing environment. Carbonation of concrete and the penetration of acidic gases into concrete are other causes of reinforcement corrosion. Others effects that influence reinforcement corrosion are the water to cement ratio, cement content, impurities in the concrete's ingredients, the presence of surface crack and the external environment. Environmental and climate conditions appear to be a main cause contributing to the deterioration process.

The deterioration process occurs when the severity of the environment is compounded by poor durability performance of the concrete or faulty design and construction practices. Deterioration grows rapidly and it cannot easily be stopped. As a result, large numbers of existing structures are deteriorating globally.

1.4 CORROSION

Corrosion is an electrochemical reaction. The important factor affecting a corroded cell is the difference in the potential of the metal. Steel reinforcement in concrete and concrete-like materials are, generally, well protected from corrosion by the alkaline nature of the cementitious matrix surrounding it. As long as it is protected, the steel inside concrete structures should not corrode. However, this alkaline environment deteriorates in real structures and reinforcing and pre-stressing steels are subject to corrosion due to carbonation and chloride ion attack. Corrosion of steel reinforcement is one of the major causes affecting the long-term performance of RC structures.

It is possible, with varying degrees of accuracy, to measure the amount of steel dissolving and forming oxides (rust). According to El Maaddawy and Soudki (2003), this is done directly as a measurement of the electric current generated by the anodic reaction:

$$Fe \rightarrow Fe^{2+} + 2e^- \tag{1.1}$$

and consumed by the cathodic reaction:

$$H_2O + \frac{1}{2}O_2 + 2e^- \rightarrow 2OH^- \tag{1.2}$$

and according to ASTM G 102-89 (1989) (as cited in Yoon et. al, 2000(b)) the Faraday's law of metal loss:

$$W_{loss} = [TC] * \frac{EW}{F} = \left\{ \sum_{j=1}^{n} \left[\frac{I_j + I_{j-1}}{2} * \left(t_j - t_{j-1}\right) \right] \right\} * \frac{EW}{F} \tag{1.3}$$

Where

W_{loss} = total weight loss of reinforcing steel, g

TC = total electric charge (in amp-s or coulombs)

EW = equivalent weight, indicating the mass of metal in grams, that is oxides.

For pure elements, the *EW* is given by $EW = W/n$; where *W* is the atomic weight of the element, and *n* is the valency of the element. For carbon steel, *EW* is approximately 28g (Yoon et. al., 2000(b)). *F* is Faraday's constant in units of electric charge (*F* = 96,490 coulombs or amp-s) and I_j is the current in amps, at time t_j, in seconds.

Cabrera (1996) and Ahmad (2003) stated that reinforcement corrosion affects the behaviour of the concrete due to two major factors that disturb the durability of the RC. Firstly, rust production causes spalling and cracking of the concrete cover due to volume expansion developing compression and then tensile stresses in the concrete. Secondly, corrosion reduces the cross-section of the steel and thus, the load carrying ability of a structure. Pitting corrosion of the rebar is more risky than uniform corrosion because it progressively reduces the cross-sectional area of rebar to a point where the rebar can no longer withstand the applied load leading to a disastrous failure of the structure.

1.5 THE APPLICATION OF NON-DESTRUCTIVE TESTING (NDT) TO THE EXAMINATION OF CORROSION IN CONCRETE STRUCTURES

Due to continuous deterioration and increasing maintenance and repair costs for civil infrastructure systems bridge managers/owners must make decisions in an uncertain environment. The introduction of health monitoring techniques using NDT are beneficial as they improve the confidence with which structural performance is assessed and predicted; hence optimise resources used for bridge inspection, maintenance and repair. Widespread corrosion problems of reinforcing steel in concrete structures have triggered a concerted demand for the development of NDT techniques to enable accurate assessment of RC structures.

1.5.1 Visual Inspection

Visual inspection is the customary inspection method. The appearance and colour of a corroded area often provides valuable insight to the cause and extent of corrosion. Moreover, the location of longitudinal cracks due to corrosion attack can be drawn as a crack map with lengths and widths recorded from their first visual observation which enables a global overview of the damage of the RC structures to be obtained (Poupard et. al., 2006).

Special tools, such as magnifying glasses, may also be used to closely inspect the subject area. However, such a technique is limited in its effectiveness to detect surface discontinuities which are often masked by corroded products and internal discontinuities which are not detectable using this method.

1.5.2 Half-cell Potential Measurements

Half-cell potential is one of the most common methods in bridge inspection in order to determine concrete rebar condition. It can be used to establish the probability of corrosion activity taking place at the time of the test (Ha et. al., 2007). The test measures the electrical potential of embedded reinforcement. This electrical potential indicates the degree of risk that the electrical activity is associated with the corrosion of the reinforcement. The standard of testing is described in BS1881: Part 201 (1986).

An electrical connection is made to the reinforcement and a high-impendence voltmeter is used to measure the electrical potential between the reinforcement and a half cell placed on the surface. A more negative voltage reading suggests that the embedded bar has more excess electrons indicating a higher probability that the bar is corroding. The half cell comprises a silver/silver chloride or copper/copper sulphate reference electrode. Figure 1.1 shows the diagram of the half cell measurements apparatus.

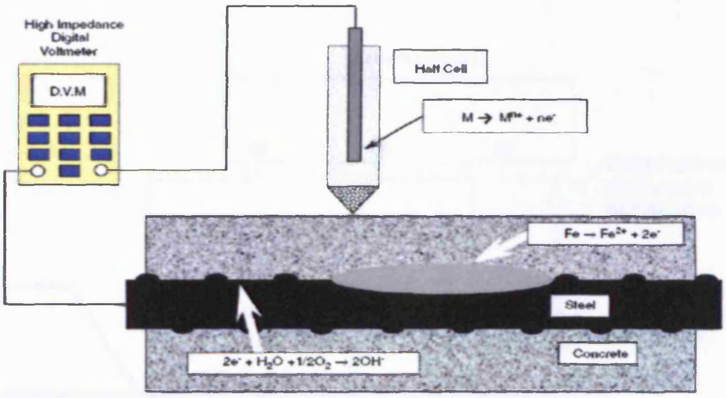

Figure 1.1: Half cell potential measurements (Ha et. al., 2007)

Even though half-cell potential mapping is the simplest of all techniques used for monitoring reinforcement corrosion, it does not provide any quantitative information (Ahmad, 2003). Additionally, the interpretation of potential mapping is often unconvincing because the measurements depend on the condition of the concrete. Moisture levels and the amount of carbonation and salt concentration can affect and give erroneous readings (Zdunek and Prine, 1995).

1.5.3 Linear Polarization Resistance (LPR)

The measurement of half cell potential is a qualitative way in assessing the corrosion state of reinforcing steel and in locating the steel area which presents high corrosion probability. However, to characterize the corrosion activity on the surface of reinforcing steel in a qualitative way, it is essential to evaluate the corrosion rate. The corrosion rate is deduced from the polarization resistance (R_P) measurements from the linear polarization resistance (LPR) method. In this method the corrosion rate is defined as,

$$I_{corr} = \frac{B}{R_P} \tag{1.4}$$

where B is constant, I_{corr} is the corrosion rate and R_P is the polarization resistance.

LPR measurements give a direct indication of the rate at which reinforcement is corroding and therefore provide quantitative data on which maintenance and repair strategies can be based. Figure 1.2 shows the LPR diagram.

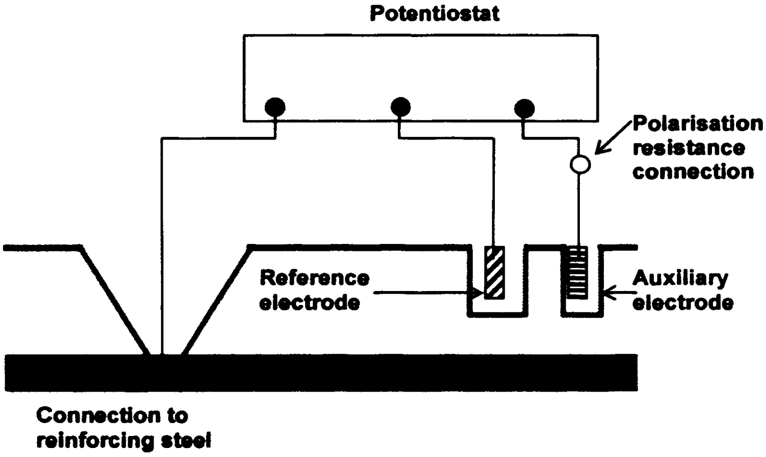

Figure 1.2: Linear Polarization Resistance (Concrete Bridge Development Group, 2002)

Gowers and Millard (1993) carried out a LPR mapping test of two RC structures in the field. Polarization resistance is particularly useful as a method to rapidly identify corrosion upsets and initiate remedial action, thereby prolonging plant life and minimizing unscheduled downtime. They identified regions of the structures, which may have been particularly susceptible to corrosion, by mapping technique of the corrosion rate. Even though LPR can provide a more quantitative assessment of corrosion rate, mapping techniques are time consuming and limited to specific areas. In other words, LPR can be applied to a location where potential and resistivity indicate active corrosion is most likely.

Law (2000) reported the effect of electrode orientation on linear polarization measurements using a sensor controlled guard ring as shown in Figure 1.3. He observed that a sensor controlled guard ring enhanced the accuracy of the linear polarization corrosion rate measurement on RC structures.

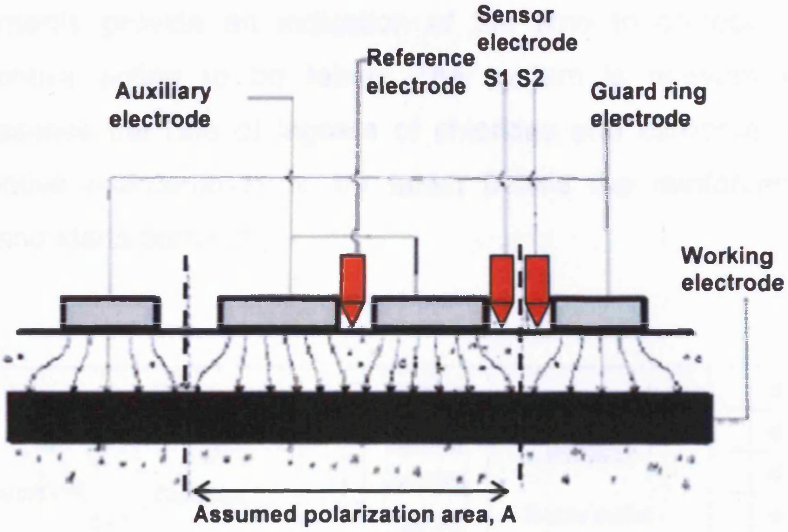

Figure 1.3: Controlled guard ring (Law et. al., 2000)

1.5.4 Galvanic Corrosion Sensor

The galvanic corrosion sensor monitoring (or anode ladder) system comprises of a series of carbon steel anodes embedded at varying depths of concrete cover with a noble metal cathode and temperature sensor.

Raupach and Schiebl (2001) devised a method to determine the chloride penetration depth level using reinforced steel electrodes acting as anodes embedded at various depths in the concrete and a stainless steel or platinum coated titanium bar as the cathode, known as an Anode-Ladder or

Expansion-Ring-System as sensor systems that monitor the corrosion risk of reinforcement. The Anode-Ladder-System has been used for new structures and the Expansion-Ring-System for existing structures. Both are capable of determining corrosion risk at different depths. Figure 1.4 shows the corrosion ladder as described by Raupach and Schiebl (2001). The system provides measurements of the following parameters:

a) galvanic current flowing between the anode and cathode
b) electrical potential between the anode and cathode
c) concrete resistivity between pairs of the anodes
d) temperature

The measurements provide an indication of the time to corrosion which enables preventive action to be taken. The system is relevant to new structures to assess the rate of ingress of chlorides and carbonation. This permits preventive maintenance to be taken before the reinforcement is depassivated and starts corroding.

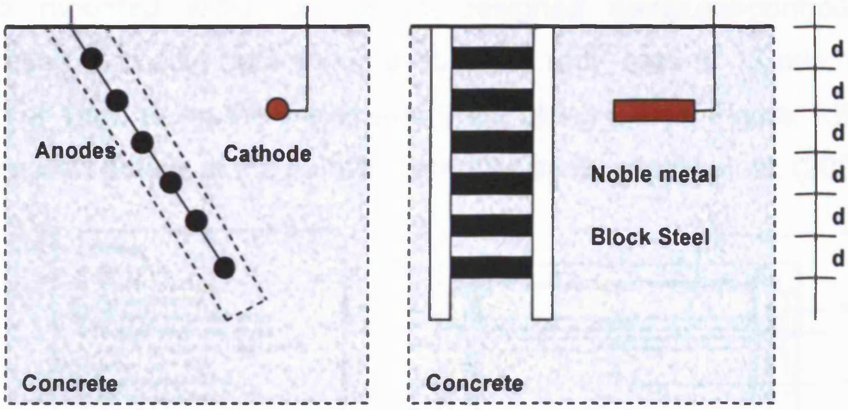

Figure 1.4: Anode ladder system (Raupach and Schiebl, 2001)

Apart from being a robust construction and relatively simple to install, this sensor provides early warning signs of potential corrosion problems before reinforcement is affected. Nevertheless, this sensor can be relatively expensive and therefore only appropriate for larger structures or sites in severe environments. It can only be fitted to new structures or during major repair or re-construction projects in this form.

1.5.5 Inductive Scanning System

A laboratory-based motorized scanning system, together with an inductive sensor, was developed and reported by Gaydecki and Burdekin (1994). This sensor system is capable of generating computer images of steel reinforcing bars and cables embedded in concrete. Signal response from an inductive sensor is related to the area and depth of the steel in the sensing region and scanned across the surface of the concrete. A controlling computer generates an image of the underlying steel by converting the signal that responds from the inductive sensor to grey-scale values mapped to the Cartesian location. The intensities of the grey-scale images are proportional to the signal strength produced by the sensor.

The year 2000 saw the development of a new sensor together with a new, lightweight portable scanning system suitable for on-site use. The sensor is mounted within a purpose-designed computer-controlled x-y scanner, used to collect data within a 400x400 mm^2 area in 18 min, using a scan step of 1mm along the x-axis and 2mm along y-axis. Figure 1.5 shows the construction details of the portable scanner by Gaydecki et. al. (2000).

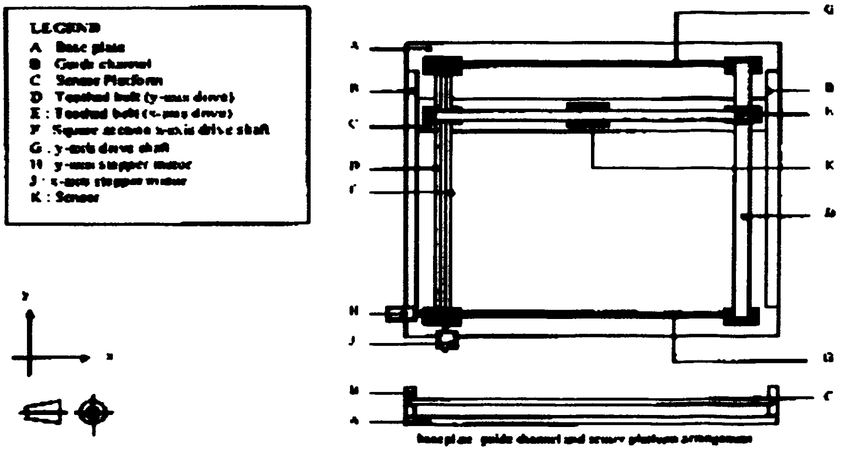

Figure 1.5: Construction details of the portable scanner (Gaydecki et.al,2000).

1.5.6 Conclusion

Table 1.1 shows a summary of the NDT techniques that have been applied to the examination of corrosion in RC structures. The majority of these methods are still under research and have potential in relation to the assessment of corrosion and the condition of RC structures. Choice of the most appropriate method is usually based on a combination of factors such as a cost, speed, reliability and accuracy of the given method. Each method has certain advantages and disadvantages and by adopting several testing methods and combining the results usually yields the best results (Idrissi and Liman, 2003). The significance of these methods is that they identify the presence of corrosion in concrete structures at discrete locations which can assist and benefit numerous groups in monitoring large scale structures. Unfortunately, in a global structural monitoring context, there is still not enough research into the application of non-destructive techniques. This also applies to monitoring the effect and the changing behaviour due to chloride-induced reinforcement corrosion in concrete structures, especially bridges.

Table 1.1: Summary of non-destructive techniques applied to monitoring RC structures subject to corrosion.

Author/s	Year	Method Used	Outcome
Ha T. H. et. al.	2007	Half Cell, Linear Polarization Resistance	Laboratory based. Describes the combination of two standard techniques for corrosion monitoring.
Poupard O. et. al.	2006	Visual observation, Half Cell and Linear Polarization Resistance	Laboratory based. Reasonably successfully for high levels of corrosion.
Gaydecki P. et. al	2005, 2003, 2002, 2000	Inductive Scanning System	Laboratory and site based. Imaging technique for visualising the corroded reinforced steel.
Leelalerkiet V. et. al.	2004	Half Cell	Laboratory based. Determines the concrete rebar condition.
Zaid M. et.al.	2004	Inductive Scanning System	Laboratory based. Useful in detecting vertically oriented cracks and steel imaging.
Quek S et. al.	2003	Inductive Scanning System	Able to detect 20mm diameter steel, 30mm below the concrete surface. Imaging technique.
Liu Y., Weyers R. E.	2003	Linear Polarization Resistance	Laboratory based. Measures the corrosion current density.
Quek S., Gaydecki P.	2003	Inductive Scanning System	Laboratory based. Enables the image of the steel be visualised.
Elsener B	2002	Linear Polarization Resistance and Half Cell	Laboratory based. Reasonably successful in pitting corrosion studies.
Pech-Canul M.A and Castro P.	2002	Linear Polarization Resistance	Large structures. Good agreement in the detection of chloride-induced corrosion for reinforcing steel in concrete.
Raupach M and Schiebl	2001	Galvanic Corrosion Sensor	Site based. Monitors corrosion risk.
Millard S.G et. al.	2001	Linear Polarization Resistance	Identifies corrosion sites. Laboratory and site based.
Law D.W et. al	2000	Potentiostatically Controlled Guard Ring (LPR)	Guard ring increases the accuracy of corrosion rate measurements. Laboratory based.
Andrade C and Alonso C	1996	Linear Polarization Method and electrochemical Impedance Spectroscopy	Reasonably successful in laboratory and site based studies. Electrochemical techniques.
Guilia Boronio et. al	1996	Linear Polarization Resistance	Gave clear information on the evolution of corrosion.
Yalcyn and Ergun	1996	Linear Polarization Resistance	Quantitative relationship between the corrosion rate of the reinforcement and the degree of pore saturation.

CHAPTER 2: ACOUSTIC EMISSION THEORY AND ITS APPLICATION IN CONCRETE MONITORING

2.1 INTRODUCTION

Acoustic Emission (AE) is the phenomenon whereby transient elastic waves are generated by the rapid release of energy from localized sources within a material. All materials produce AE during both the generation and propagation of cracks. The elastic waves travel through the structure to the surface, where they are detected by sensors. These sensors are transducers that convert the mechanical waves into electrical signals; information about the existence and location of possible damage sources can be obtained. Among structural non-destructive tests, the AE monitoring technique is the only one able to detect a damage process at the same time as it occurs.

Pollock (1989) and Esward et. al. (2002), state that AE differs from other non-destructive testing techniques in two main respects; firstly, the energy is released from within the test object itself and secondly, AE is capable of detecting the dynamic processes associated with the degradation of structures.

Grosse (2003) highlighted that one of the advantages, compared with other non-destructive evaluation techniques, is the possibility of observing the damage process during the entire load history without disturbing the specimen.

2.2 CHARACTERISTICS OF AE

AE testing is based on the fact that solid materials emit elastic waves or AE when they are mechanically or thermally stressed to the point where deformation or fracture occurs. A number of characteristics of the elastic wave need to be investigated including wave propagation, wave attenuation, wave velocity and the Kaiser effect.

2.2.1 Wave Propagation

Propagation of waves in a solid medium is complex. In an infinite medium, elastic waves propagate as bulk waves in two modes; longitudinal waves (P-wave) (Figure 2.2 a) and transverse waves (S-wave) (See Figure 2.2b). Both have different characteristic velocities depending on the density and elastic constants of the material. Transverse waves are characterised by particle motion which is perpendicular to the wave propagation direction whereas longitudinal waves consist of localised compression and rarefaction of the medium and the motion of the particle is parallel to the wave's propagation direction.

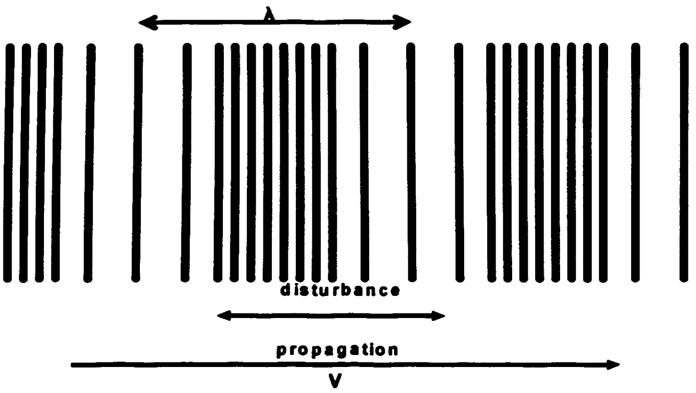

(a) Longitudinal wave

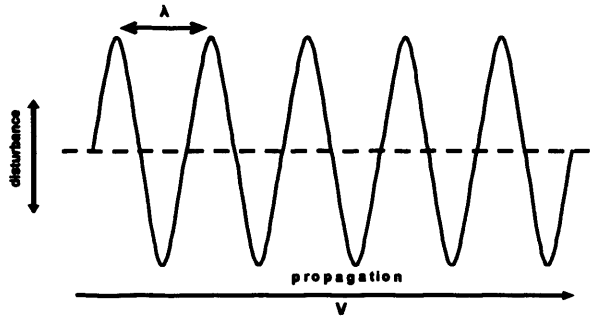

(b) Transverse wave

Figure 2.2: Two basic wave modes (Hackworth, 1997)

Rayleigh waves (R-wave) occur when the boundary condition of a surface is introduced. When this happens, the longitudinal and transverse waves that propagate in the bulk of the material combine in the region close to the surface and a compression produces a transverse displacement of the material. Considering the impact of Poisson's ratio, the overall particle motion is neither purely longitudinal nor transverse. This is known as a Rayleigh or a surface wave.

In a medium bounded by two surfaces (plates), at distances greater than a few centimetres from an AE source, surface waves can couple to produce more complex propagation modes called Lamb waves. Lamb wave behaviour is complex and characterised by dispersion, depending on the thickness of the plate and the frequency of the wave.

2.2.2 WAVE ATTENUATION

In real media, waves change in amplitude as they propagate through the solid. The decrease in amplitude that occurs as a wave travels through a medium is known as wave attenuation. There are several mechanisms responsible for this:

i. Geometric spreading.
ii. Internal friction.
iii. Dissipation of the wave into adjacent media.
iv. Velocity dispersion

When a wave is generated by a localized source, the disturbance propagates outwards in all directions from the source. The energy in the wave front remains constant but is spread over a larger spherical surface. The radius of this sphere (geometric) is equal to the distance the wave travelled from the source. In order for the energy to remain constant, the amplitude of the wave must decrease with increasing distance from the source.

When waves propagate through media with complex boundaries and discontinuities, scattering and dispersion occur, e.g. from aggregate grains in concrete. These phenomena can lead to a decrease in the amplitude of the waves and can cause wave attenuation.

Dissipation attenuation can be caused by inhomogeneities in the propagation medium which scatter the sound wave in the same material, e.g. grain structure in metals. However, it is most common in specimens in contact with an adjacent liquid, e.g. tanks and pipes. Liquids draw energy from the wave travelling in the metal and causes additional attenuation in the near field.

Attenuation due to velocity dispersion happens because the different frequency components of broadband Lamb wave travel at different velocities and the resulting spreading in time causes a loss in amplitude. The magnitude of amplitude loss depends on the slope of the dispersion curves and bandwidth of the signal.

2.2.3 WAVE VELOCITY

The measured velocity describes the speed at which an AE event travels between two fixed points in a propagation medium; this wave velocity is determined by characteristics of the material.

Theoretically, from the physics of elastic wave propagation, the wave velocity in a solid media is proportional to the square root of the elastic modulus and inversely proportional to the square root of the mass density of the media. As a result, the wave velocity is constant when the wave propagates through a media. However, in practice, the methods or techniques that had been used to measure the wave velocity found that the wave velocities were changing with distance. In this case, the terms 'apparent' wave velocity is used instead of wave velocity.

Homogenous materials, such as steel, have well-defined velocities whereas with non-homogeneous materials, such as concrete, the wave velocity is more difficult to predict. Consequently, the measured wave velocity may restrict the development of widely applicable tools as a constant wave velocity is required for most of the application. Additionally, due to the complex composition of most civil engineering structures, determination of the wave velocity is difficult because of the non-homogeneous of the material.

In order to calculate the wave velocity using AE, the determination of the initial P-wave arrival time is essential. The time of the first arrival of a P-wave can be identified from the first rise in amplitude of the signal as shown in Figure 2.3. Source location in AE is based on the arrival times of the direct body waves (P-waves). This is because the P-wave is the first signal to arrive which will not be interfered with by any signal reflections in the later phases (Schechniger and Vogel, 2007).

In AE, the most common method of estimating the arrival time (as used in many commercial systems is the threshold method) whereby the arrival time is recorded when the signal amplitude first crosses a pre-set threshold. This method is used by Holford and Carter (1999) and Ding et al. (2004) when calculating the AE wave velocity in a structure.

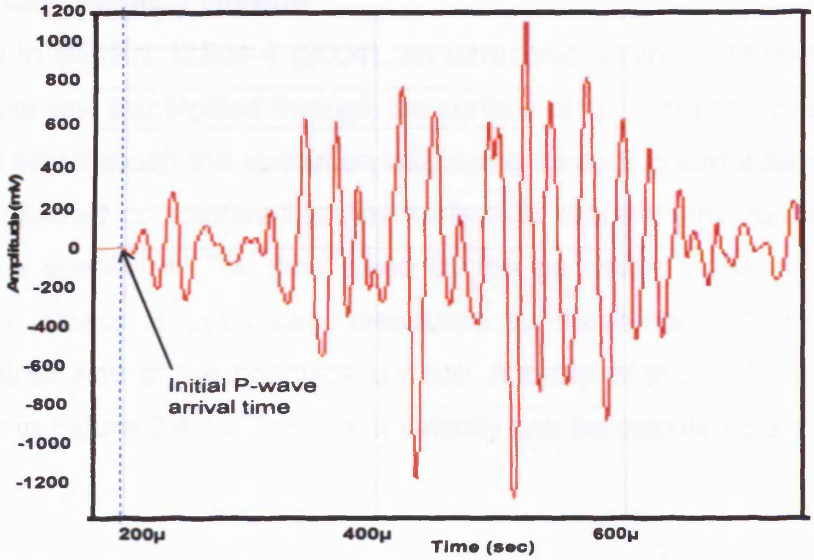

Figure 2.3: Initial P-wave determination from the recorded AE waveform

The wave velocity can be calculated using at least two sensors separated by a known distance and aligned in a straight line with the source point. The sensors were mounted on the same concrete surface to receive the waveform of the displacement generated by the arrival of waves as shown in Figure 2.4(a).

From the recorded signals, the time of arrival of the first P-wave to these two sensors can be identified by using a synchronous setting. This is when the first hit channel triggers all other synchronised channels and the arrival hit-time between different channels can be determined. The P-wave velocity can be calculated as:

$$V_{AE} = \frac{D}{\Delta t} \tag{2.1}$$

D is the distance between sensors and Δt is the time lapse between their arrivals.

As well as AE methods, there are several other methods which can be used to calculate the P-wave velocity of concrete structures. Brief descriptions of the most well-known methods are given below.

Ultrasonic Pulse Velocity Method

As described in BS EN 12504-4 (2004), an ultrasonic pulse is created by a pulse generator and transmitted through the surface of concrete to a receiver. This pulses travel through the specimen with some spreading and attenuation and will be reflected or scattered at any surface or discontinuity, such as a crack, within a specimen. The time taken by the generated pulse to travel through the concrete is accurately measured by the receiver transducer attached to other side of the concrete surface. A setup of this test is shown schematically in Figure 2.4(b). The wave velocity can be calculated similar to Equation 2.1.

Impact-Echo Method

As described in ASTM C1383-04 (2002), this test is based on the principle that stress waves (P-wave) passing through concrete are reflected at internal flaws and external surfaces. The P-wave is generated by an impact at the surface of the concrete. The reflected wave is then measured at the surface of the concrete by a receiving transducer and analysis of the results can indicate the presence of defects such as cracks, delaminations, voids and debonding. The impact-echo method is illustrated in Figure 2.4(c).

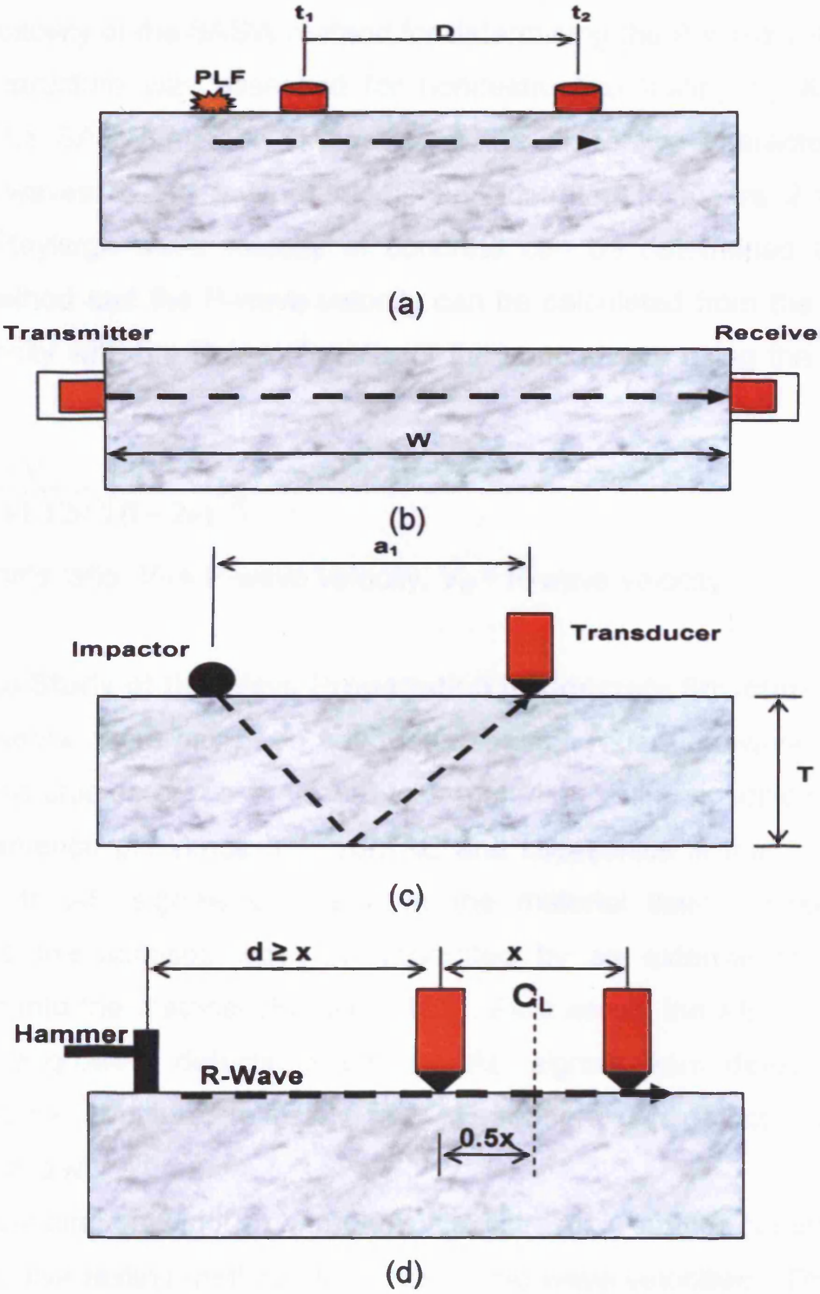

Figure 2.4: Four kinds of stress wave velocity measurements

(a) acoustic emission method, V_{AE}

(b) ultrasonic pulse-velocity method, V_{US}

(c) impact-echo method, V_{IE} (d) spectral analysis of surface wave V_{SASW}.

A Spectral Analysis of Surface Wave Method (SASW)

The applicability of the SASW method for determining the P-wave velocity in a concrete structure was assessed for nondestructive testing by Kim et al. (2006). The SASW method is based on the dispersive characteristics of Rayleigh waves in the layered media as illustrated in Figure 2.4(d). The average Rayleigh wave velocity of concrete can be determined using the SASW method and the P-wave velocity can be calculated from the Rayleigh wave velocity with the Poisson's ratio of the concrete by using the following equation:

$$V_P = \frac{1+\nu}{0.87+1.12\nu}\sqrt{\frac{2(1-\nu)}{(1-2\nu)}}V_R \qquad \textbf{(2.2)}$$

ν = Poisson's ratio, V_P = P-wave velocity, V_R = R-wave velocity

2.2.4 The Study of the Wave Propagation in Concrete Structures

In recent years, there has been adequate research regarding wave velocities in ultrasonic studies on concrete but less material relating specifically to AE. The fundamental difference between AE and Ultrasonics is that the energy converted to AE signals comes from the material itself. However, in Ultrasonics the acoustic wave is generated by an external source and introduced into the material (Beattie, 1983). As a result, the AE technique is sensitive to growing defects. Since the AE signals from defects radiate throughout the structure, relatively few AE sensors can detect and qualify defects over a large area.

Depending on various characteristics, Ultrasonic studies commonly use non-destructive testing methods to measure the wave velocities. These may include the ultrasonic pulse-velocity method (Wu et. al., 2000, Philippidis and Anggelis, 2005), the impact-echo method (Gassman and Tawheed, 2004, Kim et al., 2006) and a spectral analysis of surface wave method (SASW) (Cho, 2003). Most of these methods use a transmitter and receiver transducer.

There have been few studies in Ultrasonic in determining the P-wave velocity. One study, Philippidis and Aggelis (2005) investigated the effect of the water to cement ratio on wave velocity in concrete, where for a range of water to cement ratios between 0.375 and 0.45, the P-wave velocity varied between 3500m/s and 4700m/s. As the water to cement ratio decreased, the velocity of the P-wave increased. In addition, the authors found that at a sensor distance of 150mm, the apparent wave velocity of P-waves in concrete range from 4100m/s to 4700m/s using a signal from a 15 kHz tone burst.

Gassman and Tawheed (2004) analysed the variation in propagation wave velocity of the slab using an Impact-echo test. The authors discovered that the wave velocity in concrete, with a distance of 300mm between the two transducers, varied from 4191m/s to 4233m/s. They also found that for slab areas that exhibit no visual surface and with a distance of 210mm, the wave velocity varied from 4278m/s to 4452m/s. After the load test, a reduction of P-wave velocity ranging from 2 to 6% was observed as a result of crack propagation throughout the slab. The authors agreed that the appearance of cracks will reduce the P-wave velocity through the concrete media.

However, no previous study in AE has investigated the relationship between wave velocities with sensor distances from the source.

2.2.5 Kaiser Effect

The Kaiser effect (defined by Joseph Kaiser in 1950) is one of the important characteristics of AE. Once a given load has been applied and the AE from that stress has stopped, an additional AE will not occur until the original stress level has been exceeded.

The Kaiser effect has been used by many researchers for assessing the deterioration of concrete structures. Yuyama et al. (1999) performed a series of studies to evaluate the structural integrity of Reinforced Concrete (RC) beams and the results demonstrated that the breakdown in the Kaiser effect was directly related to the deterioration of the concrete specimen. Ohtsu et al. (2002) described a damage assessment method for RC beams associated with the Kaiser effect, comparing the Load Ratio (load at the onset of AE activity in a subsequent loading cycle/the previous load) with the

"CALM" Ratio (cumulative AE activity during unloading process cycle/total AE activity at the previous maximum loading cycle) to qualify the damage levels.

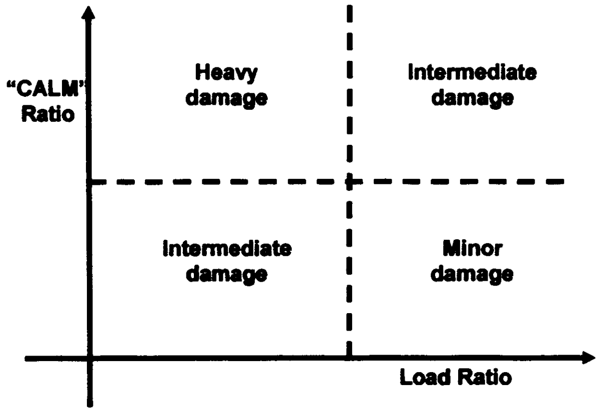

Figure 2.1: Damage assessment method associated with the Kaiser effect (Othsu, 2002).

2.3 SIGNAL PARAMETERS OF AE

AE has been classified into two different types; burst emission and continuous emission, both of which are qualitative descriptions of the type of emissions. The recorded AE signal from a burst type emission (Figure 2.6) can be summarised by a number of basic parameters such as peak signal amplitude, risetime, counts, duration and threshold. The threshold is a prime variable that controls the channel sensitivity. It also serves as a reference for the measurement of some waveform features used to characterise the hit. Amplitude is the highest peak voltage attained by the AE waveform. It is a very important parameter because it is directly related to the magnitude of the source event. To cope with the wide range of signal amplitudes that are produced, most modem AE systems measure the amplitude on a logarithmic scale in decibels (dB) whereby the signal amplitude is measured relative to a one μV signal at the transducer. The amplitude in dB is then given according to equation 2.1.

$$A = 20\log_{10}\left(\frac{V_s}{V_{ref}}\right) \tag{2.4}$$

Where: A = signal amplitude in dB
V_s = signal amplitude in µV
V_{ref} = reference voltage (1µV)

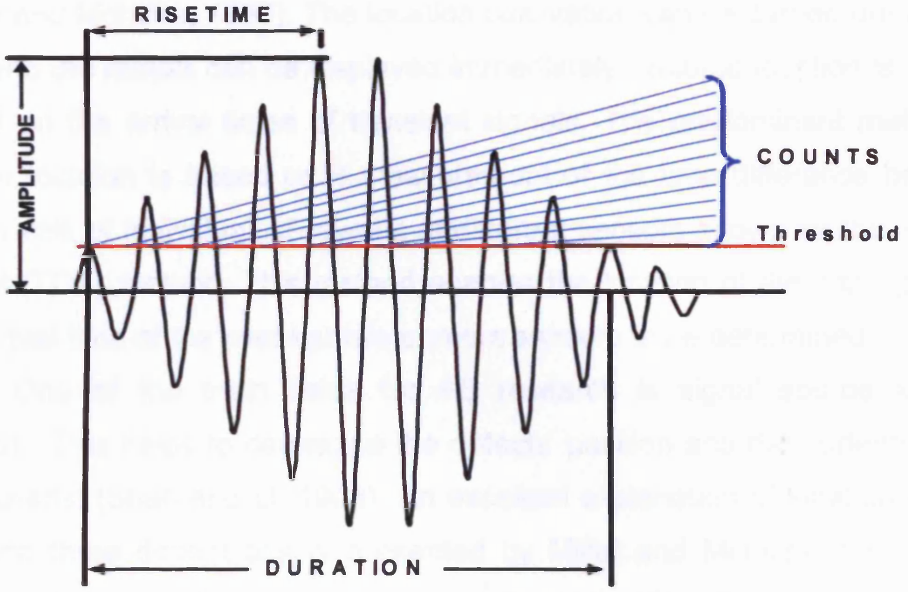

Figure 2.6: Characteristics of a burst type of AE signal (Miller and McIntire, 1987).

AE activity is attributed to the rapid release of energy in a material. Therefore, the energy content of the AE signal can be related to the energy release. AE energy can be measured using two different methods; the **M**easured **A**rea under the **R**ectified **S**ignal **E**nvelope or **MARSE** technique and an absolute energy technique. In the **MARSE** technique, the energy is not a true measure of the total energy of a source event, but a relative value proportional to the true energy of the source event. In the absolute energy technique, the energy is a true energy measure of an AE hit measured in attoJoules. A true energy measure is derived from the integral of the squared voltage signal divided by the reference resistance over the duration of the AE waveform packet. The energy used throughout this thesis is the absolute energy of an AE hit.

2.4 SOURCE LOCATION

Localisation of AE sources is important to assess the regions of active damage. Location can be defined as the determination of the spatial position of an AE source from arrival time measurement using an array of sensors (Miller and McIntire, 1987). The location calculation can be carried out in real-time and the results can be displayed immediately. Source location is usually based on the arrival times of transient signals. The predominant method of source location is based on a measurement of the time difference between the arrivals of individual AE events at different sensors known as the Time of Arrival (TOA) method. This method enables the location of the damage from the arrival time of the event at two or more sensors to be determined.

One of the main fields for AE research is signal source location applied. This helps to determine the defects' position and their orientation in the material (Shah and Li, 1994). An excellent explanation of location in one, two and three dimensions is presented by Miller and McIntire (1987). One dimensional source location is known as linear location. If a source is known to be somewhere along a straight line between a pair of transducers on the beam, a difference in the measured arrival time at the two transducers uniquely determines the source location. Pullin (2001) describes a method which determines the location of an event in one dimension between two sensors where the velocity of the signal and the time of arrival at the sensors is known.

For a plate like structure, it is possible to determine the location of the source by analyzing the time difference between arrivals to three or more sensors (Carlos, 2003). This method locates a source in two dimensions. It is possible to calculate the distance between the source and each sensor by travel times and the speed of the wave arriving at each sensor. By knowing the distance, a circle can be drawn centred at the sensors and the intersection of the three circles drawn from the three sensors should be the focus of the source. However, if the thickness of the specimen is significant relative to the other two dimensions or if the area of interest is internal to the specimen, then a three-dimensional source location is required.

Source location is an extremely powerful tool in AE analysis and can be used in a global monitoring strategy to monitor a relatively large structure with a minimum number of sensors. This is a tremendous advantage in the case of monitoring large structures such as bridges as little access is needed for the placement of AE sensors to determine the structural integrity of a bridge. In global monitoring, when regions of emission are expected, source location attempts to identify a particular area of structure that is experiencing damage. This area is then locally monitored to locate the crack and provide quantitative information about the waveforms emitted (Holford, 2001). Moreover, a reasonable sensor arrangement is of great importance for the localisation capability. However, in local monitoring, source location may be used to try and locate the crack and crack tip, especially if the crack is sub-surface or unable to locate by visual methods.

The precision of source location is dependent on the wave velocity calculation, time difference measurements and the accuracy of the sensor positions (Beck, 2004). There is a need to have reliable automatic picking tools. Manually, it would be difficult to manage the enormous amount of data recorded in the experiments. A widely used method for arrival time determination is by fixed thresholds that have already been implemented in the acquisition system. This method was used by Holford and Carter (1999) Ding et al. (2004) and Schechniger and Vogel (2007) to determine the arrival time for the calculations of AE wave velocity in structures for source location studies.

There are two types of error common to locating discrete AE sources. These errors are due to processing and/or due to natural phenomena such as attenuation, reflection, differing wave modes, refraction or dispersion. Processing errors is controllable by dictating the number and spacing of sensors relying on more than three hits and so forth. Errors caused by natural phenomena are not controllable and not totally manageable (Miller and McIntire, 1987). One of the largest sources of error is the corrected determination of wave velocity.

The computational process for location assumes a known and constant wave velocity. However, non-homogeneous materials such as concrete, the wave velocity is more difficult to predict. This makes the use of a single wave velocity, as required in the TOA method, very difficult due to the variety of wave velocities obtained. In addition, if the source cannot generate signals of adequate strength for detection by the required number of sensors, it will not be possible to calculate the location of the source.

2.5 THE APPLICATION OF AE IN CONCRETE MONITORING

The evaluation of the safety and reliability of reinforced concrete structures such as bridges, viaducts and buildings, is complex. Therefore, diagnosis and monitoring techniques are of increasing importance in the evaluation of structural conditions and reliability. AE is used as a health monitoring tool to detect, identify, locate and quantify a variety of damage mechanisms (Holford, 2000). In addition, the AE technique does not interfere with the users of the structure such as traffic and pedestrians.

Miller and McIntire (1987) and Droulilard (1996) have written a brief history of AE, including its applications and pioneers. The technology of AE traditionally began in the 1950s with the work of Joseph Kaiser. In the late 1950s and 1960s, researchers explored the fundamentals of AE, developed instrumentation specifically for AE and characterized its behaviour with many materials. The most important applications of AE to structural concrete elements started in the late 1970s when the original technology, developed for metals, was modified to suit heterogeneous materials.

In recent years, advanced signal-based AE techniques for concrete structures have gained importance. Some fundamental studies with small-scale specimens have shown that, in principle, AE analysis is an effective method for damage assessment (Li and Shah, 1994, Zdunek and Prine, 1995, Othsu and Watanabe, 2001, Suzuki and Othsu, 2004). Research on various laboratory loading tests up to full scale models of real structural components has endeavoured to relate observed AE characteristics to failure mechanisms in reinforced or pre-stressed concrete (Yoon, 2000, Othsu, 2002, Carpinteri et. al., 2007). Nevertheless, only a few applications to real civil engineering structures like concrete buildings (Sagaidak and Elizarov, 2004, Carpinteri et al., 2007) and concrete bridges exist that evaluate the structural integrity, load carrying capacity or eventual failure (Shigeshi et al., 2001, Golaski et. al., 2002). Continuous monitoring of a whole structure is also possible, e.g. the failures of high-strength steel tendons in pre-stressed concrete bridge (Yuyama et al., 2007)

At Cardiff University, extensive studies of damage assessment in concrete structures using Acoustic Emission have been carried out. This has been primarily reported by Beck (2004). These studies included identifying the most suitable sensor and method of attachment for optimum sensitivity for concrete structures, analysing laboratory-based concrete specimens using a Moment Tensor Analysis, source location of AE from fatigue cracks and the detection of damage within an in-service concrete hinge joint.

Yuyama et al. (1999) and Othsu et al (2002) studied the damage assessment associated with the Kaiser effect of reinforced concrete beams inspected with AE. The damage levels of the structures are classified based on two ratios; the "Load" ratio and the "CALM" ratio which are defined from the Kaiser effect of AE. A further example of this method was published in 2005 by Colombo et al. in association with the Japanese Society for Nondestructive Inspections (JSNDI). In this study, it was proposed that a newly developed type of AE data analysis should be used, which utilises a newly defined parameter, named the "Relaxation" ratio. This is based on the principle that the presence of AE energy during the unloading phase of an AE test is an indication of structural damage of the material and/or structure under study. This is a relatively similar description to the "CALM" ratio which had been used formerly by Yuyama et al. (1999) and Othsu et al. (2002). The values of the relaxation ratio appeared to relate to the percentage of failure load reached in a specific cycle and therefore related to the degree of damage of the beam.

A series of researchers have been interested in using AE to detect corrosion activities earlier than conventional methods such as half-cell and galvanic current measurement (Li et al, 1998, Zdunek and Prine, 1995). The experiments indicated that AE monitoring can detect the onset of rebar corrosion earlier than other methods. Idrissi and Liman (2003) carried out a similar study using AE combined with electrochemical techniques. The electrochemical techniques managed to evaluate the corrosive character of the medium used whilst the AE showed an activity characteristic of the corrosion initiation phase and the corrosion propagation phase. In addition, Yoon (2000a) carried out a test focused on assessing the AE response of corroded concrete under cyclic loading and unloading to determine the applicability of AE as a potential method of differentiating the level of corrosion in a reinforced concrete structure. This can give a further understanding on the behaviour of concrete structures affected by chloride induced reinforcement corrosion and may be considered as an earlier warning sign indicating that deterioration has occured inside the structure.

Moment Tensor Analysis (MTA) is an AE post-test analysis method used to identify the crack kinematics (crack type and crack orientation) from the recorded AE waveforms. The procedure developed for MTA was discovered by Othsu (1991) and is called **SIGMA** (**Si**mplified **G**reens function for **M**oment tensor **A**nalysis). A moment tensor analysis based on the measurement of P-wave amplitudes of detected AE waveforms is useful for quantitative evaluation of fractures in terms of crack orientation, direction of crack motions and crack type (Yuyama, 2005). Grosse et al. (1997) have developed a relative MTA method using a cluster analysis technique. A localization of the AE sources in concrete is carried out by using the first arrival times of the P-waves of the emitted signals. However, Beck (2004) concluded that any inaccuracy in determining the P-wave arrival times and amplitudes of the waveforms of an event will greatly affect the crack kinematics and location.

CHAPTER 3: EXPERIMENTAL INSTRUMENTATION AND TECHNIQUES

3.1 INTRODUCTION

This chapter explores the aspects of Acoustic Emission (AE) equipment and describes some important terms including, principles, basic procedures and data used throughout this thesis.

3.2 INSTRUMENTATION

AE instrumentation typically consists of transducers (sensors), preamplifiers, filters, amplifiers and analysis software. The following sections introduce AE instrumentation including data storage, sensor and preamplifiers that were used during this study.

3.2.1 Data Acquisition and Storage

Throughout the AE test programme, the DiSP (**D**igital **SP**ARTAN) was used. DiSP is a Physical Acoustic Corporation (PAC) product based on integrating one or more PCI-DSP cards into a computer or a multi channel chassis. The Digital Signal Processor (DSP) resides on the PCI-DSP card. A DSP is a special purpose microprocessor that is specifically made for high speed processing, data manipulation and mathematics relating to the processing of digital signals. The PCI (Peripheral Component Interconnect) is a high speed PC computer which offers 32 bit wide data paths and up to 132 Mbytes/second data transfer speed. Each PCI-DSP board provides four AE channels.

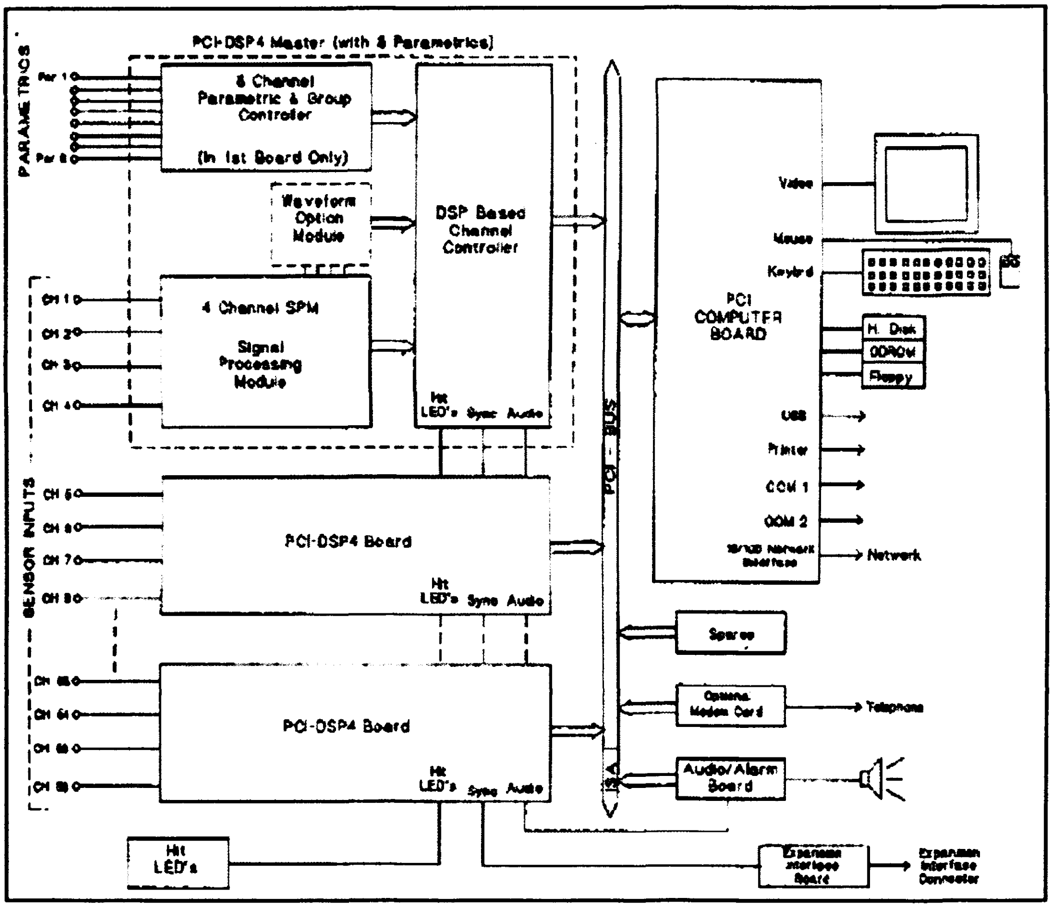

Figure 3.1: DiSP-56 System Block Diagram (PAC 2001)

The DiSP system is a fully digital, multi-channel computerized system that performs AE signal waveforms acquisition and future extraction; storing, displaying and analyzing the resulting data in real time. There are several different chassis sizes available for DiSP. They include chassis for 8, 16, 24 and 56 channels. Figure 3.1 shows a block diagram of a DiSP system. All the DiSP chassis have the same basic features regardless the number of channels. A 24 channel portable DiSP system was used throughout these tests. The DiSP-24 is a portable AE system, equipped with a handle for carrying and an integral keyboard built within the hinged front protective cover.

DiSP-LOC and DiSP-TRA are two of the software programmes that are included in the DiSP system and operated in DOS. DiSP-LOC is used for source location and for providing AE feature data (representing measurable characteristics of AE signals such as amplitude, AE signal energy, duration, counts and rise time) for a statistical analysis of the detected AE signals. The time-based information can also include parametric data from two channels. A parametric input is an external voltage proportional to a test parameter such as load, strain and deflection, which can assist in the analysis of the AE data. Standalone software, DiSP-TRA, is the transient recorder analyzer software that operates and controls the DiSP hardware to collect, transfer, display, process and store complete waveforms detected from each AE channel in the system. DiSP-TRA, enables AE signal waveforms to be recorded both independently on all channels or synchronized. In synchronized mode, the first hit channel triggers all other synchonised channels and the arrival hit-time between different channels can be determined. The speed at which the sensors are energized is negligible compared to the speed of the signal because they actually recording continuously.

AE WIN is additional software programmes that can be used in DiSP based products and operated in WINDOWS. The AE WIN program runs under the WINDOW 2000/XP operating systems. The software has all the acquisition, graphing and analysis capabilities that are expected in an AE system. Some of the AE WIN capabilities include multiple copies can be run at once, a framework for easily adding graphs is provided, has various tools bars that can be selected and many enhanced features are built in including graph zooming, panning and a setup icon toolbar. Additionally, 2D and 3D graphing are possible in AE WIN. AE Win consists of AE mode and TRA mode. AE mode is used for source location and for providing AE feature data for a statistical analysis of the detected AE signals Switching AE mode to TRA mode enables data collection options that were available in the PAC TRA programs. The most notable is the ability to collect waveform data using a synchronized and/or external trigger. The TRA mode is only a waveform collection mode.

3.2.2 AE Sensors

The main function of AE sensors is to convert the mechanical wave into an electrical AE signal. The schematic diagram of a typical AE sensor mounted on a test object is shown in Figure 3.2. The sensor is attached to the surface of the test object and a thin intervening layer of couplant is usually used. Peizoelectric sensors are principally used due to their high sensitivity, robustness, ease of use and wide range of response characteristics at a relatively low cost. The element is usually a special ceramic such as lead zirconate titanate (PZT) (McIntire and Miller 1987).

An AE sensor normally consists of several components. The wear plate protects the inside element known as the piezoelectric ceramic. The piezoelectric ceramic is the active element with electrodes on each face. One electrode is connected to earth and the other is connected to the signal lead.

The active element is surrounded by a damping material which is usually made by curing an epoxy containing high density particles. The material is designed so that acoustic waves can propagate easily with minor reflection back to the active element.

The typical AE sensor also has a case with a connector for a signal cable attachment. The case provides an integrated mechanical package for the sensor components and may also serve as a shield to minimize electromagnetic interference.

Throughout this laboratory test, the only sensor used is a Physical Acoustic Corporation (PAC) type R6D (Figure 3.3) with an operating frequency range of 35-100 kHz and resonant frequency at 60 kHz. This sensor is chosen based on a study by Beck (2004) of the optimum selection of AE sensors which suggested that the 7 kHz, 15 kHz, 30 kHz and 60 kHz resonant frequency sensors were suitable for concrete monitoring. The highest frequency was chosen in order to optimize the signal to noise ratio and because the signal attenuates quickly in concrete (Beck, 2004).

As well as resonant sensors, broadband sensors can also be used in AE. Resonant sensor implies high sensitivity over a narrow frequency range whilst broadband and wideband sensors imply high sensitivity over a large frequency range. In practice, an AE transducer can exhibit resonances but still be responsive to signal over a broad frequency range. Generally, if high sensitivity is required, a resonant type of transducer is selected. For these reasons, resonant sensors were chosen in this study. Nevertheless, for spectrum analysis, a broadband sensor is the preferred sensor.

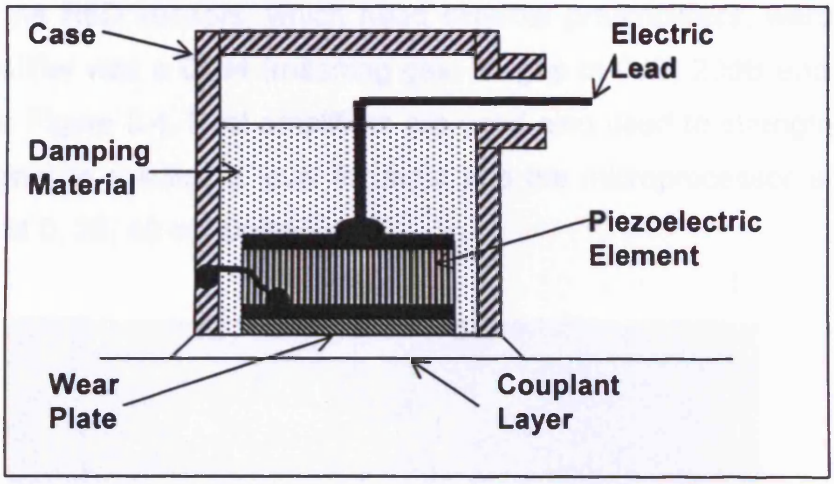

Figure 3.2: Schematic diagram of a typical AE sensor mounted on test object (Miller and McIntire, 1987)

Figure 3.3: Physical Acoustic Corporation type R6D sensor

3.2.3 The Preamplifier and Main Amplifier

According to Beattie (1983), when a cable is connected to an amplifier via a long coaxial cable, there will be a loss in sensor sensitivity. The common way to minimize interference is to place a preamplifier close to the transducer; furthermore, many transducers today are equipped with integrated preamplifiers and a variable gain amplifier in the main instrumentation. Additionally, the preamplifier provides a frequency filtering to reduce noise. In this study, the R6D sensors, which need external preamplifiers, were used. The preamplifier was a 0/2/4 (meaning gain ranges of 0dB, 20dB and 40dB) as shown in Figure 3.4. Post-amplifiers are used also used to strengthen the acoustic signal to a suitable level for input into the microprocessor and can have gains of 0, 20, 40 or 60dBAE.

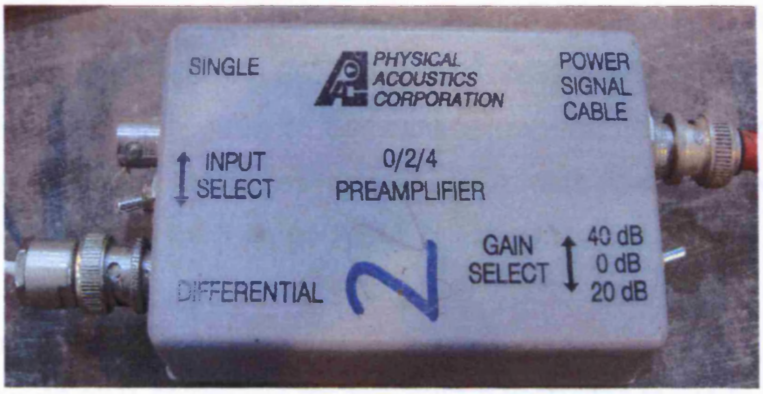

Figure 3.4: PAC's 0/2/4 preamplifier

3.3 AE TEST SET-UP

3.3.1 Hardware Set-up

System timing parameters including Peak Definition Time (PDT), Hit Definition Time (HDT) and Hit Lockout Time (HLT) are used in AE waveform measurement. These are described in the DiSP manual (Physical Acoustics Corporation 2001) and suitable values for general purpose testing are recommended. These values will depend on the objectives of the test including the test set-up and are at the discretion of the user.

The hit data set (the set of numbers representing signal features and other information, stored as result of a hit) allows selection of the measured parameters to be included in the description of each AE hit; including the waveforms that are to be collected. In the parametric set-up, hit allows a scaling of the voltage measured so that load and displacement values can be displayed in the units (kN, mm) respectively.

3.3.2 Initiation, Layout and Data Files

The most important files in the AE WIN and DiSP-LOC software are the Setup Files which are called Layout files in AE WIN and Initiation files in DiSP-LOC and distinguished by the suffix .LAY and .INI respectively. AE Test Data Files are identified by a filename extension .DTA. These are the same Setup Files but due to extensive changes in migrating to Windows, many extra capabilities have been added to the set up of the system. Therefore, the .INI file can only be used with the DOS software (DiSP-LOC) while the .LAY file can only be used with AEWIN software. However, there is compatibility between the data file structures and AE.DTA data files can be read and displayed by either the DOS or the AE WIN software.

3.3.3 Source Location Modes and Set-up

One ideal for an NDT technique for structure health monitoring is the ability to locate damage. The ability to locate sources of AE is one of the most important functions of the multi-channel instrumentation systems used in test applications. The AE wave can be detected in the form of hits on one or more channels. An event is a group of hits that is received on multiple sensors from a single signal source occurrence.

In DiSP-LOC and AE WIN there are several types of source locations - zonal, linear, arbitrary and added extras in AE WIN such as 2D planar, 3D location, cylindrical, conical and spherical. In this study linear, 2D planar and 3D location modes will be used. These modes represent the source location in one, two and three dimensions respectively. Linear location is very functional in the investigation of AE wave propagation in concrete structures and in monitoring crack propagations when the position of the source is known to be somewhere along a straight line between a pair of transducers attached to the beam. A three dimensional approach is required when monitoring large structures, such as bridges, to identify the exact location of the damage.

3.3.4 Graphical Data Displays

In this study, two different software packages DiSP-LOC and AE WIN were used to produce a variety of graphical displays. The graphical data displays can be redisplayed, changed and verified during the post-test analysis. Brief descriptions of the different types of display used in this study are as follows:

A. Historical plot

Historical plots illustrate the change in AE parameter with time. They provide an indication of source activity intensity throughout the assessment. AE parameters such as events, absolute energy, hits, counts are important and can be studied in an historical plot display. Figure 3.5 shows an example of an historical plot.

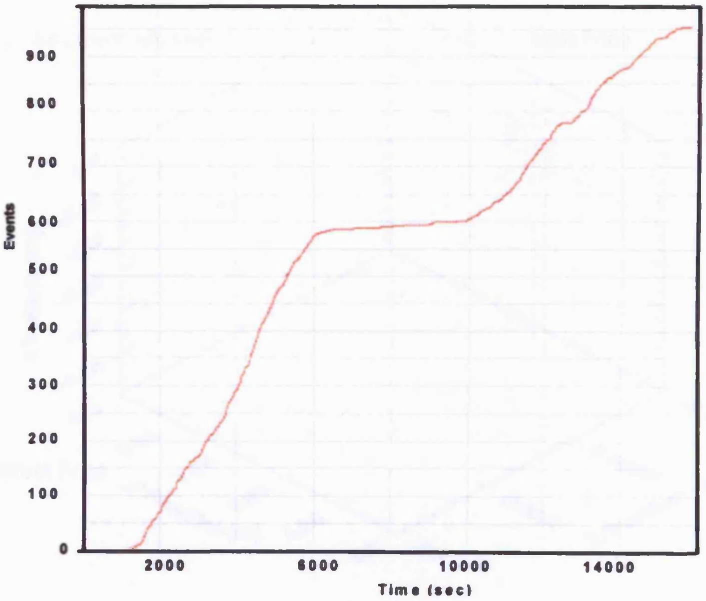

Figure 3.5: Cumulative events recorded with respect to time.

B. Location plot

A location plot is a representation of AE sources computed using an array of transducers. There are several types of source location modes. For example, a linear location plot (Figure 3.6), a 3-dimensional plot (Figure 3.7) and a 2-dimensional planar location plot (Figure 3.8). Source location plots have been used extensively throughout this thesis and are discussed in each set of results from both laboratory experiments and on-site monitoring.

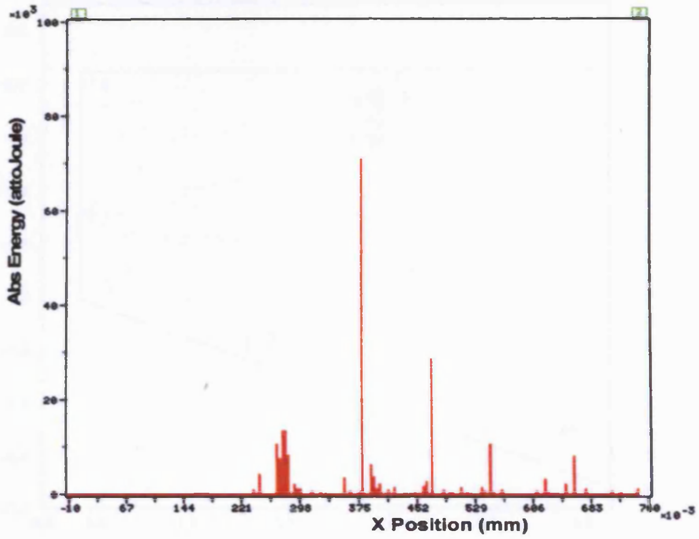

Figure 3.6: 2D linear location plot from DiSP-LOC.

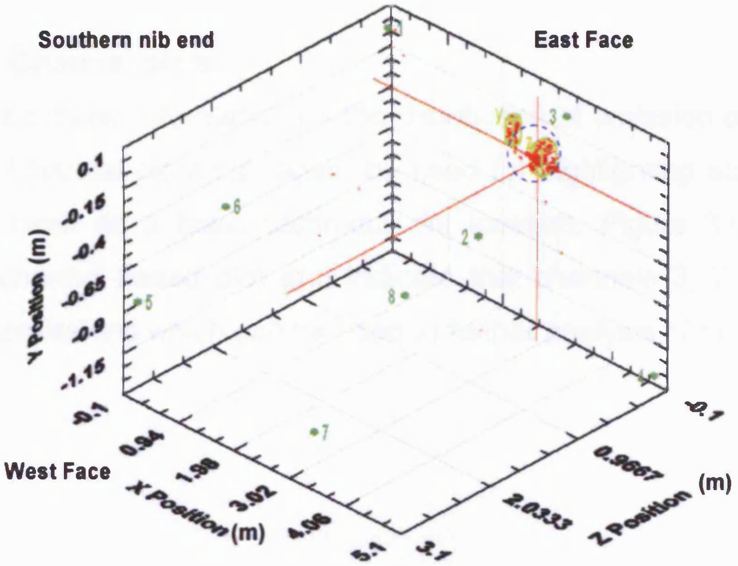

Figure 3.7: 3D location plot from AE Win.

A cluster location can be seen in Figures 3.7 and 3.8. A cluster location is an area that contains an AE source of such significance that it crosses a predefined threshold number of events in a predefined volume. This allows ranking of sources found using location monitoring. These event groups (clusters) are shown on the location plot and identify active regions. Moreover, cluster data can be shown in a tabular form which allows a comparative assessment of the activity.

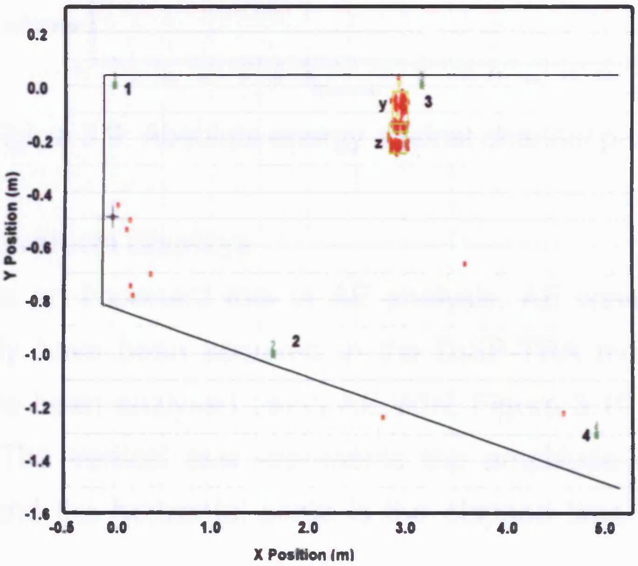

Figure 3.8: 2D location plot from AE Win

C. Channel plots

Channel plots provide information on the distribution of emission over a series of channels. Channel plots can again be used for highlighting active regions and can be used as a basic technique for location. Figure 3.9 shows an example of channel-based plot and indicate that channels 3, 7, 10 and 11 identify high emissions which can be used in further analysis of their location.

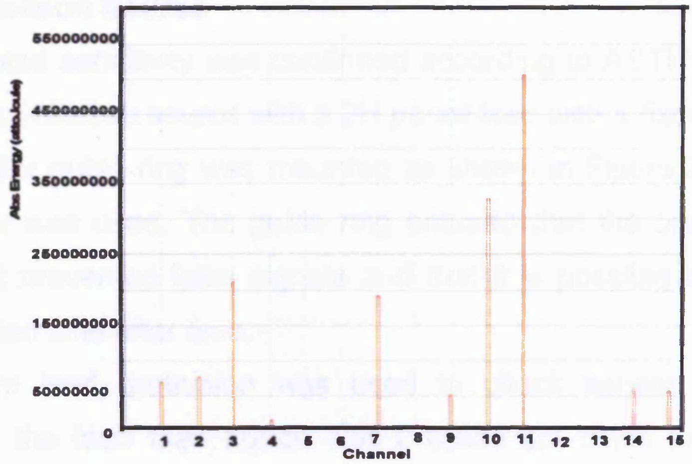

Figure 3.9: Absolute energy against channel plot.

D. Waveform displays

AE waveform is an important tool in AE analysis. AE waveforms obtained during this study have been acquired in the DISP-TRA mode of the DISP system and have been analysed using AE WIN. Figure 3.10 shows a typical AE waveform. The vertical axis represents the amplitude of the signal in millivolts [mV] and the horizontal scale is the elapsed time from the trigger point.

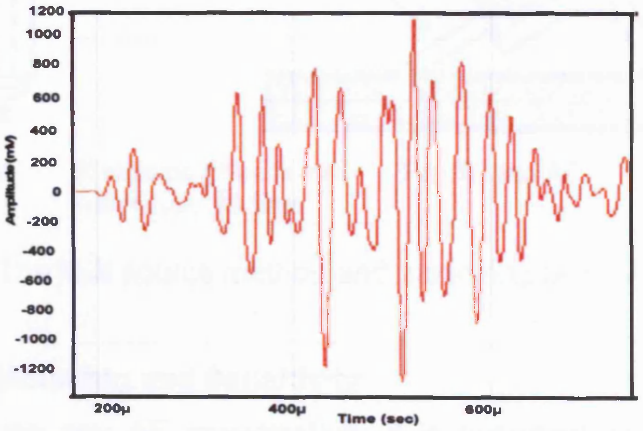

Figure 3.10: Waveform display.

3.3.5 Hsu-Neilson Source

Sensor mounted sensitivity was confirmed according to ASTM E 976 (1999), by using a Hsu-Nielsen source with a 2H pencil lead with a fixed guide tube to which a smaller guide ring was mounted as shown in Figure 3.11. A 0.5mm lead diameter was used. The guide ring ensured that the breaking position was stable, it prevented false signals and that it is possible to reproduce a similar emission time after time.

A 3mm lead protrusion was used to check sensor sensitivity. To achieve this, the lead feed button was pressed six times to achieve. The pencil was slanted towards the specimen surface until the guide ring rested on the specimen. The pencil was then pivoted on the point of contact to a steeper angle point thus causing the lead to break.

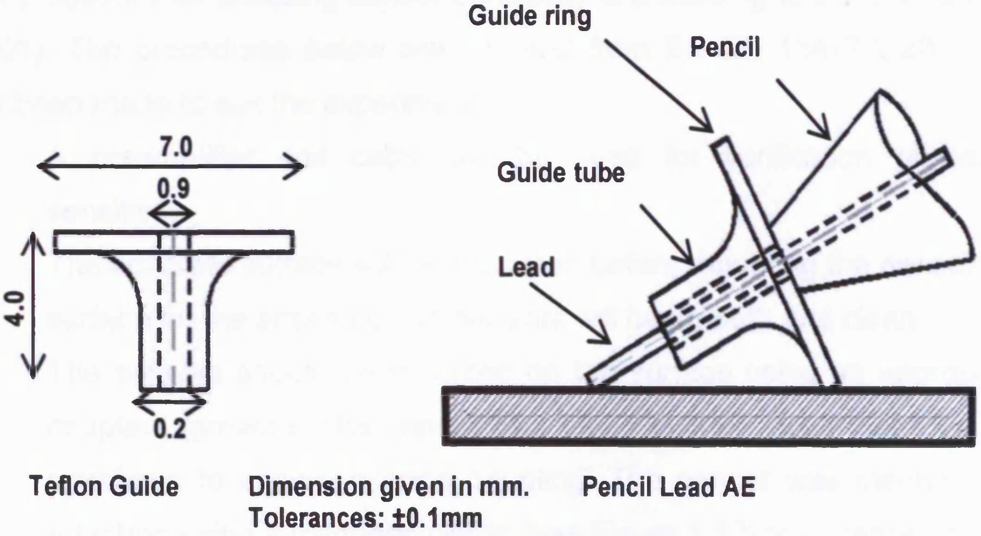

Figure 3.11: The H-N source method and guide ring (ASTM E976, 1999).

3.3.6 Sensor Mounting and Sensitivity

Before performing any AE investigation, it is important to ensure that all sensors are correctly mounted. Poor mounting of the sensor will reduce the sensitivity and lead to a loss of significant AE data. Most importantly, before mounting the sensor on the test specimen, preparation of the test specimen surfaces has to be undertaken. At the sensors location, the surface has to be cleaned and prepared to eliminate all irregularity to ensure total area contact between the sensors and the test specimen surfaces.

The piezoelectric sensor must be attached to the material under observation ensuring that the acoustic energy passes into the transducer with minimum loss at the transducer-material interface. The required intimate mechanical contact is achieved on flat surfaces by mechanical clamping using thin films of grease as a couplant between the transducer and the material. The objectives of the practice for checking sensor sensitivity are as follows:

i. to give a measure of the strength of response;
ii. to determine whether the sensor is serviceable or not; and
iii. to check the standardized performance of the sensor.

The procedure for checking sensor sensitivity is according to BS EN 13477-2 (2001). The procedures below are adopted from BS EN 13477-2:2001 that had been made to suit the experiment:

i. A preamplifier and cable will be used for verification of sensor sensitivity.
ii. The concrete surface will be prepared before mounting the sensor; the surface for the attachment of sensors will be smooth and clean.
iii. The sensors should be mounted on the surface using an appropriate couplant (grease). The sensor was pressed firmly down onto the test specimen to ensure a good coupling. The sensor was mechanically attached using a magnetic clamp (see Figure 3.12) to ascertain a good connection between the sensor and the surface of test specimen, The clamp holds the sensor in position for the entire test and ensures constant force between the test specimen and the sensor (Figure 3.13).
iv. A Hsu-Nielsen source was used to check the sensitivity of the sensor by using a pencil lead breaks. A minimum of 3 lead breaks at the prescribed position were made on the test specimen. If the difference between the lowest and highest amplitude was more than 3dB, the

procedure was repeated until a set of 3 consistent breaks had been achieved.

v. This procedure was repeated for all the sensors to confirm their sensitivity.

If a sensor gave a low signal amplitude reading (below 97dB), the magnetic clamp was checked as it may be either too tight or loose. The sensor sensitivity was then checked again using pencil lead breaks (Hsu- Nielsen source). If the readings were still low, the specimen surface where the sensor was attached was checked to make sure it was smooth and clean. If the surface was not smooth, sand paper was used. The sensor is then mounted back to the surface using grease as a couplant and again tightened using a magnetic clamp. If the problem reoccurs, the cable was checked and if possible replaced. If all this failed, the sensor was recorded as faulty and returned to the manufacturer for checking.

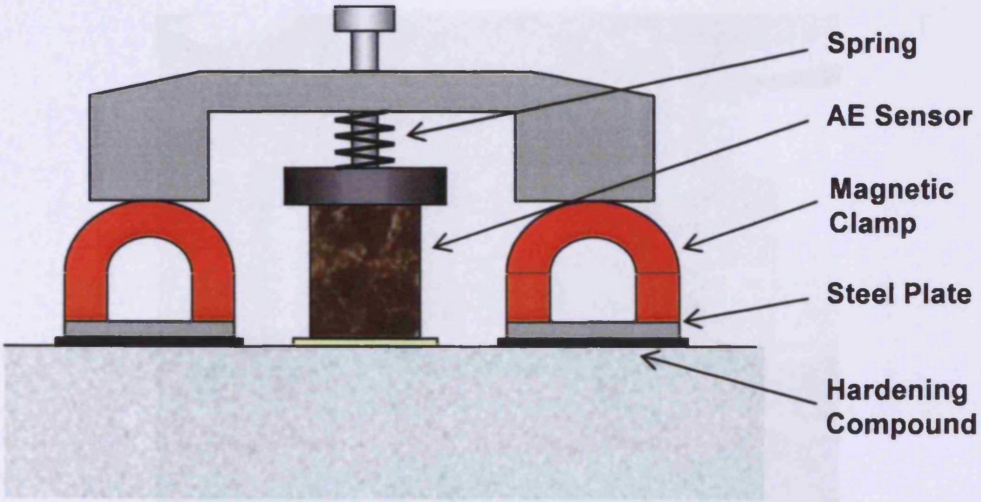

Figure 3.12: Magnetic clamp

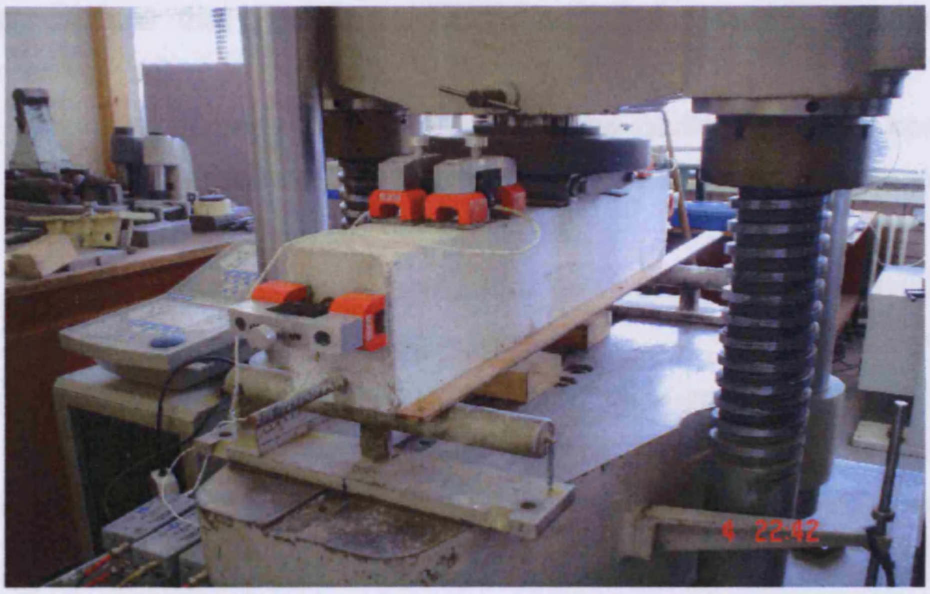

Figure 3.13: The application of magnetic clamp in laboratory test

3.4 Mechanical Testing

Mechanical testing of the pre-corroded and post-corroded concrete specimen was carried out using a 60t Avery-Denison Testing Machine retrofitted with a Dartec-9600 digital feedback control system as shown in Figure 3.14.

Figure 3.14: Avery-Denison Testing Machine.

The precautions that were taken before and during testing the concrete specimen with AE were as follows:

a) A layer of rubber was placed between the loading point and concrete specimen to minimise any unwanted noise that might be recorded by the AE sensors.

b) A very low load (1kN) was applied for 2 minutes to ensure that no noise was recorded from the testing machine.

c) At least 2 minutes was allowed between each loading step and before pausing the DiSP system in order to check for visible damage.

d) Visible damage was recorded by digital camera and sketches of the damage were produced.

CHAPTER 4: LABORATORY FLEXURAL TESTING ON REINFORCED CONCRETE BEAM WITH PRE AND POST CORRODED REINFORCING BAR

4.1 INTRODUCTION

This chapter contains a detailed description of the experimental work carried out and highlights the procedures followed during the laboratory stage of the project. This section covers the materials, the initial casting and preparation of the specimens and finally the four-point bending test monitored using Acoustic Emission (AE) sensor system. As well as this, the problems encountered, possible sources of error and the precautions taken have been included.

A parameter-based approach was used in the analysis of data acquired by the AE instrumentation. The parameter-based approach evaluates relative AE activities based on the measurement of parameters such as hits, amplitudes, absolute energy, etc. This method of analysis has been shown to be sensitive to the initiation and the growth of cracks within materials and structures. Moreover, the application of Time of Arrival (TOA) method has been used to determine the location of the damage area in linear location between sensors.

Two types of test specimen have been used in this laboratory work: pre-corroded (PR) specimen and post-corroded (PS) specimen. The corroded reinforcement exhibited a reduction of the bar section and also degradation of the composite bond between steel rebar and concrete. Pre-corroded reinforcement was cleaned before being cast in the concrete but for post-corroded reinforcement, the corrosion product was developed inside the beam, while experiencing an impressed current to accelerate the corrosion.

4.2 AIMS AND OBJECTIVES

The aims and objective of these experiments using parameter analysis were:

i. To relate AE absolute energy to the behaviour of the reinforced concrete beams due to chloride-induced reinforcement corrosion at various levels.
ii. To investigate the TOA method for locating and following the progression of a crack.

4.3 MATERIAL DETAILS

The water to cement ratio used was 0.56 and the material proportions were 1:2:2.5:0.56 by weight of cement, sand, aggregate and water respectively and the concrete design strength was 40MPa (the actual strength at 28days was 48MPa).

A total of 48 concrete cubes (100mm x 100mm), 12 cylinders (100mm x 200mm) and 16 reinforced concrete beams (100mm x 150mm x 750mm) were cast. Figure 4.1 shows the dimensions of the reinforced concrete beam specimens.

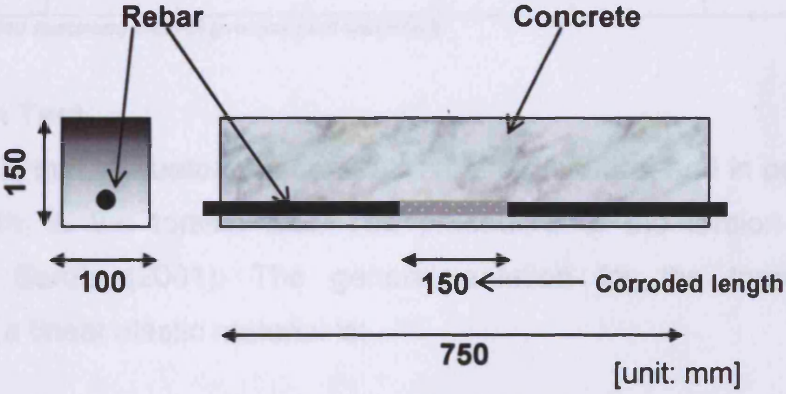

Figure 4.1: Dimension of concrete beam specimen.

4.4 HARDENED CONCRETE TEST

4.4.1 Compression Test

The cube compression tests were performed using a Contest GD10A Compression Testing Machine, compliant with the British Standards (BS 1881: Part 116: 1983). Tests were performed in order to determine the compressive strengths of the concrete mixes used. Tests at 7 and 28 days were performed primarily in order to observe the consistency of the concrete mixes and to classify the concrete used for the Acoustic Emission tests.

The procedure of the compression test is given in BS 1881: Part 116: 1983. Table 4.1 shows the concrete compressive strength of all the specimens.

Table 4.1: Concrete cube compressive strength

Concrete	**Cube Compressive Strength (MPa)**							
	7 Days		**28 Days**		**36 Days**		**60 Days**	
	Specimen	**Average**	**Specimen**	**Average**	**Specimen**	**Average**	**Specimen**	**Average**
A **(PS)**	38.84 38.19 39.40	**38.81**	48.80 48.10 47.50	**48.13**	53.20 52.60 53.90	**53.23**	54.20 55.30 54.60	**54.70**
B **(PS)**	39.52 38.30 38.42	**38.71**	50.50 48.80 47.30	**48.87**	52.60 53.60 52.80	**53.00**	54.30 55.80 55.10	**55.07**
C **(PR)**	38.28 39.73 38.16	**38.72**	48.40 49.10 48.60	**48.70**	53.30 54.60 54.30	**54.07**	54.90 55.60 56.20	**55.57**
D **(PR)**	35.62 37.89 38.00	**37.17**	48.40 45.50 46.97	**46.96**	52.50 50.60 51.30	**51.47**	55.80 54.00 52.90	**54.23**

Note: PS (post-corroded specimen) and PR (pre-corroded specimen)

4.4.2 Torsion Test

One of the tests that evaluates the concrete's characteristics, and in particular tensile strength, is the torsion test. The procedure of the torsion test is according to Sardis (2001). The general solution for the torque-twist relationship of a linear elastic material is:

$$\frac{T}{J} = \frac{\tau}{r} = \frac{G\phi}{L} \qquad \textbf{(4.1)}$$

Where:

T = torque applied

J = polar second moment of area of the cross-section

τ = shear stress at radius r

r = an average radius
G = shearing modulus
L = length over which rotation Φ is measured

The equation can be rearranged in order to determine the shear stress and shearing modulus respectively:

$$\tau = \frac{Tr}{J} \qquad \textbf{(4.2)}$$

$$G = \frac{TL}{\phi J} \qquad \textbf{(4.3)}$$

For a brittle material, which is weak in tension, failure in a torsion test is expected to happen by tensile fracture at 45° to the longitudinal axis of the core. According to Norris et. al. 1990 (as cited in Sardis, 2001), the maximum elastic shear stress f_{smax} at the surface of the specimen approaches a limiting value equal to 0.85 times the uniaxial tensile strength of the material f_t.

$$f_{s\max} = 0.85 f_t \qquad \textbf{(4.4)}$$

The torsion test method used in this work was developed from Norris et. al.,1990 (as cited in Sardis M., 2001). In this test, torsion rings are used to apply equal and opposite couples to each end of the test specimen. Two supports provide upward reactions; and a load is applied to the free end. Corresponding reactions are generated at the two supports. The load is transferred from the rig into the concrete core by a set of split collars, attached to either end of the test specimen using a small amount of adhesive, and drawn together around the core by hand tightening pairs of nuts.

The system of load and reaction points has been designed such that the distance between the pairs of loads on the collars is fixed at 250mm. Thus the applied torque can be expressed as:

$$T = 0.25P \qquad \textbf{(4.5)}$$

Stergianos, (2000) notes that the test also enables the indirect evaluation of Young's modulus of elasticity of the concrete. With Poisson's ratio, *v* taken as 0.2 for concrete which is generally acceptable, the E_c modulus is determined as:

$$E_c = 2G(1+v) \tag{4.6}$$

Figure 4.2 shows the torsion test specimen arrangement that had been used in this test. Table 4.2 shows the torsion test results.

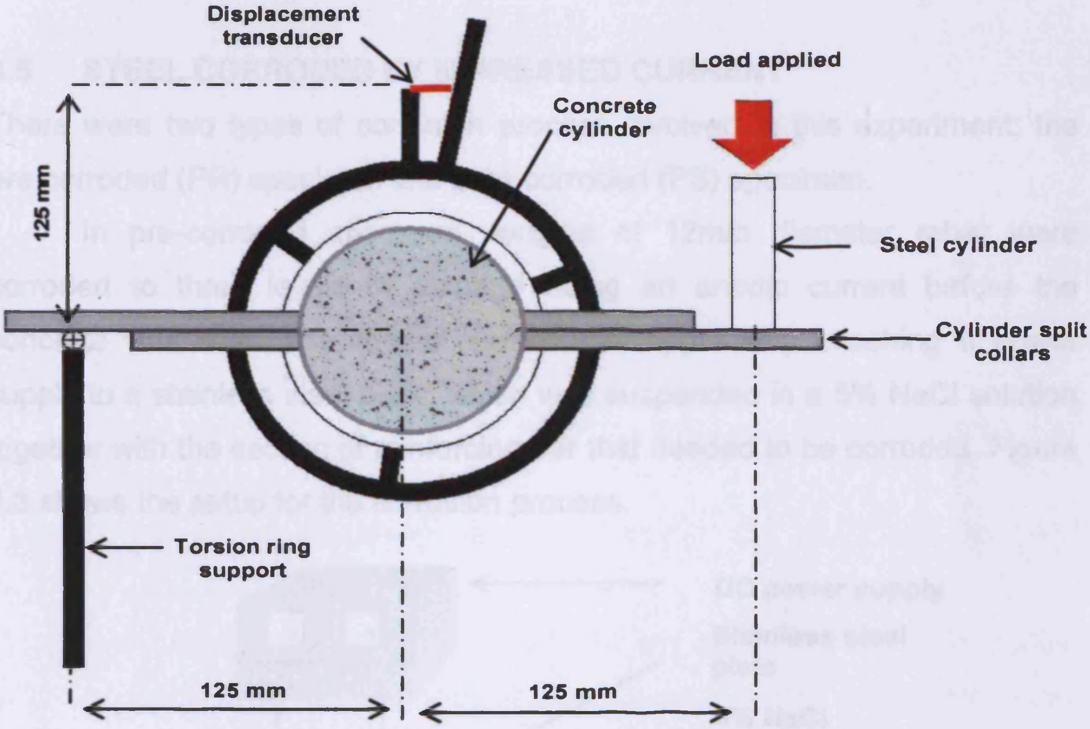

Figure 4.2: Torsion test specimen arrangement (Sardis M., 2001)

Table 4.2: Torsion Test Results – Tensile Strength (f_t)

Concrete	P_{max} (kN)	T_{max} (kNm)	f_s (MPa)	f_t (MPa)	$f_{t, mean}$ (MPa)	E (MPa)	E_{mean} (MPa)
A (PS)	2.73	0.68	3.46	4.07	4.07	26.40	26.40
	2.72	0.68	3.46	4.07		26.40	
	2.72	0.68	3.46	4.07		26.40	
B (PS)	2.94	0.73	3.72	4.38	4.00	28.32	25.92
	2.58	0.65	3.31	3.90		25.20	
	2.48	0.62	3.16	3.72		24.24	
C (PR)	2.74	0.69	3.51	4.13	4.15	26.88	26.96
	2.65	0.66	3.36	3.95		25.68	
	2.92	0.73	3.72	4.38		28.32	
D (PR)	2.72	0.68	3.46	4.07	3.84	26.40	24.96
	2.48	0.62	3.16	3.72		24.24	
	2.48	0.62	3.16	3.72		24.24	

Note: PS (post-corroded specimen) and PR (pre-corroded specimen)

4.5 STEEL CORRODED BY IMPRESSED CURRENT

There were two types of corrosion process involved in this experiment: the pre-corroded (PR) specimen and post-corroded (PS) specimen.

In pre-corroded specimen, lengths of 12mm diameter rebar were corroded to three levels of damage using an anodic current before the concrete was cast. The anodic current was applied by attaching a power supply to a stainless steel plate, which was suspended in a 5% NaCl solution together with the section of reinforcing bar that needed to be corroded. Figure 4.3 shows the setup for the corrosion process.

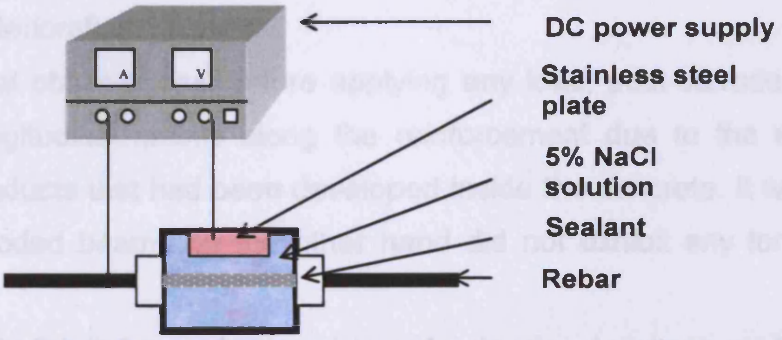

Figure 4.3: Setup for corrosion process for the pre-corroded specimen.

In the post-corroded specimens, a middle section of the reinforced concrete beam (100mm x 150mm x 750mm) was attached to an acrylic tank, facilitating immersion in 5%NaCl solution. The anodic current was applied by attaching the power supply to a stainless steel plate, suspended in the solution as shown in Figure 4.4.

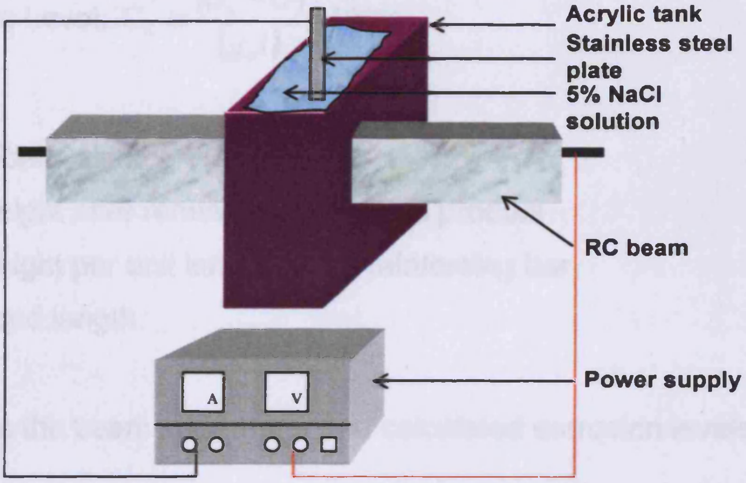

Figure 4.4: Setup for corrosion process for post-corroded specimens.

For all beams tested in this study, the reinforcement was corroded while the beams were unloaded. Mainly, the corrosion will affect:

i. the steel, due to reduction of the rebar cross section
ii. the concrete, due to cover cracking produced by the expansion of the corrosion products
iii. the composite action of the concrete and steel due to bond deterioration.

From physical observations, before applying any load, post-corroded beams exhibited longitudinal cracks along the reinforcement due to the extensive corrosion products that had been developed inside the concrete. It was noted that pre-corroded beams on the other hand did not exhibit any longitudinal cracks.

The actual degree of corrosion, or corrosion level was accordingly measured as the ratio of loss in weight of the reinforcement steel bar to the weight of the bond length before corrosion, thereby representing an average corrosion level along the bond length, as used by Fang et. al. (2001).

The corrosion level (as a percentage) is expressed using the following equation:

$$\text{Corrosion Level, } C_R = \frac{(G_o - G)}{(g_o l)} \times 100\% \qquad \textbf{(4.7)}$$

Where:

G_o = initial weight
G = weight after removal of corrosion product
g_o = weight per unit length of the reinforcing bar
l = bond length

Table 4.3 shows the beam specimens and calculated corrosion levels, C_R.

Table 4.3: Beam specimens and corrosion level.

Beam Specimens	**Corrosion Level, C_R(%)**
Pre-corroded	
A11PR	**0**
B11PR	**7.80**
C11PR	**15.60**
D11PR	**20.30**
A22PR	**0**
B22PR	**8.60**
C22PR	**16.00**
D22PR	**22.60**
Post-corroded	
A11PS	**0**
B11PS	**9.60**
C11PS	**17.00**
D11PS	**33.45**
A22PS	**0**
B22PS	**8.90**
C22PS	**14.69**
D22PS	**31.30**

Note: PR (pre-corroded specimen) and PS (post-corroded specimen)

4.6 FOUR POINT BENDING TEST MONITORED BY AE

The concrete beam specimens were tested using four-point flexural loading. The concrete mixture described earlier was used. Beam specimens with various corrosion levels (as presented in Table 4.3) were tested to simulate different levels of damage. Six R6D sensors with a frequency range of between 35-100 kHz and were used throughout the test. Their calibration certificates are presented in Appendix A. The DiSP systems hardware was set-up with threshold level of 40dB, the sample rate was 1000 kiloSample per second (kSPS), Peak Definition Time (PDT) was 1000μseconds, Hit Definition Time (HDT) was 2000μseconds and Hit Lockout Time (HLT) was 500μseconds. All the active channels were set-up according to these characteristics throughout the test. The description of the testing machine that was used in mechanical testing was as describe in section 3.4 in Chapter 3. The sensor arrangement is shown in Figure 4.5.

The test procedure was:

i. Sensor mounted and sensitivity checked according to section 3.3.5 in Chapter 3.
ii. Centre displacement of the beam was measured using LVDT located at the centre point of the beam with the tensile face of the beam facing downward.
iii. Load was applied to the compressive face of the beam through two mechanical rollers spaced 135mm in a stepwise static loading. Rate of loading remained constant at 0.25kN/sec.
iv. LVDT was initially zeroed, the load applied to the preload of 0.5kN to hold the beam in place.
v. The first load step was from 0.5kN to 2.5kN. AE was recorded continuously from the start of this load cycle to the first step of load.
vi. At the end of each loading cycle, the load was held for 2 minutes and paused to record any visual observation before reapplying the load.

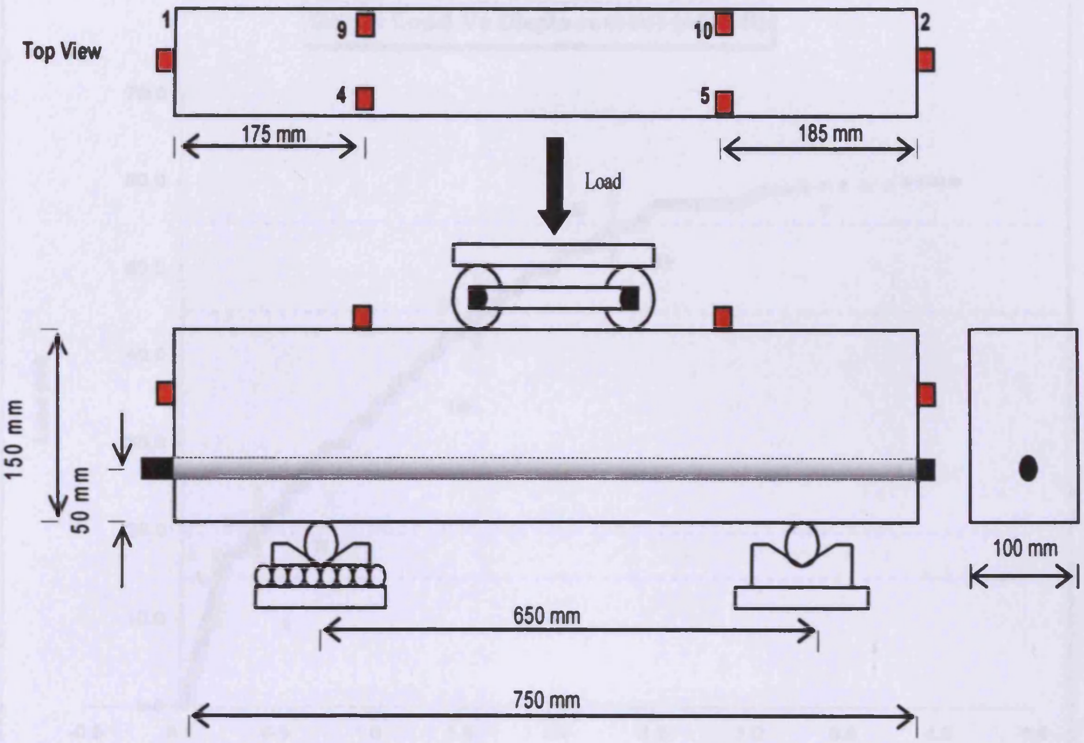

Figure 4.5: Sensor arrangements for the four point bending test.

4.7 RESULTS FOR PRE-CORRODED SPECIMENS

The mechanical behavior of concrete subjected to different loading conditions is governed by the initiation and propagation of the internal cracks and flaws during loading. Figure 4.6 shows the actual curve for the beam A22PR. Referring to this curve, the mechanical behaviour of reinforced concrete beam can be divided into five stages of failure:

i. Micro-cracking
ii. Localized crack propagation (**Point A)**
iii. Distributed flexural cracking (**Point B)**
iv. Shear cracking (**Point C)**
v. Damage localization (**Point D)**

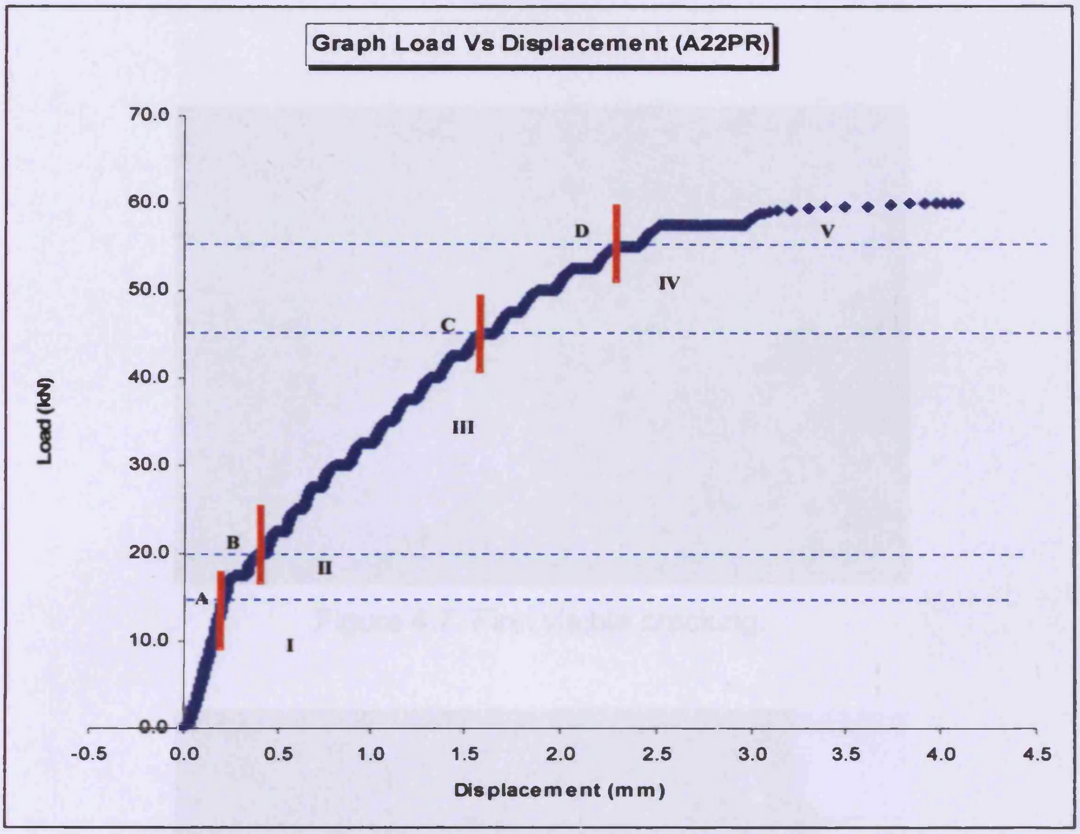

Figure 4.6: Load against displacement for beam A22PR

The micro-cracking occurs in region I (before point A). Initiation of the internal micro-cracking is negligible during the first stage. The first visible cracking was observed at point A. Before point A, no visible cracking could be detected by the naked eye. Photographs showing the progression of the visible damage are presented in Figure 4.7 to Figure 4.11.

Micro-cracking at the centre of the beam (where the maximum bending moment occurs) indicates that the damage starts to localize (after point A) which could not be detected by the naked eyes. Figure 4.7 shows the first crack that able to be detected on the concrete surface (point A). The second stage of the failure known as localized crack propagation and it occurs in region II or in between points A and B. The cracks occur primarily in the constant moment region because this is where the highest flexural stress occurs.

Figure 4.7: First visible cracking.

Figure 4.8: Distributed flexural cracks.

Figure 4.9: Beam failed in shear mode.

Figure 4.10: Damage localization.

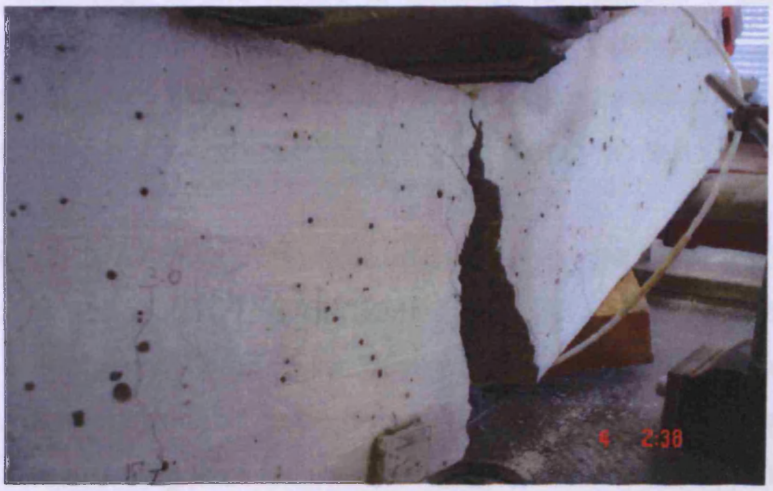

Figure 4.11: Beam failed in flexural mode.

Point B indicates the starting point of the distributed flexural cracks on the beam prior to loading. In region III, the cracks were randomly distributed over the specimen surface and propagated upward from the tensile zone to the compression zone of the beam as the load increased (Figure 4.8).

Due to vertical loading, bending moments and shear forces would have develop in the beam. When the beam is subjected to four points bending, the maximum shear forces are between the supports and the loading point and zero in the loading region, whilst for the bending moment, the maximum moment is between the two loading points of loading and increasing from the supports to the loading point. In reality, shear failures are failures under combined shear and bending between the supports and the loading points. In this area, an element in the beam would be subjected to shear stress and to horizontal normal stresses due to bending. When the principal stress in which the principal tensile stresses reach the tensile strength of the concrete, a diagonal crack will develop. The formation of the diagonal cracks can be seen clearly at point C and in Figure 4.9 and the crack propagated diagonally in region IV. Most of the beams failed in flexure/bending and did not experience the shear cracking typified in region IV. The former happens when the ratio of reinforcement to the concrete is reduced because of the corrosion of the cross section of the reinforcement, which modifies the type of failure of the concrete beams.

The final stage of the failure is damage localization (Figure 4.10) or strain localization (Shah. et. al., 1995). Region V indicates that the crack starts to localize into a major crack and which becomes wider with increasing load. The critical crack length can be observed clearly as the load reaches the peak load.

Visual observation is important in determining the failure stages of the reinforced concrete beams. The formation of the first visible crack, the random distribution of the flexural cracks, the development of the shear crack and also the critical crack length need to be determined from the experiment by visual inspection. The five stages of failure are based on the visual observations that have been made throughout the tests and the results of these tests will be basically in accordance with these stages. Table 4.4 below summaries the identification of points A, B, C, and D for all the beams tested.

Table 4.4: Summary of points A, B, C and D for all the tested beams.

Specimen	**Load at point (kN)**				
	A	**B**	**C**	**D**	**Failure**
Pre-corroded					
A11PR (0%)	**15.0**	**17.5**	**45.0**	**55.0**	**59.21**
B11PR (7.80%)	**15.0**	**25.0**	**-**	**42.5**	**54.77**
C11PR (15.60%)	**15.0**	**20.0**	**-**	**25.0**	**34.81**
A22PR (0%)	**15.0**	**20.0**	**45.0**	**55.0**	**59.54**
B22PR (8.60%)	**15.0**	**20.0**	**40.0**	**45.0**	**47.50**
C22PR (16.00%)	**15.0**	**20.0**	**-**	**25.0**	**35.08**
D22PR (22.60%)	**15.0**	**20.0**	**-**	**20.0**	**23.46**

Note: The percentage corresponds to the level of corrosion using C_R as in Equation 4.7.

The AE source location analysis was also performed according to these five stages of mechanical behavior. AE can be used to obtain a warning of developing distress and the growth of internal micro-cracking at the critical locations. Evidently, a comparison between visual observations of each failure stages and AE source location analysis indicate that the damage area due to cracking can be identified by the AE source location technique.

One of the control beams that failed in shear (A22PR) will be explained in detail and will be compared with one of the beams that failed in flexure (C22PR). This section assesses the ability of AE to detect, locate and monitor the behaviour of different levels of pre-corroded reinforced beam specimens. The results of the pre-corroded test beams will be presented in Appendix B.

A22PR was the control beam with no corrosion of the steel rebar. The beam's behaviour can be divided into five stages of failure which are micro-cracking, localized crack propagation, distributed flexural cracks, formation of shear cracks and damage localization prior to complete failure.

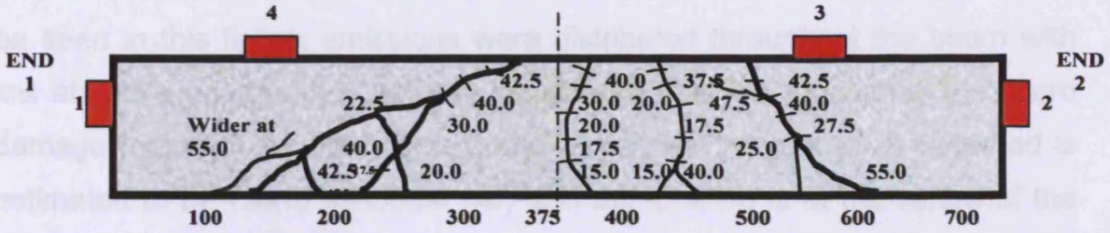

(a) Side view (Loads in kN)

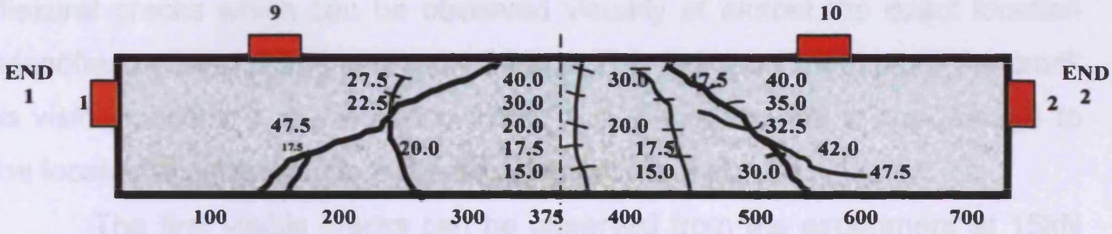

(b) Side view (Loads in kN)

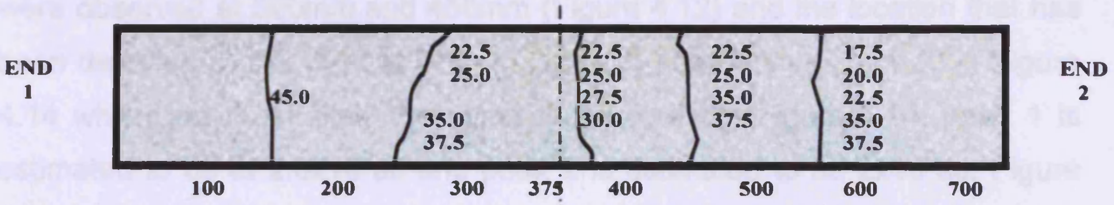

(c) Bottom view (Loads in kN)

Figure 4.12: Crack pattern from visual observation for A22PR showing crack progressing with load in kN.

Figure 4.12 indicates the crack pattern (showing crack growth stages with load) from visual observation for A22PR. Results from the AE will be compared with the observations recorded in this figure as evidence of the capability of the AE method. The first cracks were observed visually on both beam surfaces at approximately 390mm and 420mm in Figure 4.12 (a) and 390mm and 450mm in Figure 4.12 (b) at 15kN. As the load was increased, the initial cracks propagated upward to the compression zone and the formation of a diagonal shear crack occurred at 45kN before failure at 59.54kN.

Figure 4.13 shows the AE linear location in terms of Absolute Energy and x-axis during the first stage of failure that is microcracking. The loading is between 0-12.5kN before the visible cracks were observed at 15kN. As can be seen in this figure, emissions were distributed throughout the beam with low absolute energy level but it is considered that this represents the micro damage (non-visible) that occurs in the beam. The highest peak observed is estimated to be $75\text{x}10^3$attoJoule (aJ) and the location is at the centre of the beam. It is more likely that the emission was from the micro damage of the flexural cracks which can be observed visually at almost the exact location identified by the AE and at a load of 15kN. This indicates that before the crack is visibly observed, the emission from AE had enabled the micro-damage to be located accurately before the actual impairment occurs.

The first visible cracks can be observed from the experiment at 15kN and the AE source location output is shown in Figure 4.14. The actual cracks were observed at 390mm and 450mm (Figure 4.12) and the location that has been detected by AE were at 375mm (zone 1) and 440mm (zone 2) in Figure 4.14 which are most likely the same location. From Figure 4.14, peak 1 is estimated to be at $2.6\text{x}10^6$aJ and peak 2 is estimated to be $2\text{x}10^6$aJ. Figure 4.15 shows an event in arbitrary source location at 15kN when the first concrete crack occurred. From the AE line data, the first hit sensor was sensor 2 with amplitude of 85dB and $1.9\text{x}10^6$aJ of absolute energy. Sensor 3 was the second hit sensor with amplitude of 78dB and $0.24\text{x}10^6$aJ. By examination of Figure 4.15, the direct source-to-sensor distance was calculated and indicates that the event occurred at 360mm from sensor 2.

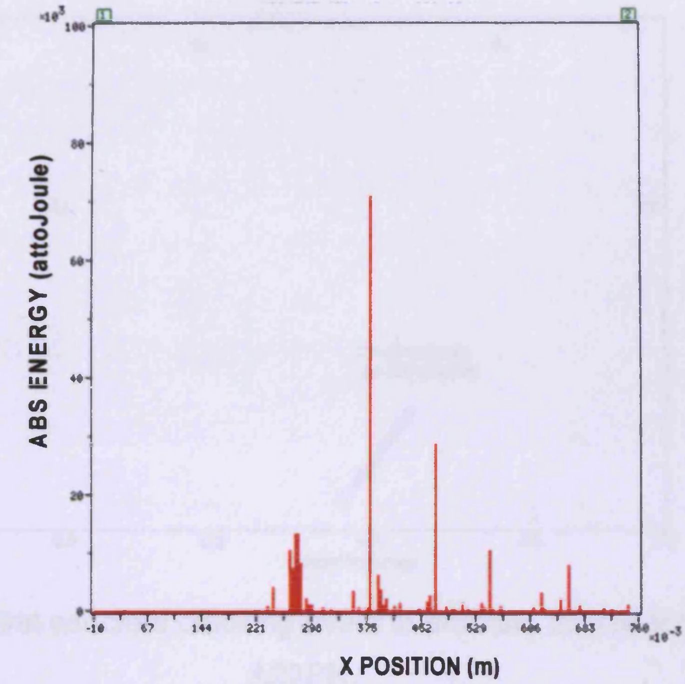

Figure 4.13: Source location of total emission during micro-cracking (0-12.5 kN) for beam A22PR

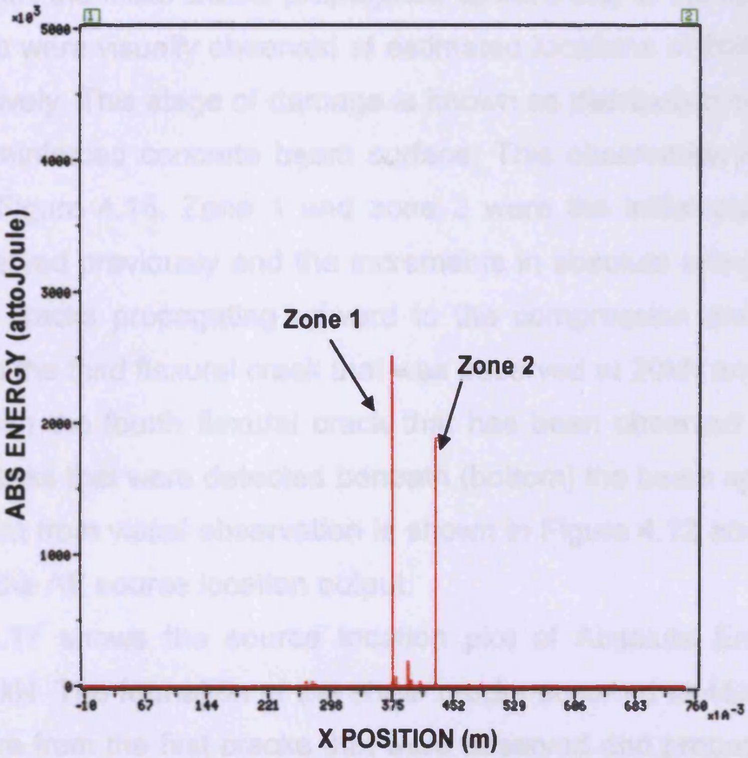

Figure 4.14: Source location of total emission at the start of the localized crack propagation (0-15.0kN) for A22PR

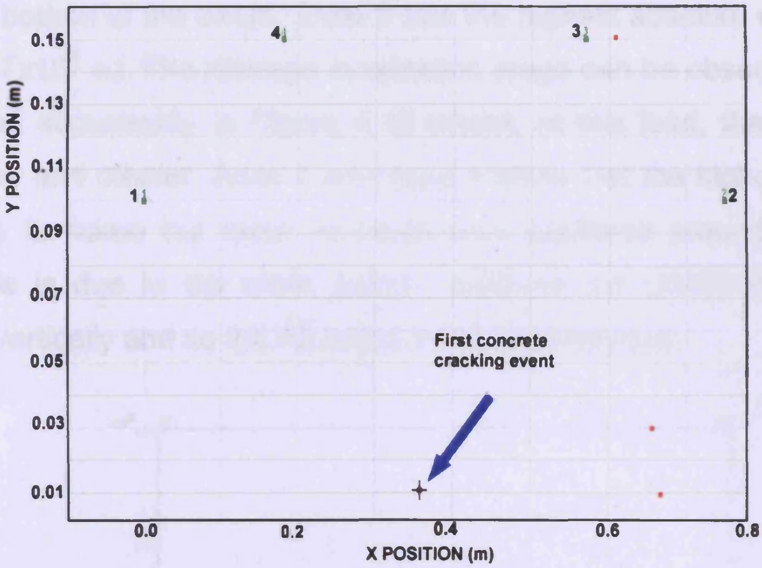

Figure 4.15: First concrete cracking event in arbitrary source location for A22PR.

At 20kN and 25kN the initial cracks propagated upward and at the same time two more cracks were visually observed at estimated locations of 260mm and 550mm respectively. This stage of damage is known as distribution of flexural cracks on the reinforced concrete beam surface. This observation is shown acoustically in Figure 4.16. Zone 1 and zone 2 were the initial cracks that have been observed previously and the increments in absolute energy levels are due to the cracks propagating upward to the compression area of the beam. Zone 3 is the third flexural crack that was observed at 20kN and zone 4 is associated with the fourth flexural crack that has been observed at 25kN including the cracks that were detected beneath (bottom) the beam specimen. The crack pattern from visual observation is shown in Figure 4.12 and can be compared with the AE source location output.

Figure 4.17 shows the source location plot of Absolute Energy for events up to 45kN. The formation of the shear cracks occurred at 45kN. Zone 1 and zone 2 are from the first cracks that were observed and propagated up the side and across the bottom of the beam. Zone 3 is related to the shear cracks and zone 4 is associated with the flexural cracks that propagated across the bottom of the beam. Zone 3 has the highest absolute energy level at almost 47×10^6 aJ. The damage localization stage can be observed visually at 55kN and acoustically in Figure 4.18 where, at this load, the cracks are getting wider and clearer. Zone 3 and zone 4 show that the highest peak did not change its value but more emission was scattered around the failure cracks. This is due to the crack pattern because the cracks do not grow absolutely vertically and so the AE locations move sideways.

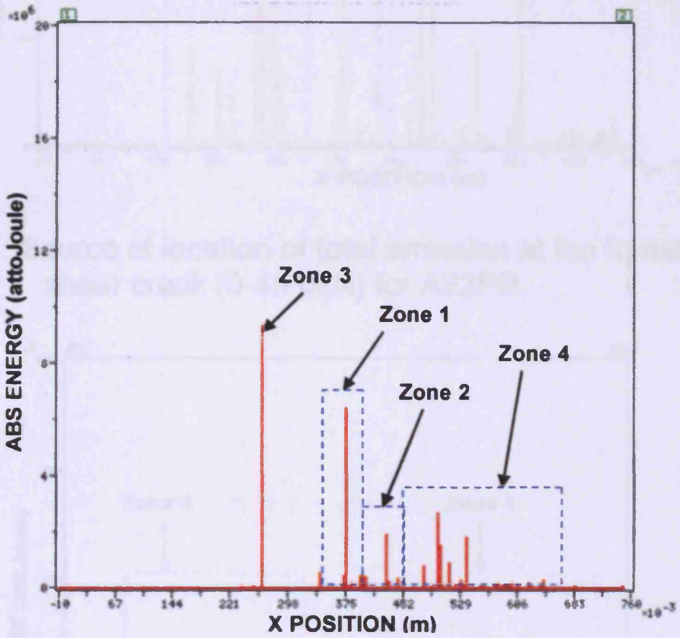

Figure 4.16: Source location of total emission at the start of distributed flexural cracks (0-20.0kN) for A22PR

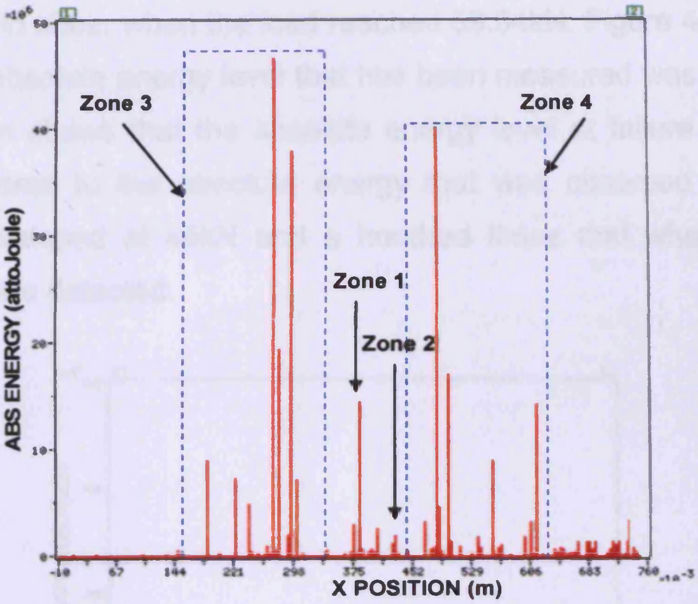

Figure 4.17: Source of location of total emission at the formation of the shear crack (0-45.0kN) for A22PR.

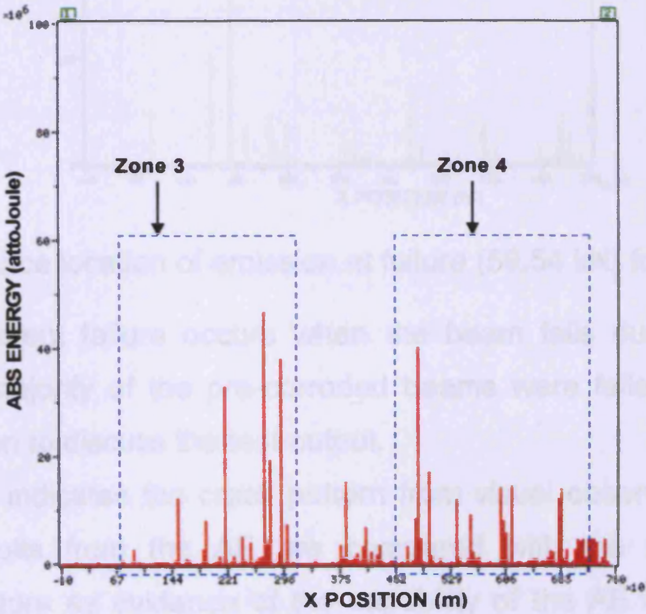

Figure 4.18: Source location of total emission during damage localization (0-55.0kN) for A22PR.

The beam failed in shear when the load reached 59.54kN. Figure 4.19 shows that the highest absolute energy level that has been measured was estimated at 17x10^{7}aJ. This shows that the absolute energy level at failure increased five times compared to the absolute energy that was observed when the shear cracks developed at 45kN and a hundred times that when the first flexural cracks were detected.

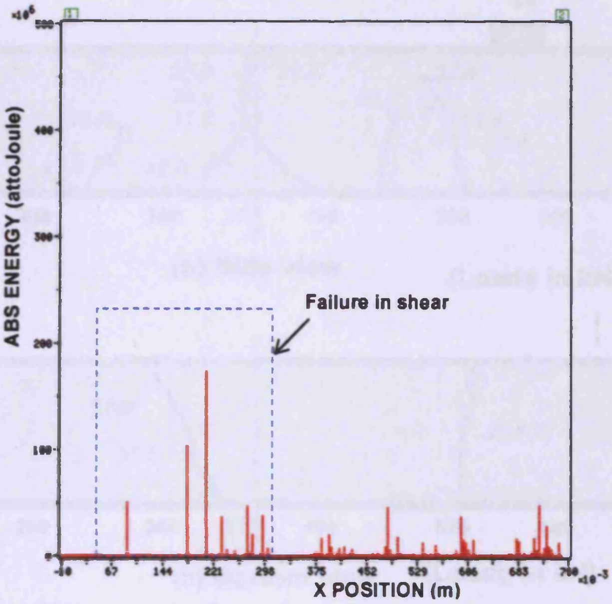

Figure 4.19: Source location of emission at failure (59.54 kN) for A22PR.

A significantly different failure occurs when the beam fails due to flexural crack. Since the majority of the pre-corroded beams were failed in flexure, C22PR will be taken to discuss the test output.

Figure 4.20 indicates the crack pattern from visual observation of the C22PR test. Results from the AE are compared with the observations recorded in this figure as evidence of the capability of the AE method. The first cracks were observed visually on both beam surfaces at approximately 300mm and 330mm in Figure 4.20 (a) and Figure 4.20 (b) respectively at 15kN. As the load was increased, the initial cracks propagated upward to the compression zone and at the peak load (35.08kN) the beam failed in flexural with failure of the steel rebar.

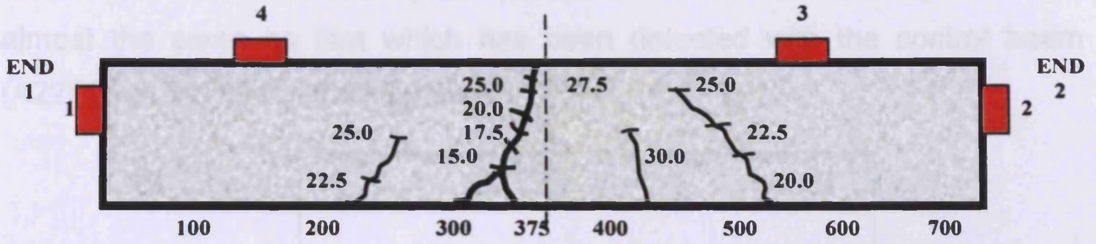

(a) Side view (Loads in kN)

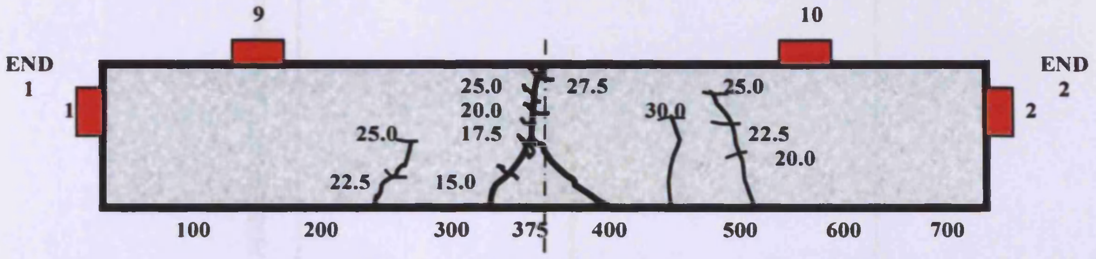

(b) Side view (Loads in kN)

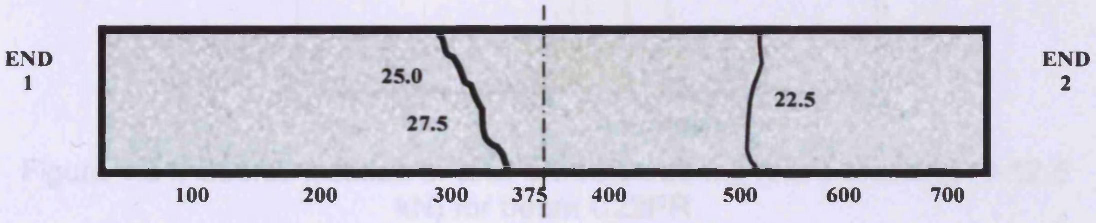

(c) Bottom view (Loads in kN)

Figure 4.20: Crack pattern from visual observation for C22PR showing crack progressing with load in kN.

Figure 4.21 shows the AE linear locations in terms of Absolute Energy and positions during the first stage of failures that is micro-cracking at a load of between 0-12.5kN and before the visible cracks were observed at 15kN. As can be seen in this figure, emission was distributed throughout the beam with low absolute energy levels and considered that this presents the micro damage. The highest peak that has been observed from that figure is estimated to be $7x10^4$aJ and the location is at the centre of the beam where the cross section of steel is reduced due to corrosion. It is more likely that the emission was from the micro damage of the flexural cracks which can be observed visually at almost the exact location identified by the AE and at a load of 15kN. The maximum peak that has been detected from Figure 4.21 is almost the same as that which has been detected with the control beam (A22PR) at the micro-cracking stage.

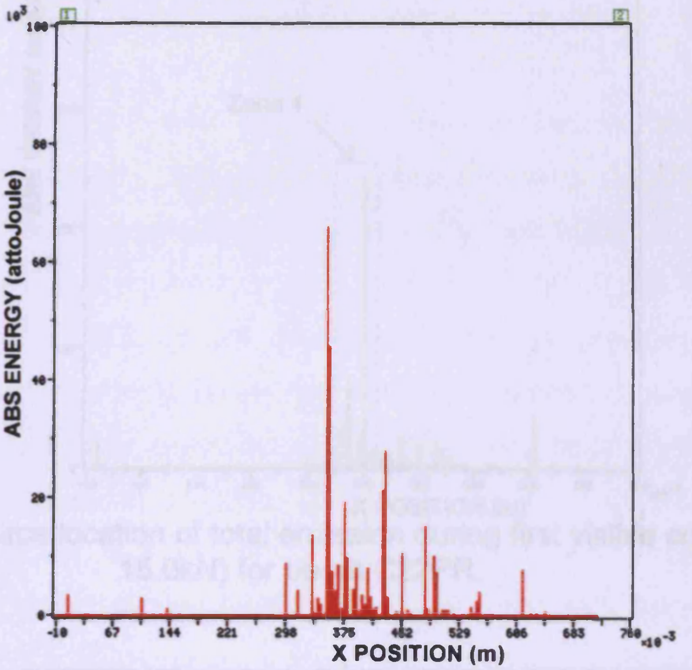

Figure 4.21: Source location of total emission during micro-cracking (0-12.5 kN) for beam C22PR

The first visible cracks can be observed from the experiment at 15kN and the AE source location output is shown in Figure 4.21. The actual cracks were observed at the both surfaces of the concrete were between 300mm and 360mm (Figure 4.20) and the location that has been detected by AE were in between 298mm and 375mm.

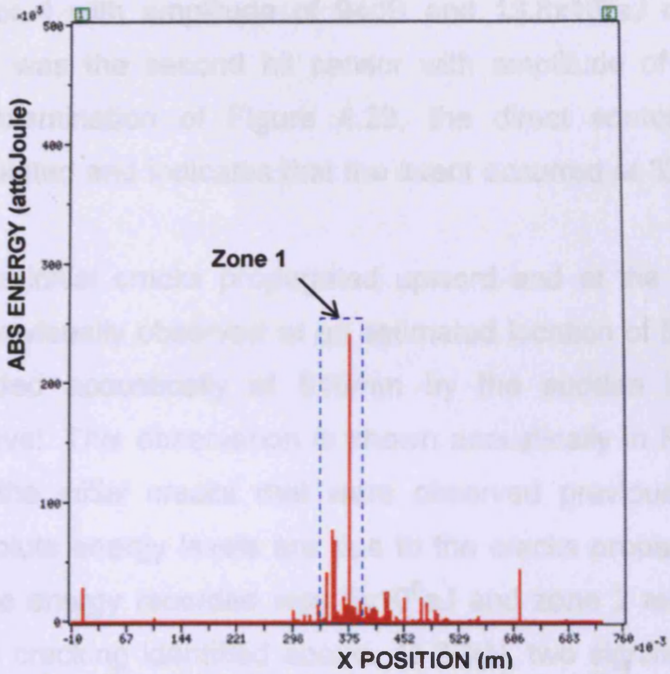

Figure 4.22: Source location of total emission during first visible cracking (0-15.0kN) for beam C22PR.

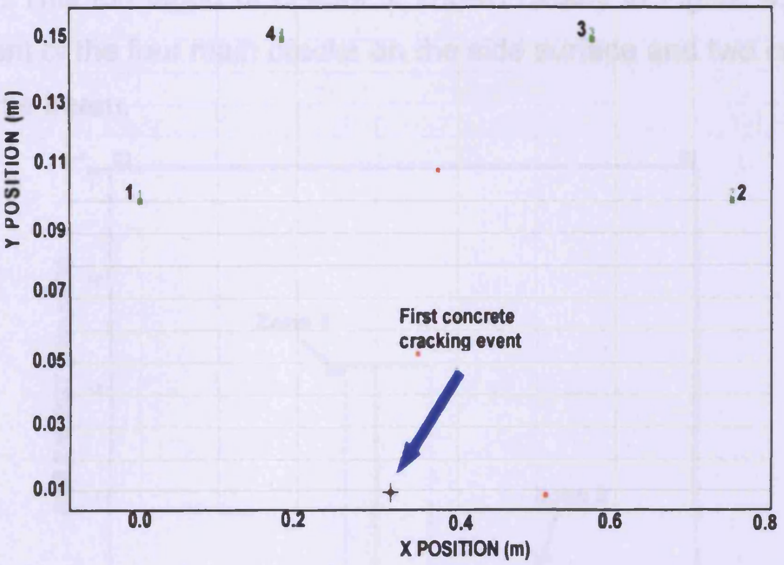

Figure 4.23: First concrete cracking event in arbitrary source location for C22PR.

Figure 4.23 shows an event in arbitrary location at 15kN when the first concrete crack occurred. From the AE line data of this event, the first hit sensor was sensor 4 with amplitude of 94dB and 13.8x10^{6}aJ of absolute energy. Sensor 1 was the second hit sensor with amplitude of 93dB and 12.7x10^{6}aJ. By examination of Figure 4.23, the direct source-to-sensor distance was calculated and indicates that the event occurred at 320mm from sensor 4.

At 20kN the initial cracks propagated upward and at the same time another crack were visually observed at an estimated location of 520mm and have been recorded acoustically at 510mm by the sudden increase in absolute energy level. This observation is shown acoustically in Figure 4.24. Zone 1 includes the initial cracks that were observed previously and the increments in absolute energy levels are due to the cracks propagating. The amount of absolute energy recorded was 5x10^{6}aJ and zone 2 relates to the propagation of the cracking identified above. At 20kN, two significant cracks were observed visually, the number of cracks increased to three when the load reached 22.5kN and the fourth crack was detected when the load reached 30kN. This formation of cracks is shown clearly in Figure 4.20 with the development of the four main cracks on the side surface and two cracks at the bottom of the beam.

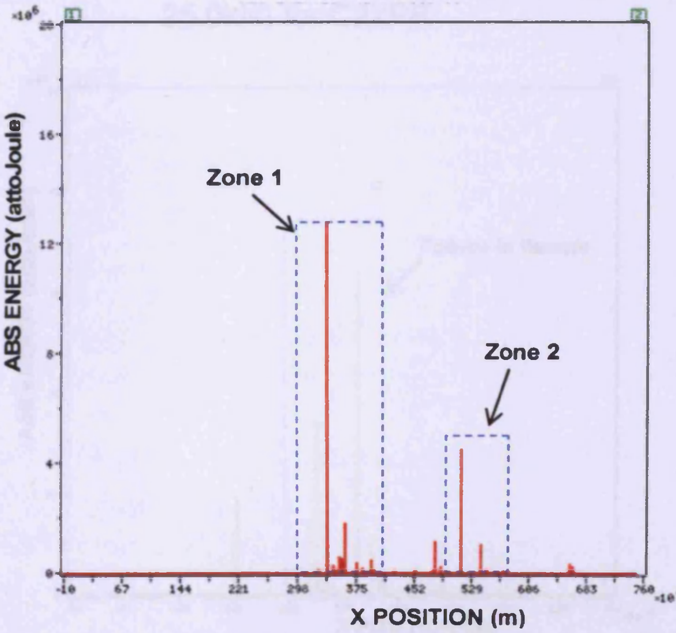

Figure 4.24: Source location of total emission at the start of distributed flexural cracks (0-20.0kN) for C22PR.

The four main cracks on the side surface of the beam are shown in Figure 4.25 in which the four peaks related to the four cracks that can be observed visually are identified. From this figure, the peak in zone 1 was the highest energy peak which signifies that it was associated with the formation of the major crack which leads to failure in flexural at 35.08kN. The amount of absolute energy level that was recorded was 35x10^{6}aJ and it fails at the centre zone of the beam which is shown in Figure 4.26.

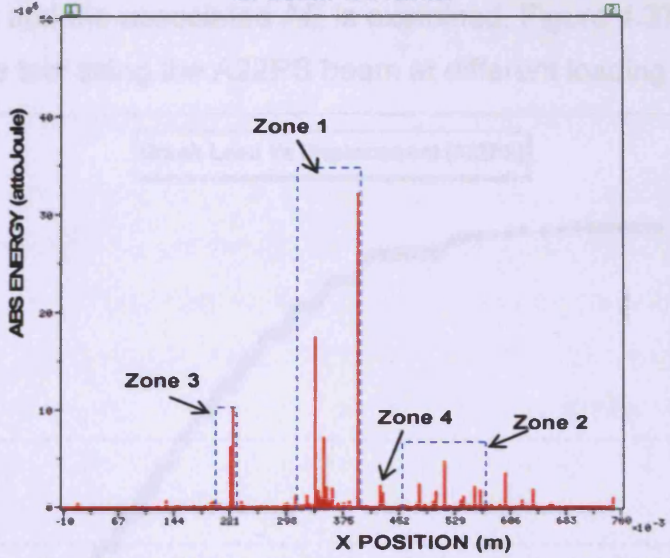

Figure 4.25: Source location of total emission during damage localization (0-25.0kN) for C22PR

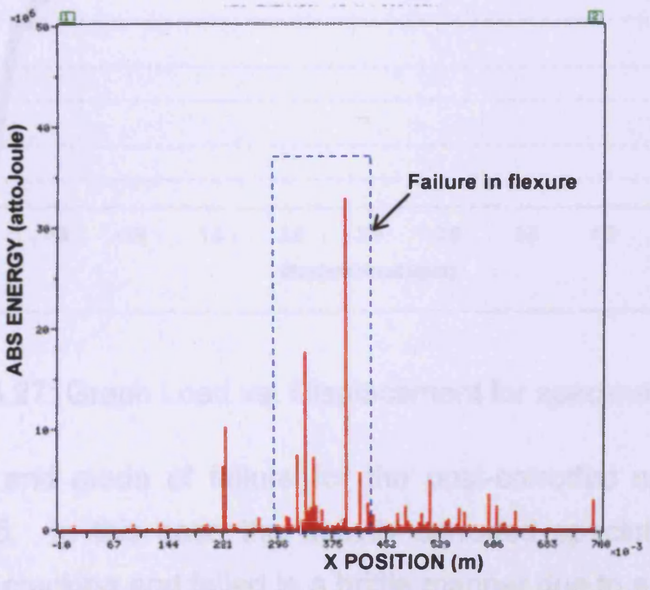

Figure 4.26: Source location of total emission at failure (35.08kN) for C22PR.

4.8 RESULTS FOR POST-CORRODED SPECIMENS

Due to the extent of corrosion products, the reinforced beam exhibited longitudinal cracks along the reinforcement, where the beam was cracked before loading. For this reason, the mechanical behaviour of the reinforced concrete beam can not be divided into five stages as was done for the pre-corroded beam specimen. Instead the tests were divided into several loading stages (2.5kN, 5.0kN, 10.0kN, 12.5kN, 17.5kN, 25.0kN, 30.0kN and 40kN) at which the damage and the associated AE is examined. Figure 4.27 shows the actual curve for the test using the A22PS beam at different loading stages.

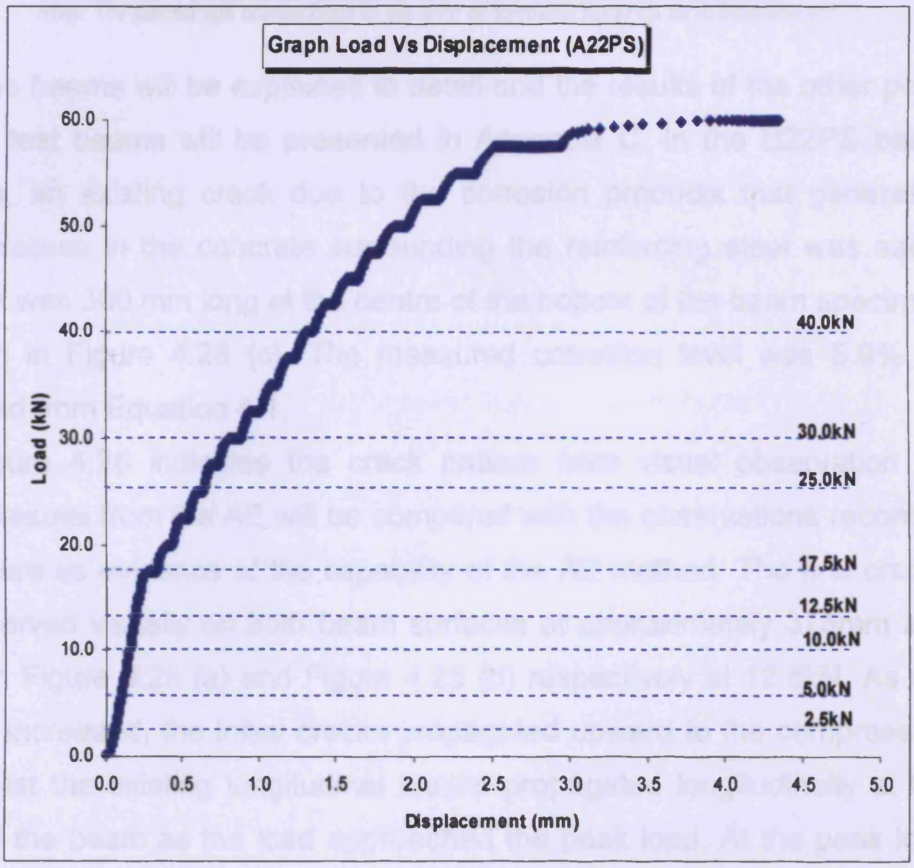

Figure 4.27: Graph Load vs. Displacement for specimen A22PS

The failure loads and mode of failure for the post-corroded specimen are given in Table 4.5. In this case the heavily corroded specimen exhibited much less flexural cracking and failed in a brittle manner due to a loss of bond between the reinforcing bar and the concrete.

Table 4.5: Failure loads and mode of failure of post-corroded specimen

Specimen **Post-corroded**	**Failure Load (kN)**	**Failure Mode**
A11PS (0%)	**54.78**	**Shear**
B11PS (9.60%)	**28.40**	**Flexure**
C11PS (17.00%)	**14.53**	**Bond**
D11PS (33.45%)	**5.98**	**Bond**
A22PS (0%)	**60.0**	**Shear**
B22PS (8.90%)	**45.92**	**Flexure**
C22PS (14.69%)	**18.84**	**Bond**
D22PS (31.30%)	**12.50**	**Bond**

Note: The percentage corresponds to the level of corrosion using C_R as in Equation 4.7.

Two of the beams will be explained in detail and the results of the other post-corroded test beams will be presented in Appendix C. In the B22PS beam specimen, an existing crack due to the corrosion products that generated tensile stresses in the concrete surrounding the reinforcing steel was seen. The crack was 300 mm long at the centre of the bottom of the beam specimen as shown in Figure 4.28 (c). The measured corrosion level was 8.9% as determined from Equation 4.1.

Figure 4.28 indicates the crack pattern from visual observation for B22PS. Results from the AE will be compared with the observations recorded in this figure as evidence of the capability of the AE method. The first cracks were observed visually on both beam surfaces at approximately 375mm and 400mm in Figure 4.28 (a) and Figure 4.28 (b) respectively at 12.5kN. As the load was increased, the initial cracks propagated upward to the compression zone, whilst the existing longitudinal cracks propagated longitudinally at the bottom of the beam as the load approached the peak load. At the peak load the beam failed in flexural mode without failure of the steel rebar.

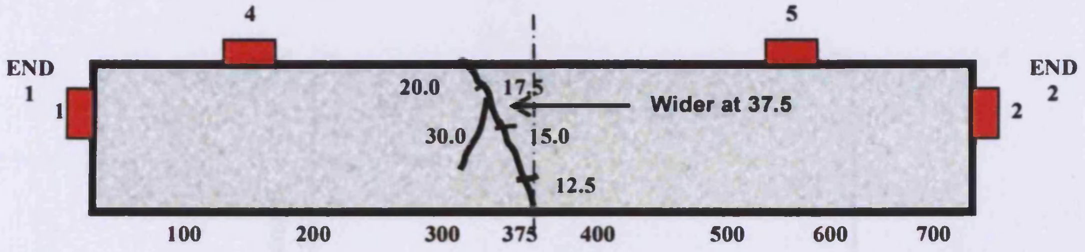

(a) Side view (Loads in kN)

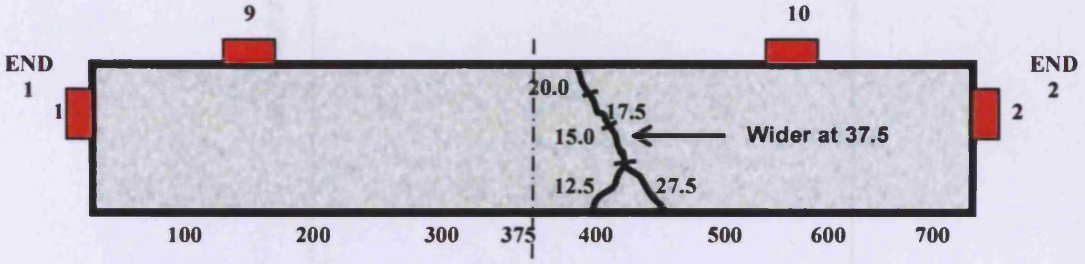

(b) Side view (Loads in kN)

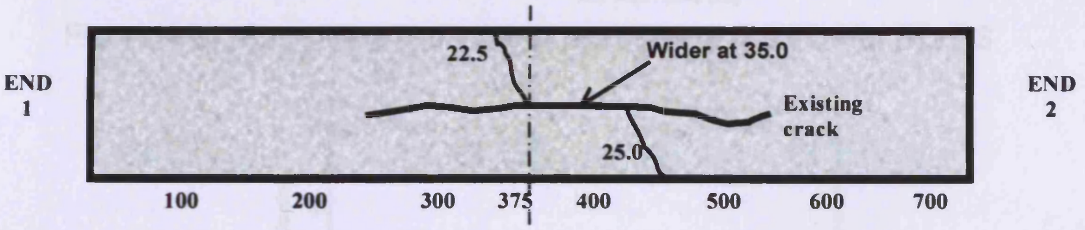

(c) Bottom view (Loads in kN)

Figure 4.28: Crack pattern from visual observation for B22PS showing crack progressing with load in kN.

Figure 4.29 and Figure 4.30 show the source location of total emission at 0-2.5kN and 0-5.0kN between two sensors (sensor 9 and 10) in linear location respectively. These show a low level of absolute energy emitted at the lower load. As the load increases, the energy is emitted at a number of locations. This energy is at a low level, but it is considered that this represents the micro damage (non-visible) that occurs in the concrete.

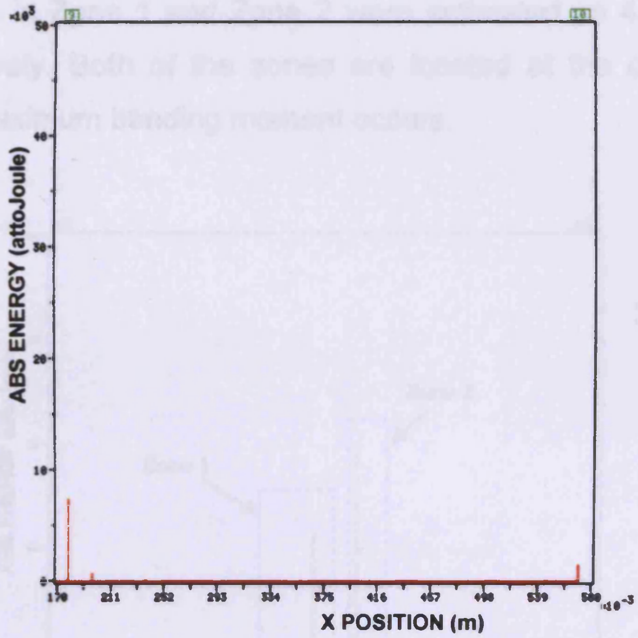

Figure 4.29: Source location of total emission at 0-2.5kN for B22PS

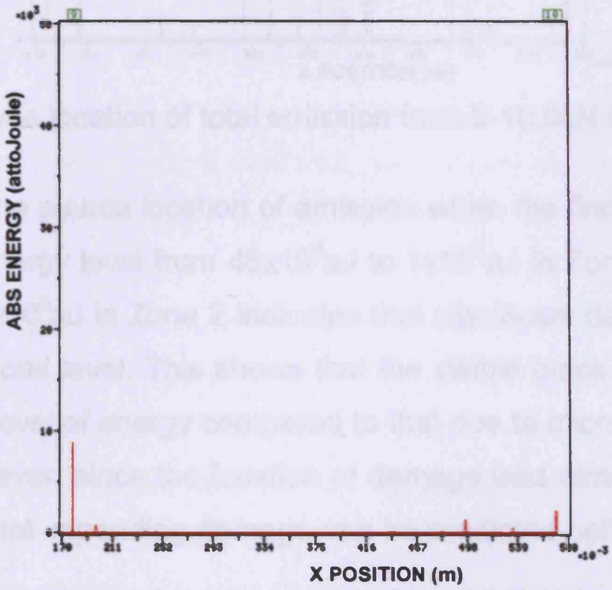

Figure 4.30: Source location of total emission at 0-5kN for B22PS

Figure 4.31 demonstrates the source location of total emission from the beginning of the test to 10.0kN. From this figure, Zone 1 and Zone 2 are related to the emerging cracks that can be observed visually at 12.5kN. Zone 1 is associated with the crack at approximately 375mm in Figure 4.28 (a) whilst Zone 2 indicates the crack at approximately 400mm in Figure 4.28 (b).

The highest peaks in Zone 1 and Zone 2 were estimated as 45×10^3aJ and 60×10^3aJ respectively. Both of the zones are located at the centre of the beam where the maximum bending moment occurs.

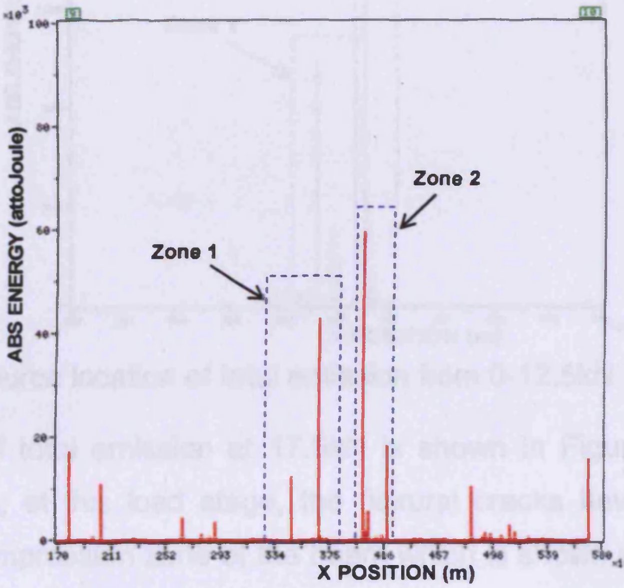

Figure 4.31: Source location of total emission from 0-10.0kN for B22PS

Figure 4.32 shows the source location of emission when the first visible crack occurs. A jump of energy level from 45×10^3aJ to 1×10^6aJ in Zone 1 and from 6×10^4aJ to nearly 2×10^6aJ in Zone 2 indicates that significant damage occurs in the beam at this load level. This shows that the visible crack is associated with a much higher level of energy compared to that due to microcracking and initial damage. However, since the location of damage was almost the same, it can be conclude that impending damage can be predicted before the actual crack occurs.

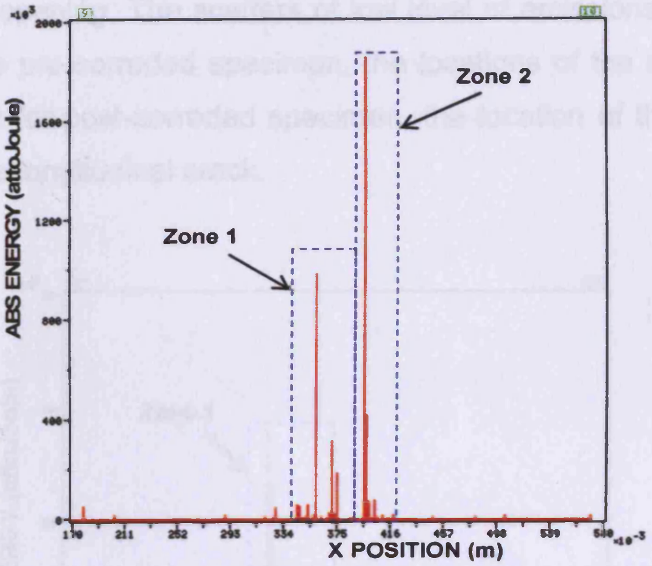

Figure 4.32: Source location of total emission from 0-12.5kN for B22PS.

Source location of total emission at 17.5kN is shown in Figure 4.33. From visual observation, at this load stage, the flexural cracks have propagated upwards to the compression zone of the beam which is shown in Figure 4.28. As the loading increased, the cracks propagate and the absolute energy increases. From Figure 4.33, more emission is detected in Zone 1 which is associated with the crack pattern in Figure 4.28 (a). The highest peak is almost 40x10^6aJ at approximately 330mm. Previously in Figure 4.32, the highest peak was located at approximately 360mm with 1x10^6aJ. Even though the location has moved, the emissions are associated to the same initial crack detected in Figure 4.28 (a). The changing locations are due to the crack pattern, where the crack propagation is not totally vertical. Any change in crack direction is reflected in the AE location. This shows that AE is capable of following the crack pattern.

As can be see from Figure 4.33, as well as high peaks, there were also locations with a low level of absolute energy emerging. These emissions were probably from the crack face rubbing. Furthermore, the beams experienced a longitudinal crack at the bottom of the beam due to corrosion process, which widens with increasing load. It most likely that the low level of emissions were associated with the crack faces rubbing and also the longitudinal crack opening. The scatters of low level of emissions are clearer Figure 4.34. In the pre-corroded specimen, the locations of the energy were more localized but for post-corroded specimen, the location of the energy is scattered along the longitudinal crack.

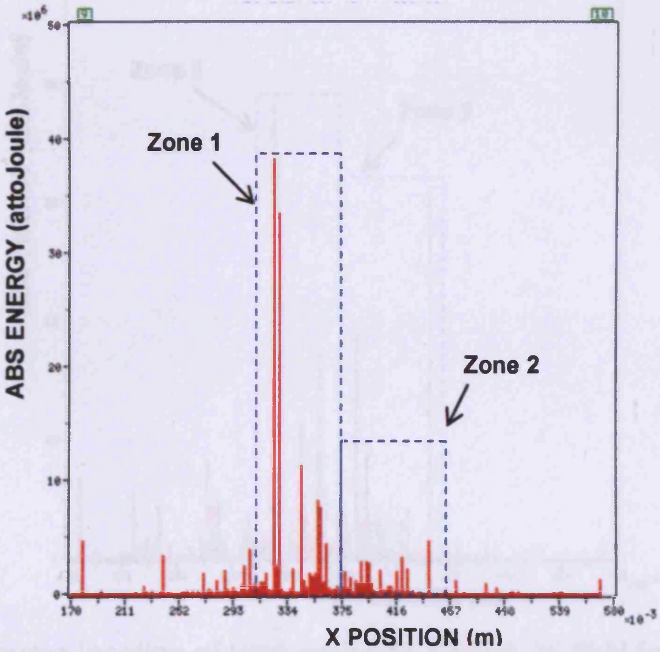

Figure 4.33: Source location of total emission from 0-17.5kN for B22PS

Figure 4.34 represents the source location of the total emissions at 25.0kN. In Zone 1, the highest peak remains the same but there are more peaks of absolute energy especially between approximately 350mm and 370mm. This is due to the crack that has propagated at the bottom of the beam at 22.5kN. In Zone 2, the increment of absolute energy is from the formation of the crack at the bottom of the beam at 25.0kN associated with the crack that has previously propagated vertically in Figure 4.28 (b). Due to the formation of this crack, the absolute energy detected is approximately $32x10^6$aJ. From visual observation at 25.0kN; the flexural cracks propagated and joined at the bottom of the beam which is shown in Figure 4.28 (c). From this figure, the crack that can be seen in Figure 4.28 (a) propagated at the bottom of the beam at 22.5kN and the crack observed in Figure 4.28 (b) propagated at the bottom of the beam at 25.0kN. The locations of these cracks are 375mm and 450mm respectively. This observation is presented in Figure 4.35. The cracks are labeled to differentiate between the existing longitudinal cracks and the cracks that occurred due to loading.

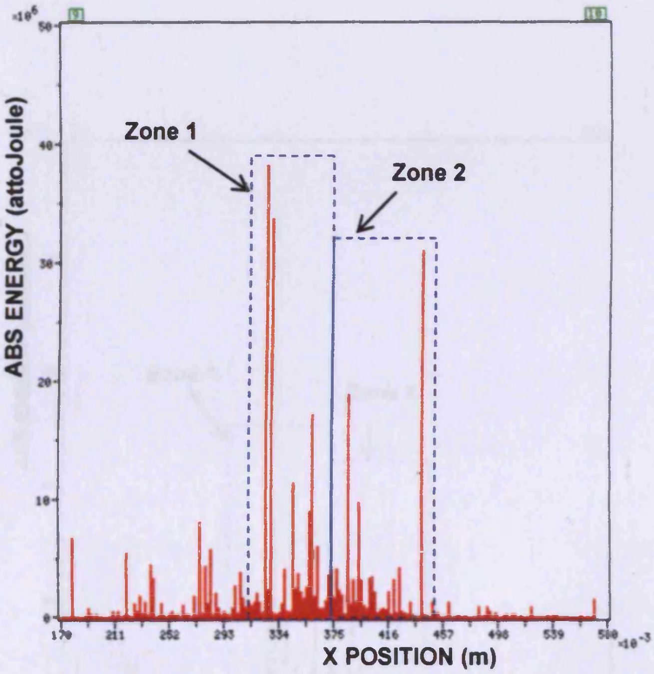

Figure 4.34: Source location of total emission from 0-25.0kN for B22PS

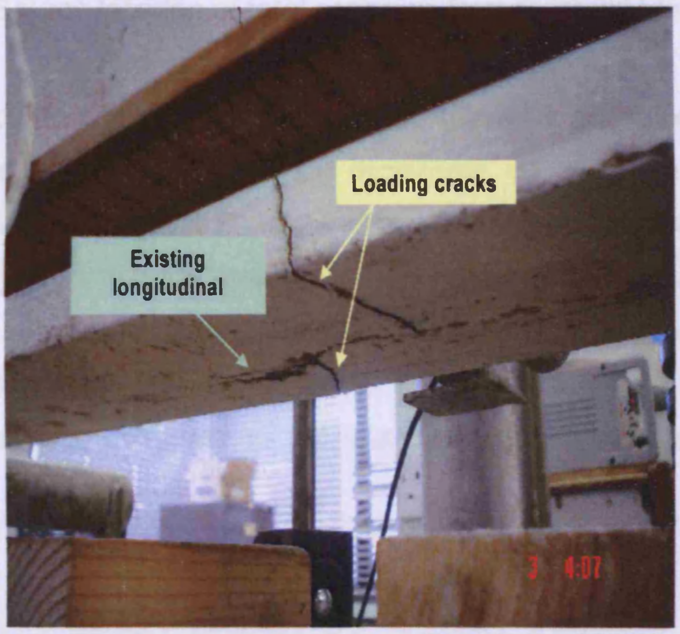

Figure 4.35: Visual observation at 25.0kN for B22PS

Figure 4.36 shows the source location of continuous emissions at 30.0kN. Most of the peak emissions that have been explained previously remain the same, but there is an increment at a location of approximately 334mm, due to the formation of a new oblique crack at 30kN which is shown in Figure 4.28(a).

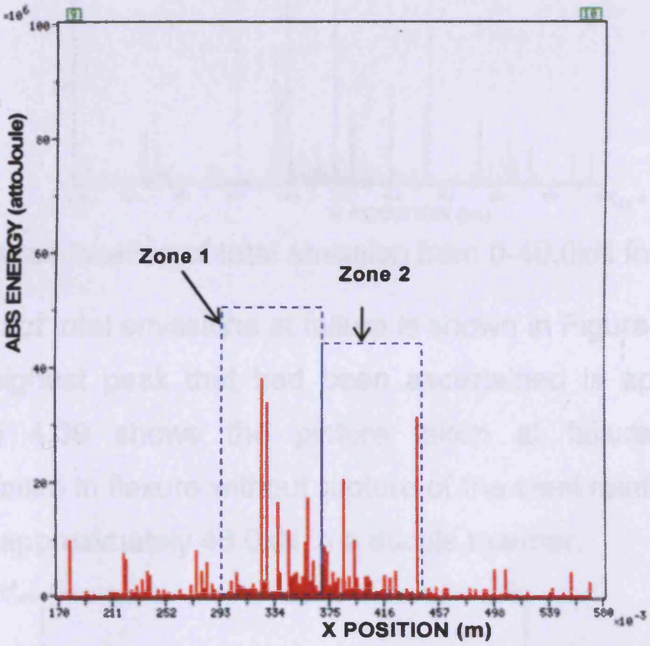

Figure 4.36: Source location of total emission from 0-30.0kN for B22PS

Figure 4.37 indicates the source location of continuous emissions at 40kN. From this figure, Zone 1 shows an increment of absolute energy of approximately 140x10^{6}aJ whilst Zone 2 indicates a highest peak estimated at 40x10^{6}aJ, which shows that the emissions in Zone 1 are more significant than those in Zone 2. From visual observations, the flexural cracks were getting wider and localized at 37.5kN and at 40kN. Furthermore the formation of an oblique crack that was observed at 30kN is also causing new emissions in Zone 1.

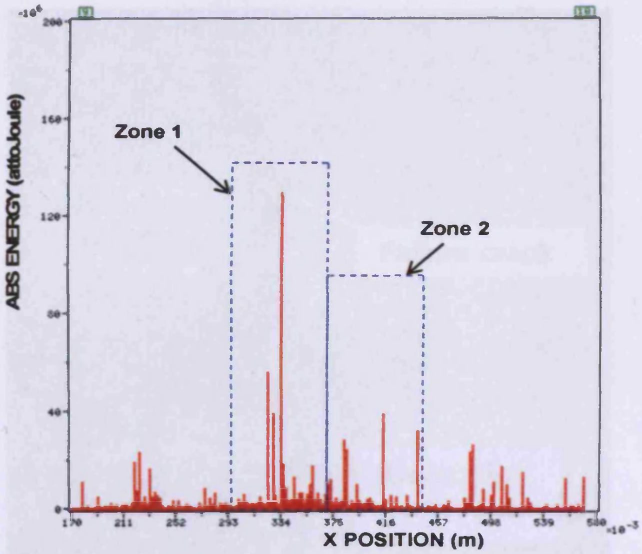

Figure 4.37: Source location of total emission from 0-40.0kN for B22PS

The source location of total emissions at failure is shown in Figure 4.38. In the failure zone, the highest peak that had been ascertained is approximately $155x10^6$aJ. Figure 4.39 shows the picture taken at failure for beam B22PS.The beam failed in flexure without rupture of the steel reinforcement at an ultimate load of approximately 46.0kN in a ductile manner.

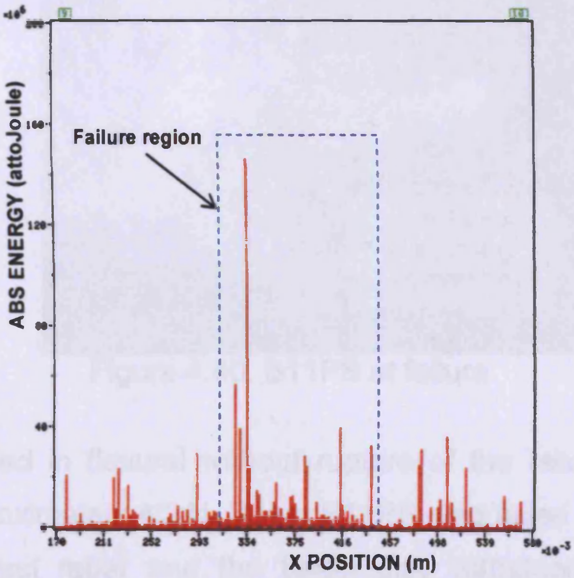

Figure 4.38: Source location of total emission at failure (45.92kN) for B22PS

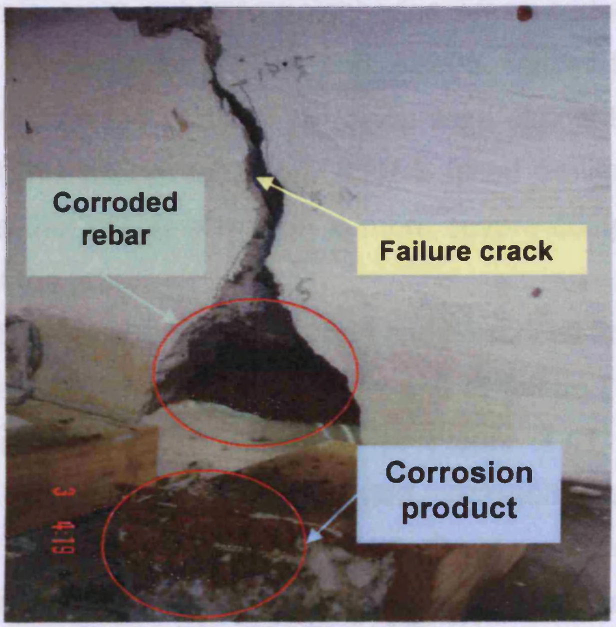

Figure 4.39: B22PS at failure

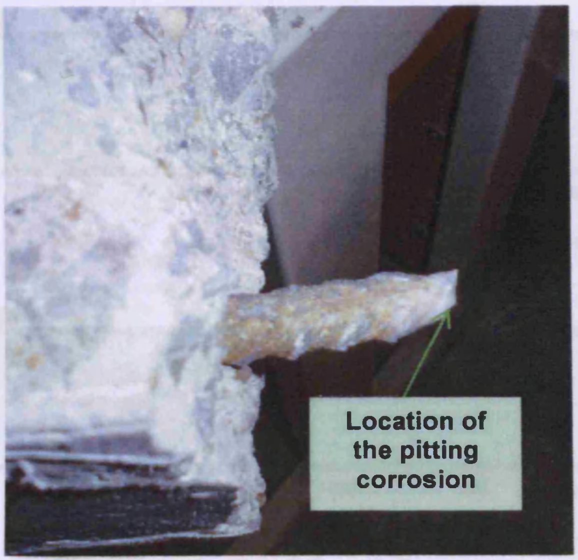

Figure 4.40: B11PS at failure

Beam B22PS failed in flexural without rupture of the rebar and reached a peak load of approximately 46kN. Beam B11PS also failed in flexure but with rupture of the steel rebar and the beam only withstood a peak load of approximately 30kN. The condition of the rebar for beam B11PS can be seen in Figure 4.40. It clearly shows that the steel rebar experienced pitting corrosion associated with the corrosion process. The rebar looked undamaged in certain areas, while in neighboring areas serious damage is present. Levels of corrosion for B11PS and B22PS were 8.9% and 9.8% respectively. Even though the levels of corrosion were almost the same, due to the formation of this pitting corrosion, B11PS failed earlier due to steel rupture. This shows that pitting corrosion is more severe compared to more uniform corrosion of the rebar.

Beam C22PS failed due to loss of bond and discussed and analysed at load of 2.5kN, 5.0kN, 10.0kN, 12.5kN, 17.5kN and at failure (18.84kN). The crack pattern observed visually is shown in Figure 4.41. The existing longitudinal cracks caused by the accelerated corrosion process can be clearly seen and is shown in Figure 4.41 (c). By visual observation, the flexural crack emerged at only 17.5kN before it failed at a load of approximately 19kN.

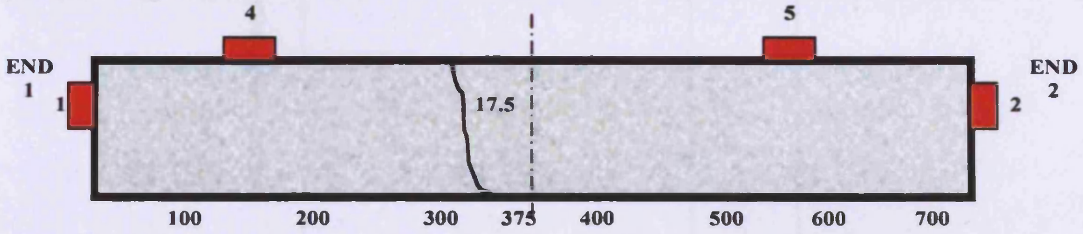

(a) Side view (Loads in kN)

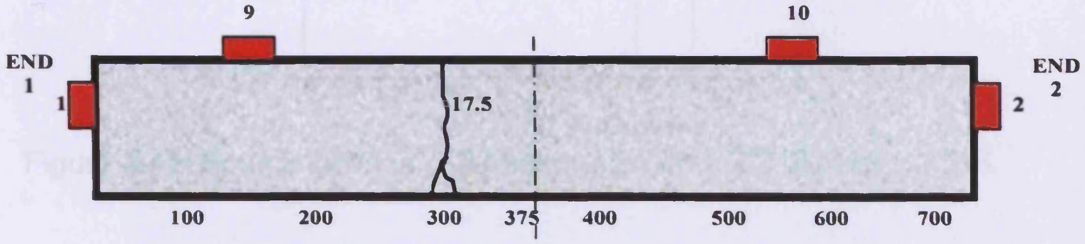

(b) Side view (Loads in kN)

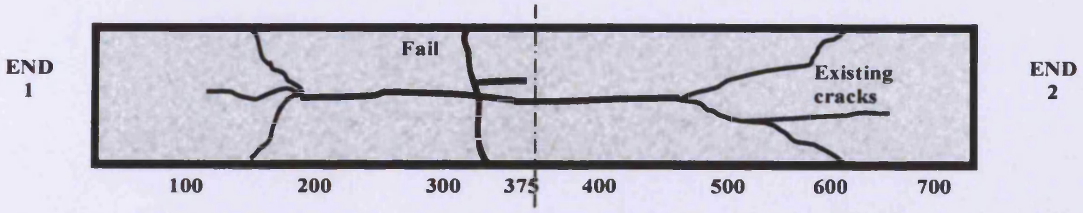

(c) Bottom view (Loads in kN)

Figure 4.41: Crack pattern from visual observation for C22PS showing crack progressing with load in kN.

Figure 4.42 indicates the source location of the total emission from 0-2.5kN for C22PS. The lower peak of absolute energy that can be seen suggests that the application of any load is associated with some damage to the beam. The highest peak that can be observed is approximately 45x10^{4}aJ. In Figure 4.43, the absolute energy is increased to approximately 15x10^{5}aJ at 5kN. The increase in energy is more than three times that observed at 2.5kN. The location that is observed from this figure is estimated to be 350mm along the x-axis. It is likely that there was internal damage which is associated with the flexural cracks which can not be seen with the naked eye since the same location of emission was later detected at 10.0kN.

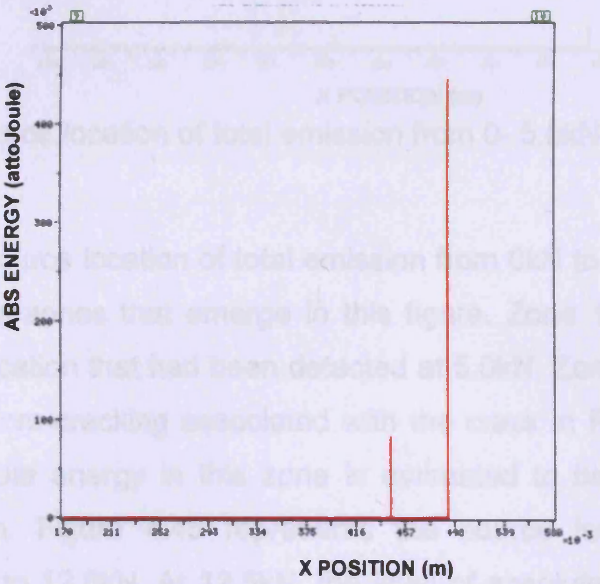

Figure 4.42: Source location of total emission from 0-2.5kN for C22PS.

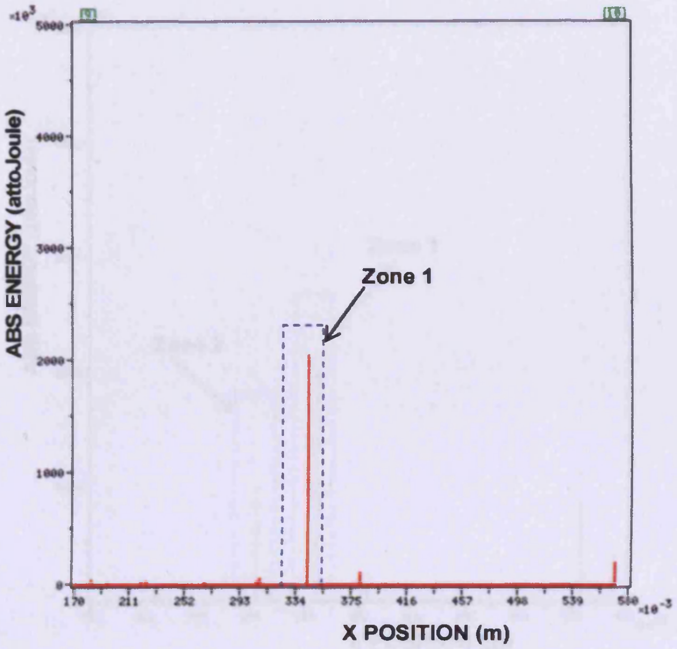

Figure 4.43: Source location of total emission from 0- 5.0kN for C22PS

Figure 4.44 is the source location of total emission from 0kN to 10.0kN. There are two significance zones that emerge in this figure. Zone 1 is associated with the previous location that had been detected at 5.0kN. Zone 2 is believed to be due to the micro-cracking associated with the crack in Figure 4.41 (b). The peak of absolute energy in this zone is estimated to be $1x10^6$aJ at a location of 300mm. Figure 4.45 represents the source location of total emission from 0kN to 12.5kN. At 12.5kN, the level of absolute energy that is observed is still low and there were no visible cracks.

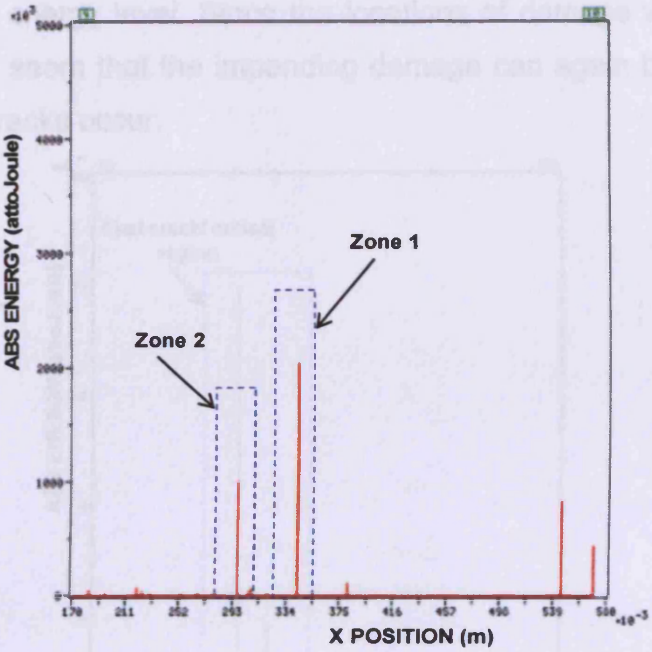

Figure 4.44: Source location of continuous emission at 0-10.0kN for C22PS

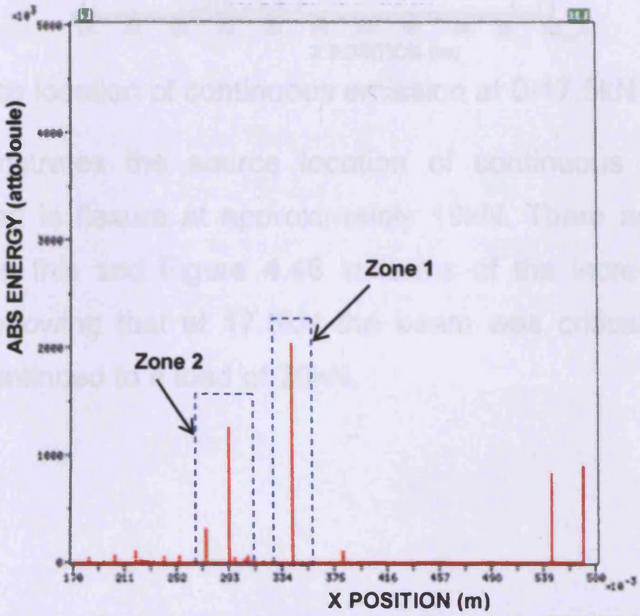

Figure 4.45: Source location of continuous emission at 0-12.5kN for C22PS

Figure 4.46 shows the source location of total emission from 0kN to 17.5kN. From this figure there are huge increments in the absolute energy level compared with Figure 4.45. The highest peak that can be detected is approximately 16x10^6aJ at 300mm along the x-axis. This location agrees with the visual observations in Figure 4.41. The first visible cracks will be a huge contribution to the energy level. Since the locations of damage were almost the same, it would seem that the impending damage can again be predicted before the actual cracks occur.

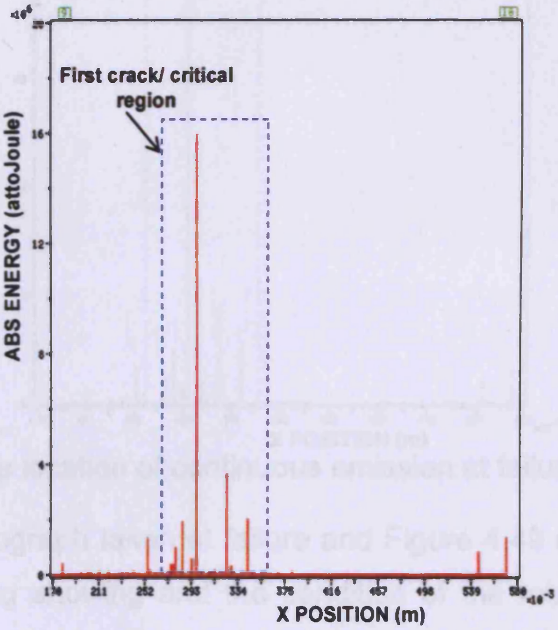

Figure 4.46: Source location of continuous emission at 0-17.5kN for C22PS

Figure 4.47 demonstrates the source location of continuous emission at failure. C22PS failed in flexure at approximately 19kN. There are not many differences between this and Figure 4.46 in terms of the increase of peak energy at failure, showing that at 17.5kN the beam was critically damaged although the test continued to a load of 20kN.

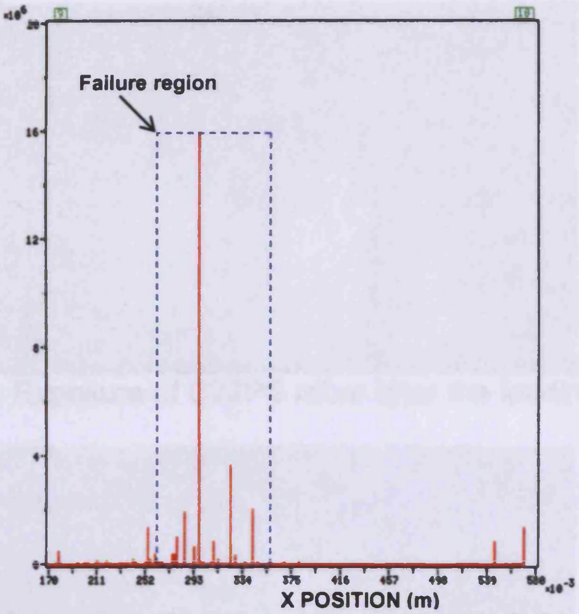

Figure 4.47: Source location of continuous emission at failure for C22PS

Figure 4.48 is a photograph taken at failure and Figure 4.49 is a photograph of C22PS after testing showing and the condition of the rebar. Figure 4.50 shows the beam C11PS at failure. The ultimate load for C11PS was approximately 15kN which is almost the same as C22PS. Both of the beams failed due to loss of bond. The effectiveness of the bond between the reinforcing steel and the concrete is reduced by deterioration of the steel and the expansion of the corrosion products from the steel. As a consequence, a bond failure occurs.

Figure 4.48: Beam C22PS at failure

Figure 4.49: Exposure of C22PS rebar after the loading test

Figure 4.50: Beam C11PS at failure.

4.9 DISCUSSION

This chapter has investigated the relationship between the absolute energy of acoustic emission and the behaviour of the RC beams due to chloride-induced reinforcement corrosion at various levels and has sought to locate and follow the progression of the resulting cracks.

From the results of testing several test specimens of pre-corroded (PR) and post-corroded (PS) samples, it has been identified that the AE method can be used to obtain a warning of developing distress and the growth of internal microcracking at critical locations. In addition, a comparison between visual observations of the cracking process and AE source location analysis indicates that areas of damage due to cracking can be clearly identified by AE source location. Moreover, the capability of the AE technique to follow crack development and to monitor structural behaviour in concrete is promising. A summary of the PR beam tests is presented in Table 4.6 and the cumulative absolute energy in each loading cycle are normalized in Table 4.7.

Table 4.6: Summary of cumulative absolute energy and loading for PR specimen.

Specimen	**Cumulative Absolute Energy (aJ)**				
	0-5kN	**0-15kN**	**0-20kN**	**0-30kN**	**Failure**
Pre-corroded					
A11PR (0%)	**4.24x10^{4}**	**3.17x10^{7}**	**4.30x10^{8}**	**4.76x10^{8}**	**8.50x10^{9}**
B11PR (7.80%)	**1.29x10^{5}**	**7.24x10^{7}**	**2.64x10^{8}**	**1.90x10^{9}**	**5.10x10^{9}**
C11PR (15.60%)	**6.87x10^{5}**	**2.28x10^{8}**	**3.10x10^{8}**	**2.13x10^{9}**	**3.37x10^{9}**
A22PR (0%)	**1.13x10^{5}**	**1.27x10^{8}**	**2.19x10^{8}**	**4.34x10^{8}**	**1.88x10^{10}**
B22PR (8.60%)	**1.04x10^{5}**	**1.75x10^{8}**	**9.86x10^{8}**	**1.35x10^{9}**	**4.08x10^{9}**
C22PR (16.00%)	**4.98x10^{5}**	**5.34x10^{8}**	**1.02x10^{9}**	**3.0x10^{9}**	**3.97x10^{8}**
D22PR (22.60%)	**7.02x10^{5}**	**8.07x10^{8}**	**1.49x10^{9}**	**-**	**2.34x10^{9}**

Note: The percentage corresponds to the level of corrosion using C_R as in Equation 4.7.

Table 4.7: Summary of normalization of cumulative absolute energy and loading for average PR specimen.

Specimen	**Normalization of Cumulative Absolute Energy**				
	0-5kN	**0-15kN**	**0-20kN**	**0-30kN**	**Failure**
Pre-corroded					
A PR (No corrosion)	**1**	**1**	**1**	**1**	**1**
B PR (Low corrosion)	**1.51**	**1.56**	**1.92**	**3.58**	**0.34**
C PR (Medium corrosion)	**7.63**	**4.80**	**2.05**	**5.65**	**0.27**
D PR (High corrosion)	**9.04**	**10.16**	**4.58**	**-**	**0.17**

Values of cumulative absolute energy for each loading stage are given. At each particular load stage, the corroded beams emit AE with higher cumulative absolute energy as the level of corrosion increases compared with uncorroded (control) beams. For instance, at 0-15kN, the A22PR beam gives 1.13x10^{5} aJ compared with the D22PR beam with 7.02x10^{5}aJ cumulative absolute energy. This is not the case at failure. At failure, the cumulative absolute energy in the control beam is highest, and this decreases as the corrosion level increases. This occurs because the beam can withstand a higher load. Lower values of cumulative AE absolute energy were recorded (shorter time of testing) as the degree of corrosion increased. The normalized data presented in Table 4.7 are the ratio of the average cumulative AE absolute energy at each corrosion level to that of the non-corroded beam. From this figure it can be seen that as the corrosion increases, the normalized values also increase except when the beam specimen failed. In this case the non-corroded beam specimen gave the highest value. The normalized values vary at each loading stage because the cracks/damage on the tested beams were not the same.

In Tables 4.8 and 4.9 the results for the PS beam specimen at each loading stage are presented. In Table 4.9, the normalized values are the average value of each loading stage. This shows that at 5kN, the highest level of corrosion gives the highest normalized value because the beams failed at the very earliest loading stage with a very high-energy emission.

In the PS specimens, at the low level of loading (0-5kN), the value of absolute energy was higher than the PR specimens at 15kN (after the first concrete cracking had occurred). This is probably due to crack face rubbing. Furthermore, PS beams exhibited longitudinal cracks along the reinforcement at the bottom of the beam due to corrosion, which widen with increasing load. Each of these events contributes to the level of absolute energy emission. A high value of cumulative absolute energy was generated in the uncorroded specimen compared with the corroded specimen; the higher the degree of corrosion, the lower the AE activity. This can be explained by the fact that the expansive forces resulting from corrosion of the steel reinforcement lead to damage and a longitudinal splitting crack in the concrete due to the severe corrosion prior to loading. Thus the majority of energy due microcraking and longitudinal cracking along the reinforced concrete beam has already been dissipated in the by damage process due to corrosion.

Different failure mechanisms such as microcracking, localized cracking, flexural cracking, shear and bond failure exhibit different quantities of AE absolute energy. Comparison between visual observations of cracking processes and AE source location analysis indicated that the damage area due to cracking can be approximately identified by the AE source location.

The AE energy recorded at each sensor is not the energy produced by the source at its origin but is energy that has attenuated through the concrete. Energy recorded is dependent on the distance from source, the specimen geometry and the condition of the specimen, for instance the presence of the existing cracks, so the results will differ between tests. Since it is not always possible to calculate the energy at the source itself, any relationship discovered will be dependent upon the source-to-sensor distance. Considering the source-to-sensor distance and the difference in material properties, it could be suggested that a laboratory-based relationship would only be appropriate for the testing of structures of similar size and detail. This makes it difficult to identify a unique relationship between AE energy and corrosion level for in-service structures. Another factor which will affect the applicability of a relationship discovered within the laboratory, is the actual material. In laboratory-based specimens, the mix proportions and curing conditions are known and can be controlled but it is different in the field.

In Figure 4.17 for the A22PR beam, the formation of a shear crack was observed and the highest peak that was recorded was 47×10^6aJ and in C22PR, the highest peak that was observed due to a flexural crack was 35×10^6aJ as in Figure 4.22. This suggests that flexural cracks and shear cracks exhibit AE emissions of the same order of magnitude.

Table 4.8: Summary of cumulative absolute energy and loading for PS specimen.

Specimen	**Cumulative Absolute Energy (aJ)**				
	0-5kN	**0-15kN**	**0-20kN**	**0-30kN**	**Failure**
Pre-corroded					
A11PS (0%)	**4.52×10^4**	**1.51×10^7**	**1.20×10^8**	**7.20×10^8**	**5.66×10^9**
B11PS (9.60%)	**2.82×10^5**	**1.70×10^7**	**6.88×10^8**	**-**	**3.51×10^9**
C11PS (17.00%)	**3.55×10^6**	**-**	**-**	**-**	**2.36×10^9**
D11PS (33.45%)	**8.92×10^7**	**-**	**-**	**-**	**5.84×10^8**
A22PS (0%)	**4.44×10^4**	**5.51×10^7**	**2.45×10^8**	**8.45×10^8**	**1.60×10^{10}**
B22PS (8.9%)	**3.57×10^5**	**3.16×10^8**	**9.20×10^8**	**4.20×10^9**	**1.49×10^{10}**
C22PS (14.69%)	**1.70×10^8**	**1.80×10^9**	**-**	**-**	**9.97×10^9**
D22PS (31.30%)	**8.30×10^6**	**-**	**-**	**-**	**8.72×10^9**

Note: The percentage corresponds to the level of corrosion using C_R as in Equation 4.7.

Table 4.9: Summary of normalization of cumulative absolute energy and loading for average PS specimen.

Specimen	Normalization of Cumulative Absolute Energy				
	0-5kN	0-15kN	0-20kN	0-30kN	Failure
Pre-corroded					
A PS (No corrosion)	**1**	**1**	**1**	**1**	**1**
B PS (Low corrosion)	**7.14**	**4.57**	**4.39**	**5.36**	**0.85**
C PS (Medium corrosion)	**58.71**	**51.2**	**-**	**-**	**0.57**
D PS (High corrosion)	**1089.29**	**-**	**-**	**-**	**0.43**

For PR specimen and control specimens, the first crack occurs primarily in the constant moment zone because this is where the highest stresses occur. The emission of this event had been recorded and even taking into account attenuation and dispersion, observations suggest that any absolute energy emission exceeding 1.0x10^{6}aJ for a single sensor is associated with concrete cracking. Moreover from Table 4.6, when the beam experienced the first crack, which is at 15kN, the previous absolute energy level was exceeded by 1.0x10^{6}aJ. This provides an indication of the level of absolute energy emission when the concrete cracks. A comparison between visual observations of the cracking process and AE source location analysis is essential in any AE monitoring. This finding will be used in Chapter 6 of this thesis when monitoring an actual RC bridge.

4.10 CONCLUSIONS

This study has assessed the ability of AE to monitor laboratory-based specimen at various levels of corrosion of the RC beam. The aim of this study was to investigate the relationship between AE absolute energy and the physical behaviour of an RC beam and to determine the ability of the AE to locate and monitor crack propagation on the RC beam. The following points summarise the most significant conclusions:

- The parameter-based approach was used in the analysis of the data acquired by the AE instrumentation and it was shown to be sensitive to the initiation and the growth of cracks within the specimens. The application of the TOA method was used to determine the location of the damage area using linear location between sensors and the results were promising. In addition, TOA location could be used to indicate internal crack growth before the crack could be observed visually and enabled the micro damage to be located accurately before the actual impairment occured.

- In pre-corroded specimens, five different stages of mechanical failure were identified; microcraking, localized cracking propagation, distributed flexural cracking, shear cracking and damage localization. However, in post-corroded (PS) specimen these five stages were not identified since the specimens exhibited longitudinal cracks along the reinforcement, such that the beam was cracked before loading.
- The AE energy recorded at each sensor is not the energy produced by the source at its origin but an energy that has attenuated through the concrete. Therefore, the energy is dependent on the distance from the source, the specimen geometry and the condition of the specimen. However, it was observed in the PR specimens that the energy due to first concrete cracking exceeded $1.0\text{x}10^{6}$aJ in arbitrary source location for a single sensor. Thus it is proposed that absolute energy in excees of $1.0\text{x}10^{6}$aJ can be used to indicate the onset of cracking.
- At a particular loading stage, it was observed that the cumulative absolute energy was higher with increased corrosion level. PS specimens gave higher emissions because of the existing longitudinal cracks, which widen and cause concrete face rubbing as the load increases. In the PR specimens, the AE level was related to the loss of cross section of reinforcing steel. However, this is not true at failure, where the cumulative energy released was lower with increasing corrosion level due to the load at which the reinforcing bar fails.

CHAPTER 5: A PRACTICAL INVESTIGATION INTO ACOUSTIC WAVE PROPAGATION IN CONCRETE STRUCTURES

5.1 INTRODUCTION

This chapter details experiments using the AE waveform or transient record to analyse the synchronous signals from artificial and true sources by exploring wave propagation in concrete structures over a variety of source-to-sensor distances. Experiments were performed on a reinforced concrete (RC) beam and an RC slab using a Hsu-Nelsen (H-N) Source (ASTM, 1999) as an artificial source. A further investigation examined concrete cracking resulting from the corrosion process as a true source. A detailed description of the experimental work is presented highlighting the procedures followed during the laboratory stage of this study and an analysis of the results is given. Source location is normally based on the arrival times of transient signals. The simplest method is known as the Time of Arrival (TOA) method, where the location of the damage can be determined from the arrival time of the event at two or more sensors. When using this method, the wave velocity of the signals that propagate through the material needs to be determined. Homogenous materials, such as steel, have well-defined velocities, but it is more difficult to predict the wave velocity in non-homogeneous materials such as concrete. This makes the use of a single wave velocity, as required in the TOA method, very difficult especially for large structures. It is therefore essential to gain an understanding of the factors that may affect the ability to obtain an accurate value of wave velocity.

The heterogeneous nature of concrete (e.g. aggregates, cracks, reinforcing bars and tendons) influences the wave propagation by scattering. Reflections and mode conversions at the interfaces and specimen boundaries cause a very complex wave field. It is often difficult to detect waves other than the P-wave which is why the arrival times of the P-waves are only considered for the quantitative analysis.

5.2 AIMS AND OBJECTIVES

The aims of the experiments were to investigate wave propagation in concrete structures over a variety of source-to-sensor distances, to investigate the P-wave velocity in concrete specimens at different pre-set threshold levels and to determine the impact of source-to-sensor distance on the calculated apparent wave velocity.

5.3 EXPERIMENTAL PROCEDURE

This investigation used a cast in-situ RC beam and an actual RC slab. The water to cement ratio for the RC beam was 0.56 and the material proportions were 1:2:2.5:0.56 by weight of cement, sand, aggregate and water respectively giving concrete design strength of 40MPa (the actual 28 day compressive strength was 48MPa). The dimensions of the RC beam were 100x150x2000mm and the RC slab was 2750mm wide by approximately 1000mm thick. The mix design and concrete properties of the RC slab were unknown. Figure 5.1 and Figure 5.2 show the RC beam test specimen and the RC slab test specimen respectively.

For both concrete samples (RC beam and RC slab), seven resonant frequency sensors (Physical Acoustic R6D), at a spacing of 250mm, were attached to the specimen. Seven pairs of steel plates were attached to the specimen surface using plastic padding and the sensors were held in position using a magnetic clamp; silicon grease was applied as an acoustic couplant. Experiments were performed using an H-N Source (ASTM, 1999); for the parallel source 100mm from sensor 1 and 100mm from sensor 7 for the normal source. The source was repeated ten times and recorded simultaneously at all sensors using a Physical Acoustic's DiSP system.

Two source modes are considered for an artificial H-N source; the source parallel and the source normal to the sensor face as shown in Figure 5.3 for the beam. For the slab, only the source parallel to the sensor face should be considered - 100mm from sensor 1, as there is no access to the normal face.

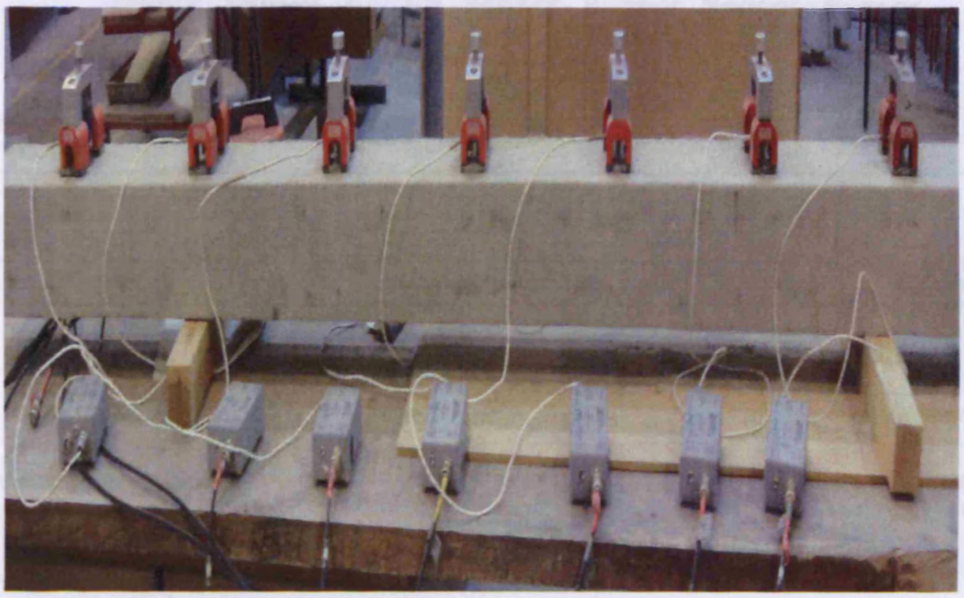

Figure 5.1: Reinforced concrete beam test specimen

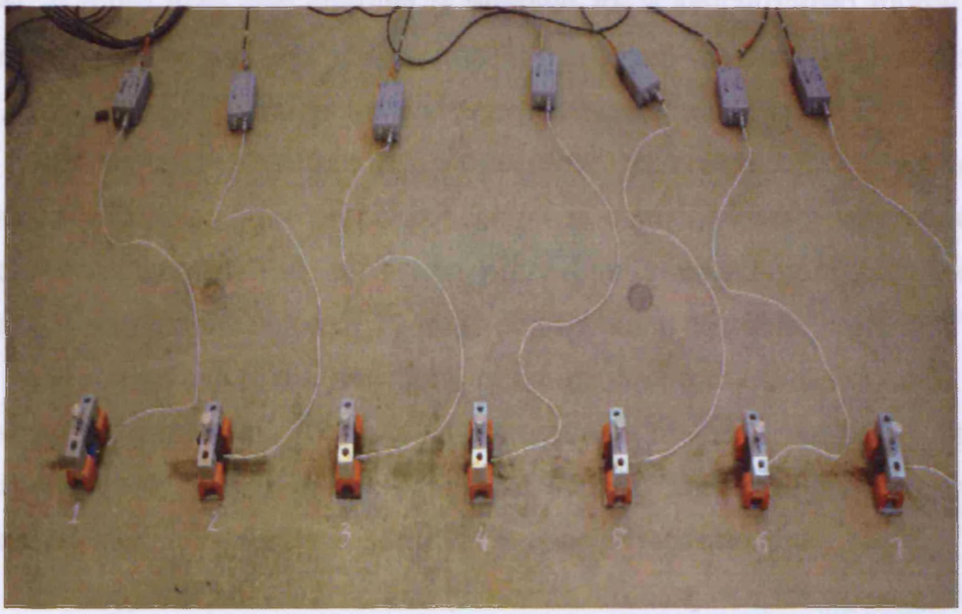

Figure 5.2: Reinforced concrete slab test specimen

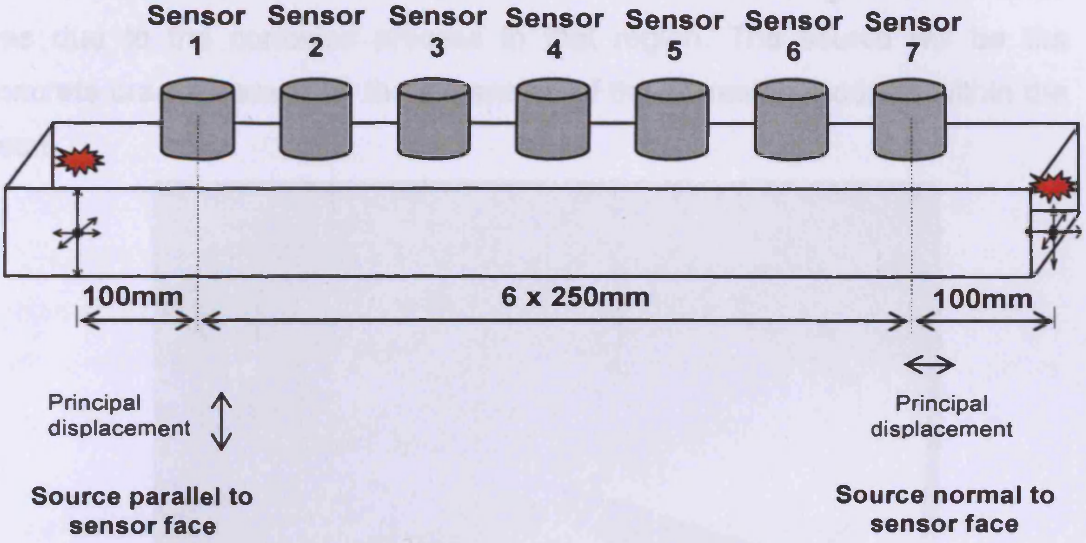

Figure 5.3: Source motion

AE Win provides the ability to collect waveform data using a synchronized trigger. If more than one channel is enabled for a synchronized trigger and begins to collect data then all channels in this group will also begin to collect data. In AE WIN, TRA mode is a waveform collection mode only.

AE signals were "corrected" in order to ensure, for a particular threshold, that the same temporal position in each waveform was used for velocity calculations. The correction procedure involved normalizing each signal of up to a peak value of 10 Volts (V), i.e. each signal is "corrected" to a 10V peak regardless of the amplitude attenuation due to the distance or path travelled by the wave,. Velocity is determined at each position using a synchronous trigger at sensor 1 (parallel source) and at sensor 7 (normal source) by identifying the time of arrival at subsequent sensors.

Emissions from a real source (concrete cracking due to corrosion) were also investigated. During this test, the sensor arrangements were the same as in Figure 5.3 but the RC beam was attached to an acrylic tank as described in section 4.4 of Chapter 4 for post-corroded (PS) specimen. The end section was immersed in a 5% NaCl solution and the anodic current was applied by attaching the power supply to a stainless steel plate suspended in the solution as shown in Figure 5.4. The distance between the middle of the tank to sensor 1 was 100mm. It was expected that the first cracking of the concrete was due to the corrosion process in that region. The source will be the concrete cracks caused by the expansion of the corrosion products within the beam.

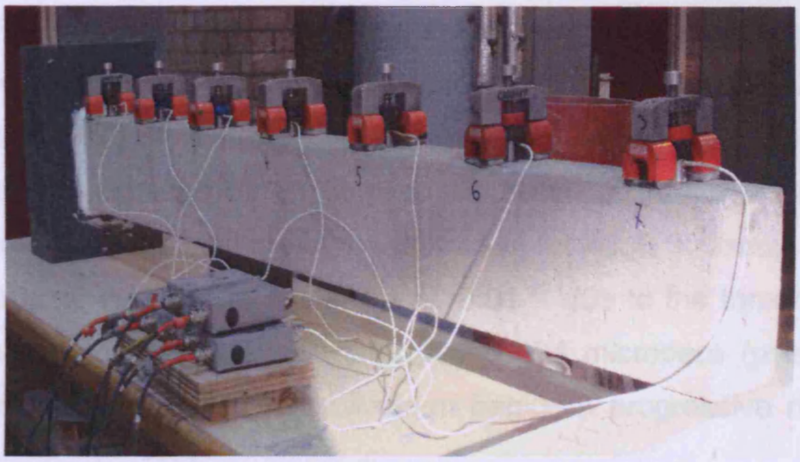

Figure 5.4: Corrosion process monitoring of RC beam.

5.4 RESULTS

Figure 5.5 shows the different pre-set threshold level of 40dB (0.01V) and 60dB (0.1V) at sensor 3 (beam) for raw and corrected signals from the H-N source. All calculated wave velocities are based on 40dB and 60dB pre-set threshold levels.

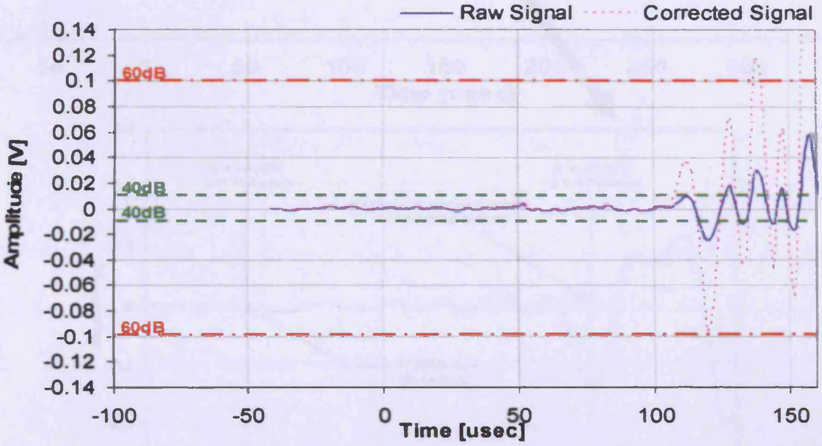

Figure 5.5: Arrival of longitudinal waves (P-waves) at different threshold levels at sensor 3 for the beam.

5.4.1 Artificial Source from H-N Source.

5.4.1.1 Source Parallel to Sensor Face

The P-wave is a primary and the fastest wave therefore it is the first to arrive at the sensor face. All other waves arrive later with a lower velocity but higher amplitude. Figure 5.6 shows the raw signal that was obtained at sensor 3. In this test, the arrival time for the P-wave or first wave was obtained at the selected pre-set threshold level. The arrival of the subsequent waves (e.g. transverse) was estimated by looking for a constant increase in amplitude. Figure 5.6 shows the arrival time of the first wave (at 40dB threshold level) as 118 microsecs (μsec) with an amplitude of -0.01 V due to the threshold. The arrival of the second wave is estimated to be 174 microsecs (μsec) which represents the time at which the waveform begins a progressive rise to its peak.

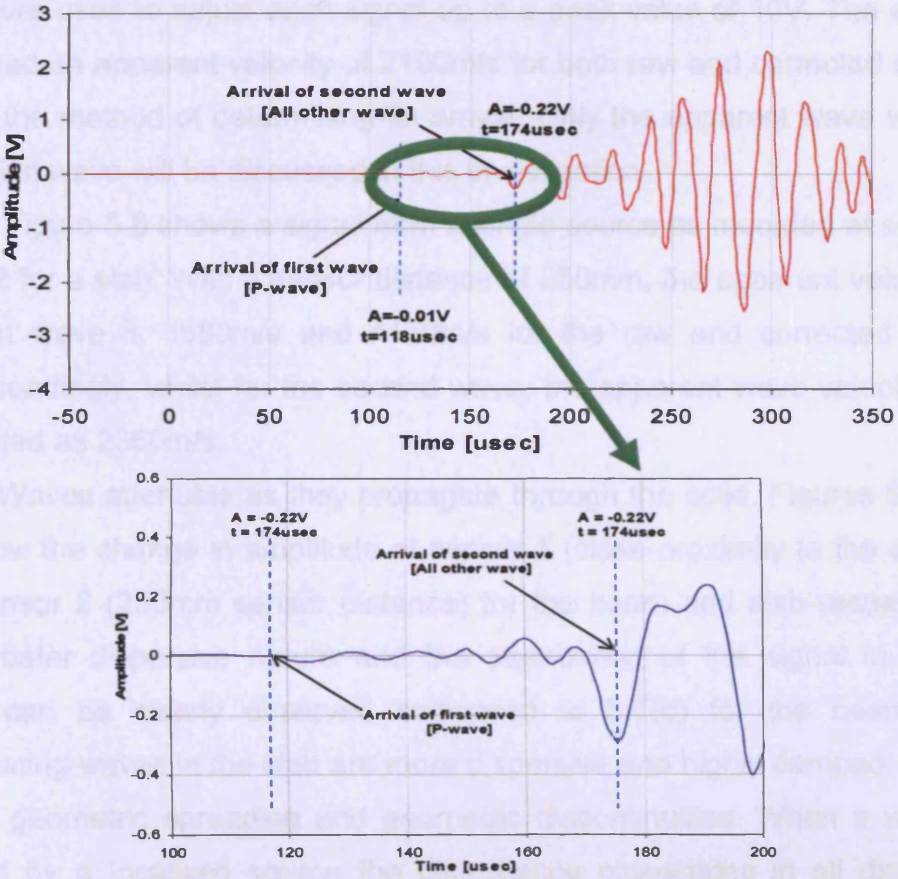

Figure 5.6: Arrival of the first and second wave.

Figure 5.7 shows a signal from a single source as recorded at sensor 1 and sensor 2 for a beam. Figure 5.7(a) shows the signal at sensor 1. From this waveform, the separation between the first and second wave is difficult to predict. This is because the sensor is close to the source. As the source-to-sensor distance increases (as in Figure 5.7(b)), the arrival of various wave modes can be seen more clearly, particularly at relatively low and high amplitudes which are known as the first wave and second waves respectively.

Using the difference between the arrival times of the signals, it is possible to determine the apparent wave velocity of the first and second wave. In Figure 5.7, at a distance of 250mm, the apparent velocity of the first wave is 4310m/s and 4630m/s for the raw and corrected signals respectively. The calculated apparent wave velocities were based on a 40dB threshold level. The corrected apparent wave velocity is higher due to the normalizing procedure used to adjust each signal up to a peak value of 10V. The second wave had an apparent velocity of 2190m/s for both raw and corrected signals due to the method of determining its arrival. Only the apparent wave velocity of the first wave will be discussed in this investigation.

Figure 5.8 shows a signal from a single source as recorded at sensors 1 and 2 for a slab. With a sensor distance of 250mm, the apparent velocity of the first wave is 3680m/s and 4170m/s for the raw and corrected signal correspondingly, whilst for the second wave, the apparent wave velocity was calculated as 2360m/s.

Waves attenuate as they propagate through the solid. Figures 5.7 and 5.8 show the change in amplitude at sensor 1 (close proximity to the source) and sensor 2 (250mm sensor distance) for the beam and slab respectively. The greater dispersive nature and the attenuation of the signal in Figure 5.8(b) can be clearly observed compared to 5.7(b) for the beam. The propagating waves in the slab are more dispersive and highly damped. This is due to geometric spreading and geometric discontinuities. When a wave is created by a localised source the disturbance propagates in all directions therefore reducing its intensity with distance, especially for a large structure such as a slab. A regularly used slab contains many geometric discontinuities such as cracks and aggregate boundaries which also contribute to a reduction in the intensity of the signal.

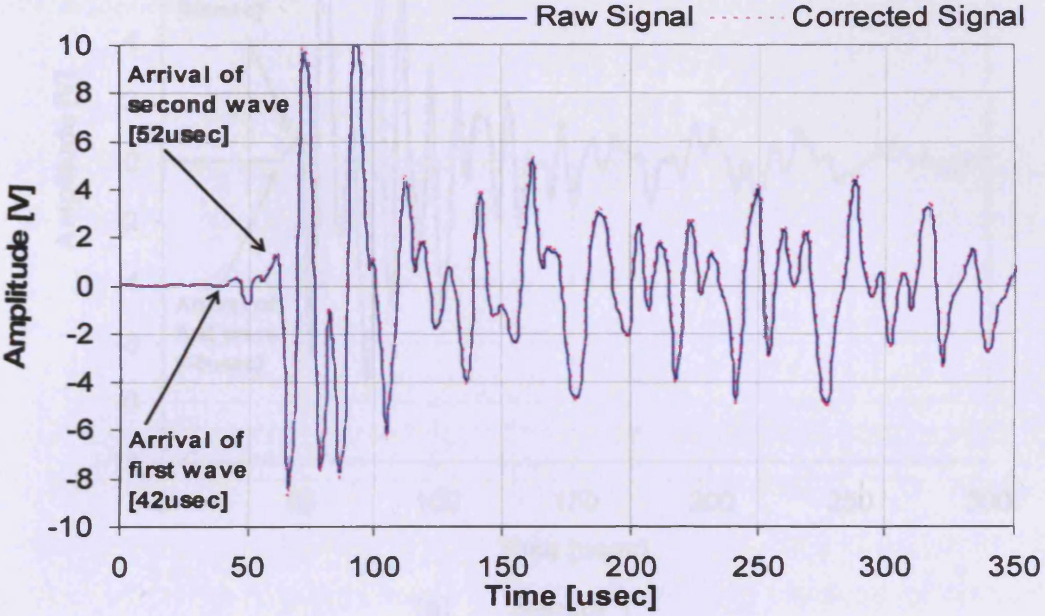

(a) Sensor 1

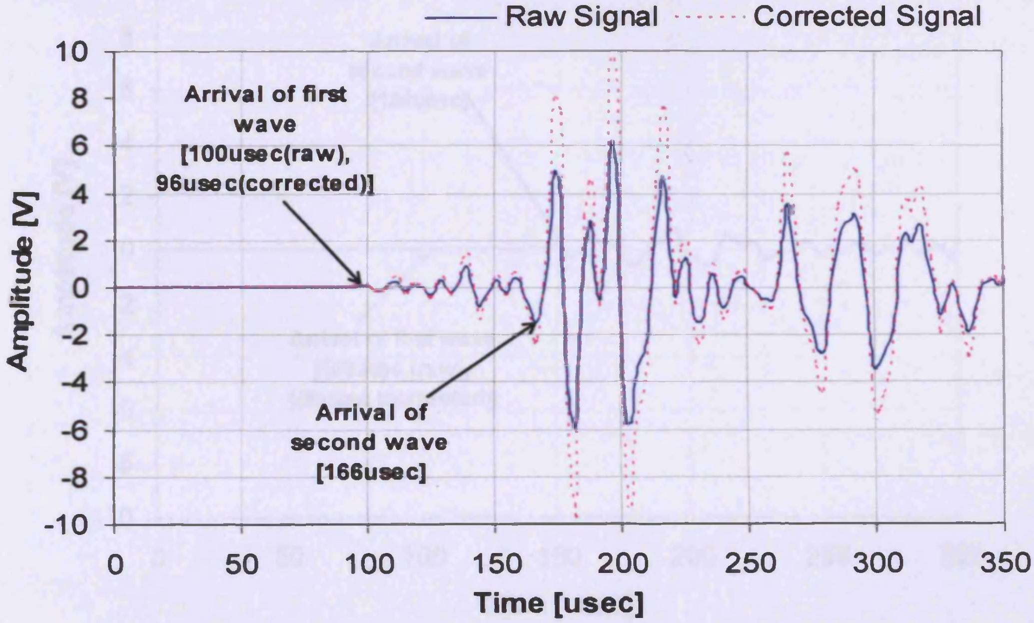

(b) Sensor 2

Figure 5.7: Results of H-N source parallel to sensor face for raw and corrected signal at (a) sensor 1 and (b) sensor 2 for the beam

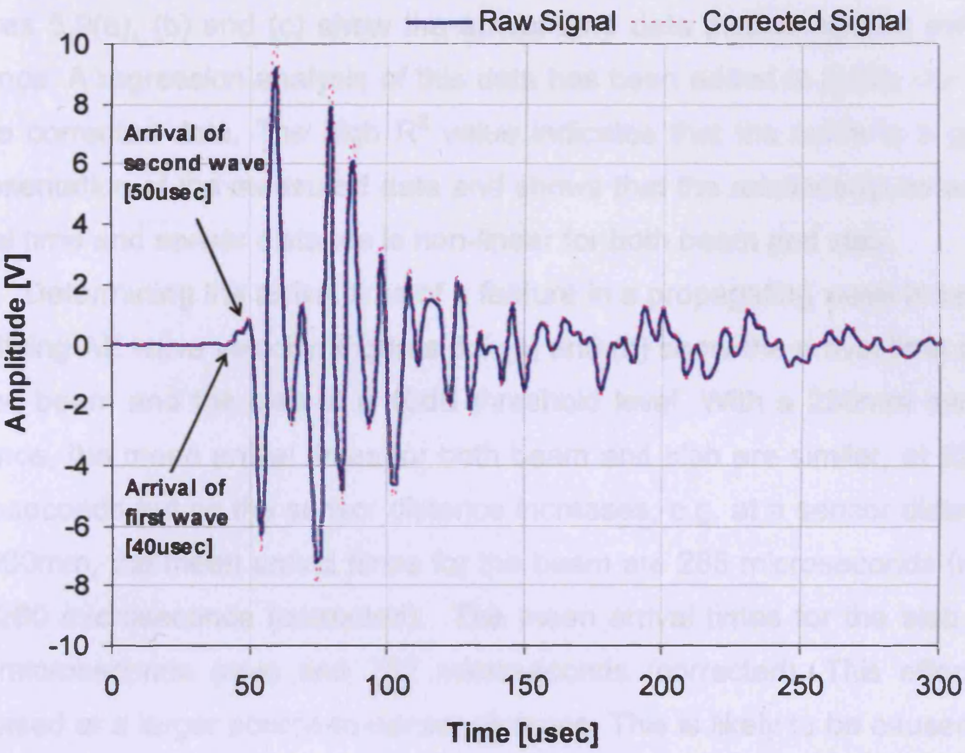

(a) Sensor 1

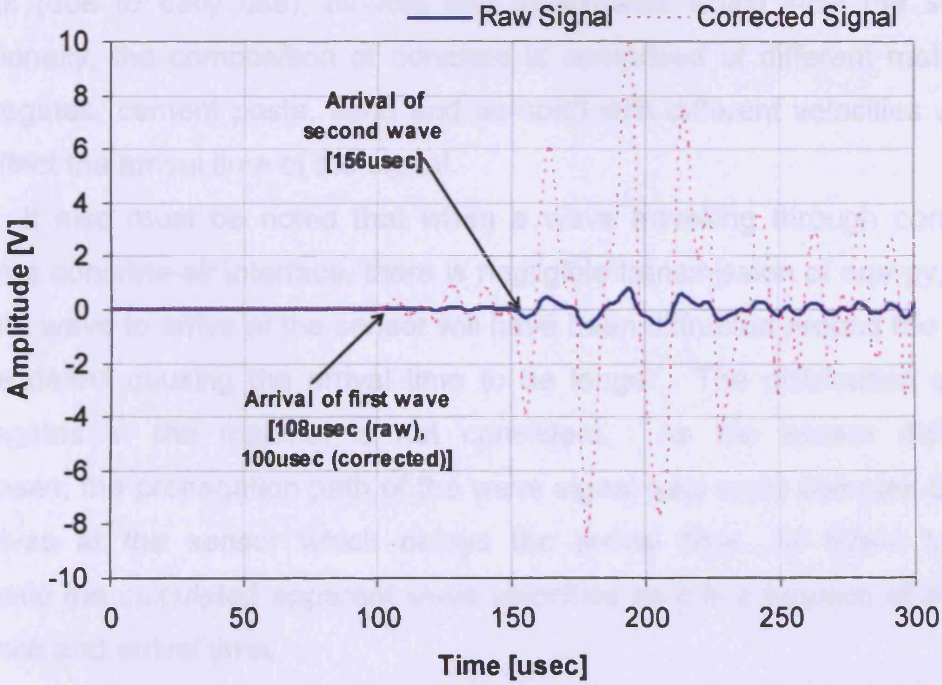

(b) Sensor 2

Figure 5.8: Results of H-N source parallel of the sensor face for raw and corrected signal at (a) sensor 1 and (b) sensor 2 for the slab.

Figures 5.9(a), (b) and (c) show the arrival time data plotted against sensor distance. A regression analysis of this data has been added to justify the use of the corrected data. The high R^2 value indicates that the curve is a good representation of the measured data and shows that the relationship between arrival time and sensor distance is non-linear for both beam and slab.

Determining the arrival time of a feature in a propagating wave is key in identifying AE wave velocity. Figures 5.9 (a) and (b) show the arrival time data for the beam and the slab at a 40dB threshold level. With a 250mm sensor distance, the mean arrival times for both beam and slab are similar, at 52-56 microseconds but as the sensor distance increases, e.g. at a sensor distance of 1000mm, the mean arrival times for the beam are 285 microseconds (raw) and 260 microseconds (corrected). The mean arrival times for the slab are 418 microseconds (raw) and 262 microseconds (corrected). This effect is increased at a larger source-to-sensor distance. This is likely to be caused by the real signal path being longer than the direct path because of concrete cracks (due to daily use), air-void and aggregates which slow the signal. Additionally, the composition of concrete is comprised of different materials (aggregates, cement paste, sand and air-void) with different velocities which will affect the arrival time of the signal.

It also must be noted that when a wave travelling through concrete meets a concrete-air interface, there is negligible transmission of energy, thus the first wave to arrive at the sensor will have been diffracted around the edge of the defect causing the arrival time to be longer. The distribution of the aggregates in the material is not consistent. As the sensor distance increases, the propagation path of the wave signal gets more complex before it arrives at the sensor which delays the arrival time. All these factors influence the calculated apparent wave velocities as it is a function of sensor distance and arrival time.

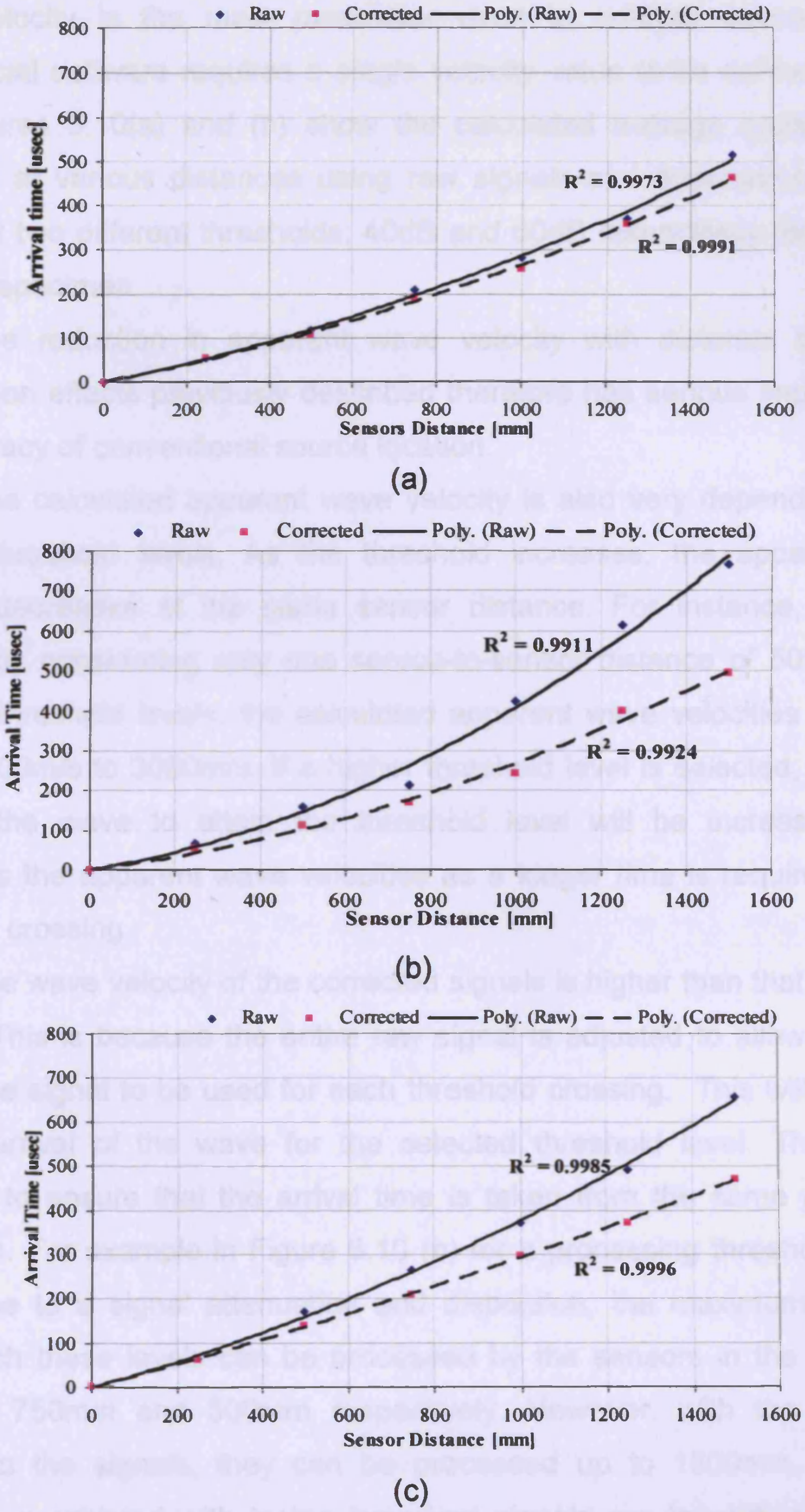

(a)

(b)

(c)

Figure 5.9: Regression analysis of arrival time against sensor distance of source parallel to sensor face at (a) 40dB threshold (RC Beam), (b) 40dB threshold (RC Slab) and (c) 60dB threshold (RC Beam).

Wave velocity is the main parameter used to analyse source location. Commercial software requires a single velocity value to be defined for each test. Figures 5.10(a) and (b) show the calculated average apparent wave velocities at various distances using raw signals and attenuation corrected signals at two different thresholds; 40dB and 60dB respectively for the beam and slab specimen.

The reduction in apparent wave velocity with distance due to the propagation effects previously described therefore has serious implication for the accuracy of conventional source location.

The calculated apparent wave velocity is also very dependent on the pre-set threshold levels. As the threshold increases, the apparent wave velocity decreases at the same sensor distance. For instance, in Figure 5.10(a), by considering only one source-to-sensor distance of 500mm, with different threshold levels, the calculated apparent wave velocities are in the range 4500m/s to 3000m/s. If a higher threshold level is selected, the arrival time of the wave to attain the threshold level will be increased. This influences the apparent wave velocities as a longer time is required prior to threshold crossing.

The wave velocity of the corrected signals is higher than that of the raw signals. This is because the entire raw signal is adjusted to allow the same part of the signal to be used for each threshold crossing. This will affect the time of arrival of the wave for the selected threshold level. This method attempts to ensure that the arrival time is taken from the same part of the waveform. For example in Figure 5.10 (b) for a processing threshold level of 60dB, due to a signal attenuation and dispersion; the maximum distances over which these levels can be processed by the sensors in the beam and slab are 750mm and 500mm respectively. However, with the correction applied to the signals, they can be processed up to 1500mm. Therefore problems associated with losing important signals are low when using the corrected signals. These results also indicate that attenuation cannot be avoided when dealing with concrete structures. With a sensor distance of 1.5

metres, the signal amplitude that was recorded was only 40dB for the slab. This suggests that the ability to locate damage in concrete structures is limited. It is suggested that a lower threshold level or increased sensor density is required for structural monitoring.

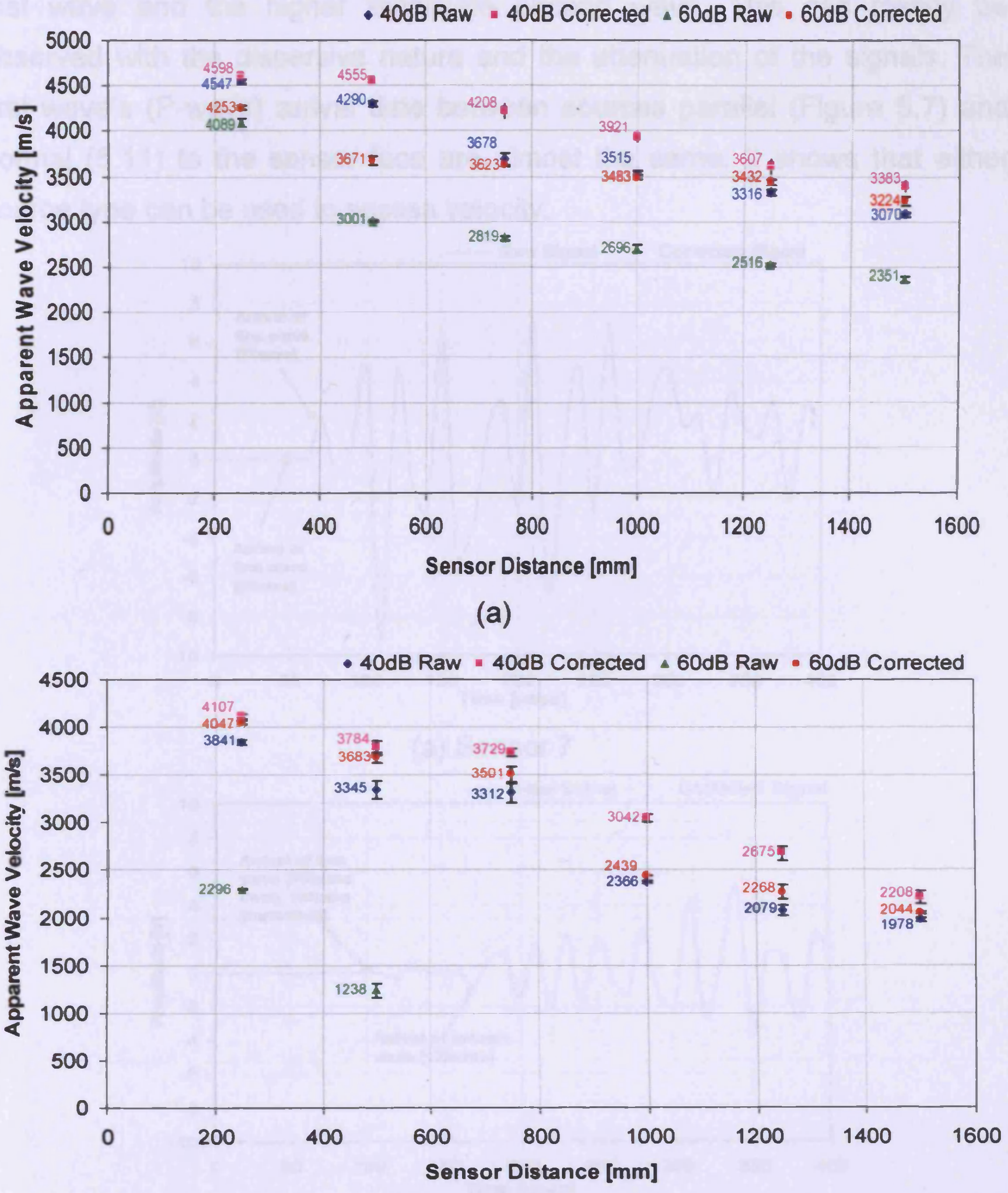

(a)

(b)

Figure 5.10: Apparent wave velocity for raw and corrected signal of source parallel to sensor face for (a) RC beam and (b) RC slab at 40dB and 60dB.

5.4.1.2 Source Normal to Sensor Face

Figure 5.11 (a) and (b) show the response of sensors 7 and 6 as a result of an H-N source normal to the sensor face. The location of the H-N source was 100mm from sensor 7. The signals illustrate the arrival of the low amplitude first wave and the higher amplitude second wave. This can clearly be observed with the dispersive nature and the attenuation of the signals. The first wave's (P-wave) arrival time between sources parallel (Figure 5.7) and normal (5.11) to the sensor face are almost the same. It shows that either source type can be used to assess velocity.

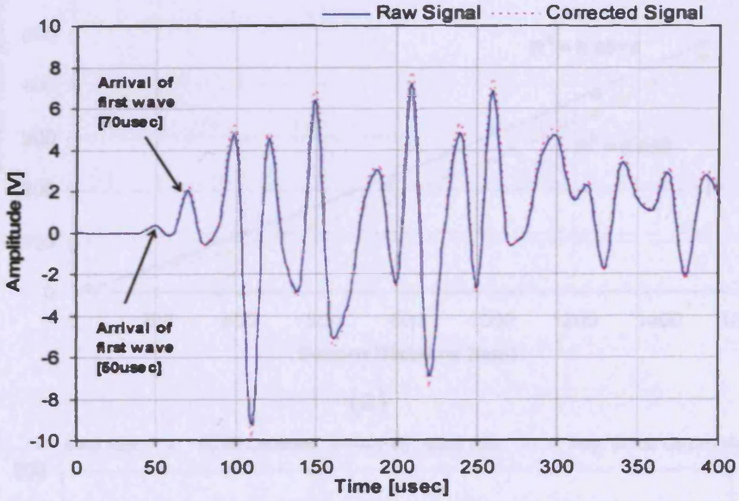

(a) Sensor 7

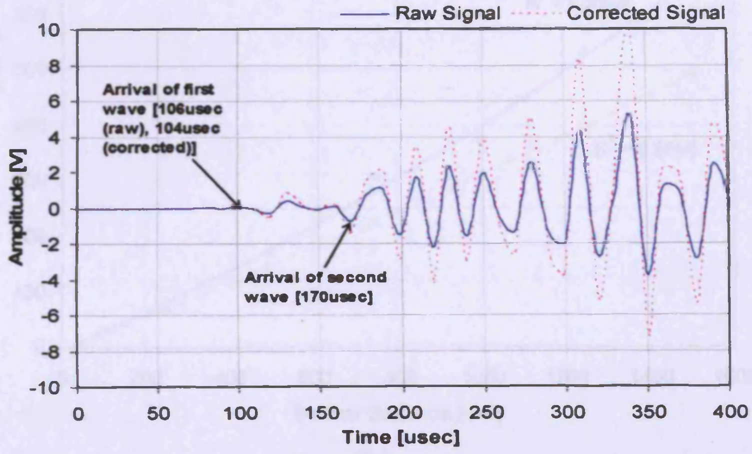

(b) Sensor 6

Figure 5.11: Results of an H-N source normal to the sensor face for a raw and corrected signal at (a) sensor 7 and (b) sensor 6 for RC beam.

Figures 5.12 (a) and (b) show the regression analysis of the arrival time data plotted against sensor distance for 40dB and 60dB respectively. The high R^2 value indicates that the curve is a good representation of the measured data and concurs that the relationship between arrival time and sensor distance is non-linear for source normal to sensor face.

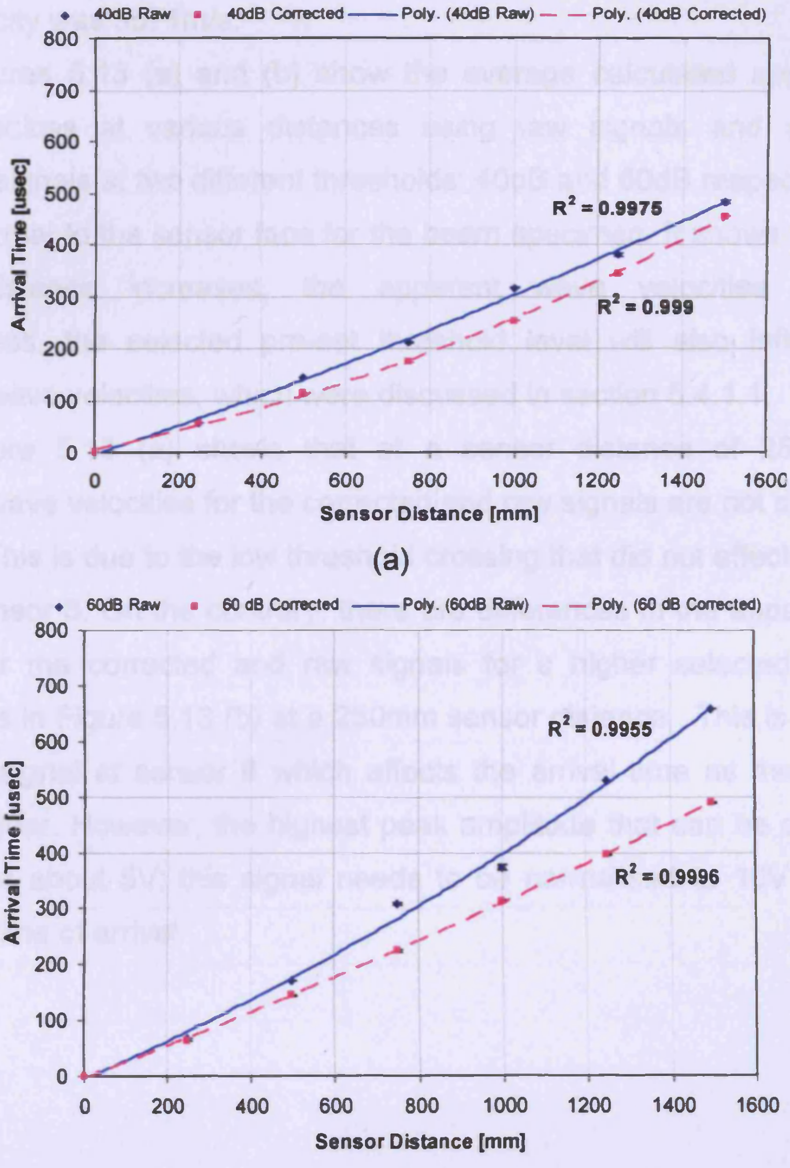

(a)

(b)

Figure 5.12: Regression analysis of arrival time against time of source normal to sensor face at (a) 40dB threshold (RC Beam), (b) 60dB threshold (RC Beam).

The velocity of the wave can be determined by calculating the difference between the signals' arrival time and the threshold crossings. At a sensor distance of 250mm and a threshold level of 40dB, the apparent velocity of the first wave is 4467m/s and 4630m/s for the raw and corrected signals correspondingly. There was no further analysis of the corrected signal's second wave therefore, based on its arrival time, the calculated apparent wave velocity was 3571m/s.

Figures 5.13 (a) and (b) show the average calculated apparent first wave velocities at various distances using raw signals and attenuation corrected signals at two different thresholds; 40dB and 60dB respectively for a source normal to the sensor face for the beam specimen. It shows that as the sensor distance increases, the apparent wave velocities decrease. Nevertheless, the selected pre-set threshold level will also influence the apparent wave velocities, which were discussed in section 5.4.1.1.

Figure 5.13 (a) shows that at a sensor distance of 250mm, the apparent wave velocities for the corrected and raw signals are not significantly different. This is due to the low threshold crossing that did not affect the arrival time at sensor 6. On the contrary, there are differences in the apparent wave velocity for the corrected and raw signals for a higher selected threshold crossing as in Figure 5.13 (b) at a 250mm sensor distance. This is due to the corrected signal at sensor 6 which affects the arrival time as the threshold level is higher. However, the highest peak amplitude that can be detected at sensor 6 is about 5V; this signal needs to be normalised to 10V which will affect the time of arrival.

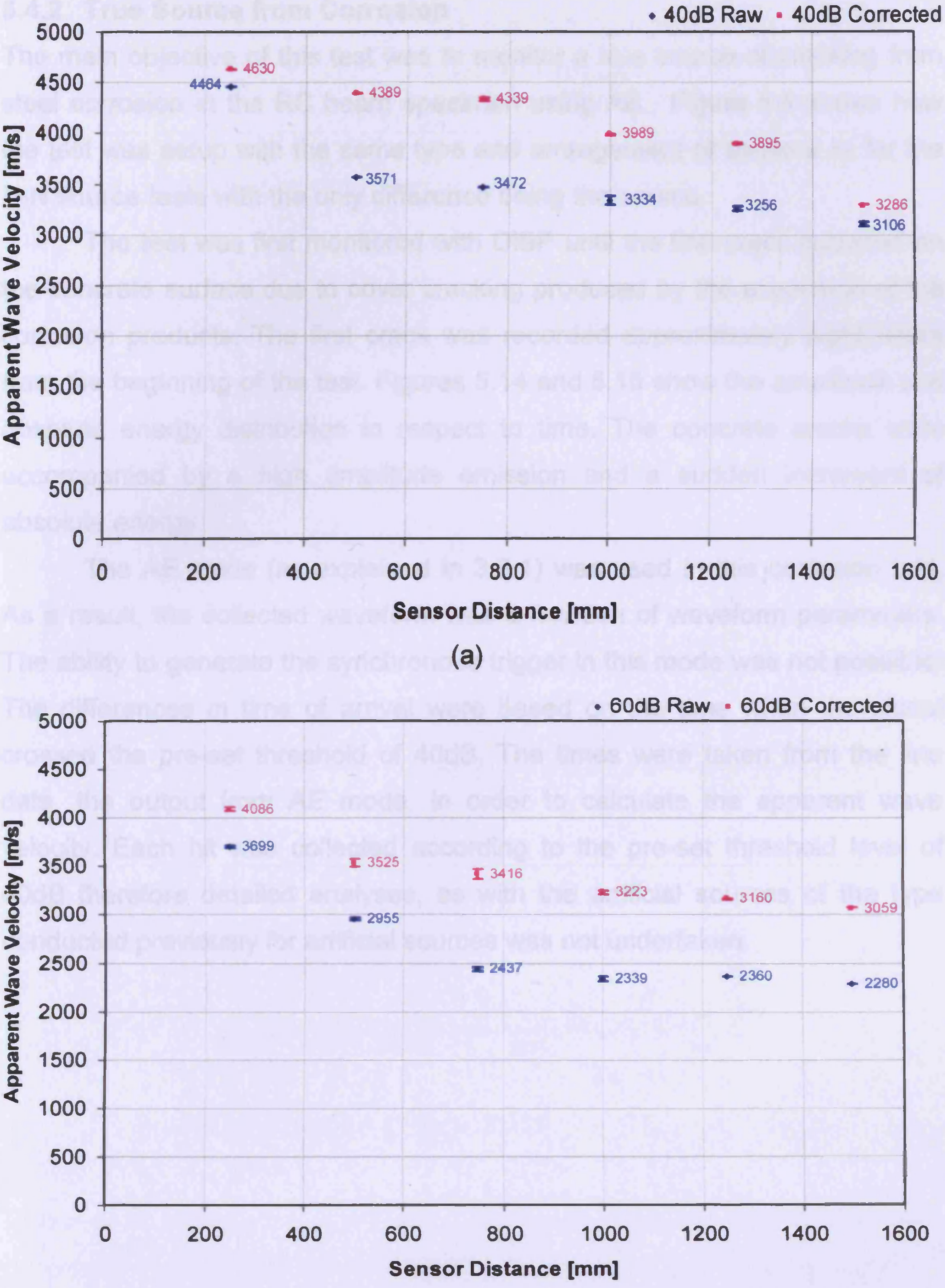

(b)

Figure 5.13: Apparent wave velocity for raw and corrected signal of source normal to sensor face for RC beam at (a) 40dB and (b) 60dB.

5.4.2 True Source from Corrosion

The main objective of this test was to monitor a true source of cracking from steel corrosion in the RC beam specimen using AE. Figure 5.4 shows how the test was setup with the same type and arrangement of sensors as for the H-N source tests with the only difference being the source.

The test was first monitored with DiSP until the first crack occurred on the concrete surface due to cover cracking produced by the expansion of the corrosion products. The first crack was recorded approximately eight hours from the beginning of the test. Figures 5.14 and 5.15 show the amplitude and absolute energy distribution in respect to time. The concrete cracks were accompanied by a high amplitude emission and a sudden increment of absolute energy.

The AE mode (as explained in 3.2.1) was used in this corrosion test. As a result, the collected waveform was a function of waveform parameters. The ability to generate the synchronous trigger in this mode was not possible. The differences in time of arrival were based on the time when the signal crossed the pre-set threshold of 40dB. The times were taken from the line data, the output from AE mode, in order to calculate the apparent wave velocity. Each hit was collected according to the pre-set threshold level of 40dB therefore detailed analyses, as with the artificial sources of the type conducted previously for artificial sources was not undertaken.

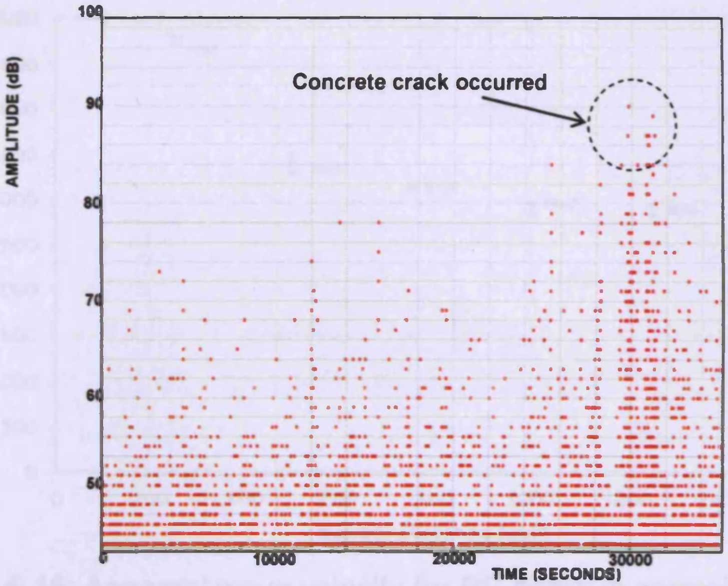

Figure 5.14: Amplitude distribution in respect to time.

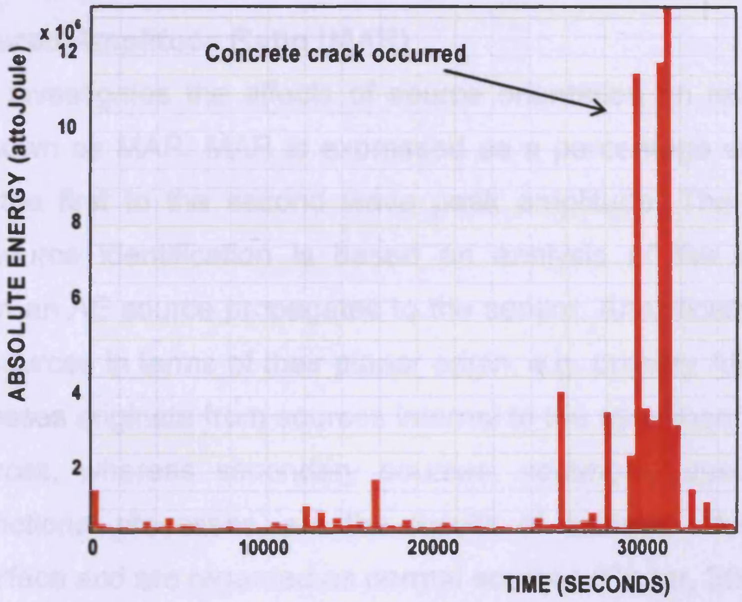

Figure 5.15: Absolute Energy distribution in respect to time.

Figure 5.16 shows the average of the apparent wave velocity that was generated by a true source of corrosion using a 40dB pre-set threshold level. For a distance of 250mm based on three events, the average of the calculated apparent wave velocity (raw signal) is 4762m/s. For a sensor distance of 1.5m, the average apparent wave velocity (raw signal) is 2523m/s.

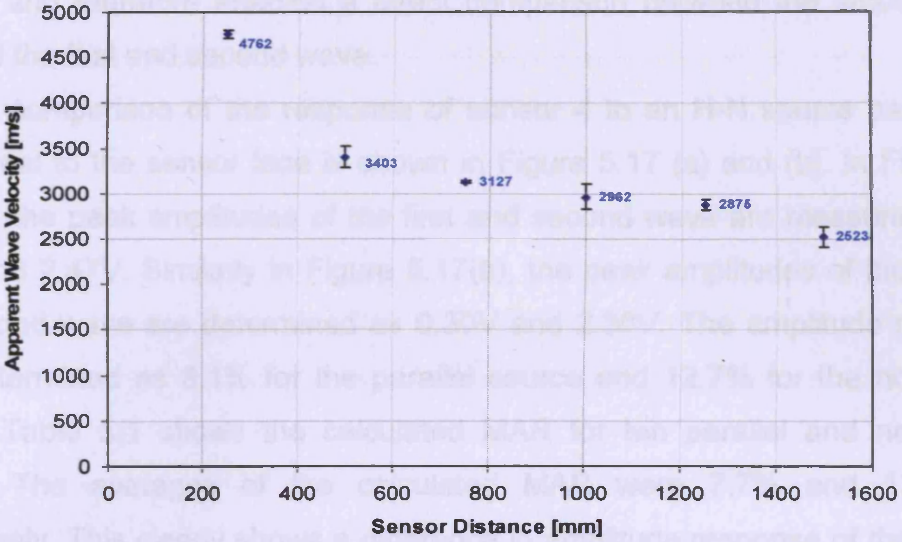

Figure 5.16: Apparent wave velocity for RC beam in corrosion test.

5.4.3 Measured Amplitude Ratio (MAR)

This section investigates the effects of source orientation on relative modal amplitude known as MAR. MAR is expressed as a percentage which equals the ratio of the first to the second wave peak amplitude. The principle of modal AE source identification is based on analysis of the way energy released from an AE source propagates to the sensor. Analytically it is useful to consider sources in terms of their planar origin, e.g. primary AE from crack growth processes originate from sources internal to the specimen they termed parallel sources, whereas secondary sources, commonly associated with noise and frictional processes, are the results of external interaction with specimen surface and are regarded as normal sources (Carter, 2000).

In this investigation, two types of artificial source were generated using an H-N source; one source parallel and one source normal to the sensor face. The source that parallel to the sensor face was generated at 100mm from sensor 1 whereas the source normal to the sensor face was generated at 100mm from sensor 7 as shown in Figure 5.3. Although all sensors were the same (R6D), their characteristics can vary between individual sensors. Sensor 4 was selected for investigation as it was the fourth sensor for both sources and therefore enabled a direct comparison between the amplitude ratio and the first and second wave.

A comparison of the response of sensor 4 to an H-N source parallel and normal to the sensor face is shown in Figure 5.17 (a) and (b). In Figure 5.17 (a), the peak amplitudes of the first and second wave are measured as 0.20V and 2.47V. Similarly in Figure 5.17(b), the peak amplitudes of the first and second wave are determined as 0.30V and 2.36V. The amplitude ratios were determined as 8.1% for the parallel source and 12.7% for the normal source. Table 5.1 shows the calculated MAR for ten parallel and normal signals. The averages of the calculated MAR were 7.7% and 13.2% respectively. This clearly shows a difference in amplitude response of the two parallel and normal source modes. Consequently, when an H-N source is parallel to the sensor face, the majority of the displacement appropriate to the source is normal to the beam. However, due to the Poisson effect, there is still deformation parallel to the sensor face plane. When the source is normal to the sensor face, the reverse should therefore be true

Carter (2000) and Pullin (2005) examined the amplitude of the two dominant plate modes in an 8mm steel I-beam and an aerospace grade steel. They both found that it was possible to determine the orientation of the source by examining the MAR. Carter (2000) found that with a steel I-beam specimen, the MAR values for the source parallel to the sensor face was around 10% and 30%-60% for a source normal to sensor face. Pullin (2005) found that with aerospace grade steel, the MAR values for the source parallel to the sensor face was 9.9% and 29.0% for the source normal to sensor face. Both studies were related to steel specimens. In these concrete specimens, the MAR values for a source parallel to the sensor face was 7.7% and for a source normal 13.2%. Even though the effects of the test are variable (individual frequency response, selection of sensor type, materials) on measured MAR values, the same trend is observed, i.e. a low MAR value for a parallel source and high MAR value for a normal source. Furthermore, it is clear that the measured MAR value appears to vary depending on orientation of the H-N source. Additionally, the MAR value is affected by the path propagation from source-to-sensor, subject to variation due to interference from reflections which can cause first and second wave's mode peak superposition.

Since the MAR is based on the amplitude measurement of two different wave modes, it is clear that the relative response of the sensor to the individual frequency characteristics of each wave mode will significantly influence the resulting value (Carter, 2000). A broadband sensor can be used to "weigh" the amplitudes of the two modes equally. However, the relatively low sensitivity of these sensors can cause them to be impractical for field use.

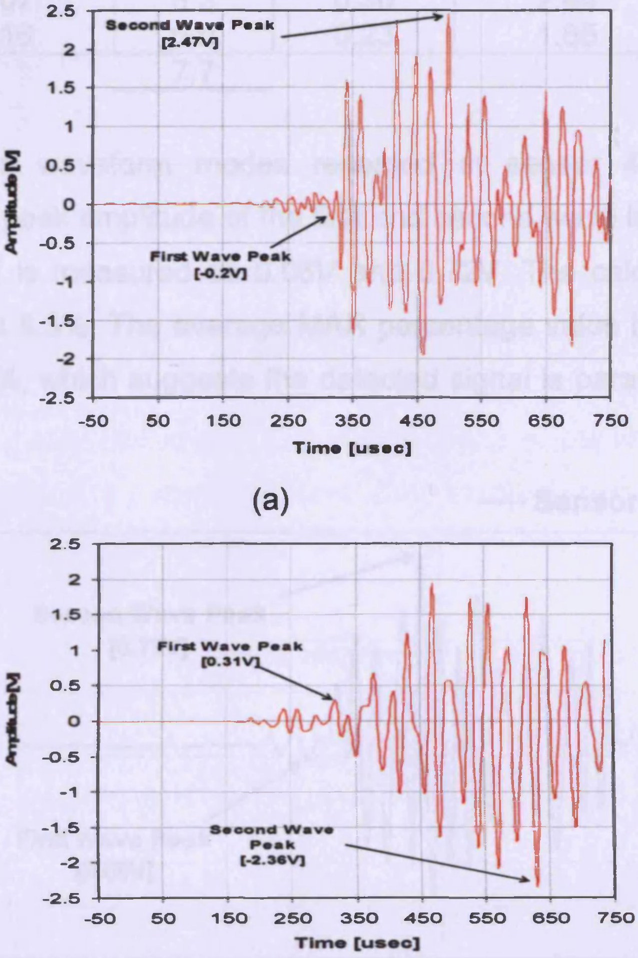

(a)

(b)

Figure 5.17: Results of an H-N source at sensor 4 for (a) parallel and (b) normal to sensor face.

Table 5.1: Calculated Measured Amplitude Ratio (MAR) for artificial source.

Parallel Source			Normal Source		
Amplitude (v)		MAR (%)	Amplitude (V)		MAR (%)
Peak First Wave	Peak Second Wave		Peak First Wave	Peak Second Wave	
0.15	2.02	7.4	0.33	2.58	12.8
0.15	1.83	8.2	0.27	1.81	14.9
0.12	1.40	8.5	0.31	2.35	13.2
0.15	1.68	8.5	0.35	2.89	12.1
0.20	2.47	8.1	0.30	2.36	12.7
0.16	1.93	8.3	0.39	2.40	16.6
0.17	2.11	8.1	0.27	2.20	12.3
0.16	2.12	7.6	0.31	2.67	11.6
0.13	2.07	6.3	0.30	2.44	12.3
0.13	2.16	6.0	0.23	1.65	13.9
Average		7.7			13.2

Figure 5.18 shows waveform modes recorded at sensor 4 during the corrosion test. The peak amplitude of the first and second wave is also shown in Figure 5.18 and is measured as 0.06V and 0.72V. The calculated MAR percentage value is 8.3%. The average MAR percentage value based on the three events is 8.1%, which suggests the detected signal is parallel to sensor face.

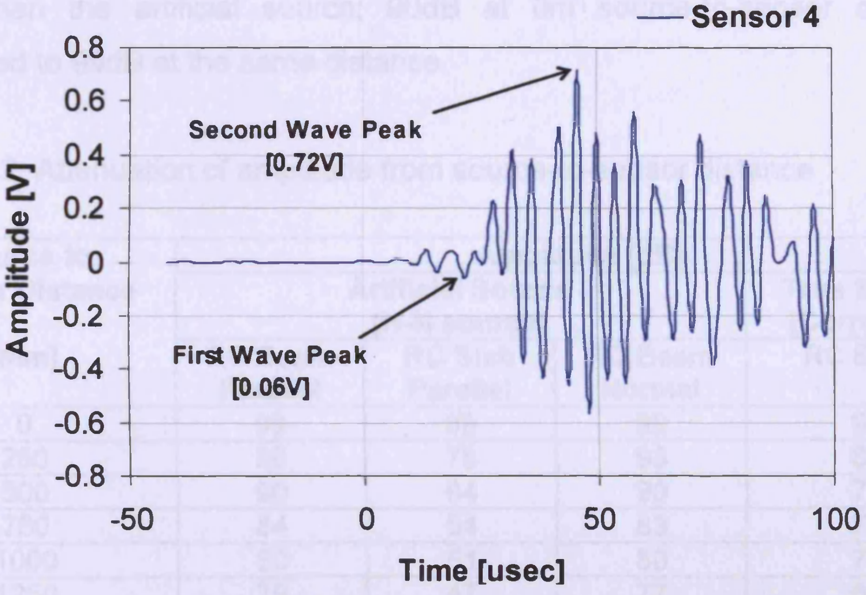

Figure 5.18: Signal recorded at sensor 4 during corrosion test.

From this investigation, it is clear that the MAR values appear to vary depending on the orientation of the H-N source. However, before any inference can be drawn to a physical meaning and practical use of the ratios, several factors must be considered. The foregoing MAR values are based on measurements taken from a single signal at a single source-to-sensor distance by a single sensor type. If MAR values are to be interpreted to provide an insight into source orientation in a more arbitrary situation, further information on the effects of propagation distance and sensor type for a greater number of sample signals are required.

5.4.4 Signal Attenuation

Signal attenuation is the reduction in AE signal amplitude as a wave propagates. Table 5.2 shows the attenuation of the signal amplitude for different source-to-sensor distances. Figure 5.19 presents this data in graph form where the signal attenuation trends for both sources parallel and normal to sensor face for the beam were not dissimilar. This is likely due to the specimen being the same even though the source orientation was different. The true source from the corrosion signal was also from the same specimen but the attenuation curve was lower. This is due to the signal strength being lower than the artificial source; 90dB at 0m source-to-sensor distance compared to 99dB at the same distance.

Table 5.2: Attenuation of amplitude from source-to-sensor distance

Source to Sensor Distance [mm]	**Amplitude [dB]**			
	Artificial Source [H-N source]			**True Source [Corrosion]**
	RC Beam Parallel	**RC Slab Parallel**	**RC Beam Normal**	**RC Beam**
0	99	99	99	90
250	96	78	93	82
500	90	64	90	78
750	84	54	83	75
1000	80	51	80	70
1250	79	47	77	68
1500	78	44	73	65

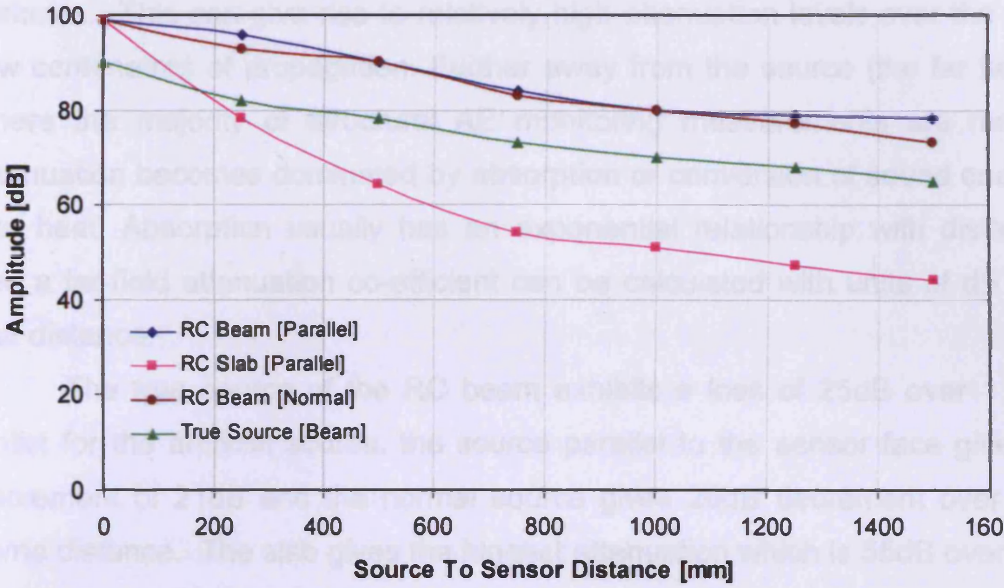

Figure 5.19: Attenuation of signal in dB at a different source-to-sensor distance.

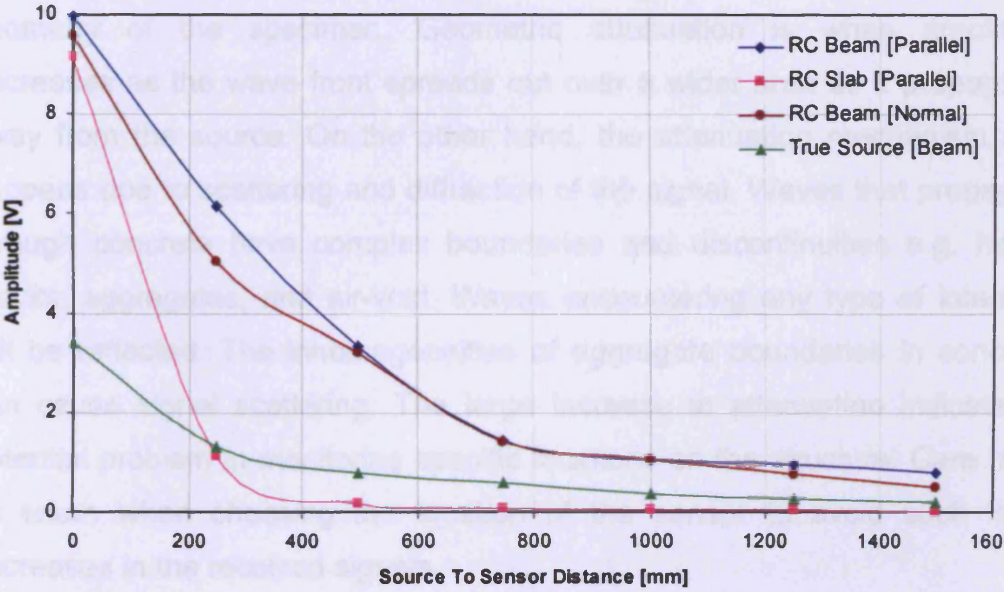

Figure 5.20: Attenuation of signal in Volts at a different source-to-sensor distance.

Figure 5.19 and Figure 5.20 show the attenuation of signal in dB and Volts at a different source-to-sensor distance. In Figure 5.20, a high drop of amplitude in Volts was recorded at 250mm and was almost stable at longer source-to-sensor distances. Theoretically, wave amplitude decreases inversely with distance in three and two dimensions as the square root of the propagation distance. This can give rise to relatively high attenuation levels over the first few centimetres of propagation. Further away from the source (the far field), where the majority of structural AE monitoring measurements are made, attenuation becomes dominated by absorption or conversion of sound energy into heat. Absorption usually has an exponential relationship with distance and a far-field attenuation co-efficient can be calculated with units of dB per unit distance.

The true source of the RC beam exhibits a loss of 25dB over 1.5m, whilst for the artificial source, the source parallel to the sensor face gives a decrement of 21dB and the normal source gives 26dB decrement over the same distance. The slab gives the biggest attenuation which is 55dB over the same 1.5m source-to-sensor distance.

This observation shows that slab gives a bigger attenuation compared to beam specimen. One of the factors that can cause attenuation is the geometry of the specimen. Geometric attenuation is when amplitude decreases as the wave front spreads out over a wider area as it propagates away from the source. On the other hand, the attenuation mechanism also happens due to scattering and diffraction of the signal. Waves that propagate through concrete have complex boundaries and discontinuities e.g. holes, cracks, aggregates, and air-void. Waves encountering any type of interface will be reflected. The inhomogeneities of aggregate boundaries in concrete can cause signal scattering. The large increase in attenuation indicates a potential problem in monitoring specific locations on the structure. Care must be taken when choosing the location of the sensor to avoid such large decreases in the received signals.

5.5 DISCUSSION

Theoretically, from the physics of elastic wave propagation, the wave velocity is proportional to the square root of the elastic modulus and inversely proportional to the square root of the mass density of the concrete. Therefore, the wave velocity is constant when the wave propagates through a medium. However, in AE practice, the methods or techniques that were used to measure the wave velocity revealed that the 'apparent' wave velocities were not constant when the wave propagates through a medium. This ambiguous velocity leads to difficulty in the techniques used to locate the source of AE events.

On the whole, this work has investigated signal attenuation and wave in concrete structures over a variety of source-to-sensor distances. It has been shown that apparent wave velocities decrease as the sensor distance increases. Acoustic waves are modified as they propagate through the material due to scattering, absorption, attenuation and retransmission through different materials such as aggregates, cement paste, reinforcement, air-void due to cracks etc which will affect the wave propagation (Miller and McIntire, 1987).

The presence of steel reinforcement in the RC specimen will affect the calculated apparent wave velocity. Since the wave velocity through steel is greater than concrete the wave signal may be refracted into the bars and transmitted to the receiver at the wave velocity of the steel. The apparent velocity through the member will be greater than the actual velocity through the concrete.

The measured apparent wave velocity may also be affected by the presence of cracks or voids along the propagation path from source-to-sensors. The wave signal may be diffracted around the discontinuities thus increasing the travel path and travel time. Consequently, the apparent wave velocity will be measured incorrectly through time of arrival techniques.

Apart from investigating the wave propagation in concrete structures over a variety of source-to-sensor distances; a selected threshold level also has an impact on the measured apparent wave velocities. As the selected threshold level increases, the arrival times increase hence causing a decrease in the apparent wave velocities. For a source-to-sensor distance of 1.5m, the signal amplitude recorded was only 40dB, whereas for 60dB, the maximum source to distance was 0.5m. Consequently, the ability to locate damage in concrete structures is limited to a higher threshold level.

There have been few studies in determining the P-wave velocity in Ultrasonics. Philippidis and Aggelis (2005) investigated the effect of the water to cement ratio on wave velocity in concrete, where for a range of water to cement ratios between 0.375 and 0.45, the P-wave velocity varied between

3500m/s and 4700m/s. As the water to cement ratio decreased, the velocity of the P-wave increased. Additionally, the authors found that using a signal from a 15 kHz tone burst at a sensor distance of 150mm, the apparent wave velocity of P-waves in concrete ranged from 4100m/s to 4700m/s. This suggests that, as well as steel reinforcement, aggregates, air-void, cracks and path propagation, the moisture content of the specimen is an important factor in influencing the calculated apparent wave velocities. Gassman and Tawheed (2004) and Chang et al. (2006) discovered that the wave velocity in concrete varies from 3500m/s to 4000m/s depending on concrete composition, age and condition.

These factors must be taken into consideration with regards to the reduction in velocity; the increase in distance is an important result as AE users often take a velocity measurement at one distance and use it in location studies over a range of distances. Furthermore the source location will be greatly affected when considering the inaccuracy in determining the P-wave arrival times. Source location is of prime interest for modern AE analysis as it can be used to evaluate damage localization and crack propagation. Additionally, accurate source location is essential for quantitative AE analysis using moment tensor analysis (Li, 1996).

There is a similarity in measuring wave velocity techniques between Ultrasonics and AE. Both techniques define wave velocity as a distance from the source-to-sensors over the time travelled from the source-to-sensor. The method that was used in this investigation is similar to indirect transmission in determining pulse velocity in Ultrasonics. However, from the regression analysis, the results show that this experimental programme does not concur with the hypothesis proposed in BS EN 12504-4 (2004) for the testing of concrete using Ultrasonics. In this standard, the determination of the Ultrasonic pulse velocity is obtained by assuming that the relationship between the arrival time data and sensor distance is linear. The slope of the best-fit straight line is drawn through the measured arrival time data over sensor distance and the slope is taken as the mean wave velocity along the concrete surface. On the other hand, the best fit lines through the data for both specimens using the AE data shows that the relationship between the arrival time and sensor distance is non linear. Consequently, the apparent wave velocity decreases as the sensor distance increases as the wave propagates through the medium.

Signal attenuation involves the measurement of wave amplitudes as a function of propagation distance. There are two basic mechanisms by which a wave is attenuated: (1) geometric attenuation; (2) material attenuation. Geometric attenuation is the phenomena by which the amplitude of the wave decreases as the wave front spreads out over a wider area as it propagates away from the source. Material attenuation can be by either absorption or scattering. Due to attenuation, the monitoring of large structures e.g. concrete bridges, requires the use of many sensors placed sufficiently close together to ensure that an event emanating from any point on the structure will not be attenuated sufficiently to escape detection.

The MAR value was determined to investigate the effect of source orientation as to the viability of modal AE in structural monitoring applications. It was discovered that a source parallel to sensor face exhibited lower MAR values than a source normal to sensor face. However, if the MAR is to be viable as a practical discriminant, further quantitative information on factors that influence its absolute value for a specific source or a sensor position is required.

Several factors can complicate the use of MAR value as a source identification discriminant in structural monitoring. If conclusions on source orientation are to be drawn from MAR measurement, consideration on how the sensor mounting position and orientation relative to other elements influences its response to sources in various regions of the beam is required. This becomes complex if the precise source position is unknown, as is the case with global AE inspection. Furthermore, with an unknown source position, peak superposition and source depth, it is clear that the use of a single value MAR discriminant in a large area is unlikely to be practically viable.

5.6 CONCLUSION

In this study, it can be concluded that:

- RC concrete is a non-homogeneous material which consists of several materials (reinforced steel, aggregates, cement paste, sand and air voids). Therefore an apparent wave velocity was used as the wave velocity was not constant during propagation through the RC concrete. The apparent wave velocities were reduced due to attenuation and dispersion of the wave signal which affected the length of time in reaching the subsequent sensor.

- A practical investigation of two concrete structures shows that as the source–to-sensor distance increases, the calculated wave velocity decreases.
- The apparent wave velocities are between 4800m/s to 3100m/s for the beam specimen and 3841m/s to 2000m/s for the slab specimen for a source-to-sensor distance from 250mm to 1500mm with a 40dB pre-set threshold. This shows that the apparent wave velocity is not constant as the wave propagates through the concrete. Additionally, the apparent wave velocities varied between one specimen and another.
- The apparent wave velocity used in automatic TOA should be carefully selected considering both the distance at which measurements will be taken and the threshold used. A low threshold level is recommended in order to locate damage in large concrete structures.
- There is a tendency of a low MAR value for a parallel source and a high MAR value for a normal source on the relative distribution of values rather than absolute value measured. The MAR value of a signal from a given source is dependent on sensor frequency response characteristics and mounting orientation relative to the source. Additionally, the MAR value measurement is subject to variation due to interference from reflections which can cause first and second wave mode peak superposition.
- Propagation of the elastic waves in concrete is affected by the geometry of the sample, the path taken from the source-to-sensor and the concrete composition and condition. These need to be taken into consideration when determining the RC concrete's apparent wave velocity.

CHAPTER 6: ACOUSTIC EMISSION ASSESSMENT OF M4 ELEVATED CROSSHEAD

6.1 INTRODUCTION

Four reinforced concrete crossheads supporting the elevated section on the M4 West of Junction 1 in West London were assessed using Acoustic Emission Monitoring (AEM). This work was undertaken by Physical Acoustic Limited (PAL) and the data was made available to Cardiff University for further analysis.

The four crossheads were; Crosshead number 66 (AEM 1), Crosshead number 68 (AEM 2), Crosshead number 74 (AEM 3) and Crosshead number 82 (AEM 4) as indicates in Figure 6.1. These crossheads were selected due to the presence of visually identifiable surface cracks and advanced corrosion damage.

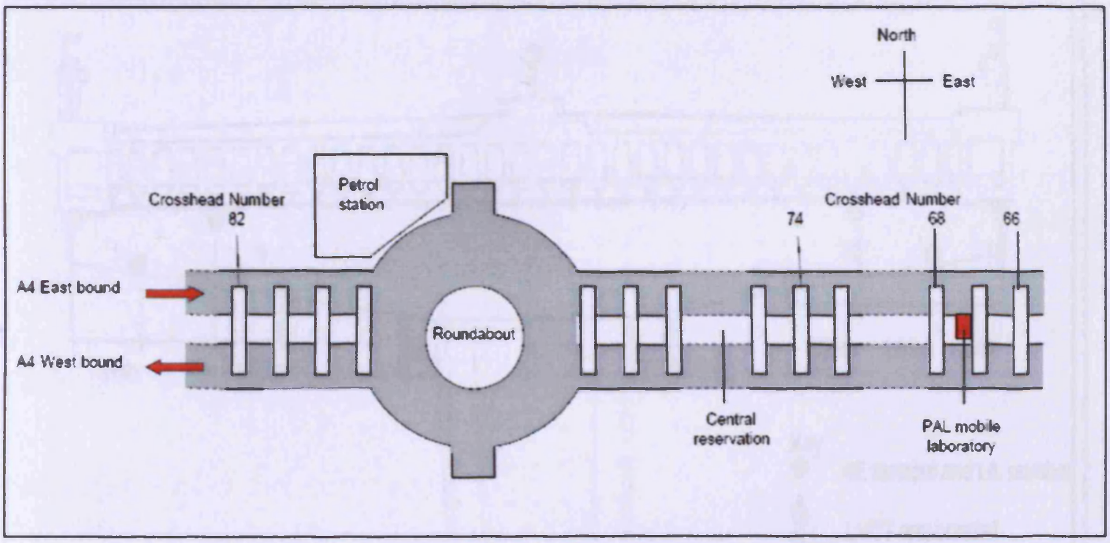

Figure 6.1: Plan of site and location of monitoring.

Figure 6.2 shows Crosshead 68 of the M4 elevated section. Figure 6.3 and 6.4 show the east and west face of Crosshead 68 showing the AE sensors and LVDT positions.

Figure 6.2: Crosshead 68.

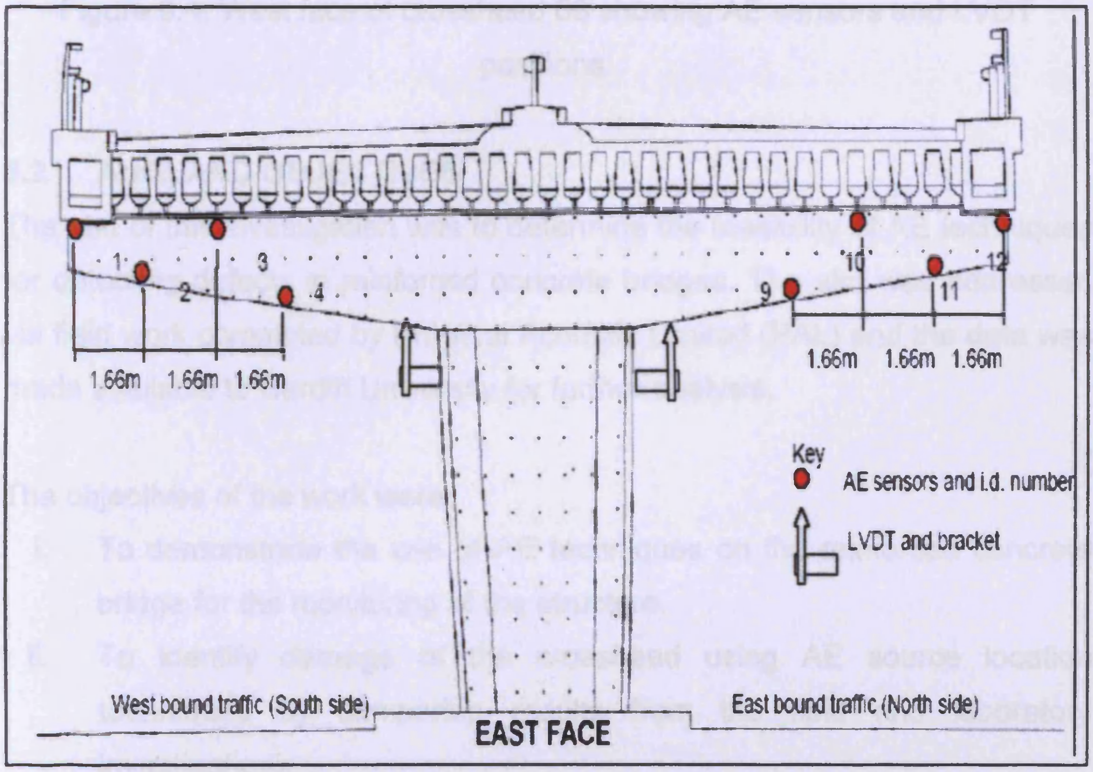

Figure 6.3: East face of crosshead 68 showing AE sensors and LVDT positions.

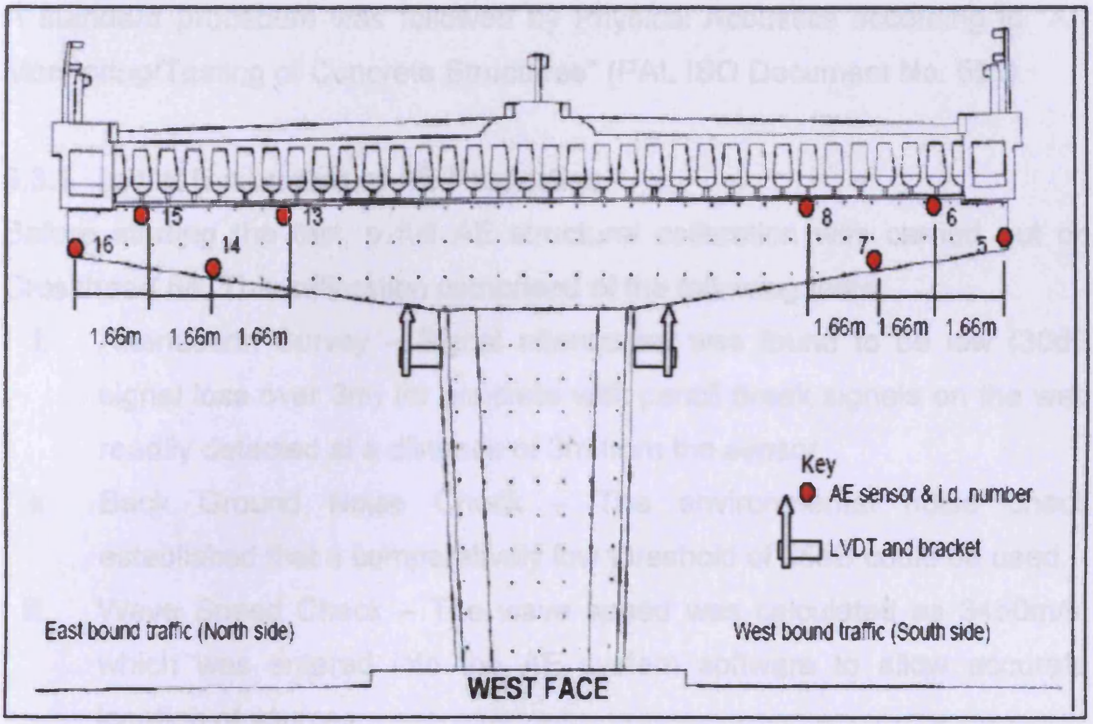

Figure 6.4: West face of crosshead 68 showing AE sensors and LVDT positions.

6.2 AIMS AND OBJECTIVES

The aim of this investigation was to determine the feasibility of AE techniques for detecting defects in reinforced concrete bridges. The aim was addressed via field work completed by Physical Acoustic Limited (PAL) and the data was made available to Cardiff University for further analysis.

The objectives of the work were:

i. To demonstrate the use of AE techniques on the reinforced concrete bridge for the monitoring of the structure.

ii. To identify damage of the crosshead using AE source location techniques by comparing results from the field and laboratory investigations.

iii. To provide a more detailed analysis than that conducted in the initial PAL report.

6.3 EXPERIMENTAL PROCEDURE

A standard procedure was followed by Physical Acoustics according to "AE Monitoring/Testing of Concrete Structures" (PAL ISO Document No. 551).

6.3.1 Initial Evaluation of AE Properties

Before starting the test, a full AE structural calibration was carried out on Crosshead 68. This calibration comprised of the following tests:

i. Attenuation Survey – Signal attenuation was found to be low (30dB signal loss over 3m) for concrete with pencil break signals on the web readily detected at a distance of 3m from the sensor.
ii. Back Ground Noise Check – The environmental noise check established that a comparatively low threshold of 35dB could be used.
iii. Wave Speed Check – The wave speed was calculated as 3450m/s, which was entered into the AE system software to allow accurate location of sources.

Using the information from the AE structural survey, the sensor spacing was calculated. Arrays of four sensors per side of the crosshead nib were installed. Eight nibs (2 per crosshead) were each instrumented with 8 R6I sensors. Sensors were spaced no greater than 3 m apart in a linear array and were identical for each array.

Figure 6.5 and Figure 6.6 shows the sensor position on the Southern nib and Northern nib of the Crosshead 68.

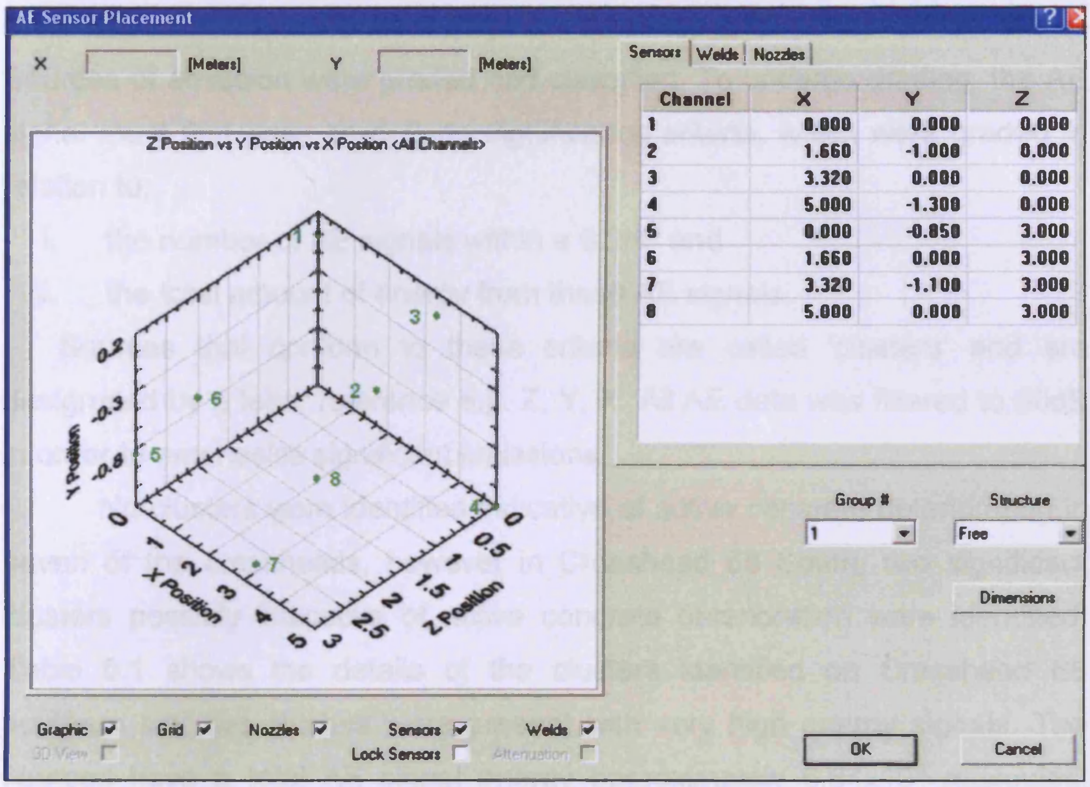

Channel	X	Y	Z
1	0.000	0.000	0.000
2	1.660	-1.000	0.000
3	3.320	0.000	0.000
4	5.000	-1.300	0.000
5	0.000	-0.850	3.000
6	1.660	0.000	3.000
7	3.320	-1.100	3.000
8	5.000	0.000	3.000

Figure 6.5: Sensor position on the Southern nib of Crosshead 68.

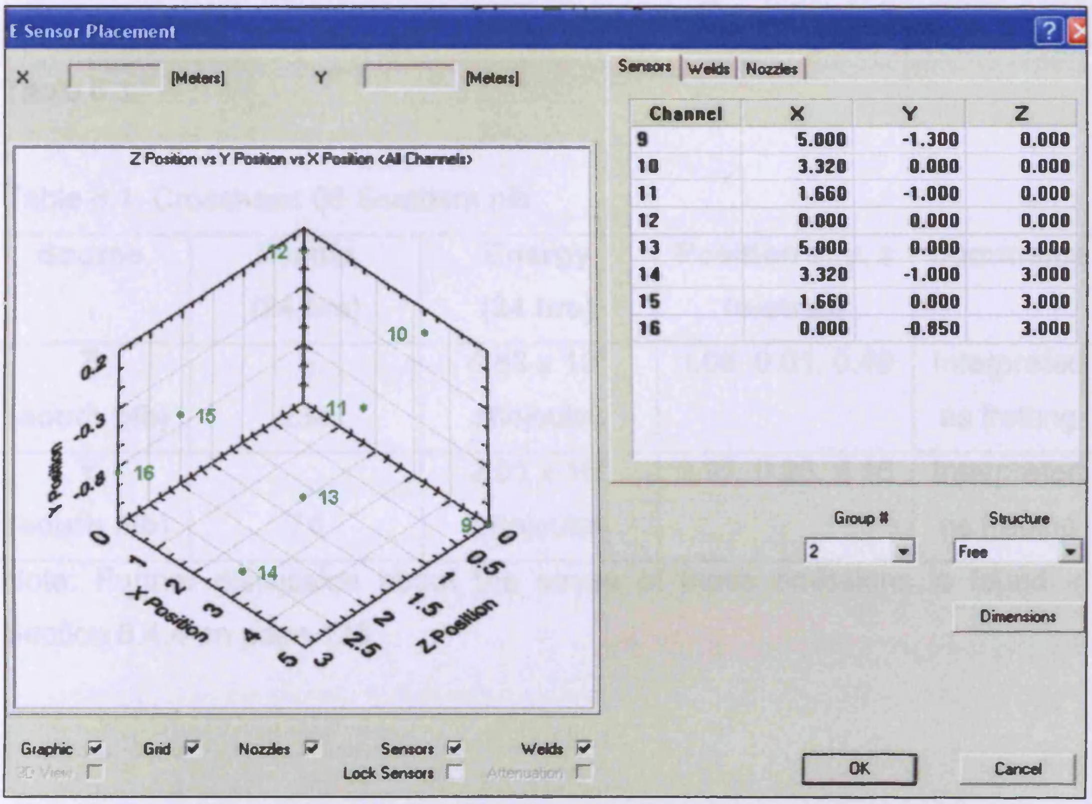

Channel	X	Y	Z
9	5.000	-1.300	0.000
10	3.320	0.000	0.000
11	1.660	-1.000	0.000
12	0.000	0.000	0.000
13	5.000	0.000	3.000
14	3.320	-1.000	3.000
15	1.660	0.000	3.000
16	0.000	-0.850	3.000

Figure 6.6: Sensor position on the Southern nib of Crosshead 68.

6.3.2 Results Reported from Physical Acoustic LTD (PAL)

Sources of emission were graded and classified. To undergo grading, the AE signal must first pass predefined significance criteria, which were graded in relation to;

i. the number of AE signals within a 0.2m^3 and
ii. the total amount of energy from these AE signals.

Sources that conform to these criteria are called 'clusters' and are designated by a letter reference e.g. Z, Y, X. All AE data was filtered to 50dB in order to emphasise significant emissions.

No clusters were identified indicative of active concrete deterioration in seven of the crossheads, however in Crosshead 68 South, two significant clusters possibly indicative of active concrete deterioration were identified. Table 6.1 shows the details of the clusters identified on Crosshead 68 southern nib; two clusters were present with very high energy signals. The sources have a total AE signal energy approximately 6.84x10^8 attojoules. Figure 6.7 shows the Crosshead 68 southern nib AE source location in a three dimension (3D) view and defines the coordinates system referred to in Table 6.1.

Table 6.1: Crosshead 68 Southern nib.

Source	**Events (24 hrs)**	**Energy (24 hrs)**	**Position x, y, z (metres)**	**Comments**
Z (south nib)	234	4.83 x 10^8 attojoules	3.09, 0.01, 0.49	Interpreted as fretting
Y (south nib)	74	2.01 x 10^8 attojoules	2.97, 0.26, 0.16	Interpreted as fretting

Note: Further discussion about the cause of these emissions is found in Section 6.4.4 on page 126.

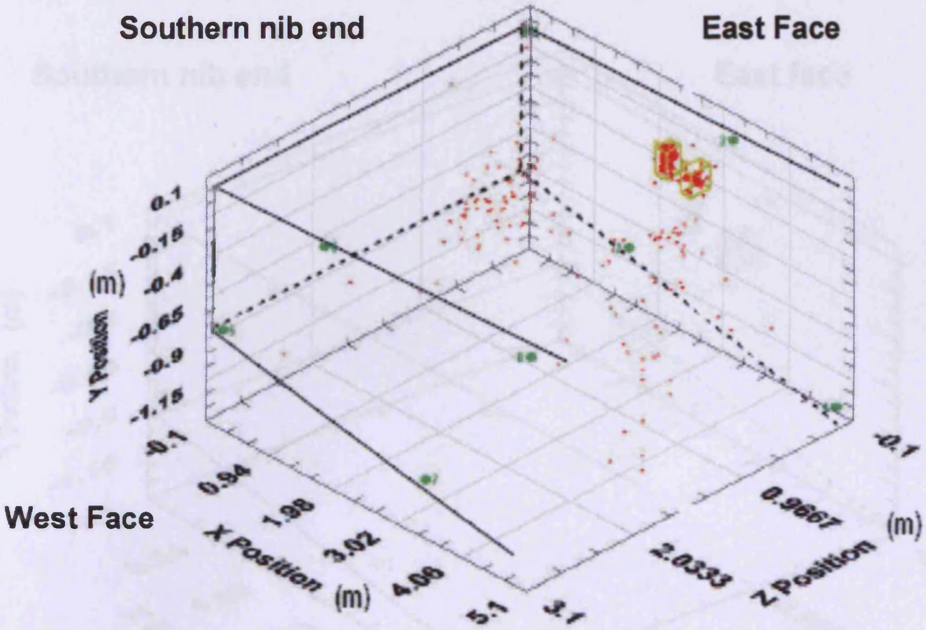

Figure 6.7: Crosshead 68 Southern Nib AE Source Location – 3D View.

PAL reported that the clusters identified were located relatively close together and were thought to be due to fretting of the surfaces at the top corner of the side of the crosshead or under a bearing. The signals produced occur at or during significant vertical displacement during heavy loading of the structure. Further visual inspection of this area revealed no immediately obvious surface damage or deterioration to the concrete.

6.4 FURTHER INVESTIGATION

6.4.1 Introduction

Crosshead 68 was identified for further investigation as part of this project due to the presence of two clustered sources on the east face of the Southern nib.

Figure 6.8 shows the Crosshead 68 Southern nib AE source location in 3D view after filtering to 70dB. This enables closer observation of the high energy signals believed to be related to severe damage which gives high amplitude and energy levels.

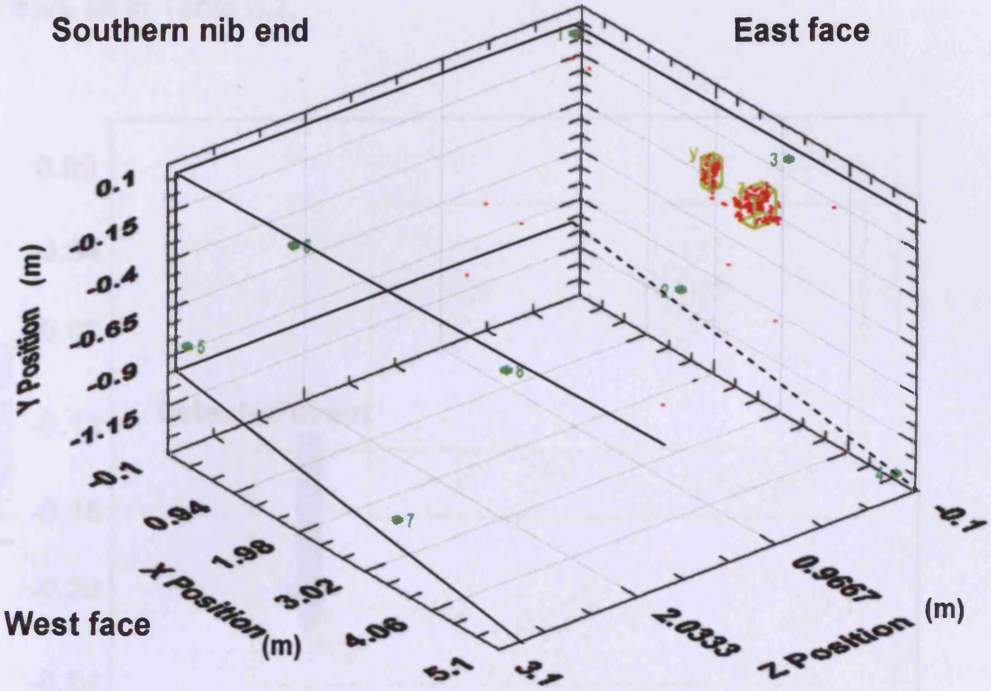

Figure 6.8: Crosshead 68 Southern nib AE source location–3D (filtered at 70dBAE).

6.4.2 Clustered Events

The clustered events were analysed in relation to the number of AE signals with a cluster size of $0.2m^3$ and amplitude of 70dB.

Figure 6.9 illustrates the same clustered events as shown in Figure 6.8 in 2D location. There is a difference in quantity of events for 3D and 2D location, because of the criteria used to define an event in the location software. In 3D location, at least five hit sensors are required for the signal to be considered as one event; three hit sensors on the one surface and two hit on the other surface. Meanwhile for 2D location, at least 3 hit sensors are required on the same surface. As a result, there are some hits that can not be located in 3D due to the number of sensors that must be hit for the emission to be considered as one event.

In the earlier section, PAL results suggested that the clustered events were due to fretting and this was confirmed by carrying out a Half Cell study of the structure. The clustered event was selected as shown in Figure 6.8 and

6.9. This event was extracted to observe all the parameters and all the hit sensors as in Table 6.2.

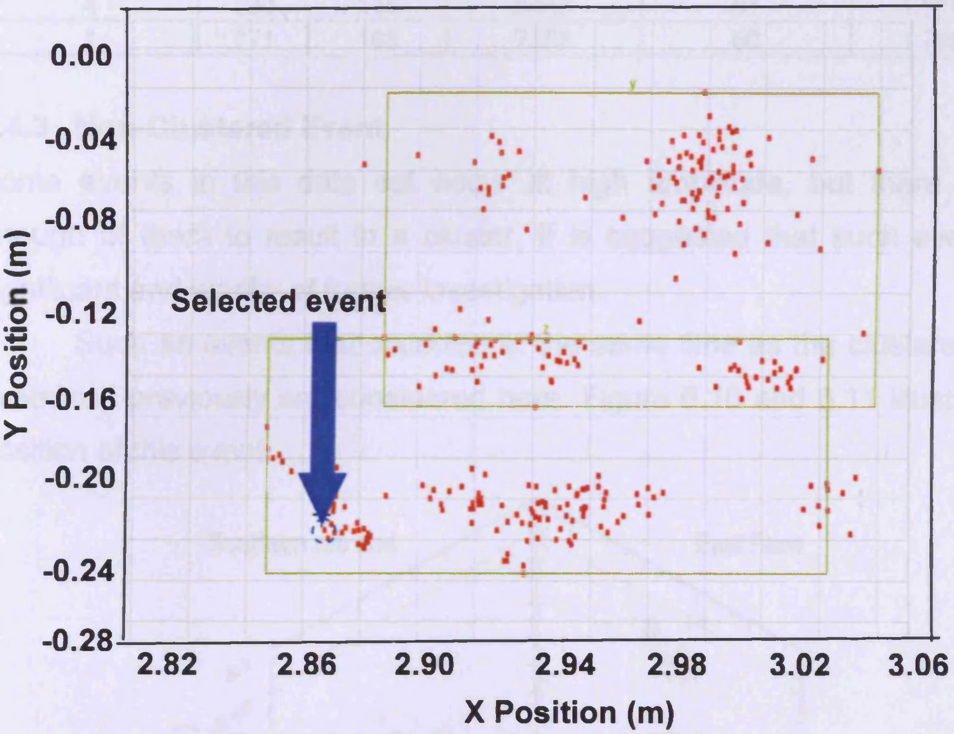

Figure 6.9: Clustered event in 2D location.

The first hit sensor was at channel 3 with an absolute energy of 6.10x10^5 attojoules and an amplitude of 82dBAE. The calculation of the source-to-sensor distance was 0.49m. From an observation of a series of laboratory experiments which can be found in Chapter 4 of this thesis, the first concrete cracking was determined as the absolute energy levels exceed 1.0x10^{6}aJ for a single sensor with evidence from the visual observation. However, for this clustered event, the absolute energy level was significantly less than the justification for the first concrete cracking in the laboratory test. In addition, there was no evidence of concrete crack at the cluster location on the crosshead. As a result, it is believed that this clustered event is not due to fretting but due to microcracking within the structure.

Table 6.2: Clustered event characteristic.

CHANNEL	RISE (µsec)	COUNT	DURATION (µsec)	AMPLITUDE (dB)	ABS-ENERGY (attoJoules)
3	311	179	6089	82	6.10E+05
2	430	204	6672	72	1.55E+05
4	520	115	5448	61	1.81E+04
1	771	183	7057	60	1.76E+04

6.4.3 Non-Clustered Event

Some events in this data set occur at high amplitude, but there are not enough of them to result in a cluster. It is suggested that such events are significant and worthy of further investigation.

Such an events that occurred at the same time as the clustered event examined previously are considered here. Figure 6.10 and 6.11 illustrate the position of this event.

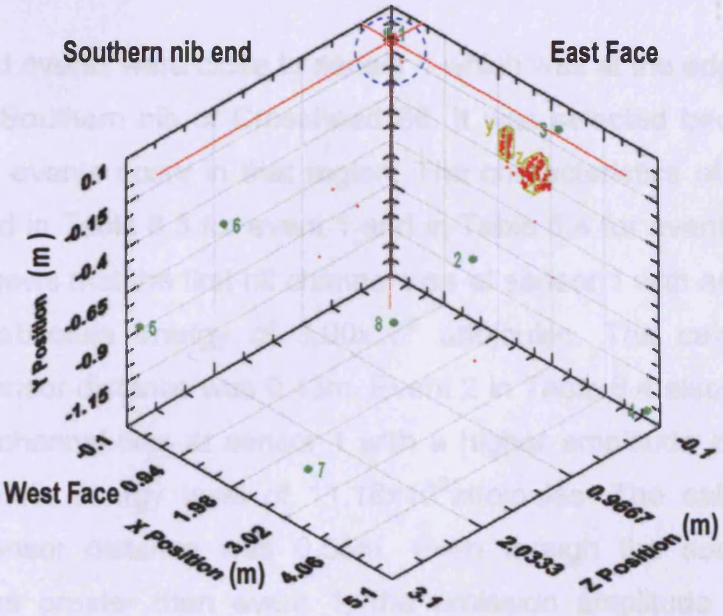

Figure 6.10: Non-clustered event in 3D location.

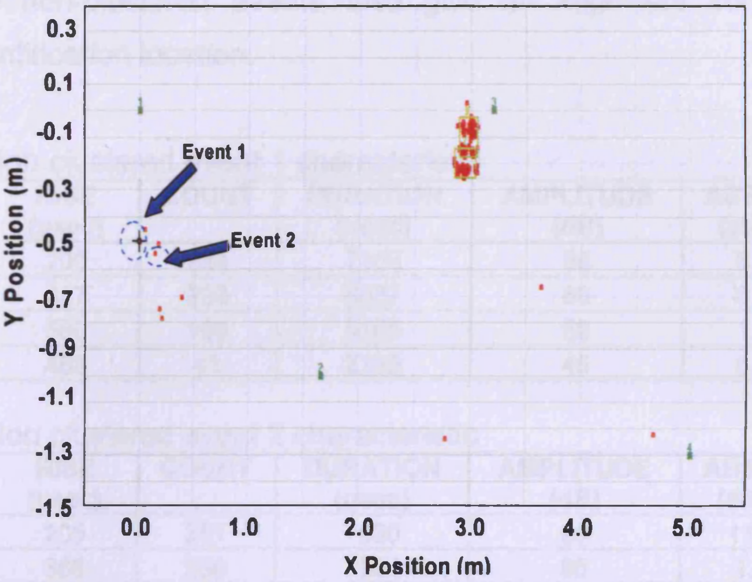

Figure 6.11: Non-clustered events in 2D location.

The selected events were close to sensor 1 which was at the edge of the west face of the Southern nib of Crosshead 68. It was selected because several high energy events occur in that region. The characteristics of these events are tabulated in Table 6.3 for event 1 and in Table 6.4 for event 2. Event 1 in Table 6.3 shows that the first hit channel was at sensor 1 with an amplitude of 86dB and absolute energy of 3.90×10^6 attojoules. The calculated direct source-to-sensor distance was 0.43m. Event 2 in Table 6.4 also indicates that the first hit channel was at sensor 1 with a higher amplitude of 90dB and a higher absolute energy level of 11.18×10^6attojoules. The calculated direct source-to-sensor distance was 0.55m. Even though the source-to-sensor distance was greater than event 1, the emission amplitude and absolute energy are still higher than event 1. Although the non-clustered event 2 is more attenuated, the significant absolute energy indicates that important events had occurred here. Furthermore, this second event had a comparable energy to that released during the cracking of a concrete specimen in the laboratory test. It is therefore proposed that this event is associated with active cracking within this area. Apart from being interested in the clustered events, the non-clustered events also give an important contribution to damage identification location.

Table 6.3: Non clustered event 1 characteristic

CHANNEL	RISE (μsec)	COUNT	DURATION (μsec)	AMPLITUDE (dB)	ABS-ENERGY (attoJoules)
1	200	224	7109	86	3.90E+06
2	357	230	6627	80	6.10E+05
3	560	169	5185	59	1.49E+04
4	468	43	2733	45	5.95E+02

Table 6.4: Non clustered event 2 characteristic

CHANNEL	RISE (μsec)	COUNT	DURATION (μsec)	AMPLITUDE (dB)	ABS-ENERGY (attoJoules)
1	205	251	7530	90	11.16E+06
2	366	256	7564	85	1.66E+06
3	969	186	5475	63	40.10E+06
4	628	83	4100	49	1.62E+03

6.4.4 Visual Observation

Localisation of AE sources is important to assess the region of active damage. As mentioned earlier, the PAL interpretation of these results were that the clustered events were the result of fretting. With a further study of the data and from comparison with the visual observations made during the test, an interesting result emerges. Figure 6.12 and Figure 6.13 show the plan view for the Northern and Southern nib of Crosshead 68 respectively.

Sensor 10 (Northern nib) and Sensor 3 (Southern nib) were at a similar location x, y, z (3.32, 0.00, 0.00). Figure 6.13 and Figure 6.14 show that the intensity of events near these two sensors were high. From visual observation, it had been recorded by PAL that there was no damage on that area but both sensors were within the carriageway, which perhaps contributes to the high intensity of the events around those two sensors. It was believed that these emissions were related to heavy vehicles passing over the crosshead. However, observation of the characteristics of the clustered event in section 6.4.2, would suggest that microcracking is present.

In fact, further observation of the evidence upholds this view. Cracks at the Southern nib end which were not included in the PAL report are evidenced in a photograph. This evidence is shown in Figure 6.14 and Figure 6.15. With a further examination the characteristics of the event (section 6.4.3), it shows that this is an active crack.

Apart from these observations, there was also major spalling of the concrete at the junction of the column and the crosshead (as in Figure 6.15). The structural significance of this spalling is that it will affect the integrity of the whole crosshead since it is at this location that the maximum moment will occur. Further attention should be given to identifying the true significance of this damage.

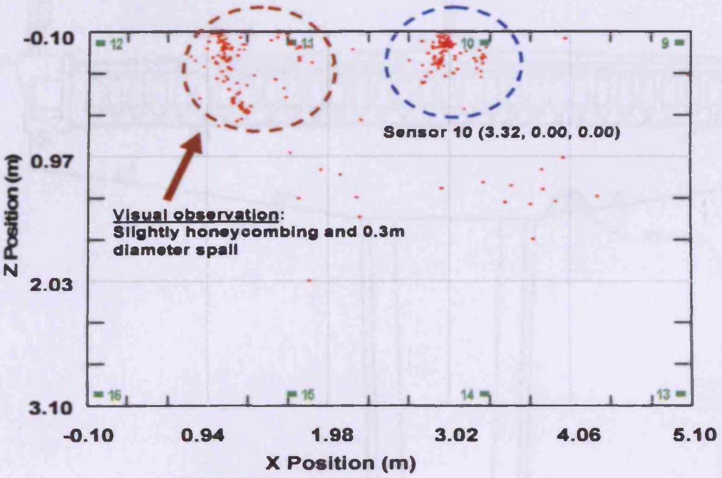

Figure 6.12: Northern nib of Crosshead 68 from plan view.

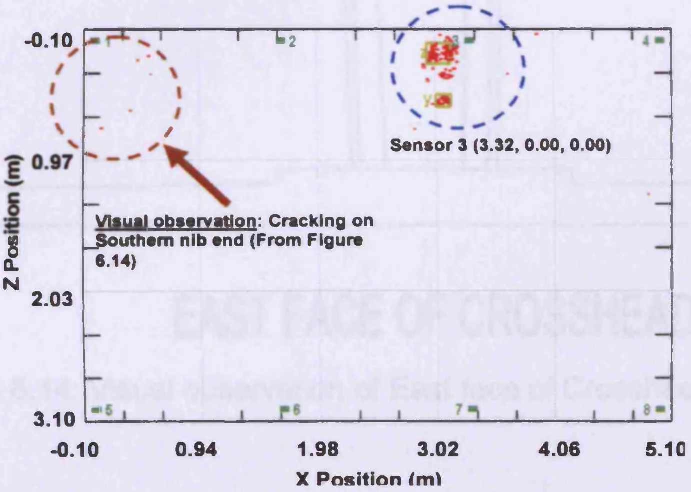

Figure 6.13: Southern nib of Crosshead 68 from plan view.

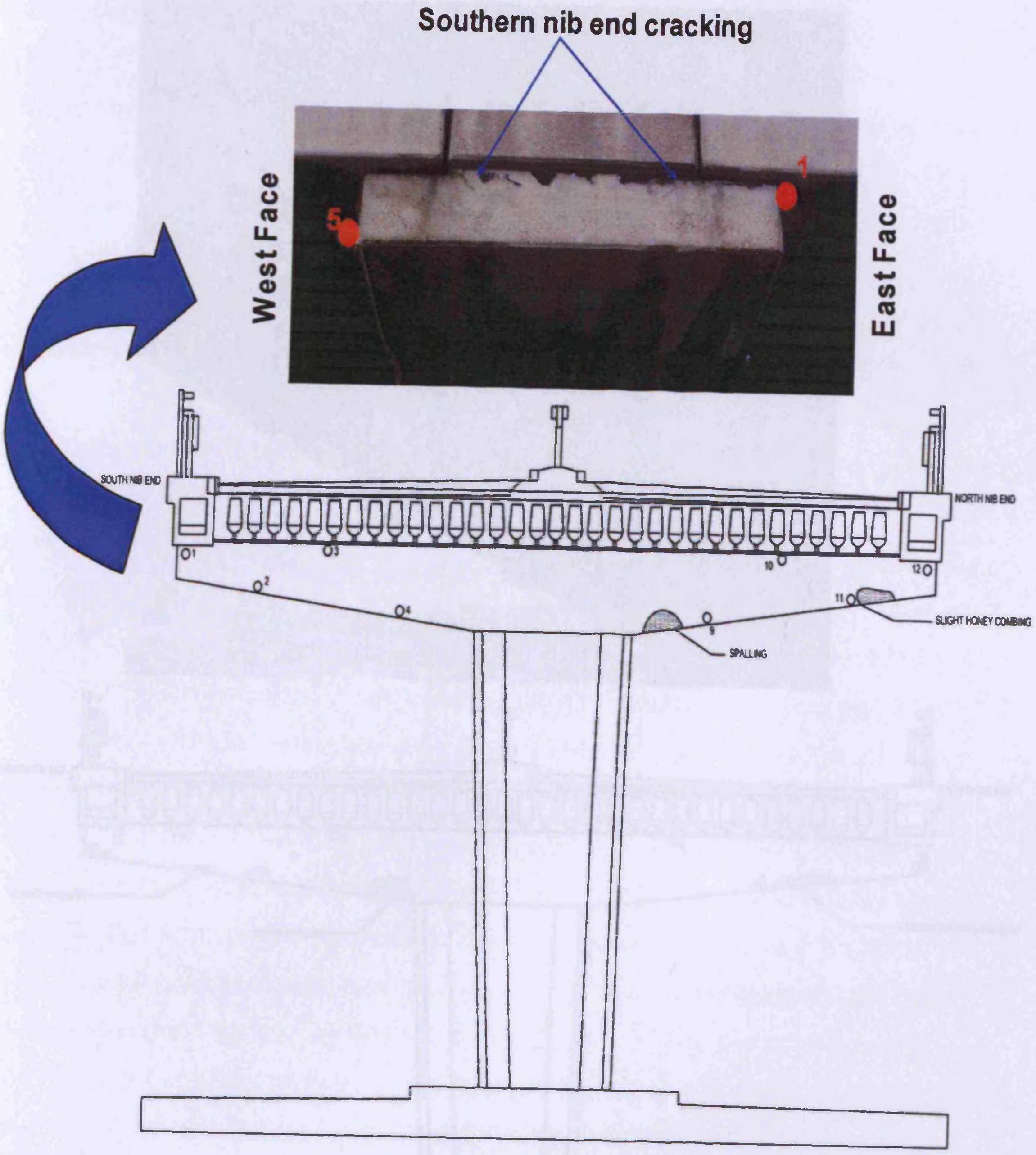

EAST FACE OF CROSSHEAD 68

Figure 6.14: Visual observation of East face of Crosshead 68.

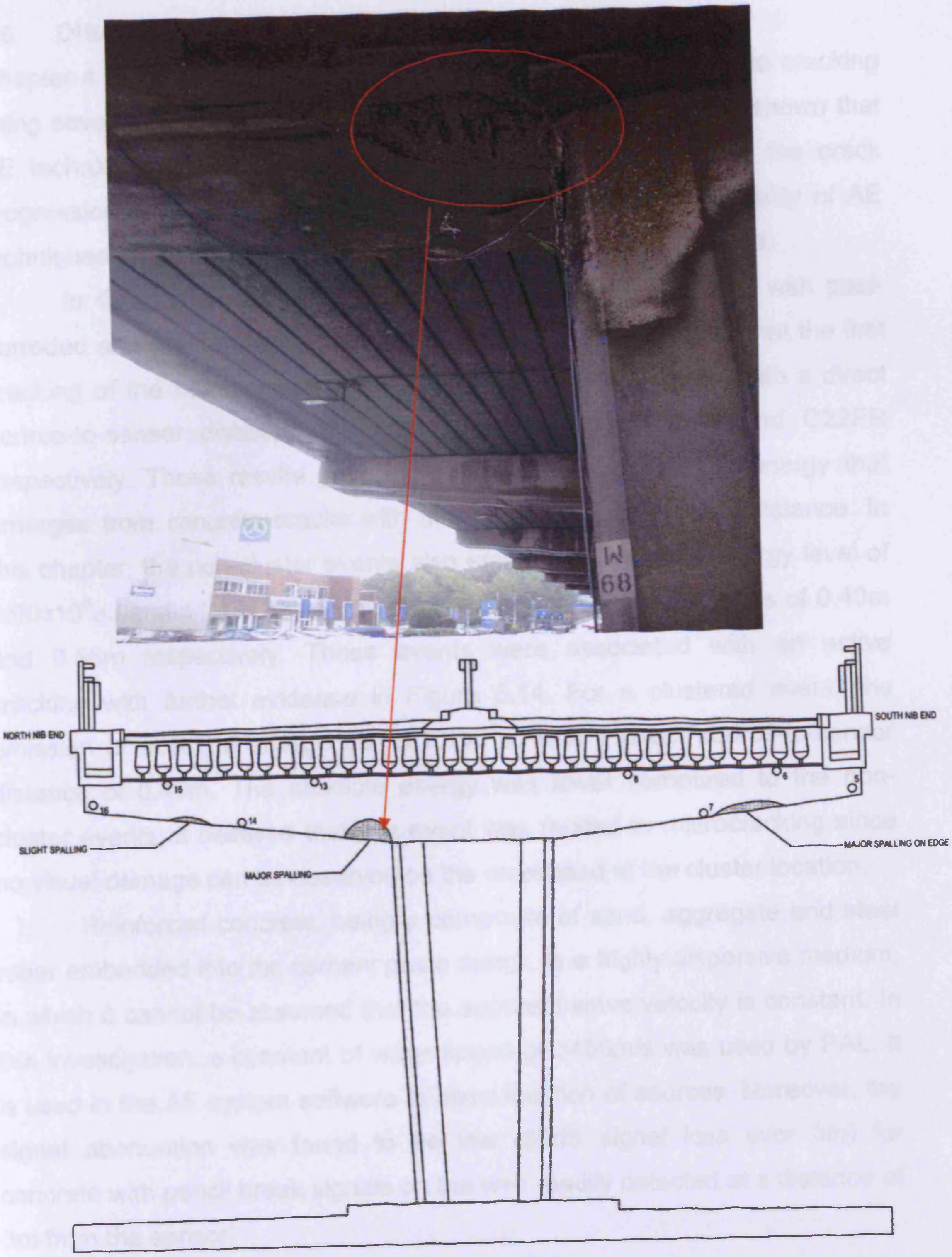

Figure 6.15: Visual observation of West face of Crosshead 68.

6.5 DISCUSSION

Chapter 4 assessed the ability of AE to detect and locate concrete cracking using several AE sensors on laboratory-based specimens. It was shown that AE techniques could be used to detect, locate and monitoring the crack progression until the failure. This chapter has investigated the ability of AE techniques to detect defects within a real concrete bridge crosshead.

In Chapter 4, a series of laboratory tests was conducted with post-corroded and pre-corroded RC beam specimen. It was observed that the first cracking of the beam emerged at 1.90×10^6aJ and 13.79×10^6aJ with a direct source-to-sensor distance of 0.36m and 0.32m for A22PR and C22PR respectively. These results gave a justification of the absolute energy that emerges from concrete cracks with the direct source-to-sensor distance. In this chapter, the non-cluster events also emit a high absolute energy level of 3.90×10^6aJ and 11.18×10^6aJ with direct source-to-sensor distances of 0.43m and 0.55m respectively. These events were associated with an active cracking with further evidence in Figure 6.14. For a clustered event, the emission of absolute energy was 6.10×10^5aJ with a direct source-to-sensor distance of 0.49m. The absolute energy was lower compared to the non-cluster events; it believed that this event was related to microcracking since no visual damage can be observed on the crosshead at the cluster location.

Reinforced concrete, being a composite of sand, aggregate and steel rebar embedded into the cement paste matrix, is a highly dispersive medium, in which it cannot be assumed that the apparent wave velocity is constant. In this investigation, a constant of wave speed of 3450m/s was used by PAL. It is used in the AE system software to allow location of sources. Moreover, the signal attenuation was found to be low (30dB signal loss over 3m) for concrete with pencil break signals on the web readily detected at a distance of 3m from the sensor.

In Chapter 5 of this thesis, it was shown that attenuation cannot be avoided when dealing with non homogeneous material such as concrete. The signal attenuation of the RC beam exhibits a loss between 21-26dB over 1.5m source-to-sensor distance whilst for a slab specimen, the attenuation signal loss was 55dB over the same distance. For the actual structure (Crosshead 68) a lower threshold level that was used (35dB) as further away from the source (the far field), where the majority of structural AE monitoring measurements are made, attenuation becomes dominated by absorption or conversion of sound energy into heat. Due to this reason, with a lower threshold level is believed that the inspection is capable of locating sources over a broad area.

It has also been reported earlier that a slab has a slower apparent wave velocity compared to a beam specimen with the same source-to-sensor distance. This happens because when a wave is generated by a localised source; the disturbance propagates outwards in all directions from the source. The wave propagates further for a larger structure with a different and complicated wave path. Moreover, the real signal path is probably longer than the direct path due to concrete cracks (due to daily use) and aggregates which increase the propagation distance to the sensor. In addition, the components in concrete consist of different materials with different velocities which will affect the apparent wave velocity as the source-to-sensor distance increases.

A cluster location is an area of predefined size on the structure that contains AE sources found using location monitoring. Most AE users are interested in the clustered events because these are associated with damage localization. However, apart from being interested in the clustered events, the non-clustered events also give an important contribution to damage detection. It is important to analyse the non-clustered events as well and compare the output with visual observation and laboratory-based results, leading to a viable technique for assessing the integrity of the structure. Nevertheless it is recommended by PAL that all crossheads be retested within 4 years using AE to allow assessment of any deterioration and change in condition especially on Crosshead 68.

Visual observation is a predominant inspection method and essential before proceeding with any NDT techniques. The external appearance of the crosshead, which was badly stained and heavily spalled, again suggested that internal corrosion might be expected. There was a major spalling of the concrete at the junction of the column and the crosshead. Monitoring of this area is essential since this spalling will affect the integrity of the whole crosshead since it is at this location that the maximum moment will occur.

In monitoring large structures, especially RC, an accurate source location will depend on the calculated wave velocity, time difference measurements, precise and adequate sensors positions and knowledge to interpret the output with an association to visual observation and laboratory-based results. However, if the source cannot generate waves of sufficient strength for detection by the required number of sensors, then it will not be possible to calculate the location of the source.

According to Carter (2000), a successful AE monitoring requires a thorough understanding of all the factors that govern the AE process. Simply attaching the AE sensors arbitrarily to the structure and recording the subsequent data is woefully inadequate. If suitable raw data is to be acquired, the specification and configuration of an AE monitoring system must be tailored around the detection of sources of interest and the informatics requirements for source analysis. The following factor is important to take into consideration in global monitoring:

- AE wave propagation and structural acoustics
- The implication of the structure details
- Identification of the key AE sources of interest
- The properties of these AE sources
- Environmental and structural noise effects
- The capabilities and limitations of the AE equipment and processing software.

6.6 CONCLUSIONS

This chapter has assessed the ability of AE to detect, locate and monitor damage in an RC bridge using AE sensors. The conclusions are:

- The ability of AE techniques to detect defects within a real RC bridge crosshead was promising with a detailed investigation.
- Reinforced concrete is a highly dispersive medium, in which wave velocity cannot be assumed to be constant. The significant effect of using a constant wave velocity is in source location. Most probably an error in detecting the exact location of emission can occur because of this effect. In AE, the commercial software requires a single wave velocity value to be defined for each test. In reality, the wave velocity will not be constant as the source-to-sensor distance increases which has been discussed thoroughly in Chapter 5 of this thesis.
- A lower threshold level (just above the noise level) is required when monitoring large structures. This is due to the requirement that the technique has the capability to locate the source within a large area.
- From further analysis of the AE data from Crosshead 68, two significant clusters possibly indicative of microcracking were identified and it was confirmed that the emissions were related to heavy vehicles passing over the crosshead. However, a retest is required in the future to allow assessment of any deterioration and change in condition especially on Crosshead 68.
- The non-clustered events are believed to be indicative of active cracking on the southern end nib of Crosshead 68. A further investigation is needed to monitor the progress of this cracking.
- A visual inspection is important before deciding where to locate the sensors. Consideration should be given to the major spalling of concrete at the crosshead column since this is where the maximum moment occurs and at the Crosshead 68 Southern nib where the active cracking occurred.

CHAPTER 7: CONCLUSIONS AND RECOMMENDATION FOR FUTURE WORK

7.1 CONCLUSIONS

This thesis has examined the role of acoustic emission in the monitoring laboratory-based and in-service reinforced concrete specimens and structures. The aim of this research was to further the understanding of AE techniques for use in global and local structural monitoring of concrete damage, in order to provide a commercial tool for the non-destructive evaluation of reinforced concrete structures. Three key themes have been investigated; (i) a study of the capability of the AE technique to follow crack development and to monitor structural behaviour in pre-corroded and post corroded specimen in order to implement the source location to determine deterioration/crack location, (ii) an investigation of the nature of wave propagation in concrete structures over a variety of source to sensor distances and (iii) the use of AE to monitor the integrity of an in-service concrete bridge crosshead.

7.1.1 Pre-corroded (PR) and Post-corroded (PS) RC Beam Specimens.

AE absolute energy was found to relate to the behaviour of the RC beam and determined the ability of the AE to locate and monitor crack propagation on the RC beam. The significant conclusions that can be made from this chapter are:

- The mechanical behaviour of concrete can be related to the emission of absolute energy within the laboratory-based specimens since the loading conditions are known. However, it is difficult to extrapolate these relationship to the in service behaviour of a structure due to unknown loading conditions. Nevertheless, an important criteria was established by determining the emissions associated with the onset of concrete cracking and these criteria can be used in field tests. It was found that, whenever the AE absolute energy (single sensor event or cumulative hits) exceeded 1.0×10^6aJ, concrete cracks had occurred. This was implemented in Chapter 6 of this thesis and was validated by a visual inspection.

- The ability of the TOA method to detect and monitor the crack propagation was promising. In addition, it was found that AE could identify the location of microcraking before the first crack was visually observed. This demonstrated that the micro damage can be located before the actual impairment occurs.

7.1.2 Acoustic Wave Propagation in Concrete Structures.

This work investigated signal attenuation and wave propagation in concrete structures over a range of source-to-sensor distances. The attenuation of AE signals from different signal modes has proven to be an important factor in deciding the applicability of the technique. It was also observed that the apparent wave velocities were reduced due to attenuation and dispersion of the wave signal affecting the time to reach the subsequence sensors. In this study it can be concluded that:

- The determination of a 'corrected' signal can be used in order to ensure that, for a particular threshold, the same temporal position in each waveform was used for velocity calculations. As a consequence, problems associated with losing important signals are low when using the corrected signals. However the determination of the P-wave initial arrival times, amplitudes and normalising of an event was a long and tedious process.
- The source location is of prime interest for modern AE analysis; however it is greatly affected when considering the inaccuracy in determining the P-wave arrival times in calculating the wave velocities. It was shown that the apparent wave velocity decreases as the sensor distance increases. In addition, the selected threshold level also has an impact on the measured wave velocities. In order to detect and locate AE, low threshold levels are

needed with sensors pairs in close proximity to each another. However, in field test, it is not cost-effective because this requires a large number of sensors to be placed closed together in order to detect and locate damage.

- In this study, the propagation of the elastic waves in concrete was confirmed to be affected by; the geometry of the sample, the path taken from the source to sensor and the concrete composition and condition, all of which influences the apparent wave velocity of the RC concrete.
- An attenuation study, showed that a slab suffered the most attenuation compared to the beam specimen (55dB over 1.5m from the source compared to 21dB for the beam over the same source-to-sensor distance). The large increase in attenuation indicates a potential problem in monitoring specific locations on the structure. Care must be taken when choosing the location of the sensors to avoid such large decreases in the received signals.
- Measured Amplitude Ratio (MAR) analysis revealed that a relatively low MAR value occurs for parallel sources and a higher MAR value for normal sources. However, if conclusions on source orientation are to be drawn from the MAR measurements, consideration of how the sensor mounting position and orientation relative to other elements influence its response to sources in various regions of the beam is required. This becomes complex if the precise source position is unknown, as is the case with global AE inspection.

7.1.3 Acoustic Emission Assessment on M4 Elevated Crosshead.

The key conclusions from this investigation are:

- Signal attenuation in the concrete bridge was low, permitting H-N source detection at source-to-sensor distance in excess of 3m.

- Emission levels were related to traffic volume and individual vehicle mass.
- Non-clustered events give an important contribution to damage localization. It is important to analyse the non-clustered events and compare the output with visual observations and laboratory-based results in order to obtain a clearer understanding, leading to a viable technique for assessing the integrity of the structure. In complex structures, not all events will reach sufficient sensors to be clustered, but such events can still be important.
- A visual inspection is important before deciding where to locate the sensors; important consideration should be given to the major spalling.

To summarise, the most important aspect of AE testing is its ability to continually monitor entire sections of the structure in-situ. Appropriate methods of AE detection, source location and characterisation are central to this aim. The most significant challenge of source location is in global monitoring. Most AE sources can be readily located if data is received on the requisite number of sensors. However in light of the economics constraints, it is desirable to minimise the number of sensors used to monitor the structure. This limits the hardware investment and the expense of mounting and maintaining the equipment, it also reduces the logistic complexity of installing the instrumentation. A reduction in the number of sensors used may be achieved in two ways; by carefully targeting critical zones of the structure where the flaws of interest are most likely to concur, or by increasing the sensor spacing. Both methods require a thorough understanding of the history and behaviour of the structure in question and all aspects of source detection. Therefore, in global monitoring, sensor configuration is a carefully judged compromise between system sensitivity and cost. This is not usually the case in local monitoring where the sensors are in much closer to the source and can be used for source location with a high degree of confidence.

This thesis is part of a significant contribution to the enhancement the concrete structure knowledge in NDT method specifically in AE technique. It is a vital to have a NDT method which can detect and locate faults as soon as possible. This thesis had covered one of the important criteria by determining the emissions associated with the onset of cracking and had determined that this criterion can be used in field test. However, looking back to the laboratory test for PR and PS specimen, it will give more understandable results if all the beams were design to fail in flexure. Hence the comparison of the data can be done with the same concrete failure. The calculated apparent velocity gave an important awareness of source location method and Moment Tensor method whereby the calculated P-waves were decreases as the sensor distance increases. In this chapter, the descriptions of the factors that may effect the ability to obtain an accurate value of wave velocity were stated. The bridge monitoring investigation had discovered the importance of non-cluster event in damage localization. If permission was given, it will be appropriate to revisit the structure (Crosshead 68) and to undertake the area of investigation as a near field. Hence it can be benefit to obtain a clearer understanding of the emission. Most of all these small important information may be added to the immature nature of concrete structure behaviour associated with AE which will benefit all researchers in concrete area.

7.2 RECOMMENDATIONS FOR FURTHER WORK

In light of the conclusions of this work, the following topics are recommended for further study:

- A detailed investigation into the optimum set-up for the monitoring of reinforced concrete structures. This investigation will need to consider the lowest possible threshold, optimum sensor spacing and selection of sensors to enhance the applicability of AE for the monitoring of concrete structures.
- A large of laboratory based corrosion study (Chapter 4) to collect a database of signals to aid in the evaluation of the behaviour of the RC

beams subjected to corrosion levels similar to those found in real bridge structures.

- A laboratory-based investigation of full size models of RC beam with varying degrees of damage monitored using the AE technique. This should include study of wave propagation in damaged and undamaged RC specimens and mortar specimen to investigate the significance of material influences on the signal behaviour.
- Investigation of the significance of statistical representations of MAR value data from a range of parallel and normal sources. This will further the understanding of the role of MAR value in AE source identification. Furthermore, a study of the influence of source-to-sensor distances on MAR value is appropriate.
- The development of an automated software package to improve the accuracy and reduce the time taken in the determination of the initial P-wave amplitude and arrival time.

CHAPTER 8: REFERENCES

Ahmad, S., 2003, Reinforcement corrosion in concrete structures, it's monitoring and service life prediction - A review, Cement & Concrete Composites, Vol. 25, pp 459-471.

Ahmad, S. and Bhattacharjee B., 1995, A simple arrangement and procedure for in-situ measurement of corrosion rate of rebar embedded in concrete, Corrosion Science, Vol. 37, No. 5, pp 781-791.

Alonso C., Andrade C., 1996, Corrosion rate monitoring in the laboratory and on-site, Construction & Building Materials, Vol. 10, No. 5, pp 315-328.

ASTM ,1991, Standard terminology for non-destructive examinations. ASTM. ASTM Designation: E1316 - 91b.

ASTM C1383-04, 2002, Standard test method for measuring the P-wave speed and the thickness of concrete plates using the impact-echo method.

ASTM E976, 1999, Standard guide for determining the reproducibility of Acoustic Emission sensor response, The American Society for Testing and Materials.

Beattie A. G., 1983, Acoustic emission, principles and instrumentation, Journal of Acoustic Emission, Vol. 2, Part 1, pp 95-128.

Beck P., 2004, PhD Thesis- Quantitative damage assessment of concrete structures using acoustic emission, Cardiff School of Engineering, University of Wales, Cardiff.

BS 1881 Testing Concrete. Part 201:1986, Guide to the use of non-destructive methods of test for hardened concrete.

BS EN 12504-4, 2004, Testing concrete, Part 4: Determination of ultrasonic pulse velocity, pp. 9 (Annex A).

BS EN 13477-2, 2002, Non-destructive testing-Acoustic Emission-Equipment characterization, Part 2: Verification of operating characteristic, British Standard.

Carbera J. G., 1996, Deterioration of concrete due to reinforcement steel corrosion, Cement & Concrete Composites, Vol. 18, pp 47-59.

Carlos, M. F., 2003, Acoustic Emission: Heading the Warning Sounds from Materials.<URL:http://www.astm.org/SNEWS/OCTOBER_2003/carlos_oct.html>
[Accessed 2 February 2004].

Carpinteri A., Lacidogna G., Pugno G., 2007, Structural damage diagnosis and life-time assessment by acoustic emission monitoring, Engineering Fracture Mechanics, Vol 74, pp 273–289.

Carter, D. C., 2000, "Acoustic Emission Techniques for the Structural Integrity Monitoring of Steel Bridges", PhD Thesis, Cardiff University.

Chaix, J. F., Garnier V., Corneloup. G., 2006, Ultrasonic wave propagation in heterogeneous solid media: Theoretical analysis and experimental validation, Ultrasonic, Vol. 44, pp 200-210.

Cho Y. S., 2003, Non-Destructive testing on high strength concrete using spectral analysis of surface waves, NDT&E International, Vol. 36, pp. 229-235.

Colombo S., Fordo M. C., Main I. G., Shigesgi M., 2005, Predicting the ultimate bending capacity of concrete beams from the 'relaxation ratio' analysis of AE signals, Construction and Building Materials, Vol. 19, pp 746-754.

Concrete Bridge Development Group, 2002, Technical guide 2- Guide to testing and monitoring the durability of concrete structure, The Concrete Society, ISBN 0946691 79 7.

Culshaw B., 1996, Smart structures and Materials. Glasgow ISBN 0-89006-681-7, Artech House Inc., Boston, London.

Ding Y., Reuben R.L., Steel J. A, 2004, A new method for waveform analysis for estimating AE arrival times using wavelet decomposition, NDT & E International, Vol 37, pp. 279-290.

Droullard T. F., 1996, A history of AE, Journal of AE, Vol 14, No 1, pp 1-34.

Dukes R. and culpan E. A., 1984, AE- Its techniques and applications, IEE Proceedings, Vol. 131, Pt. A, No. 4, pp 241-251.

El Maaddawy T.A, Soudki K.A., 2003, Effectiveness of impressed current technique to simulate corrosion of steel reinforcement in concrete, Journal of Materials in Civil Engineering/ January/February, pp 41-47.

Elsener, B., 2002, Macrocell corrosion of steel in concrete-implication for corrosion monitoring, Cement & Concrete Composites, Vol. 24, pp 65-72.

Esward T.J, Theobald P. D., Dowson S.P, Preston R.C., 2002, An Investigation Into the Establishment and Assessment of a Test Facility for The Calibration of Acoustic Emission Sensors. Middlesex, National Physical Laboratory, pp 65.

Gaydecki P, Burdekin F. M., 1994, An inductive scanning system for two-dimensional imaging of reinforcing components in concrete structures, Measurement Science Technology, Vol. 5, pp 1272-1280.

Gaydecki P., Silva I., Fernandes B. T., Yu Z. Z., 2000, A portable inductive scanning system for imaging steel-reinforcing bars embedded within concrete, Sensors and Actuators, Vol. 84, pp 25–32.

Gaydecki P., Quek S., Miller G., Fernandes B., Zaid M., 2002, Design and evaluation of an inductive Q-detection sensor incorporating digital signal processing for imaging of steel reinforcing bars in concrete, Measurement Science and technology, Vol 13, pp 1327-1335.

Gaydecki P., Quek S., Fernandes B. T., Miller G., 2003, Multiple layer separation and visualisation of inductively scanned images of reinforcing bars in concrete using a polynomial-based separation algorithm, NDT & E International, Vol. 35, pp 233-240.

Gassman S.L. and Tawhed W.F., 2004, Nondestructive assessment of damage in concrete bridge decks, Journal of Performance of Construction Facilities ASCE, November 2004, pp. 220-231.

Golaski L., Gebski P., Ono K., 2002, Diagnostics of reinforced concrete bridges by acoustic emission. Journal of Acoustic Emission, Vol. 20, pp 213-221.

Gowers K. R., Millard S. G., 1993, On-Site linear polarization resistance mapping of reinforced concrete structures, Corrosion Science, Vol. 35, No. 5, pp 1593-1600.

Gowers K. R. and Millard S. G., 1999, Electrochemical techniques for corrosion assessment and reinforced concrete structures, Proceedings Institute of Civil engineers, Structure & Building 134 (Paper No. 11797), pp 129-137.

Grosse C, Reinhardt H, Dahm T, 1997, Localization and classification of fracture types in concrete with quantitative acoustic emission measurement techniques, NDT & E International, Vol 34, No 4, pp 223-230

Grosse C. U, Reinhardt H. W., Finck F., 2003, Signal-based Acoustic Emission techniques in civil engineering, Journal of Materials in Civil Engineering @ ASCE May / June, pp 274-279.

Guilia Boronio, Berra M., Bertolini L., Pastore T., 1996, Steel corrosion monitoring in normal and total-lightweight concretes exposed to chloride and sulphate solutions. Part II: Polarization resistance measurements, Cement & Concrete Research Journal, Vol. 26, pp 691-696.

Ha T. H., Muralidran S., Bae J. H., Ha Y. C., Lee H. G., Park K. W., Kim D. K., 2007, Accelerated short-term techniques to evaluate the corrosion performance of steel in fly ash blended concrete, Building and Enviroment, Vol. 42, pp 78-85.

Hartmut V, 2002, AE testing fundamentals, equipment, applications, NDT.net Vol.7, No.9, <URL: http://www.ndt.net/article/v07n09/05/05.htm> [Accessed 17 November 2005].

Holford K. M., 2000, Acoustic emission – basic principles and future directions, Strain, Vol 36, No 2, pp 51-54.

Holford K.M., 2001, Damage location in steel bridges by acoustic emission Journal of Intelligent Material Systems and Structures, Vol 12, pp 567-576.

Holford K.M, Carter D.C., 1999, Acoustic emission source location. Key Engineering Material: Damage Assessment Structure, 167-168, pp. 162-171.

Idrissi H., Liman A., 2003, Study and characterization by acoustic emission and electrochemical measurements of concrete deterioration caused by reinforcement steel corrosion, NDT & E International, Vol. 36, pp 563-569.

Jung W. Y. and Sohn Y. M., 2003, Predicting the remaining service life of land concrete by steel corrosion, Cement & Concrete Composite, Vol. 33, pp 663-677.

Kim D. S., Seo W. S., Lee K. M., 2006, IE-SASW method for non-destructive evaluation of concrete structure, NDT & E International, Vol. 39, pp 143-154.

Law D.M, Millard S. G., Bungey J.H., 2000, Linear polarization resistance measurements using a potentiostatically controlled guard ring, NDT & E International, Vol. 33, pp 15-21.

Leelalerkiet V., Kyung J. W., Ohtsu M., Yokata M., 2004, Analysis of half cell potential measurement for corrosion of reinforced concrete, Construction and Building Materials, Vol. 18, pp 155-162.

Li Z., Shah P 1994, Localization of microcracking in concrete under uniaxial tension. ACI Materials Journal, Vol 91, pp 372–81.

Li Z, Li F, Zdunek A, Landis E, Shah S P, 1998, Application of Acoustic Emission technique to detection of reinforcing steel corrosion in concrete, ACI Materials Journal, Vol 1, pp 68-76

Liu Y, Weyers R. E., 2003, Comparison of guarded and unguarded linear polarization CCD devices with weight loss measurement, Cement & Concrete Research, Vol. 33, pp 1093-1101.

Matsuyama K., Ishibashi A., Ohtsu M., 1993, Field application of acoustic emission for the diagnosis of structural deterioration of concrete, Journal of Acoustic Emission, Vol. 11, No. 4, pp S65-S73.

Millard S. G., Law D.W, Bungey J.H, Cairns J., 2001, Environmental influences on linear polarization corrosion rate measurement in reinforced concrete, NDT & E International, Vol. 34, pp 409-417.

Miller G., Gaydecki P., Quek S., Fernandes B., Zaid M.,2005, A combined Q and heterodyne sensor incorporating real time DSP for reinforcement imaging, corrosion detection and material characterisation, Sensor and Actuators, Vol. A 121, pp 339-346.

Miller R.K, McIntire P., 1987, Nondestructive Testing Handbook: Acoustic Emission Testing, Vol 5, second edition, American Society for Nondestructive Testing, pp. 151.

Mirmaran A., Philip S., 2000, Comparison of acoustic emission activity in steel-reinforced and FRP-reinforced concrete beams, Construction and Building Maintenance, Vol. 14, pp 299-310.

Mix p. E., 1998, Introduction to non-destructive testing- a training guide, John Willey & Sons, Texas, United State of America.

Othsu M., 1991, Simplified moment tensor analysis and unified decomposition of AE source: application to in situ Hydrofacturing test, Journal of Geographical Research, Vol 96, No B4, pp 6211-6221.

Othsu M., Uchida M., Okamoto T., Yuyama S., 2002, Damage assessment of reinforced concrete beams qualified by Acoustic Emission, ACI Structural Journal (Technical Paper), July-August, pp 411-417.

Othsu M., Watanabe H., 2001, Quantitative damage estimation of concrete by AE, Construction and Building Materials, Vol. 15, pp 217-224.

Owino, J. O., Jacobs, L. J., (1999), Attenuation measurements in cement-based materials using laser ultrasonics, Journal of Engineering Mechanics June: 637-647.

Park S. Y., Kim Y. B., 2002, Non-destructive damage detection in large structure via vibration monitoring, Electronic Journal of Structural Engineering 2 < URL: http://www.ejse.org > [Accessed 20 July 2004], pp 59-75.

Pech-Canul M. A, Castro P., 2002, Corrosion measurements of steel reinforcement in concrete exposed to a tropical marine atmosphere, Cement & Concrete Research Journal, Vol. 32, pp 491-498.

Philippidis T.P., Aggelis D. G., 2005, Experimental study of wave dispersion and attenuation in concrete, Ultrasonics, Vol. 43, pp. 584-595.

Physical Acoustic Corporation, 2001, DiSP User Manual, Physical Acoustic Corporation, Princeton Junction, New Jersey, US.

Physical Acoustic Corporation, 2002, AEWin Software User's Manual, Physical Acoustic Corporation, Princeton Junction, New Jersey, US.

Physical Acoustic Limited, 2005, Procedure: AE monitoring of concrete structures. Document Number 551, Issue No. 2. Physical Acoustic Limited Company (PAL), Cambridge, UK.

Physical Acoustic Limited, 2005, Acoustic emission of M4 Elevated Crosshead, Report No. FT03287, Physical Acoustic Limited Company (PAL), Cambridge, UK.

Pollock, A. A., 1989, Acoustic Emission Inspection, Metal Handbook Volume 17, pp 278-294.

Poupard O., L'Hostis V., Catinaud S., Petre-Lazar I., 2006, Corrosion damage diagnosis of a reinforced concrete beam after 40 years natural exposure in marine environment, Cement and Concrete Research, Vol. 36, pp 504-520.

Pullin, R. ,2001, PhD Thesis- Structural Integrity Monitoring of Steel Bridges Using Acoustic Emission Techniques. School of Mechanical Engineering. Cardiff, UK, University of Wales, College of Cardiff.

Quek, S., Gaydecki P., Zaid M.A.M, Miller G, Fernandes B.T., 2003, Three-dimensional image rendering of steel reinforcing bars using curvilinear models applied to orthogonal line scans taken by an inductive sensor, NDT & E International, Vol. 36, pp 7-18.

Raupach M, Schiebl P., 2001, Macrocell sensor systems for monitoring of corrosion risk of the reinforcement in concrete structures, NDT & E International, Vol. 34, pp 435-442.

Rochinni G., 1993, Corrosion rate monitoring by linear polarization resistance, Corrosion Science, Vol. 34, No. 12, pp 2031-2044.

Rochini G., 1999, Some considerations on the polarization resistance method, Corrosion Science, Vol. 34, No. 12, pp 2353-2367.

Sagaidak A.I., Elizarov S.V., 2004, The relationship of acoustic-emission signals with the processes of deformation and fracture of building structures, Russian Journal of Nondestructive Testing, Vol. 40, No. 11, pp 739-745.

Sardis M. S., 2001, Msc Thesis- Earthquake resistance design procedure for High-strength Concrete Structures. School of Civil & Structural Engineering. Cardiff University, Wales, UK.

Sarveswaran V., Roberts M. B., Ward J. A., 2000, Reliability assessment of deteriorating reinforced concrete beams, Proceedings Institute Civil Engineers, Structure & Buildings, Vol. 140, pp 239-247.

Schechniger B., Vogel T., 2007, Acoustic emission for monitoring a reinforced concrete beam subject to four-point-bending, Construction and Building Materials, Vol. 21, pp 483-490.

Shigeishi M, Colombo C, Broughton K J, Rutledge H, Batchelor A J, Forde M C, 2001, Acoustic emission to assess and monitor the integrity of bridges, Construction and Building Materials, Vol 15, pp 35-49

Stern M. and Geary A. L., 1957, A theoretical analysis of the shape of polarization curves, Journal of the Electrochemical Society, Vol. 104, No. 1, pp 56-63.

Suzuki T, Othsu M, 2004, Quantitative damage evaluation of structural concrete by a compression test based on AE rate process analysis, Construction and Building Materials, Vol 18 ,pp 197–202.

Taylor M. 1997, Msc Thesis- Characterisation of normal and high-strength plain and fibre-reinforced concretes by means of strength, fracture and combined fracture/ relaxation test, School of Civil & Structural Engineering, Cardiff University, Wales, UK.

Tuuti K., 1982, Corrosion of steel in concrete, Swedish Cement and Concrete, Research Institute, ISSN 0346-6906, pp 469-476.

Othsu M., 2003, Detection and identification of concrete cracking in reinforced concrete by acoustic emission, Proceeding of the AIP Conference, Vol. 657, Part 1, pp 1455-1462.

Uomoto T. 1987, Application of acoustic emission to the field of concrete engineering, Journal of Acoustic Emission, Vol. 6, No. 3, pp 137-144.

Wu T. T., Sun J. H., Tong J. H., 2000, On the study of elastic wave scattering and Rayleigh wave velocity measurement of concrete with steel bar, NDT&E International, Vol. 33, pp. 401-407.

Yalcyn H, Ergun M., 1996, The prediction of corrosion rates of reinforcing steels in concrete, Cement & Concrete Research, Vol. 26, No. 10, pp 1593-1599.

Yoon D. J, Weiss W. J., Shah S. P., 2000a, Assessing damage in corroded reinforced concrete using acoustic emission, Journal of Engineering Mechanics(March), pp 273-283.

Yoon D. J., Weiss W. J., Shah S. P., 2000b, Detecting the extent of corrosion with acoustic emission, Transportation Research Record 1698, Paper No. 00-1425, pp 54-60.

Yoon S., Wang K., Weiss W. J, Shah S.P., 2000, Interaction between loading, corrosion and serviceability of reinforced concrete, ACI Materials Journal Vol. 97, No. 6, pp 1-8.

Yuyama S., 2000, Acoustic emission evaluation in concrete, Acoustic Emission- Beyond the Millenium, Tokyo, Elsevier, pp 187-214.

Yuyama S., Okamoto T., Shigeishi M., Othsu M., Kishi T., 1999, Proposed standard for evaluating structural integrity of reinforced concrete beams by acoustic emission, ASTM Special Technical Publication, No. 1353, pp 25-40.

Yuyama S., 2005, Acoustic emission for fracture studies using moment tensor analysis, The Journal of Strain Analysis for Engineering Design, Vol. 40, No. 1, pp 33-44.

Yuyama S., Yokoyama K., Niitani K., Ohtsu M., Uomoto T., 2007, Detection and evaluation of failures in high-strength tendon of prestressed concrete bridges by acoustic emission, Construction and Building Materials, Vol 21, Pp 491-500.

Zaid M., Gaydecki P., Quek S., Miller G., Fernandes B., 2004, Extracting dimensional information from steel reinforcing bars in concrete using neural networks trained on data from an inductive sensor, NDT & E International, Vol. 37, pp 551-558.

Zdunek A. D, Prine D., 1995, Early detection of steel rebars corrosion by acoustic emission monitoring, Infrastructure Technology Institute. <URL: http://www.iti.nwu.edu/publications/technical_reports/tr16.html > [Accessed 19 December 2003].

APPENDIX A

SENSOR CALIBRATION CERTIFICATES

PHYSICAL ACOUSTICS CORPORATION
A MISTRAS Holdings Company

AE SENSOR CALIBRATION CERTIFICATE

Sensor Name: R6D
Sensor S/N: 86
Comment:

Test Date: 9/25/01
Tested By: C.P.

Max. Value (dB): 80.09
Peak Freq.(kHz): 7.32

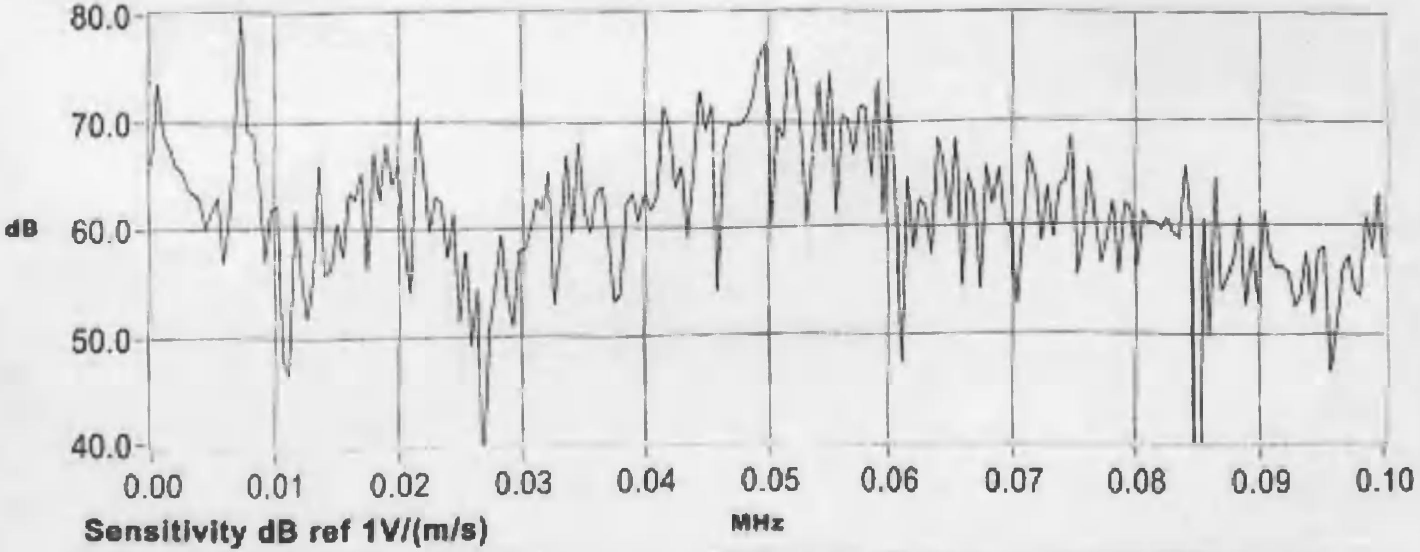

Sensitivity dB ref 1V/(m/s)

PAC Certifies that this sensor meets all performance, environmental and physical standards established in applicable PAC specifications. Calibration methodology based on ASTM standard E1106- "Standard Method for Primary Calibration of Acoustic Emission Sensors."

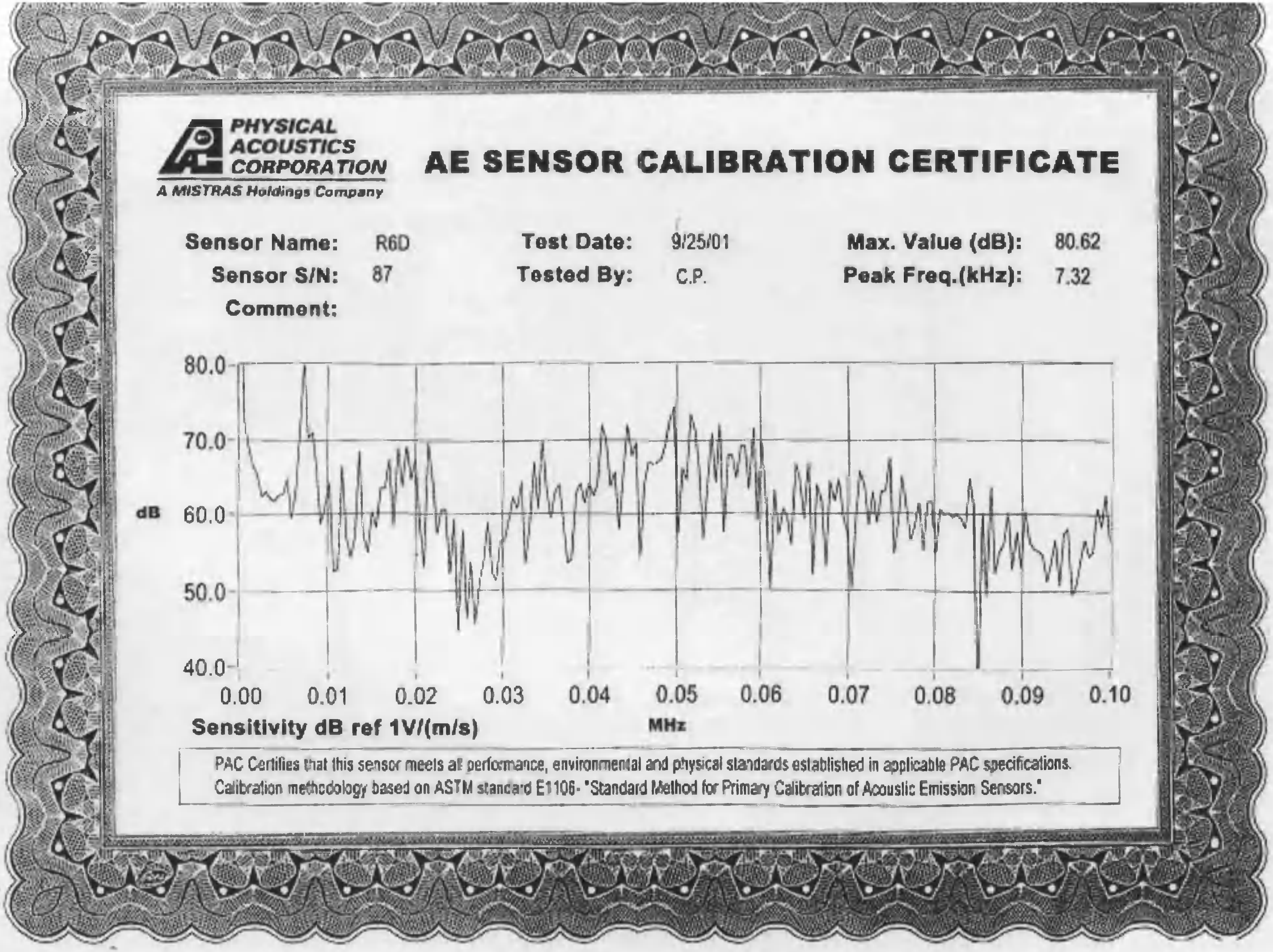

PHYSICAL ACOUSTICS CORPORATION
A MISTRAS Holdings Company

AE SENSOR CALIBRATION CERTIFICATE

Sensor Name:	R6D	**Test Date:**	9/25/01	**Max. Value (dB):**	80.62
Sensor S/N:	87	**Tested By:**	C.P.	**Peak Freq.(kHz):**	7.32
Comment:					

Sensitivity dB ref 1V/(m/s)

PAC Certifies that this sensor meets all performance, environmental and physical standards established in applicable PAC specifications. Calibration methodology based on ASTM standard E1106- "Standard Method for Primary Calibration of Acoustic Emission Sensors."

PHYSICAL ACOUSTICS CORPORATION
A MISTRAS Holdings Company

AE SENSOR CALIBRATION CERTIFICATE

Sensor Name: R6D
Sensor S/N: 92
Comment:

Test Date: 9/25/01
Tested By: C.P.

Max. Value (dB): 79.95
Peak Freq.(kHz): 7.32

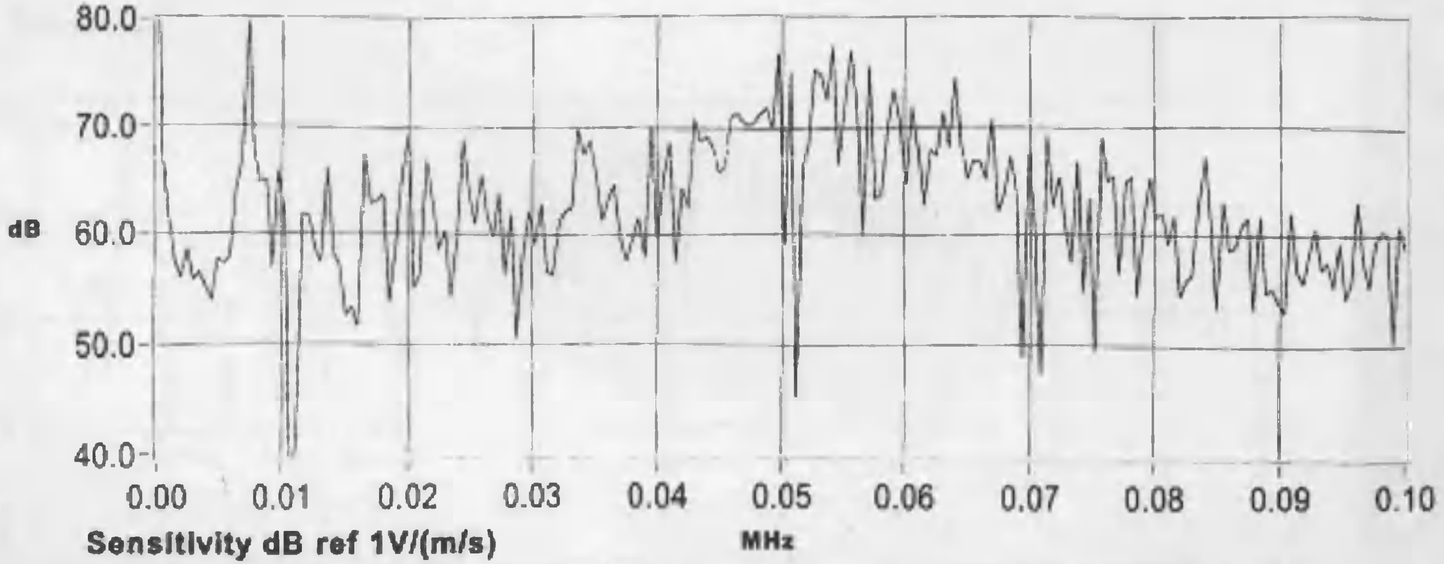

PAC Certifies that this sensor meets all performance, environmental and physical standards established in applicable PAC specifications. Calibration methodology based on ASTM standard E1106- "Standard Method for Primary Calibration of Acoustic Emission Sensors."

PHYSICAL ACOUSTICS CORPORATION
A MISTRAS Holdings Company

AE SENSOR CALIBRATION CERTIFICATE

Sensor Name: R6D
Sensor S/N: 93
Comment:

Test Date: 10/31/01
Tested By: C.P.

Max. Value (dB): 83.44
Max. Freq.(kHz): 7.32

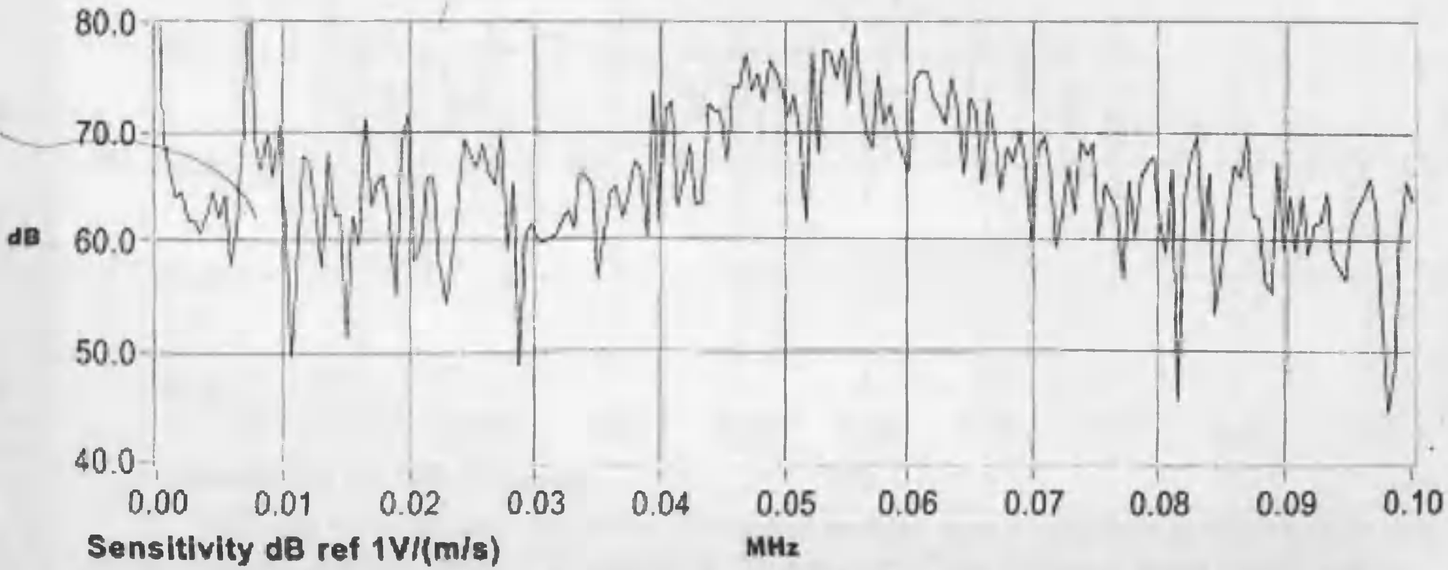

PAC Certifies that this sensor meets all performance, environmental and physical standards established in applicable PAC specifications. Calibration methodology based on ASTM standard E1106- "Standard Method for Primary Calibration of Acoustic Emission Sensors."

PHYSICAL
ACOUSTICS
CORPORATION
A MISTRAS Holdings Company

AE SENSOR CALIBRATION CERTIFICATE

Sensor Name: R6D
Sensor S/N: 94
Comment:

Test Date: 10/31/01
Tested By: C.P.

Max. Value (dB): 83.80
Max. Freq.(kHz): 7.32

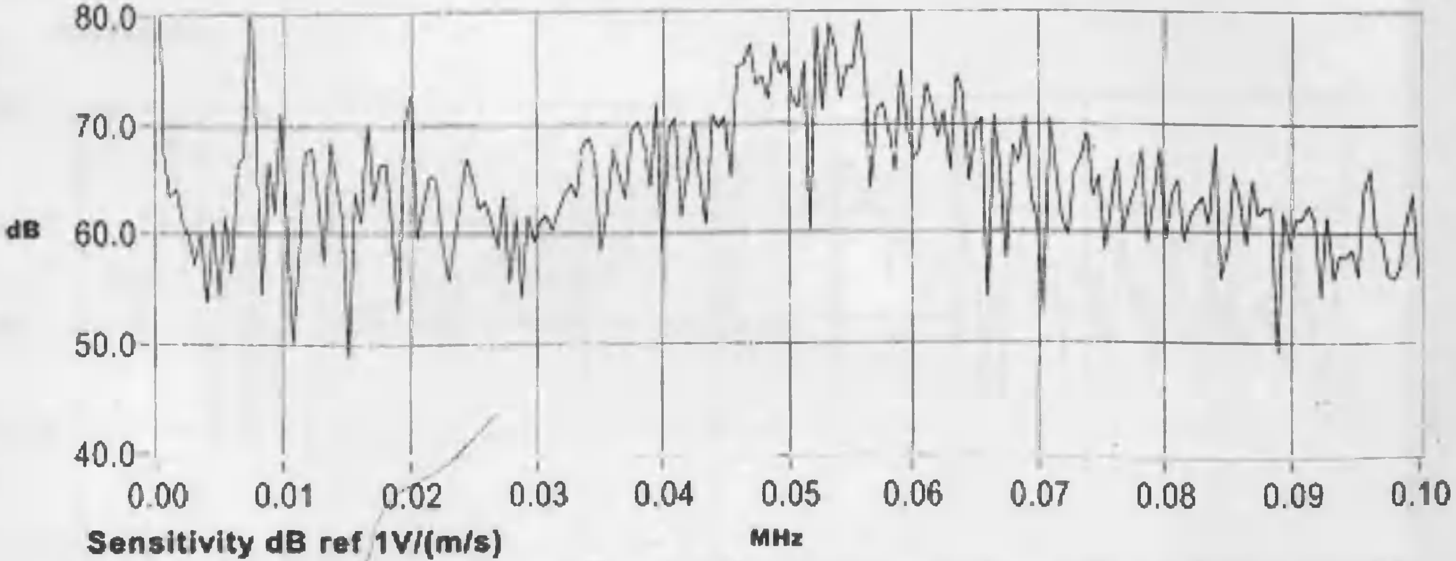

PAC Certifies that this sensor meets all performance, environmental and physical standards established in applicable PAC specifications. Calibration methodology based on ASTM standard E1106- "Standard Method for Primary Calibration of Acoustic Emission Sensors."

PHYSICAL ACOUSTICS CORPORATION
A MISTRAS Holdings Company

AE SENSOR CALIBRATION CERTIFICATE

Sensor Name: R6D
Sensor S/N: 95
Comment:

Test Date: 10/31/01
Tested By: C.P.

Max. Value (dB): 83.52
Max. Freq.(kHz): 7.32

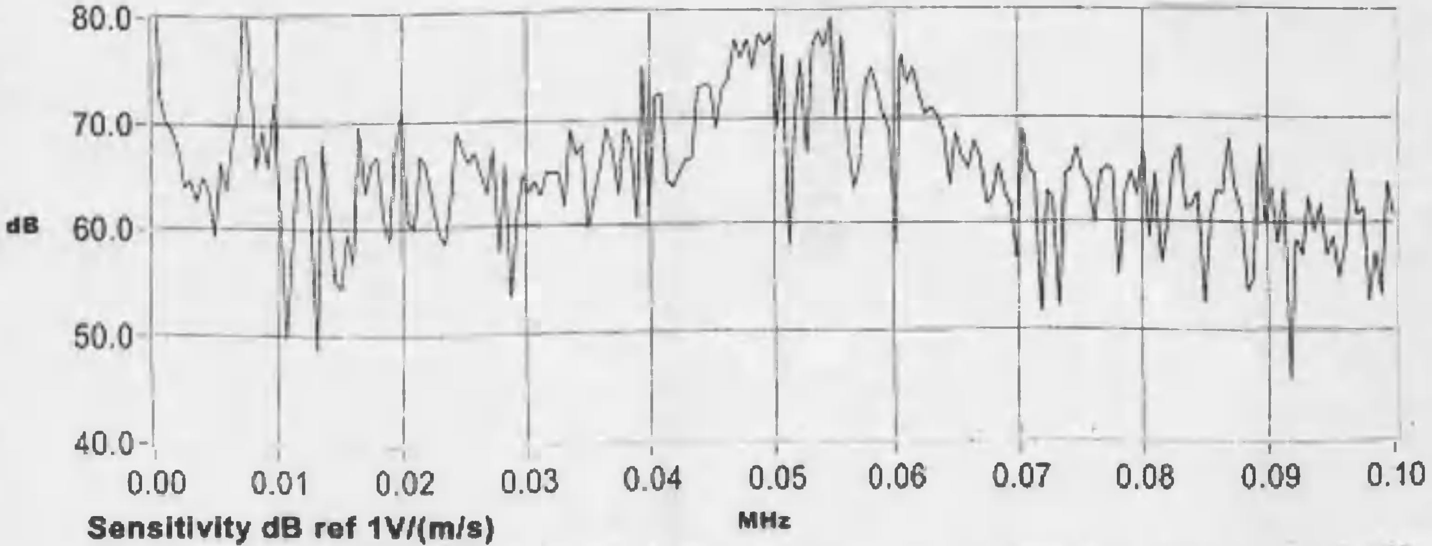

PAC Certifies that this sensor meets all performance, environmental and physical standards established in applicable PAC specifications. Calibration methodology based on ASTM standard E1106- "Standard Method for Primary Calibration of Acoustic Emission Sensors."

APPENDIX B

RESULTS FOR PRE-CORRODED (PR) SPECIMENS

APPENDIX B: RESULTS FOR PRE-CORRODED (PR) SPECIMENS.

1. A11PR

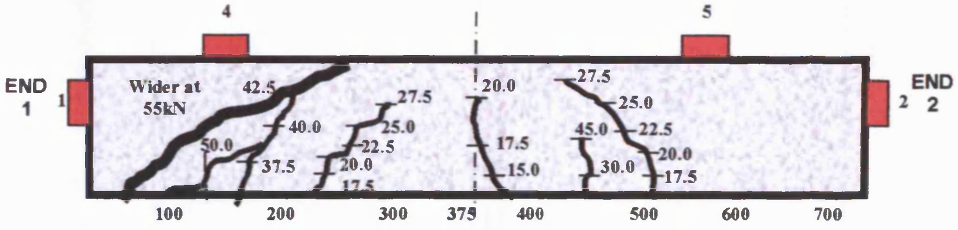

(a) Side view (Loads in kN)

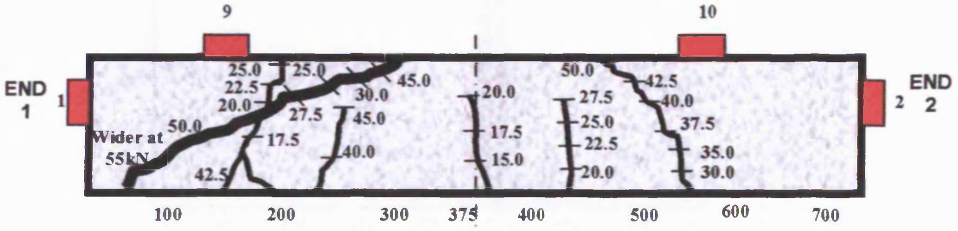

(b) Side view (Loads in kN)

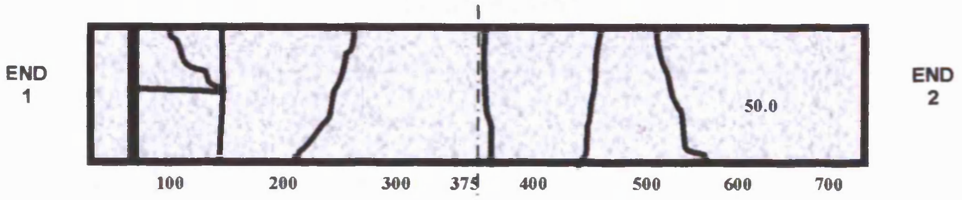

(c) Bottom view (Loads in kN)

Figure B1: Crack pattern from visual observation for A11PR

Note for Beam A11PR:

Zone 1 associated with crack that can be observed visually at 370-400mm.

Zone 2 associated with crack that can be observed visually at 450-500mm.

Zone 3 associated with crack that can be observed visually at 240-300mm

Zone 4 associated with crack that can be observed visually at 50-270mm (shear crack).

Failure in shear at 59.21kN.

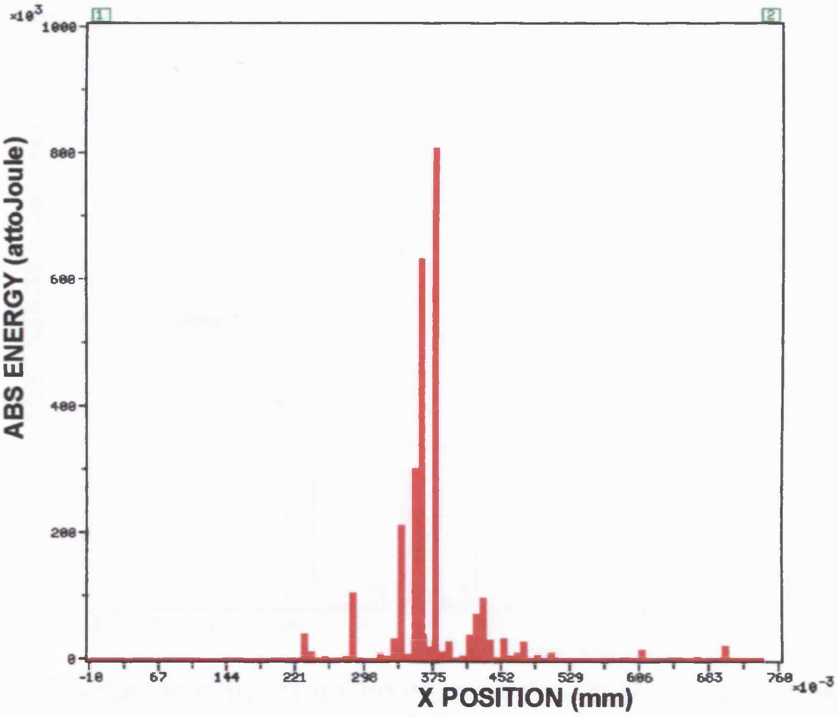

Figure B2: Source location of total emission during micro-cracking (0-12.5 kN) for beam A11PR

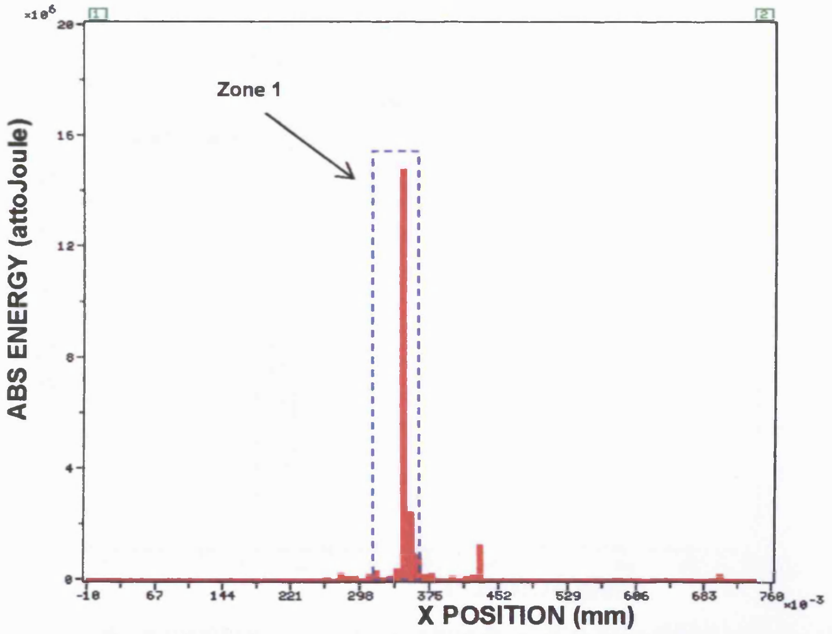

Figure B3: Source location of total emission at the started of the localized crack propagation (0-15.0kN) for A11PR

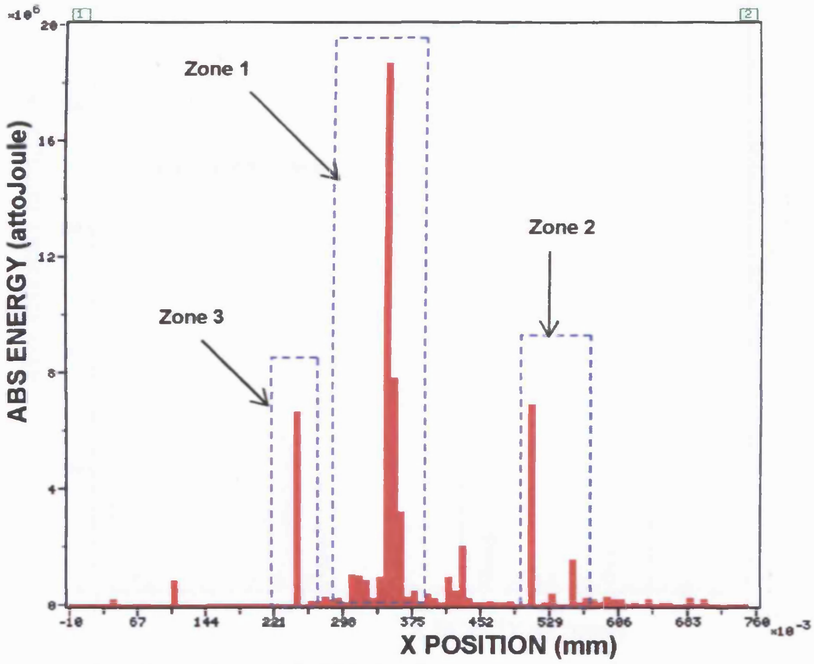

Figure B4: Source location of total emission at the started of distributed flexural cracks (0-17.5kN) for A11PR.

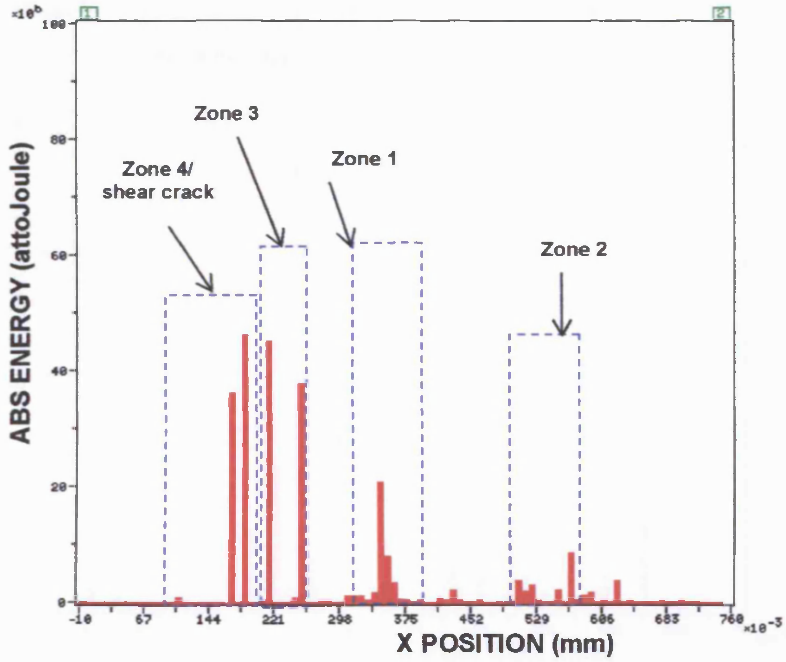

Figure B5: Source of location of total emission at the formation of the shear crack (0-45.0kN) for A11PR.

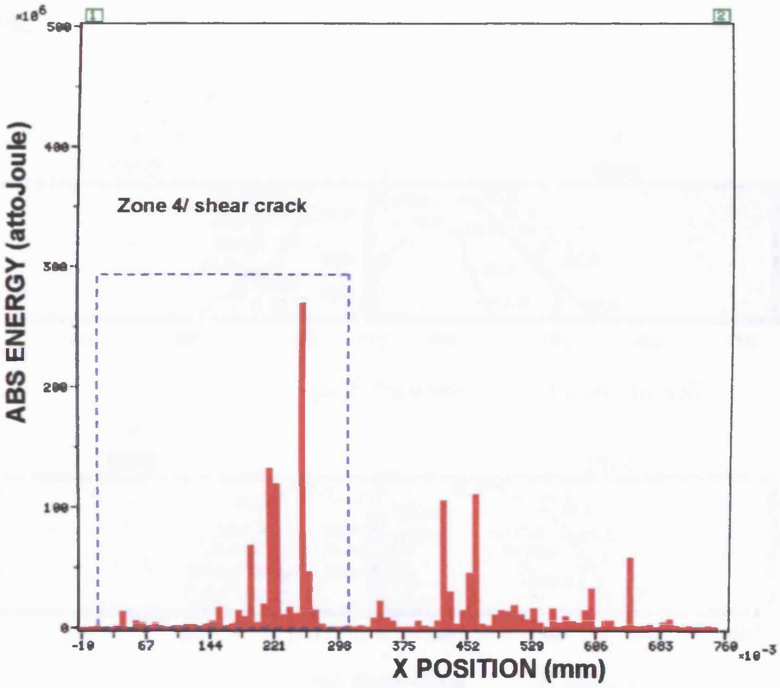

Figure B6: Source location of total emission during damage localization (0-55.0kN) for A11PR.

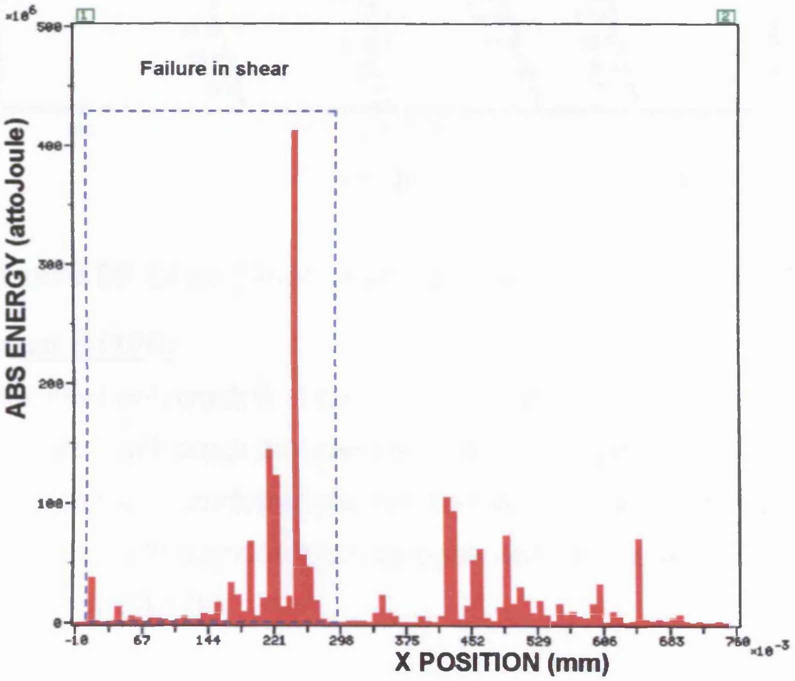

Figure B7: Source location of emission at failure (59.21kN) for A11PR

2. B11PR

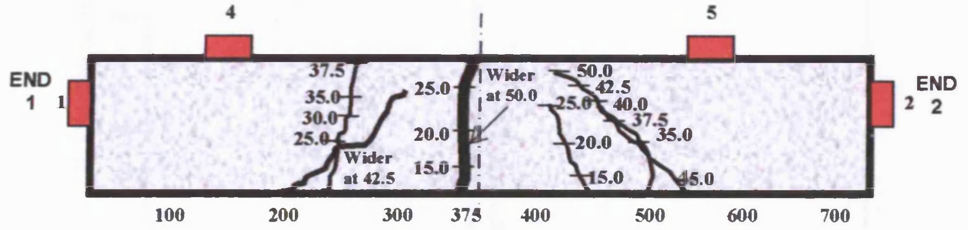

(a) Side view (Loads in kN)

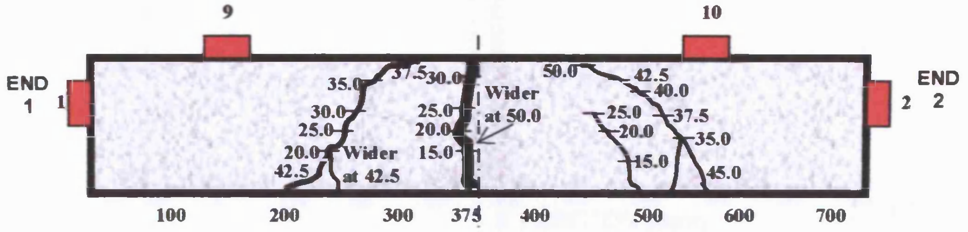

(b) Side view (Loads in kN)

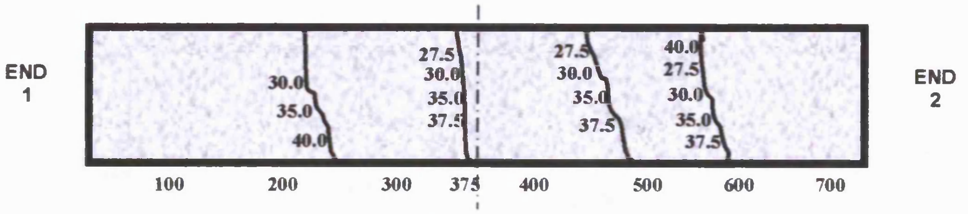

(c) Bottom view (Loads in kN)

Figure B8: Crack pattern from visual observation for B11PR

Note for Beam B11PR:

Zone 1 associated with crack that can be observed visually at 360-375mm.

Zone 2 associated with crack that can be observed visually at 450-480mm.

Zone 3 associated with crack that can be observed visually at 200-330mm

Zone 4 associated with crack that can be observed visually at 450-560mm.

Failure in flexure at 54.77kN.

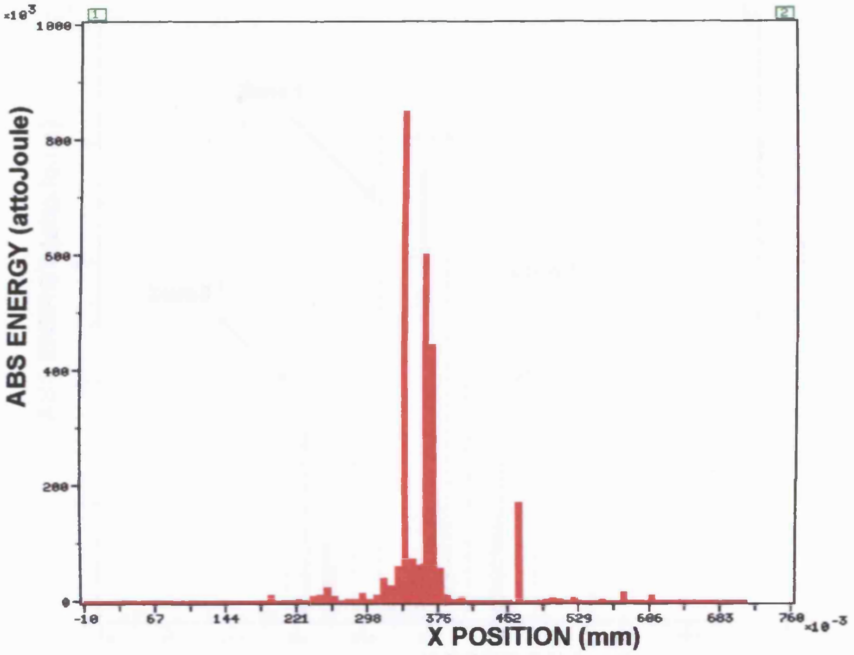

Figure B9: Source location of total emission during micro-cracking (0-12.5 kN) for beam B11PR.

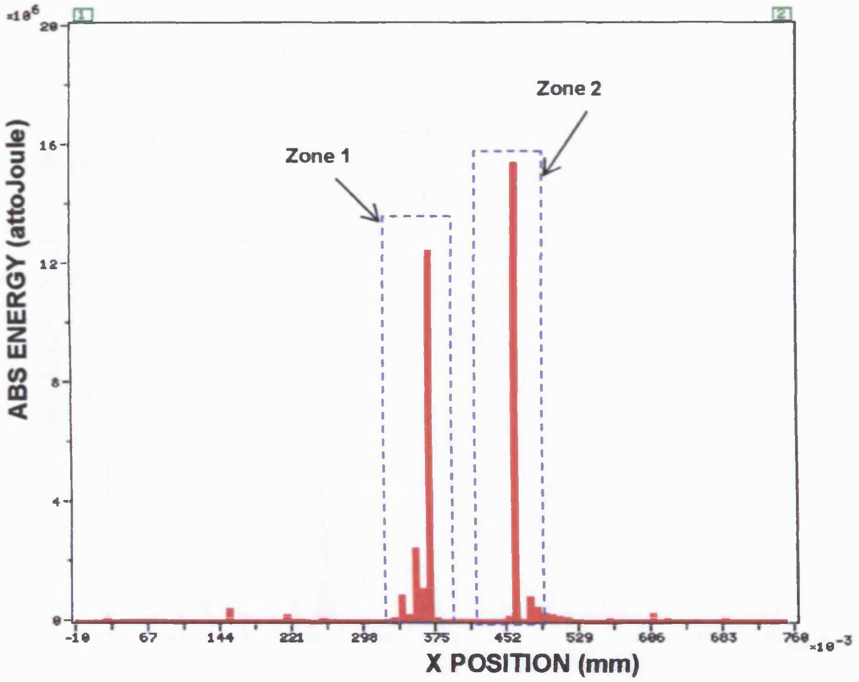

Figure B10: Source location of total emission at the started of the localized crack propagation (0-15.0kN) for B11PR

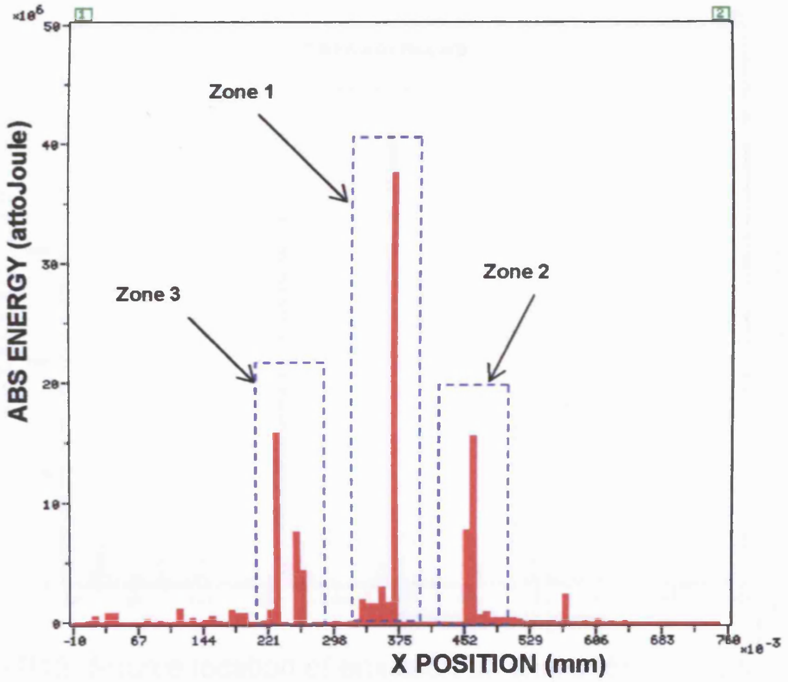

Figure B11: Source location of total emission at the started of distributed flexural cracks (0-25.0kN) for B11PR.

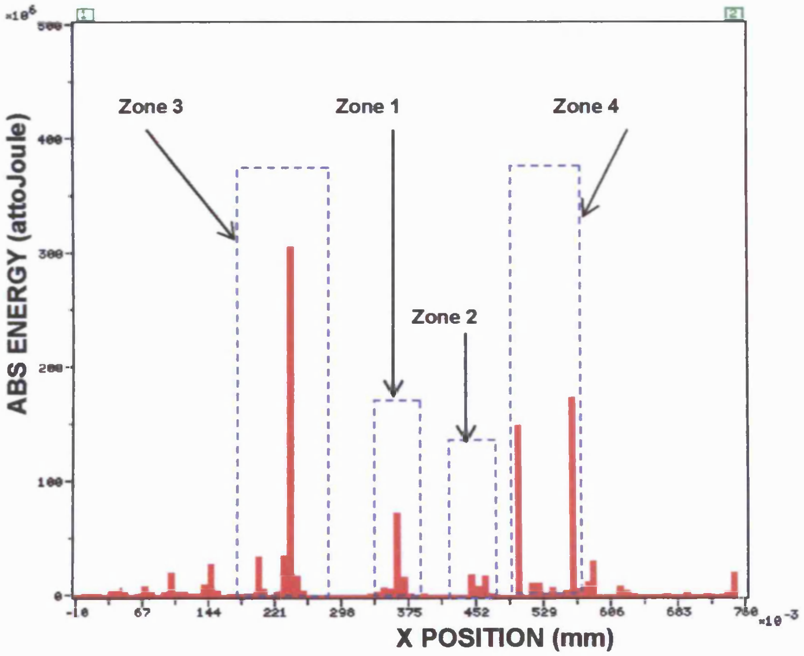

Figure B12: Source location of total emission during damage localization (0-42.5kN) for B11PR.

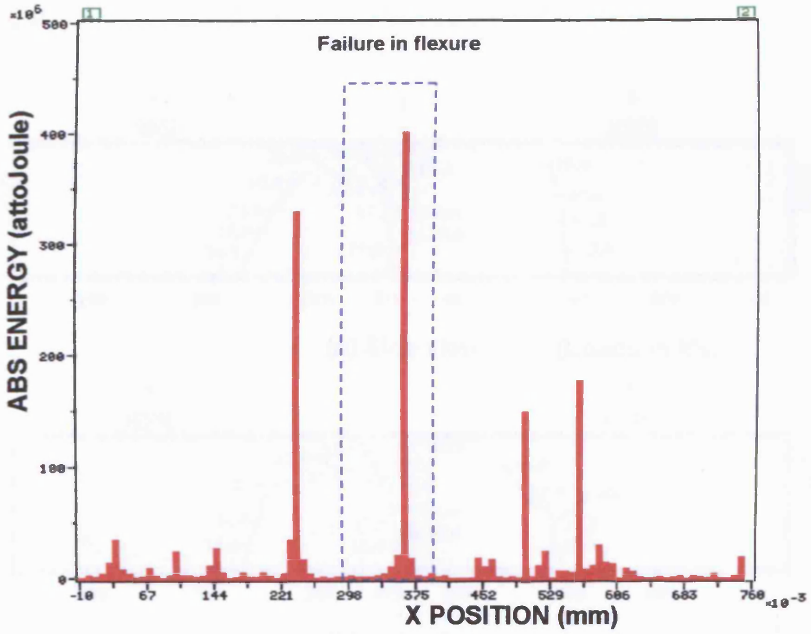

Figure B13: Source location of emission at failure (54.77kN) for B11PR

3. C11PR

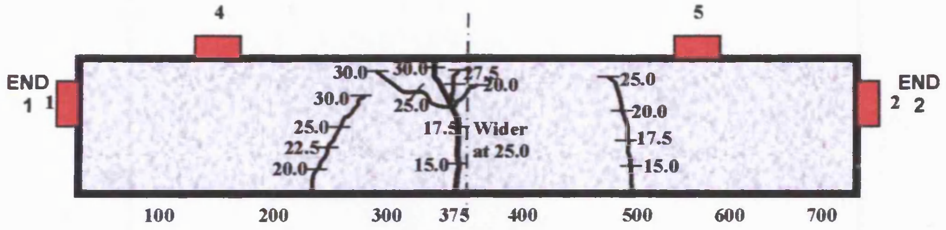

(a) Side view (Loads in kN)

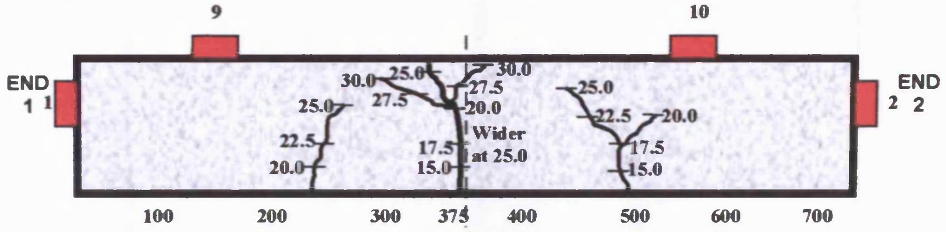

(b) Side view (Loads in kN)

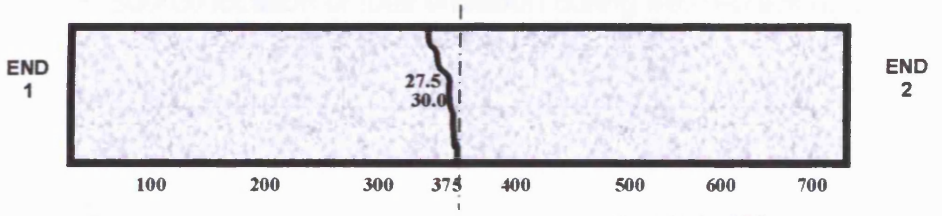

(c) Bottom view (Loads in kN)

B14: Crack pattern from visual observation for C11PR

Note for Beam C11PR:

Zone 1 associated with crack that can be observed visually at 290-400mm.

Zone 2 associated with crack that can be observed visually at 470-530mm.

Zone 3 associated with crack that can be observed visually at 230-280mm

Failure in flexure at 34.18kN.

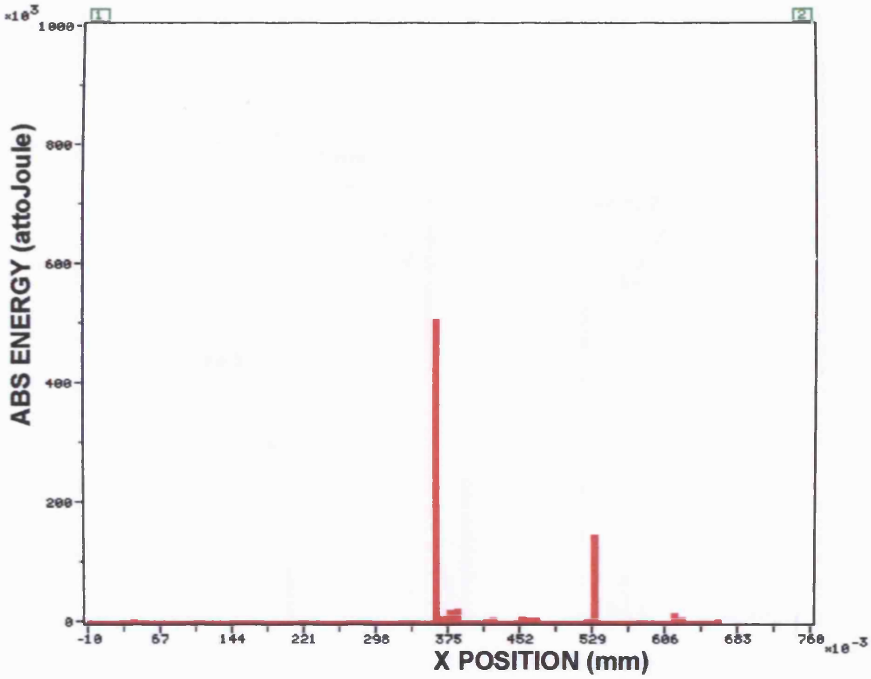

Figure B15: Source location of total emission during micro-cracking (0-12.5 kN) for beam C11PR.

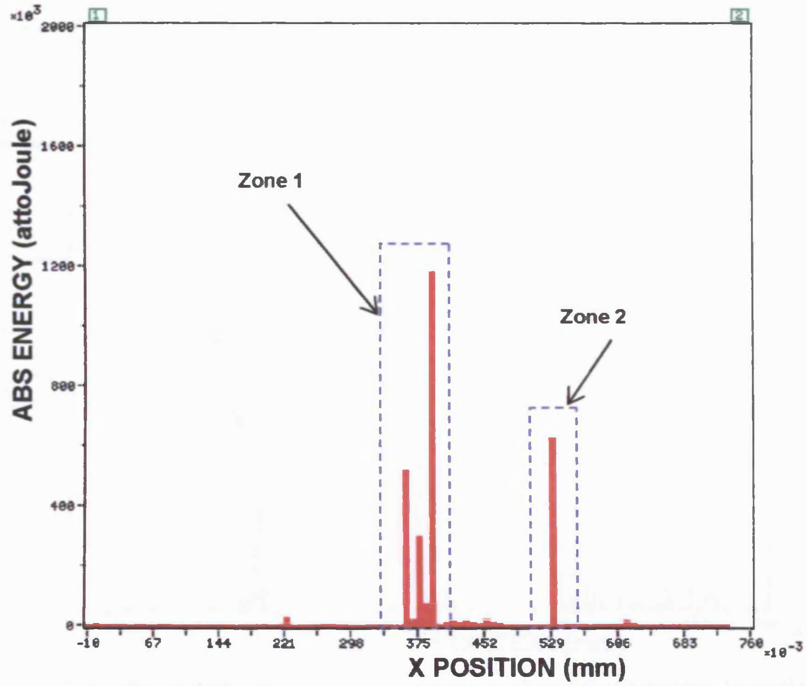

Figure B16: Source location of total emission at the started of the localized crack propagation (0-15.0kN) for C11PR.

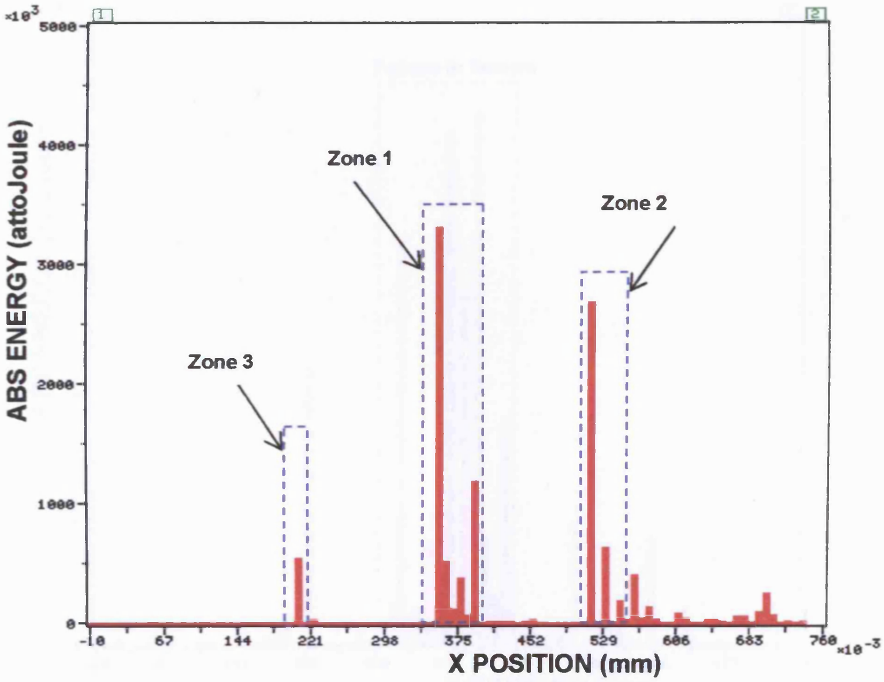

Figure B17: Source location of total emission at the started of distributed flexural cracks (0-20.0kN) for C11PR.

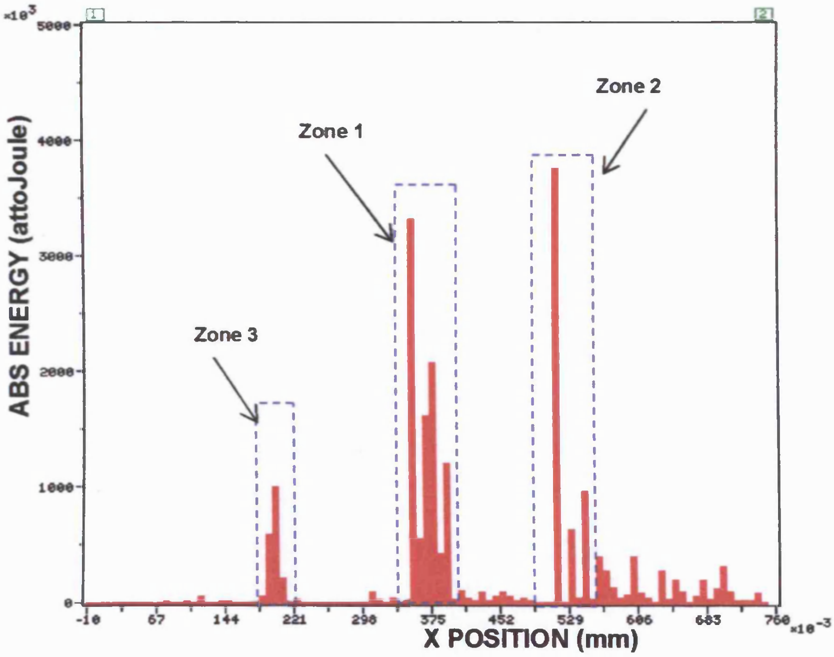

Figure B18: Source location of total emission during damage localization (0-25.0kN) for C11PR.

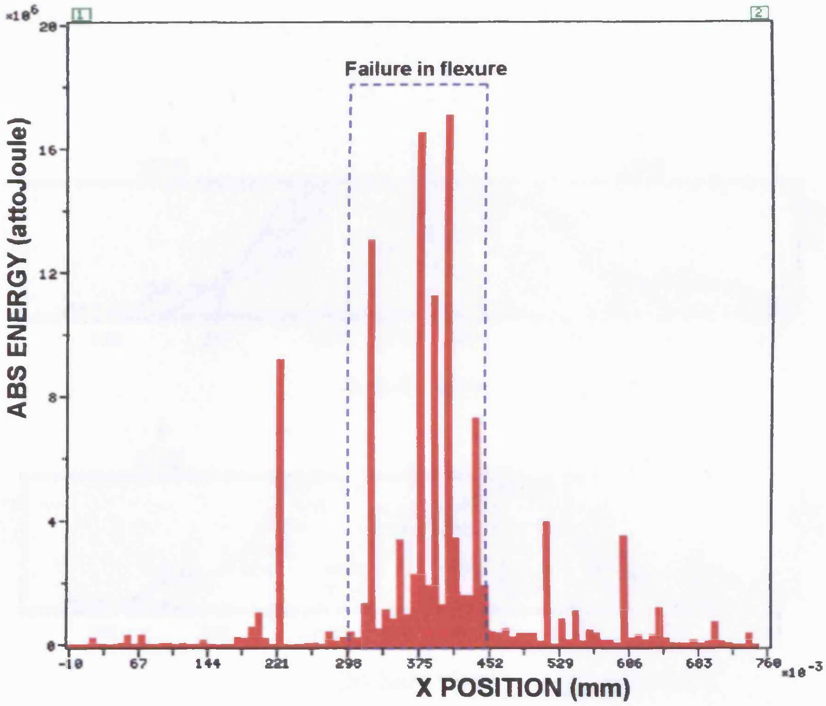

Figure B19: Source location of emission at failure (34.18kN) for C11PR.

4. B22PR

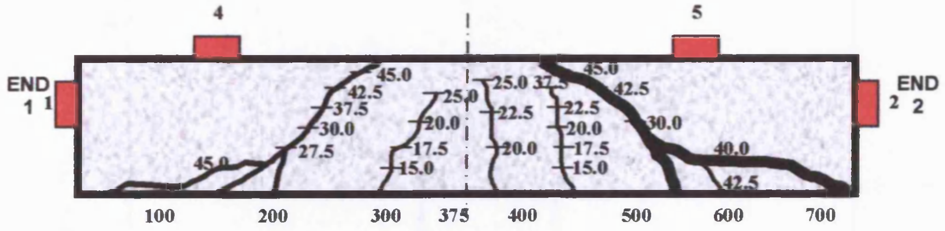

(a) Side view (Loads in kN)

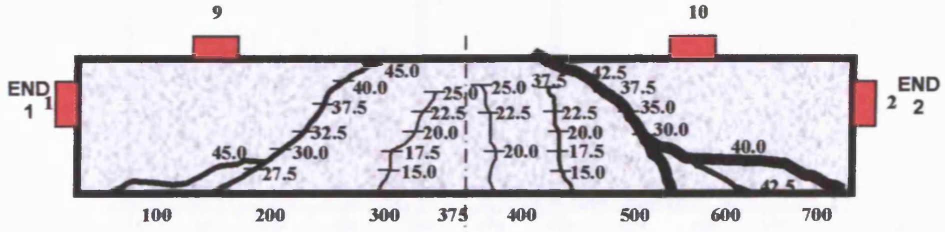

(b) Side view (Loads in kN)

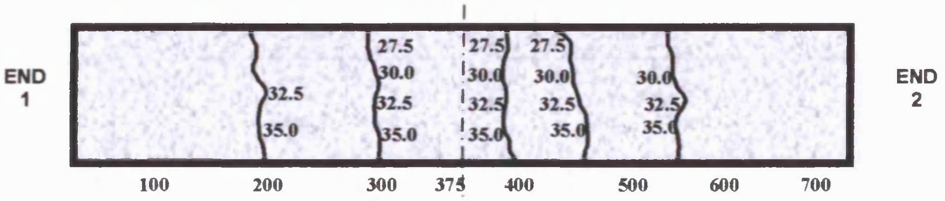

(c) Bottom view (Loads in kN)

Figure B20: Crack pattern from visual observation for B22PR

Note for Beam B22PR:

Zone 1 associated with crack that can be observed visually at 300-350mm.

Zone 2 associated with crack that can be observed visually at 440-450mm.

Zone 3 associated with crack that can be observed visually at 380-390mm

Zone 4 associated with crack that can be observed visually at 50-300mm

Zone 5 associated with crack that can be observed visually at 450-700mm (shear crack).

Failure in shear at 47.50kN.

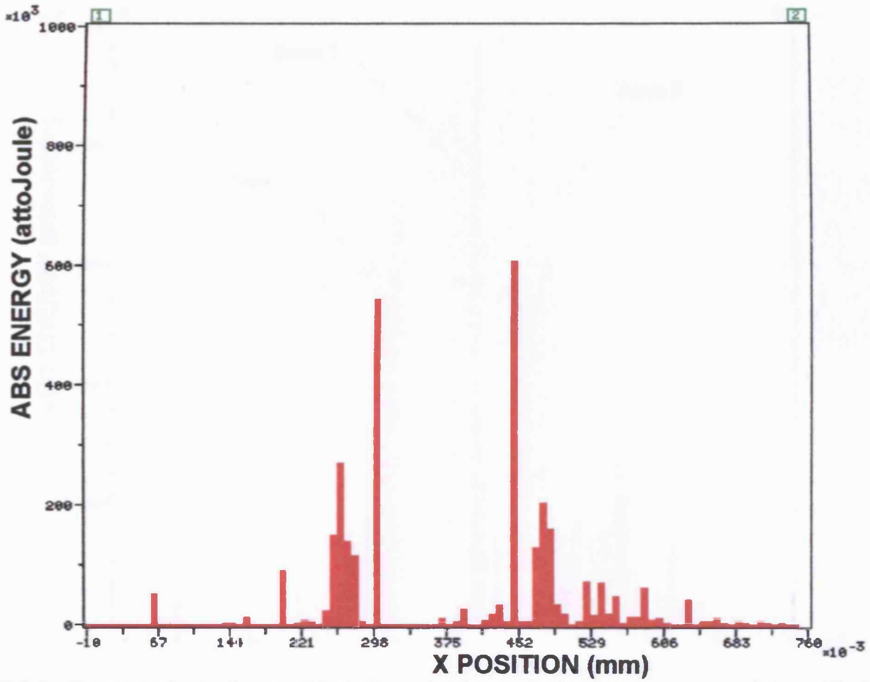

Figure B21: Source location of total emission during micro-cracking (0-12.5 kN) for beam B22PR.

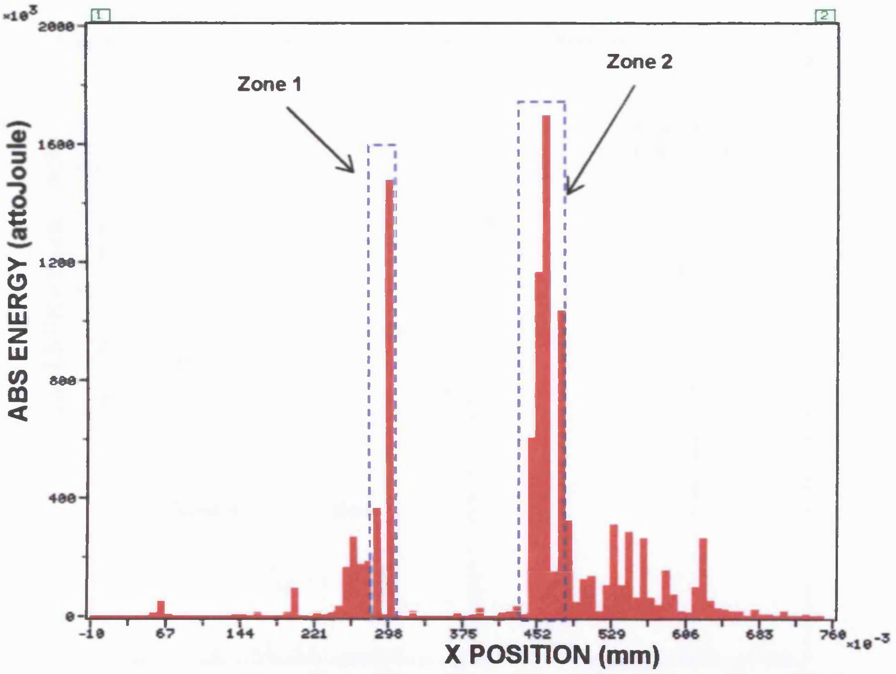

Figure B22: Source location of total emission at the started of the localized crack propagation (0-15.0kN) for B22PR.

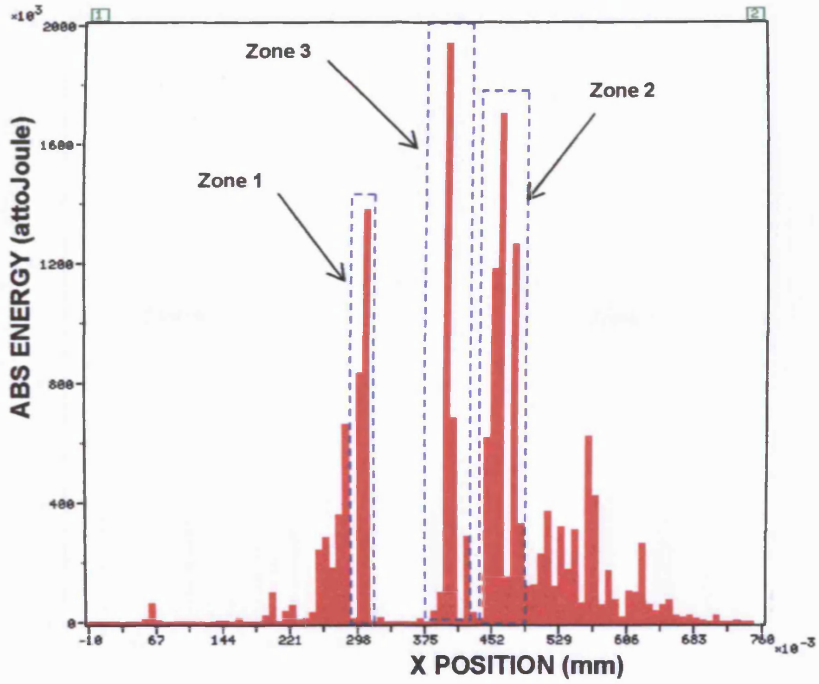

Figure B23: Source location of total emission at the started of distributed flexural cracks (0-20.0kN) for B22PR.

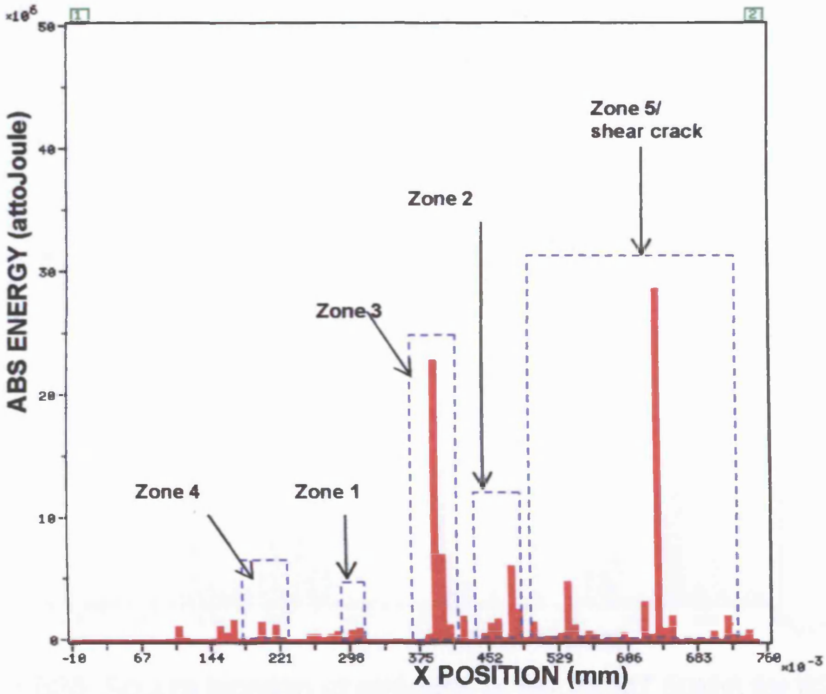

Figure B24: Source of location of total emission at the formation of the shear crack (0-40.0kN) for B22PR.

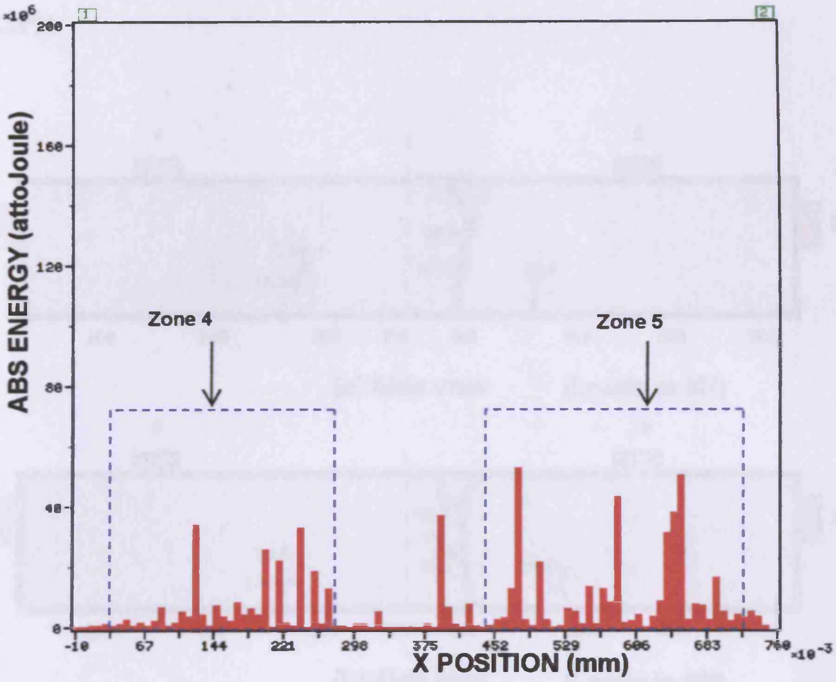

Figure B25: Source location of total emission during damage localization (0-45.0kN) for B22PR.

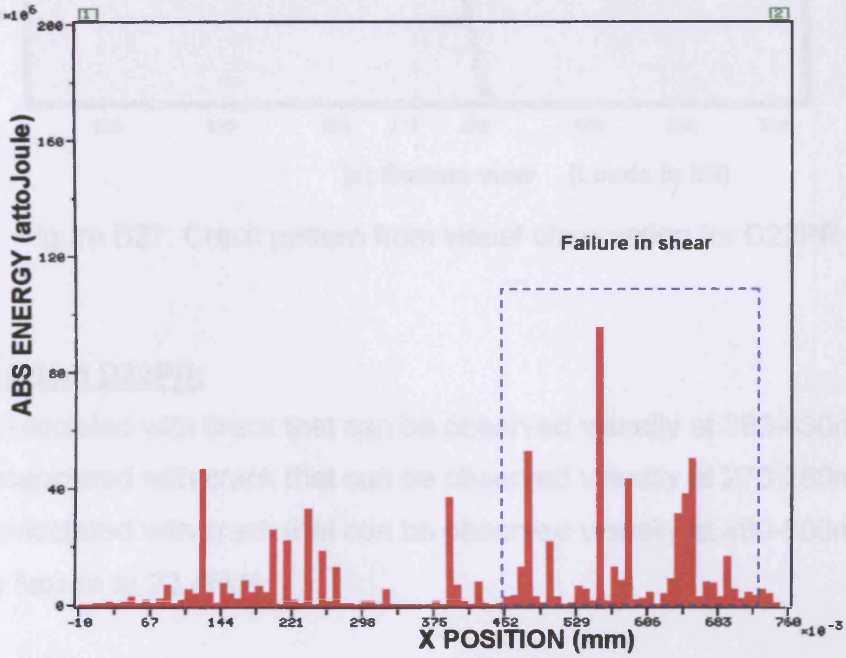

Figure B26: Source location of emission at failure (47.50kN) for B22PR.

5. D22PR

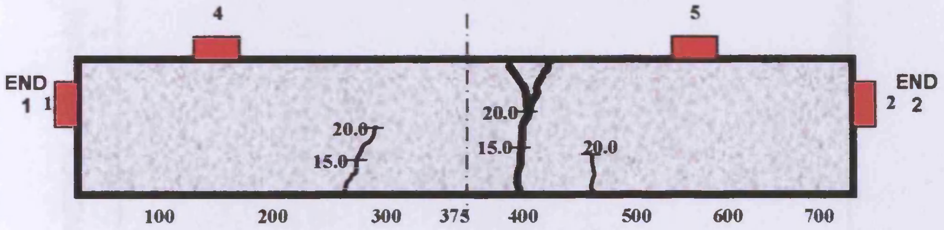

(a) Side view (Loads in kN)

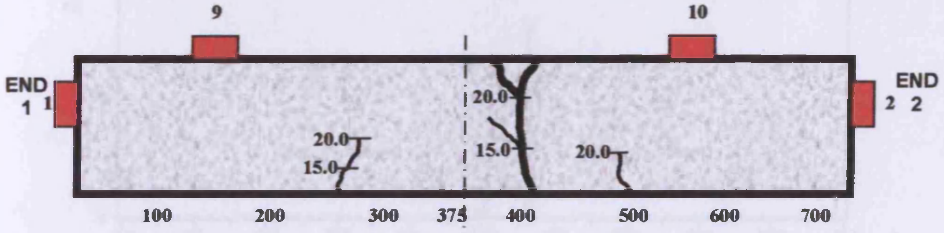

(b) Side view (Loads in kN)

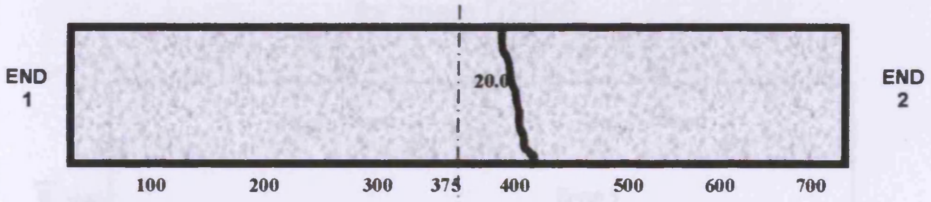

(c) Bottom view (Loads in kN)

Figure B27: Crack pattern from visual observation for D22PR

Note for Beam D22PR:

Zone 1 associated with crack that can be observed visually at 380-430mm.

Zone 2 associated with crack that can be observed visually at 270-280mm.

Zone 3 associated with crack that can be observed visually at 480-500mm.

Failure in flexure at 23.46kN

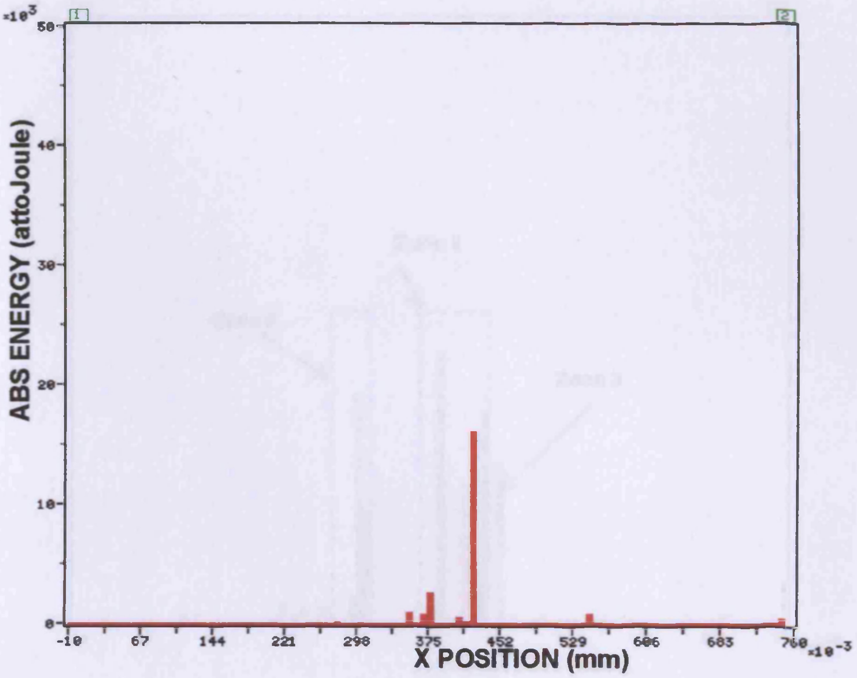

Figure B28: Source location of total emission during micro-cracking (0-12.5 kN) for beam D22PR.

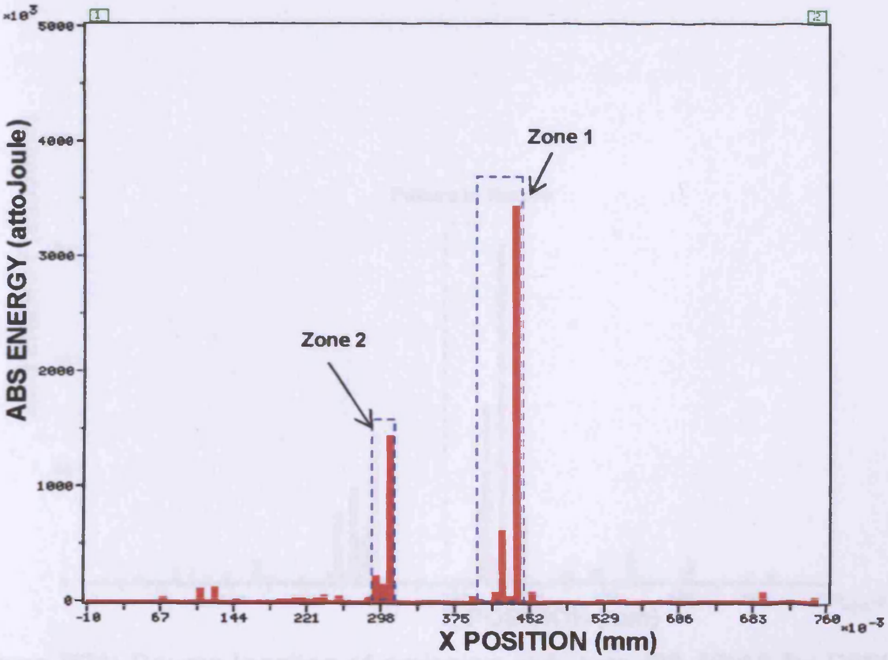

Figure B29: Source location of total emission at the started of the localized crack propagation (0-15.0kN) for D22PR.

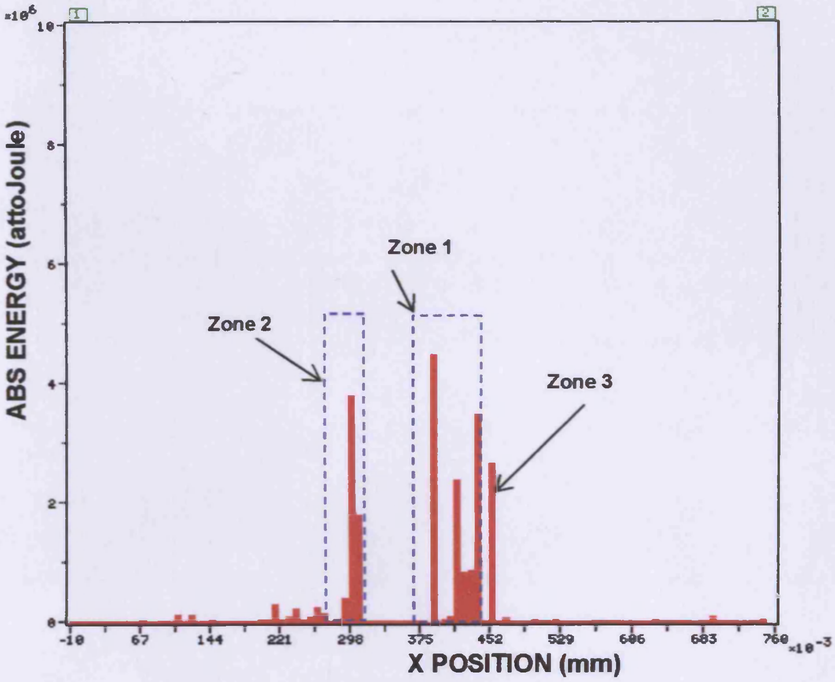

Figure B30: Source location of total emission at the started of distributed flexural cracks and damage localization (0-20.0kN) for D22PR.

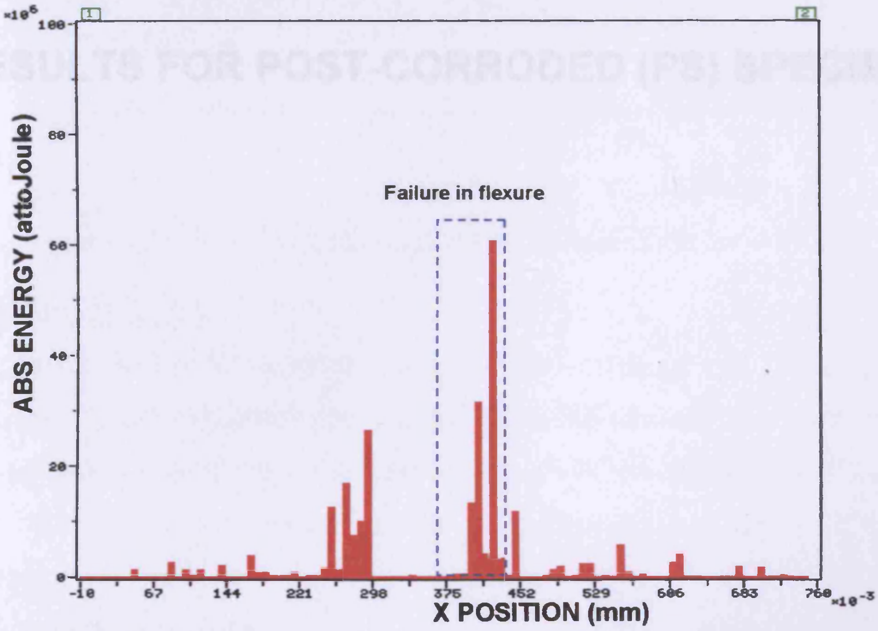

Figure B31: Source location of emission at failure (23.46kN) for D22PR.

APPENDIX C

RESULTS FOR POST-CORRODED (PS) SPECIMENS

APPENDIX C: RESULTS FOR POST-CORRODED (PS) SPECIMENS.

1. BEAM A11PS

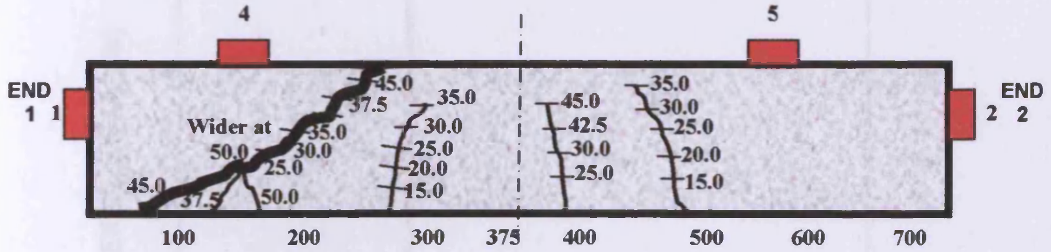

(a) Side view (Loads in kN)

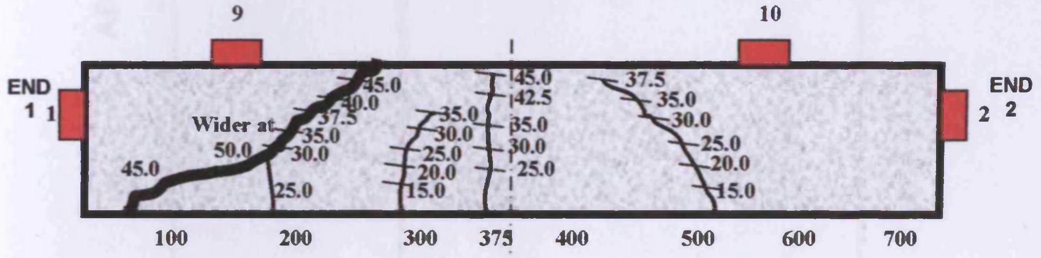

(b) Side view (Loads in kN)

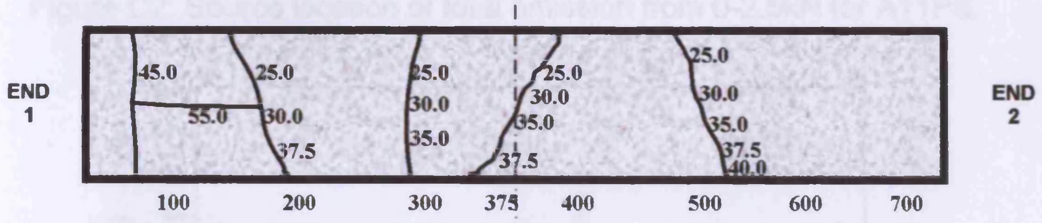

(c) Bottom view (Loads in kN)

Figure C1: Crack pattern from visual observation for A11PS

Note for Beam A11PS:

Zone 1 associated with crack that can be observed visually at 280-320mm.

Zone 2 associated with crack that can be observed visually at 450-530mm.

Zone 3 associated with crack that can be observed visually at 360-400mm

Zone 4 associated with crack that can be observed visually at 50-260mm (shear crack).

Failure in shear at 55.0kN.

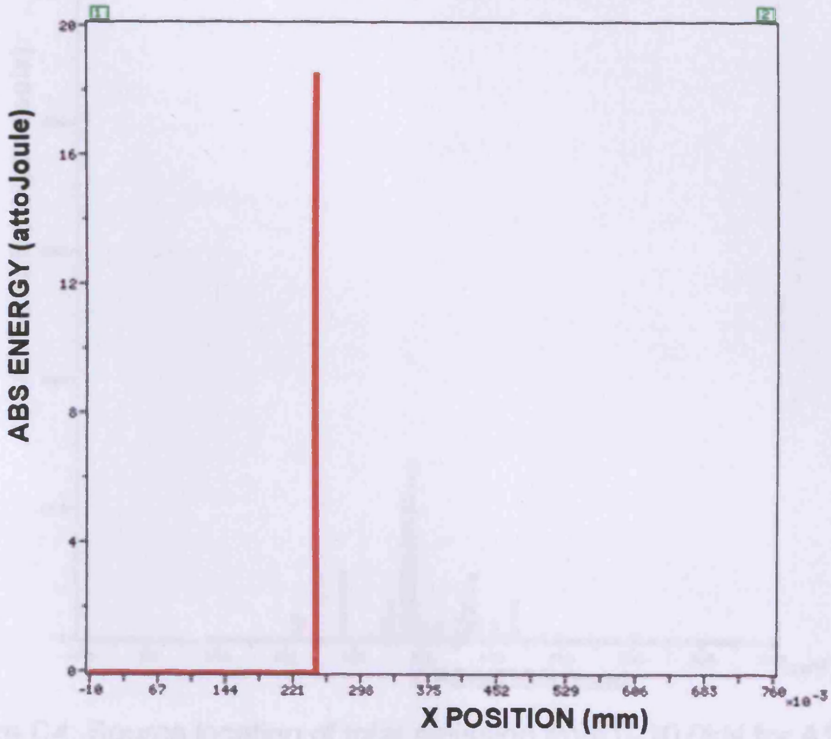

Figure C2: Source location of total emission from 0-2.5kN for A11PS.

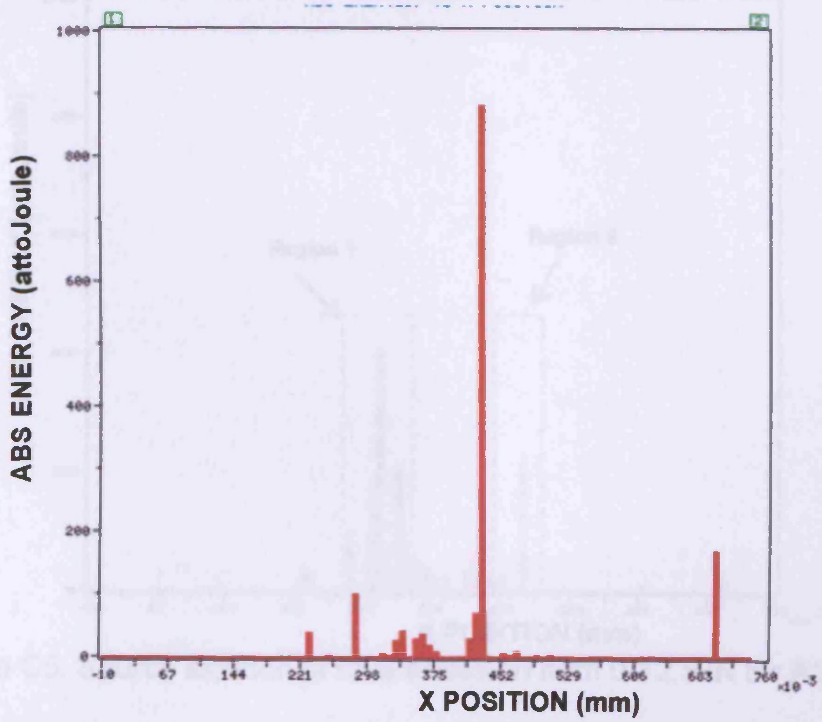

Figure C3: Source location of total emission from 0-5.0kN for A11PS.

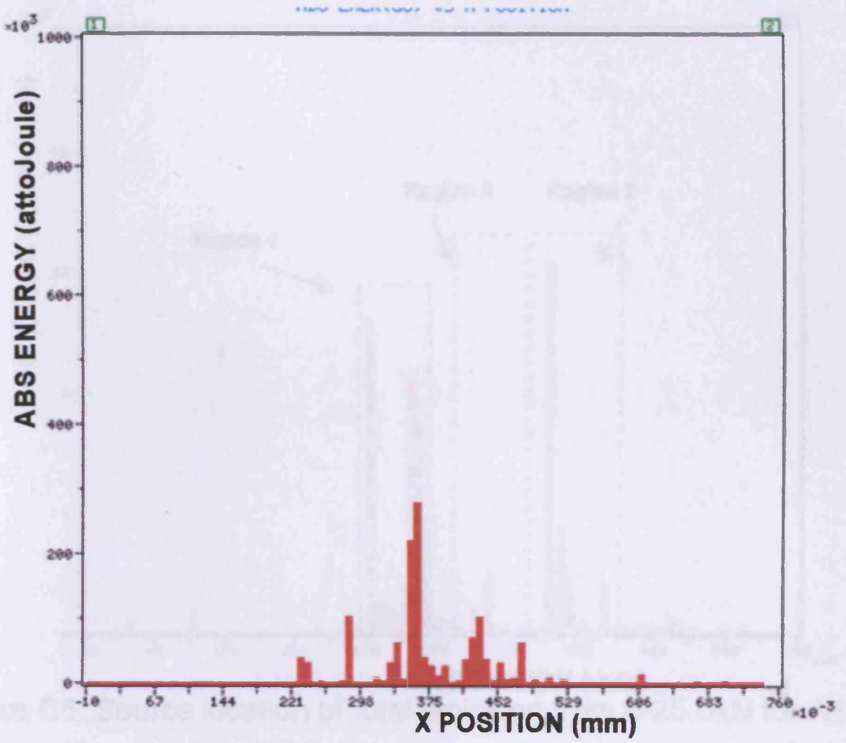

Figure C4: Source location of total emission from 0-10.0kN for A11PS.

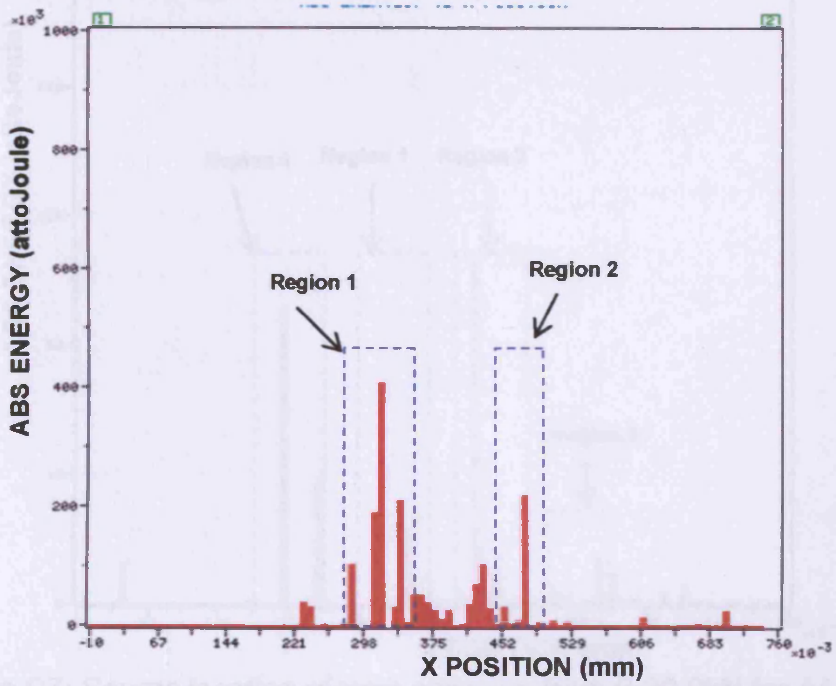

Figure C5: Source location of total emission from 0-12.5kN for A11PS.

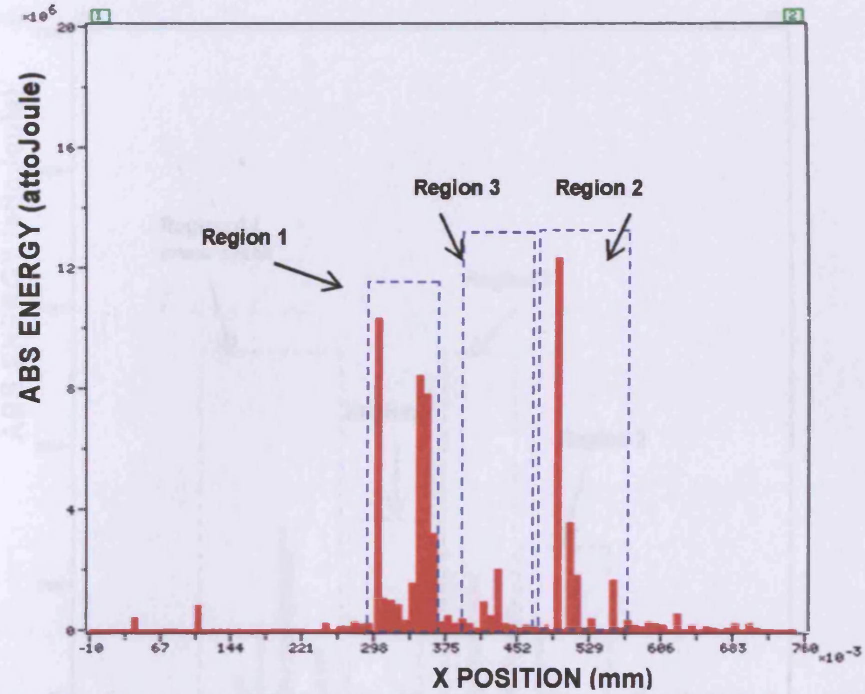

Figure C6: Source location of total emission from 0-25.0kN for A11PS.

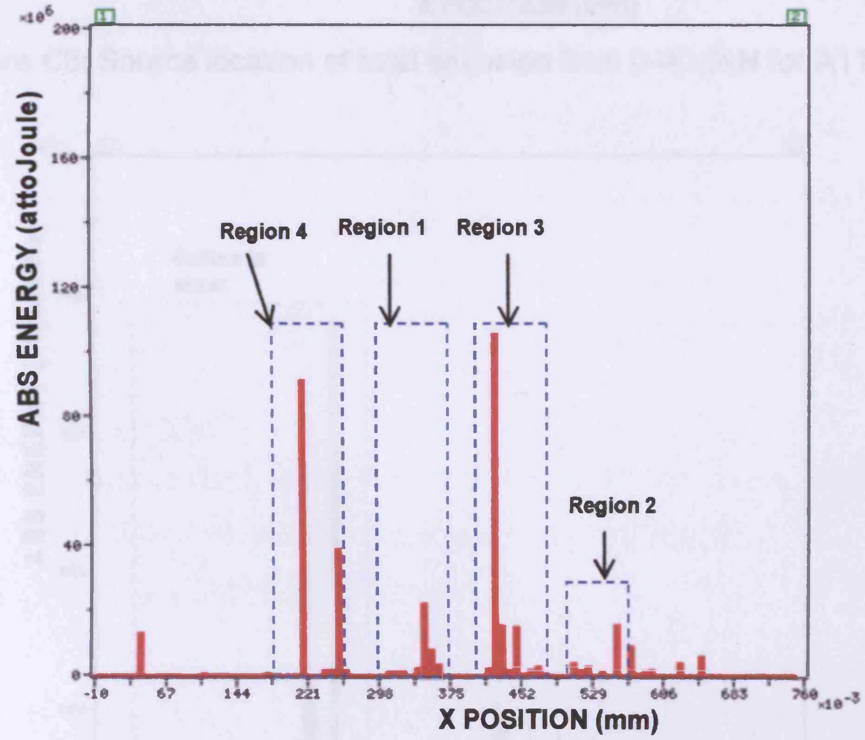

Figure C7: Source location of total emission from 0-30.0kN for A11PS.

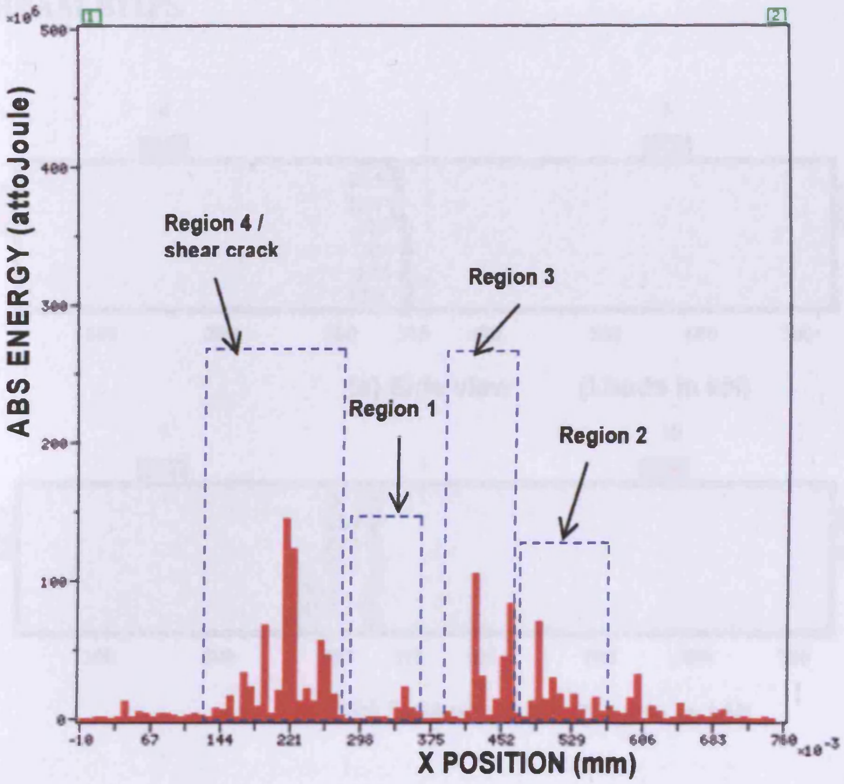

Figure C8: Source location of total emission from 0-40.0kN for A11PS.

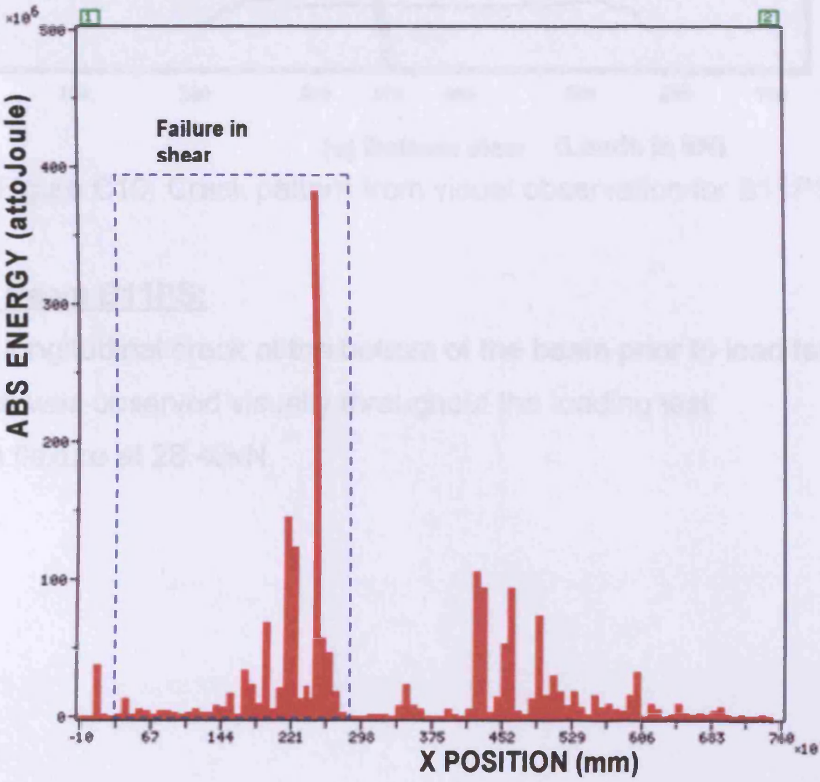

Figure C9: Source location of total emission at failure for A11PS.

2. **BEAM B11PS**

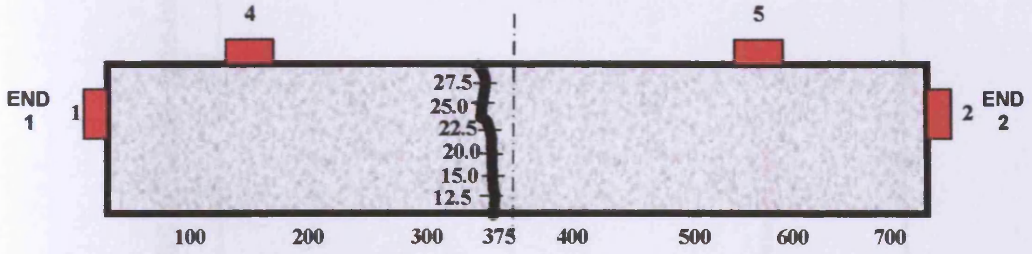

(a) Side view (Loads in kN)

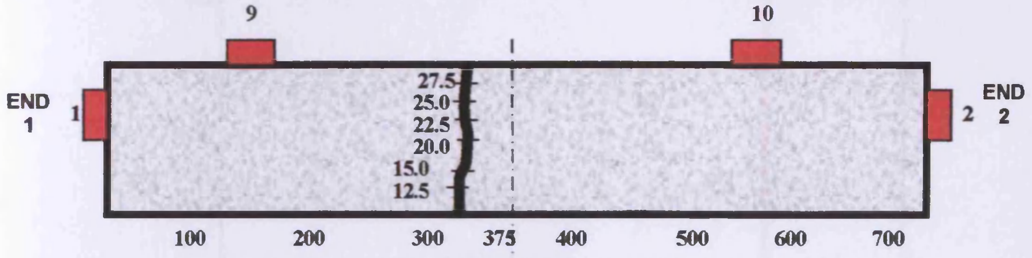

(b) Side view (Loads in kN)

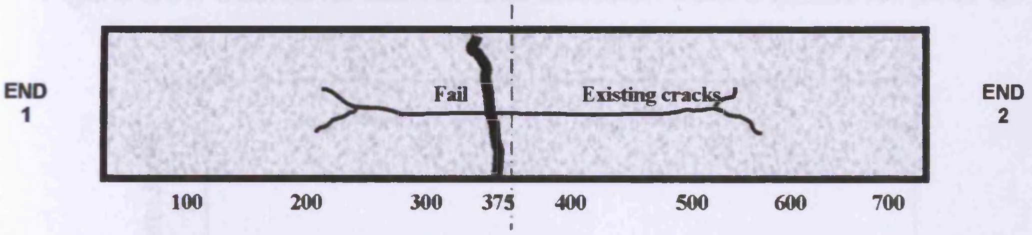

(c) Bottom view (Loads in kN)

Figure C10: Crack pattern from visual observation for B11PS

Note for Beam B11PS:

Exhibit a longitudinal crack at the bottom of the beam prior to load test.

One crack was observed visually throughout the loading test.

Failure in flexure at 28.40kN.

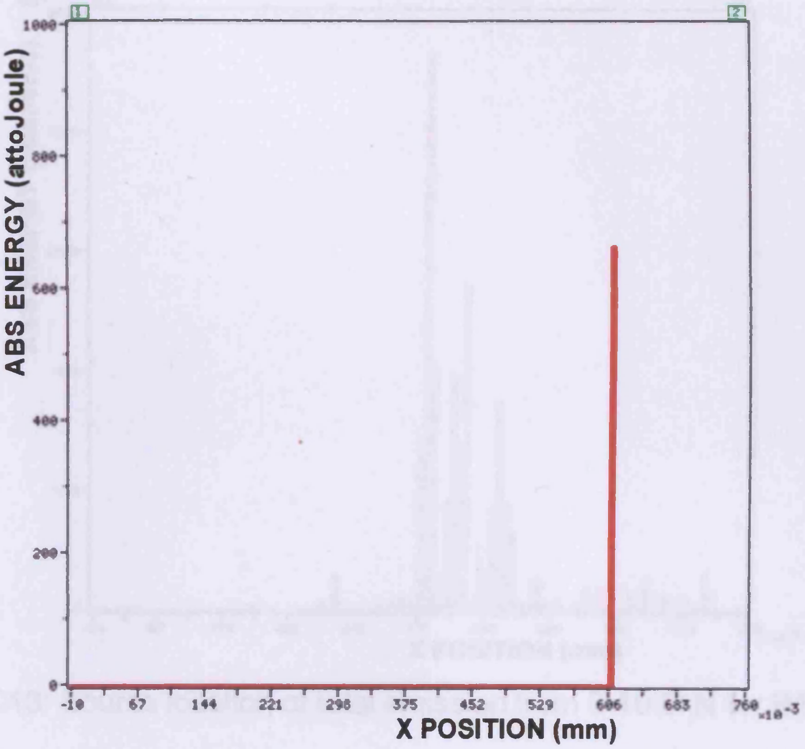

Figure C11: Source location of total emission from 0-2.5kN for B11PS.

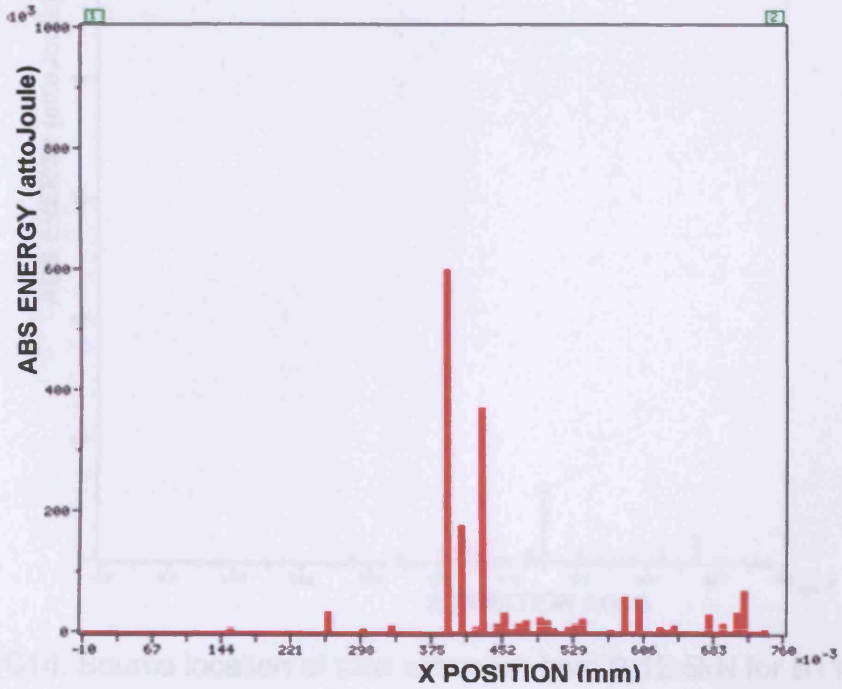

Figure C12: Source location of total emission from 0-5.0kN for B11PS.

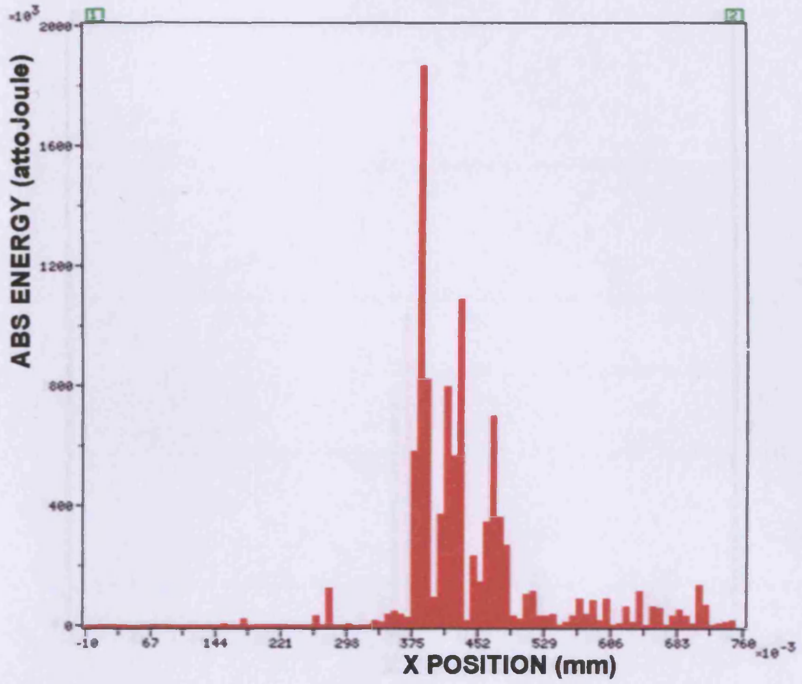

Figure C13: Source location of total emission from 0-10.0kN for B11PS

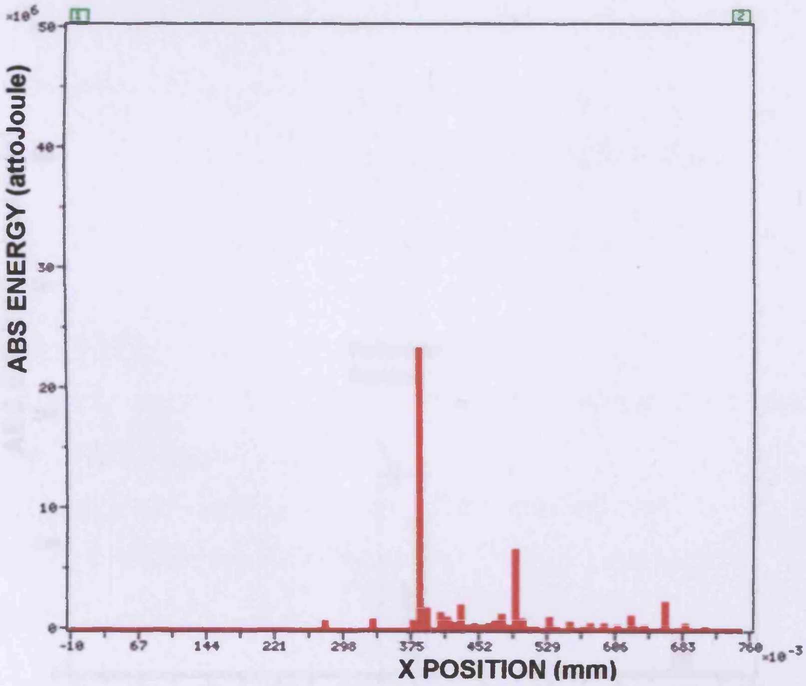

Figure C14: Source location of total emission from 0-12.5kN for B11PS.

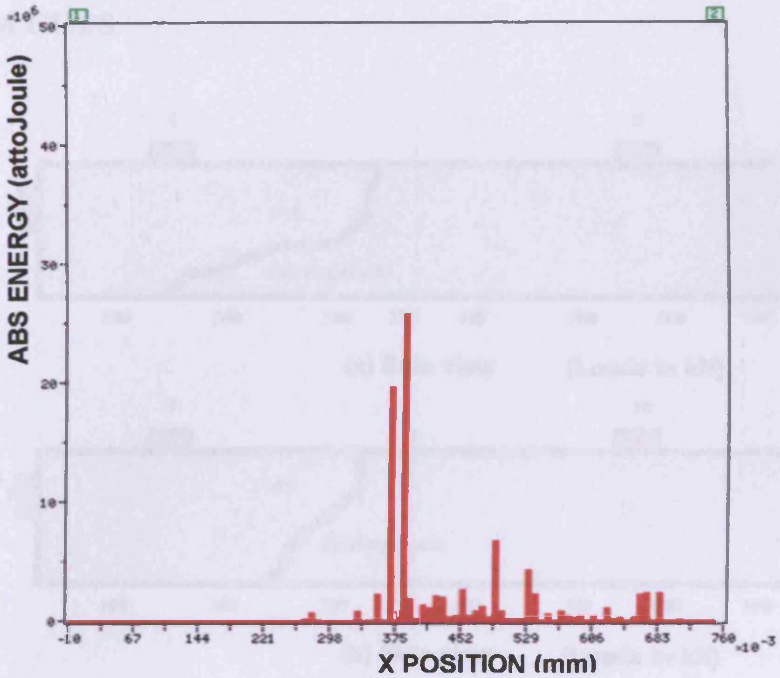

Figure C15: Source location of total emission from 0-25.0kN for B11PS.

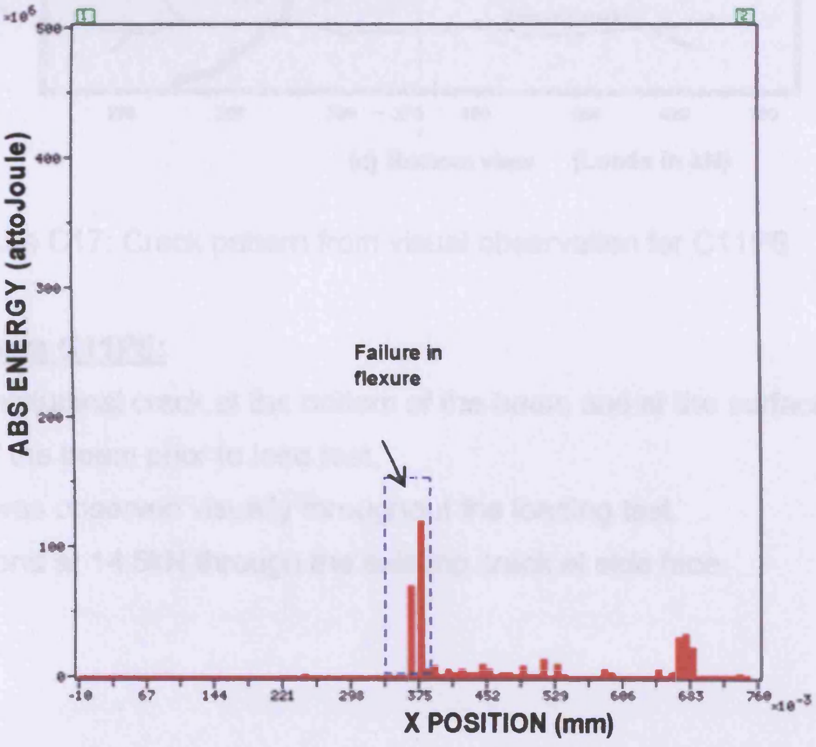

Figure C16: Source location of total emission at failure for B11PS.

3. BEAM C11PS

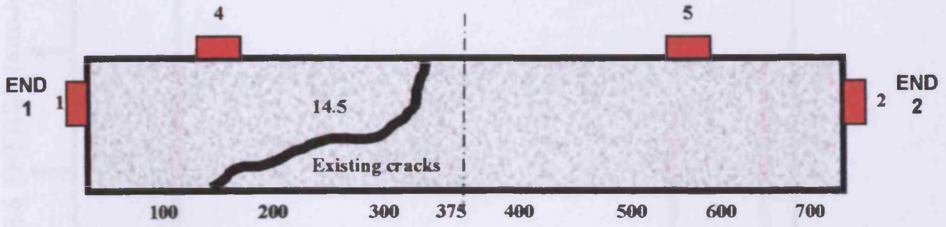

(a) Side view (Loads in kN)

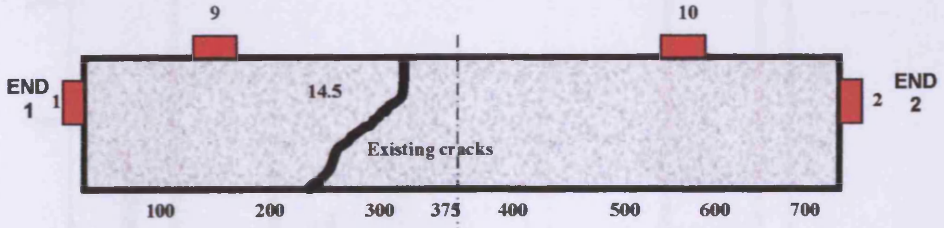

(b) Side view (Loads in kN)

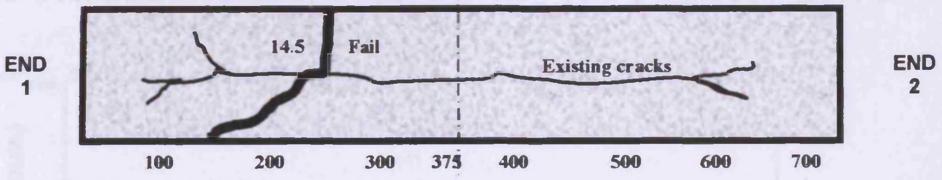

(c) Bottom view (Loads in kN)

Figure C17: Crack pattern from visual observation for C11PS.

<u>Note for Beam C11PS:</u>

Exhibit a longitudinal crack at the bottom of the beam and at the surface on both side of the beam prior to load test.

One crack was observed visually throughout the loading test.

Failure in bond at 14.5kN through the existing crack at side face.

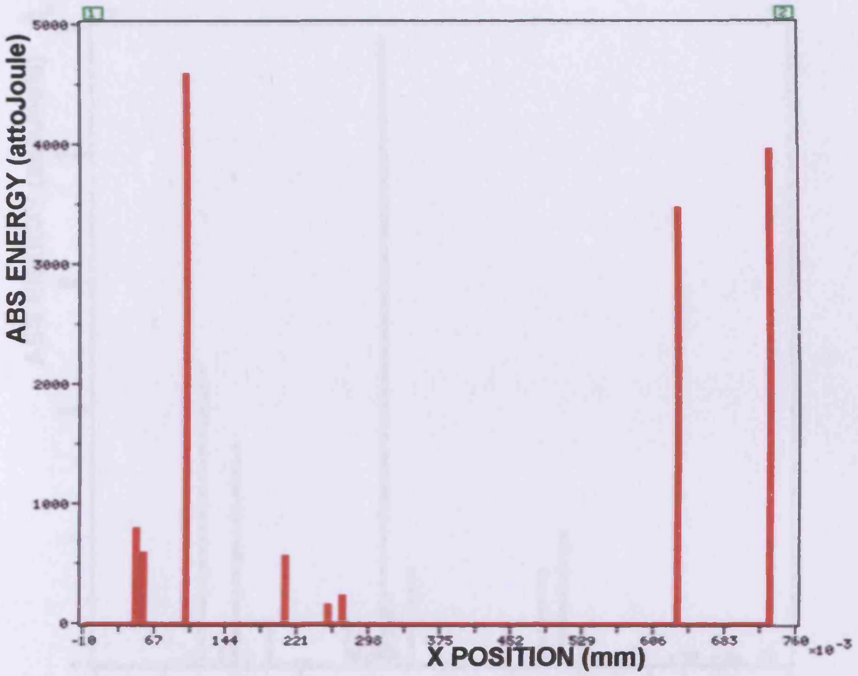

Figure C18: Source location of total emission from 0-2.5kN for C11PS.

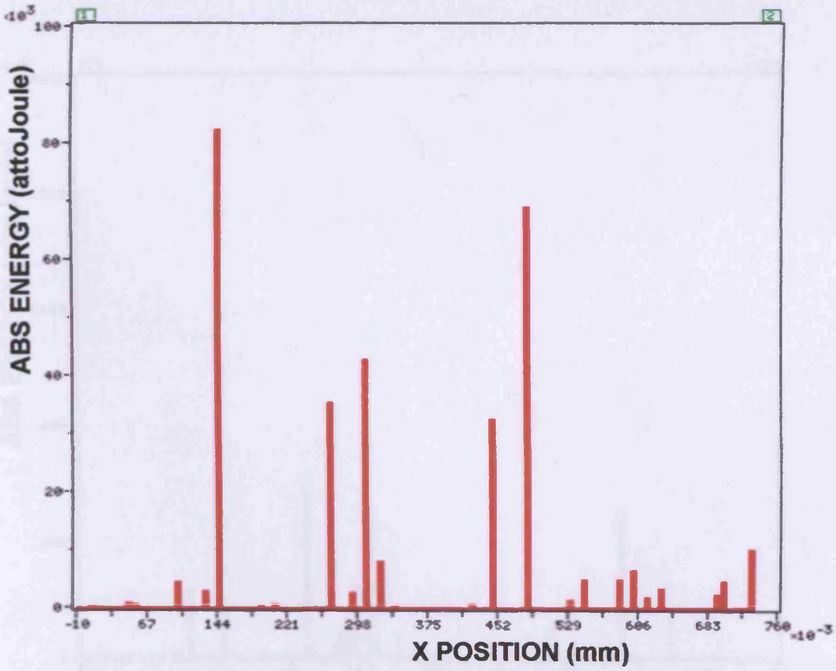

Figure C19: Source location of total emission from 0-5.0kN for C11PS.

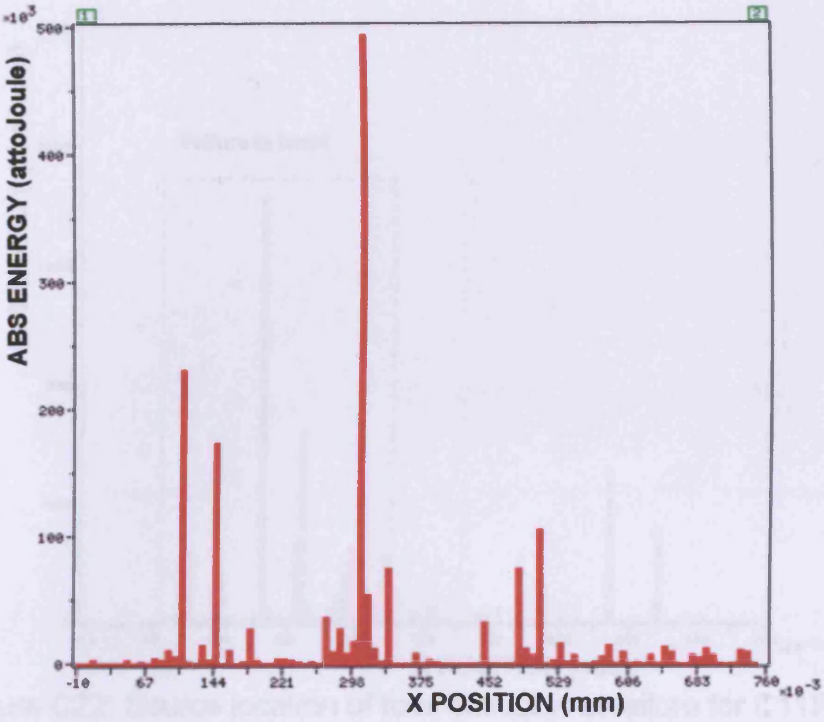

Figure C20: Source location of total emission from 0-10.0kN for C11PS.

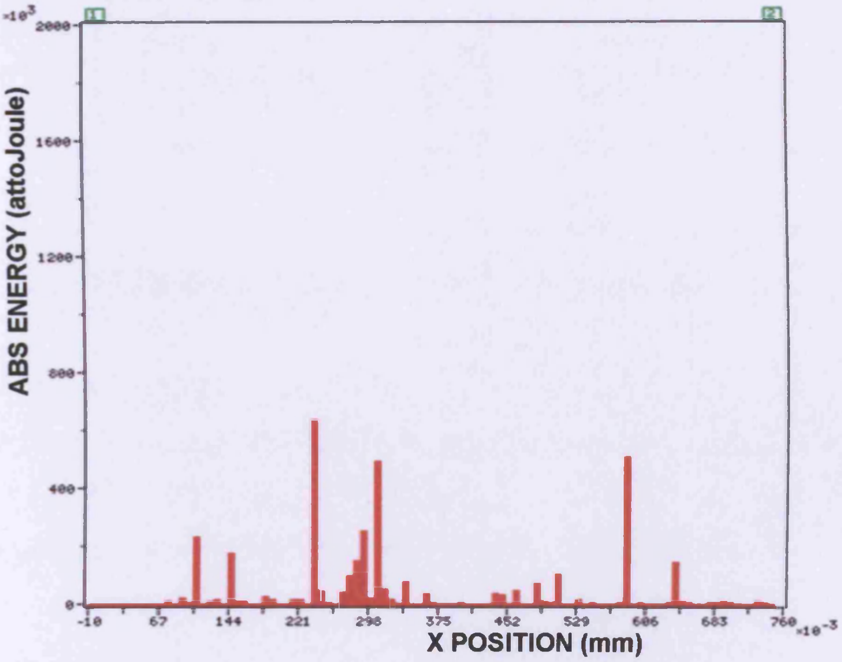

Figure C21: Source location of total emission from 0-12.5kN for C11PS.

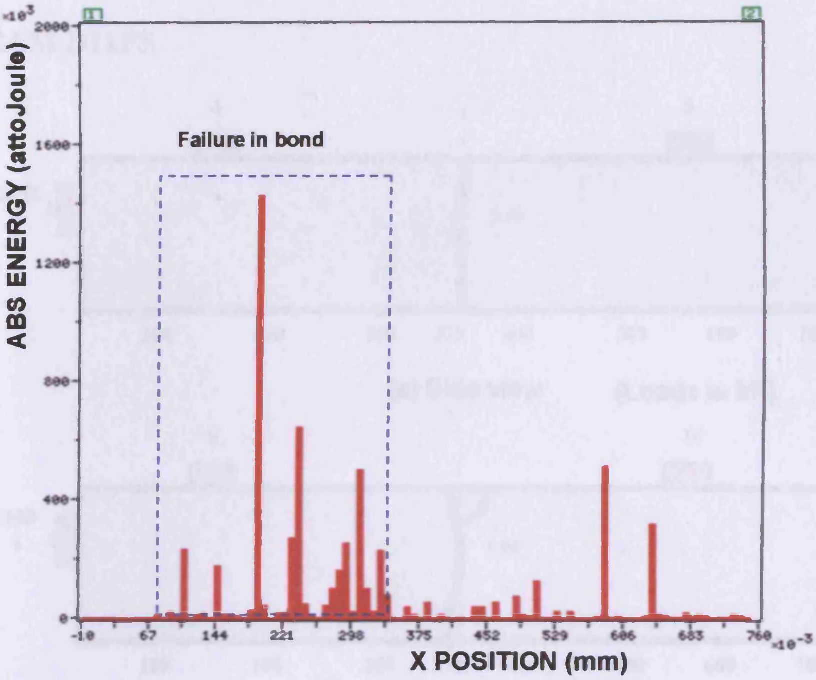

Figure C22: Source location of total emission at failure for C11PS.

4. BEAM D11PS

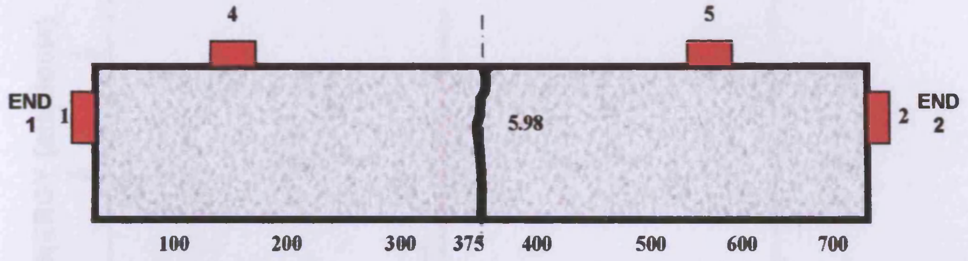

(a) Side view (Loads in kN)

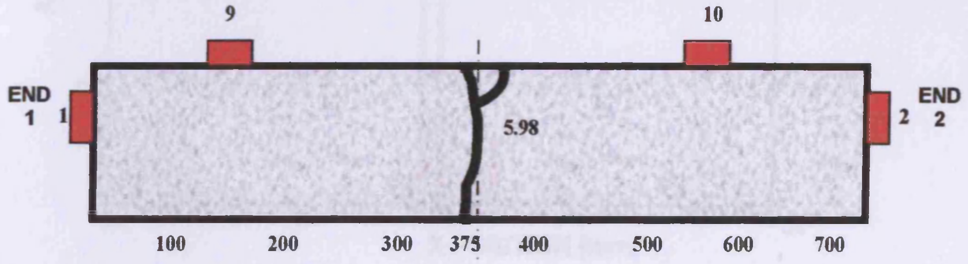

(b) Side view (Loads in kN)

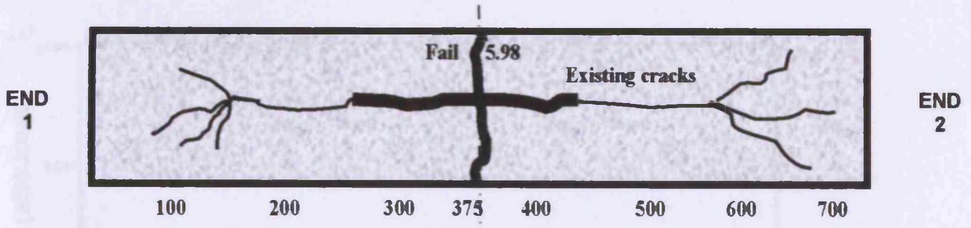

(c) Bottom view (Loads in kN)

Figure C23: Crack pattern from visual observation for D11PS

Note for Beam D11PS:

Exhibit a longitudinal crack (severe) at the bottom of the beam prior to load test.

One crack was observed visually throughout the loading test.

Failure in bond at 5.98kN.

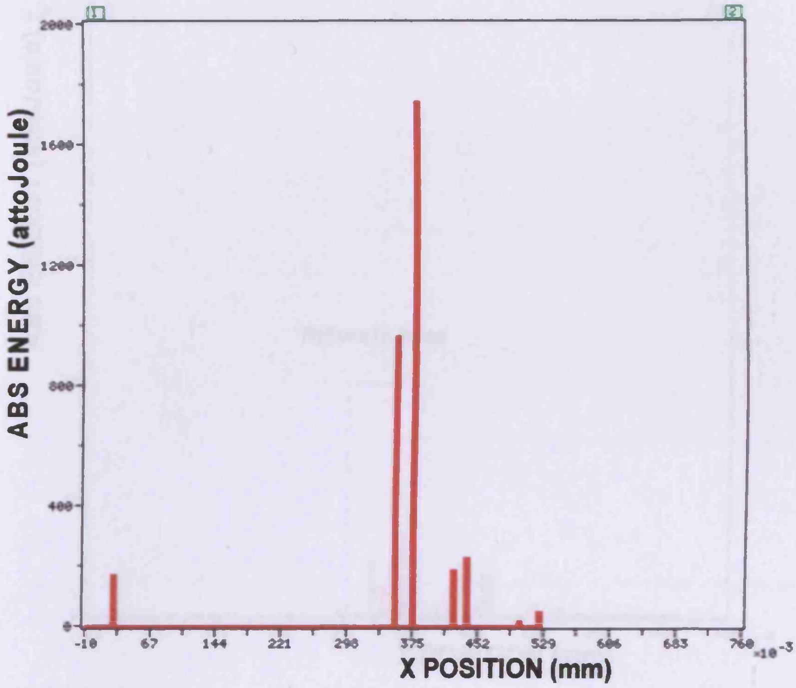

Figure C24: Source location of total emission from 0-2.5kN for D11PS.

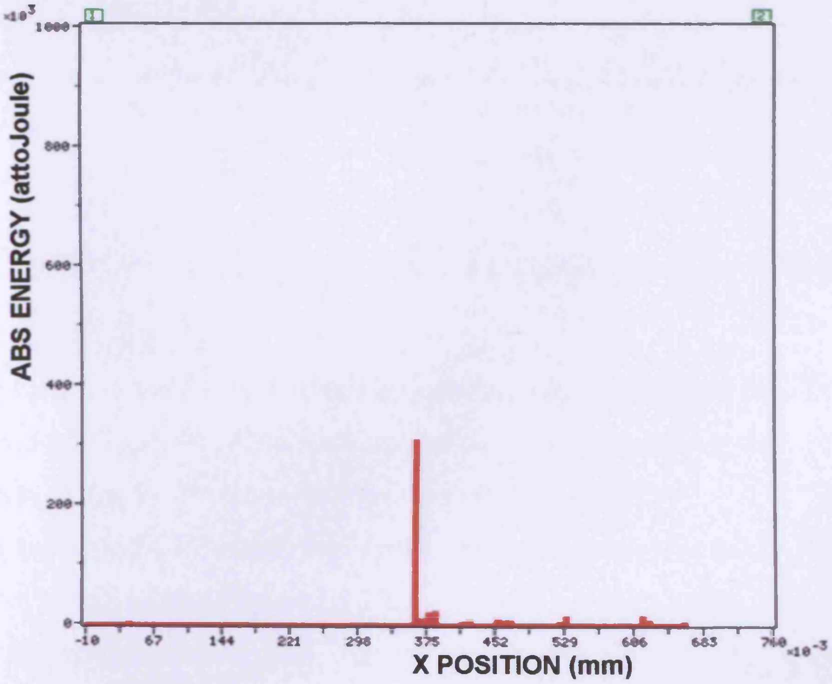

Figure C25: Source location of total emission from 0-5.0kN for D11PS.

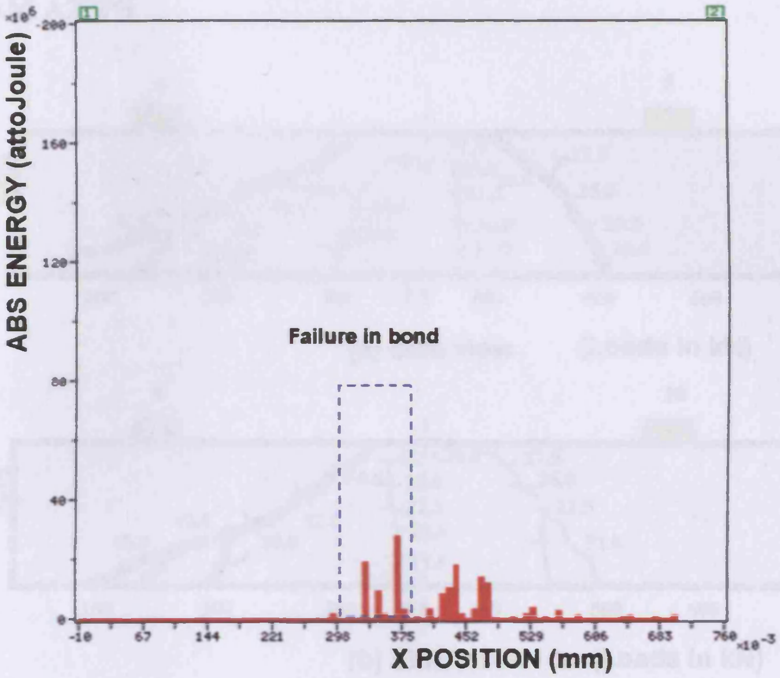

Figure C26: Source location of total emission at failure for D11PS.

5. BEAM A22PS

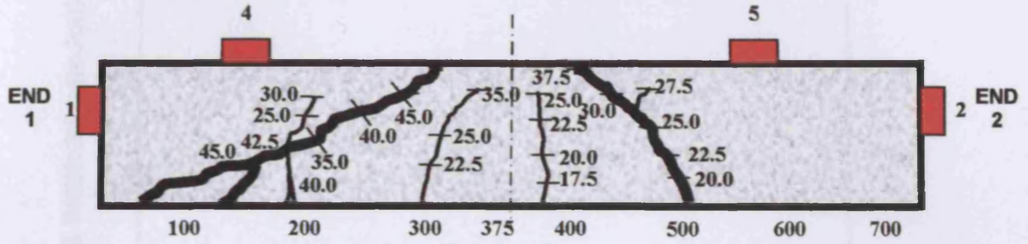

(a) Side view (Loads in kN)

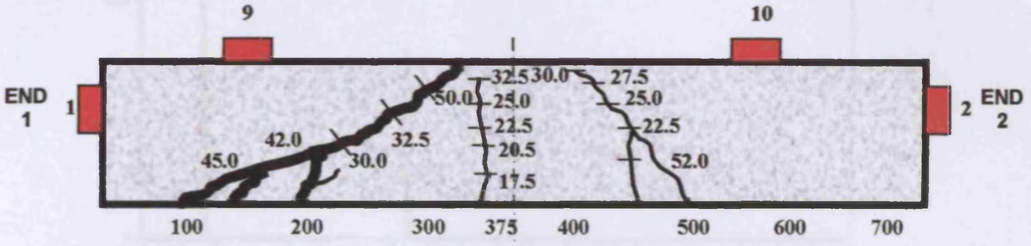

(b) Side view (Loads in kN)

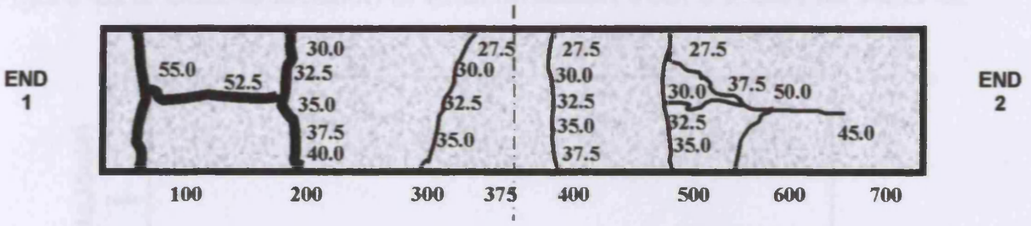

(c) Bottom view (Loads in kN)

Figure C27: Crack pattern from visual observation for A22PS

Note for Beam A22PS:

Zone 1 associated with crack that can be observed visually at 350-390mm.

Zone 2 associated with crack that can be observed visually at 400-550mm.

Zone 3 associated with crack that can be observed visually at 300-350mm

Zone 4 associated with crack that can be observed visually at 480-660mm (at the bottom of the beam, Figure C27 (c)).

Zone 5 associated with crack that can be observed visually at 50-330mm (shear crack)

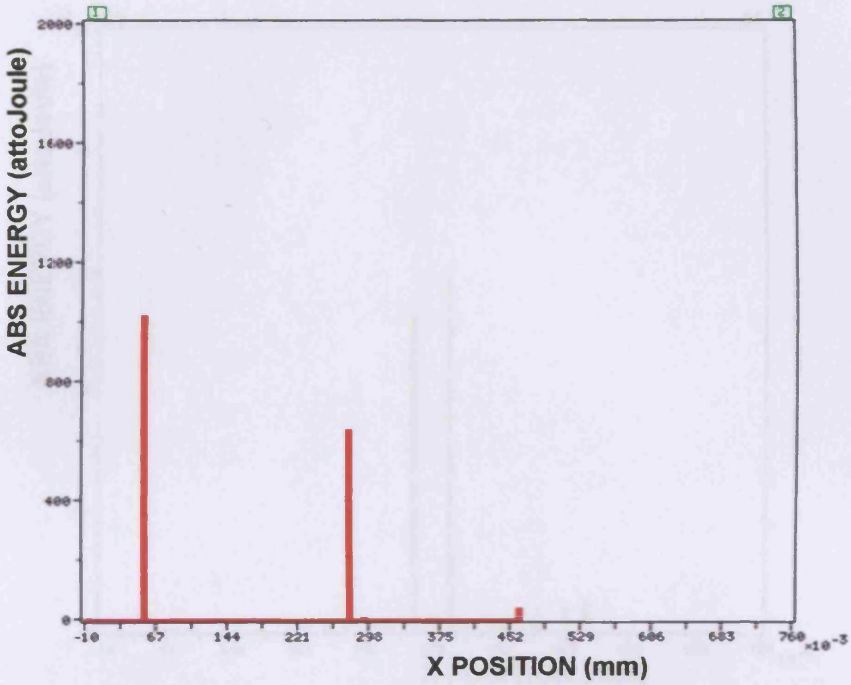

Figure C28: Source location of total emission from 0-2.5kN for A22PS.

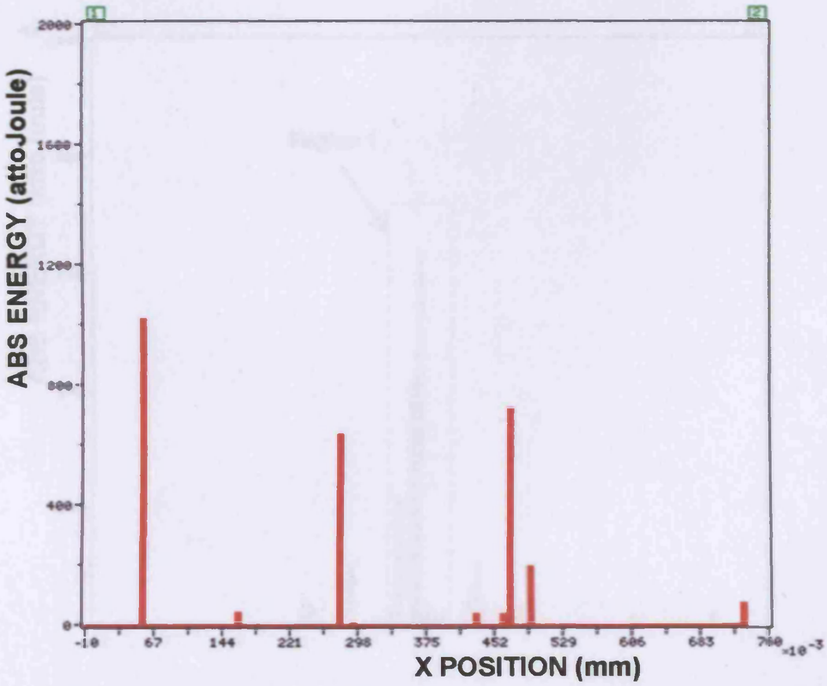

Figure C29: Source location of total emission from 0-5.0kN for A22PS.

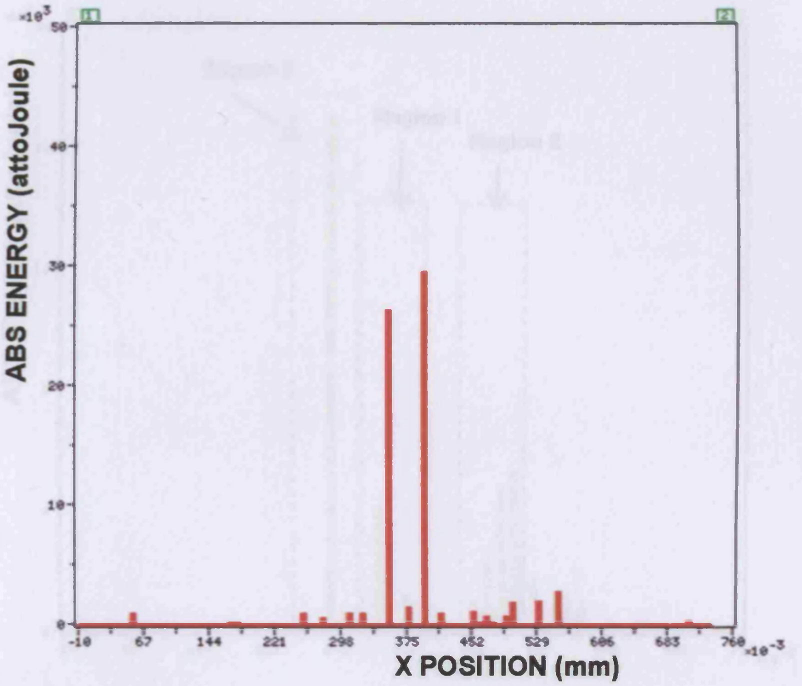

Figure C30: Source location of total emission from 0-10.0kN for A22PS.

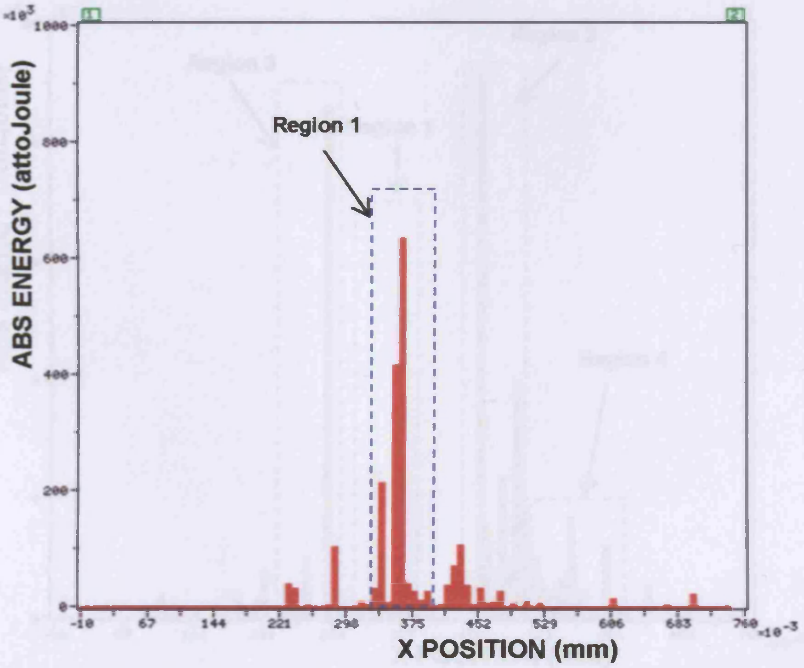

Figure C31: Source location of total emission from 0-12.5kN for A22PS.

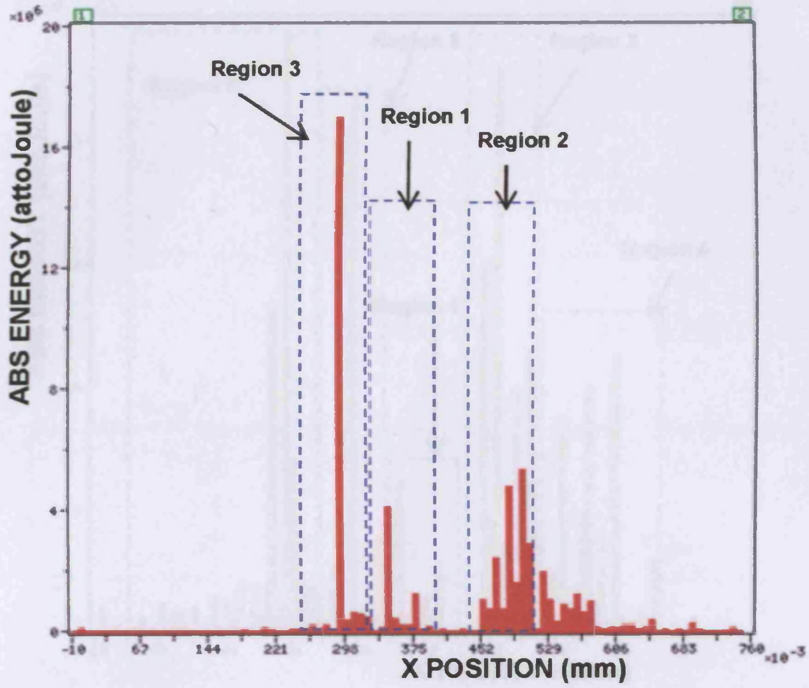

Figure C32: Source location of total emission from 0-25.0kN for A22PS.

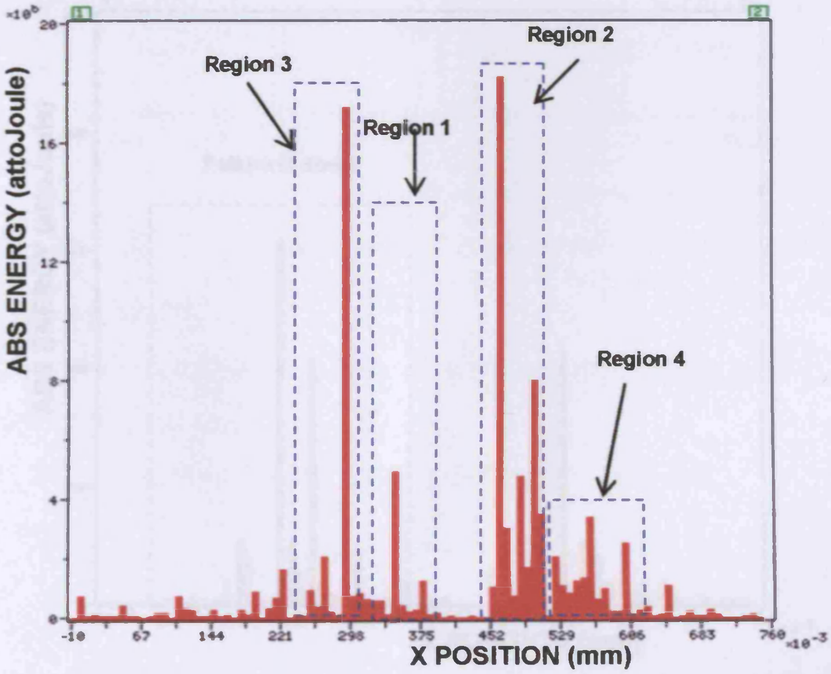

Figure C33: Source location of total emission from 0-30.0kN for A22PS.

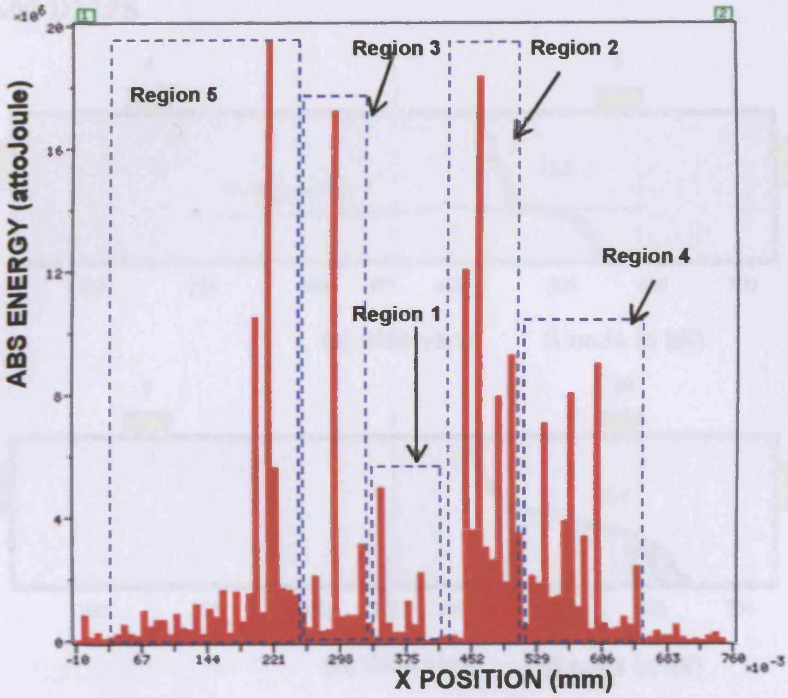

Figure C34: Source location of total emission from 0-40.0kN for A22PS.

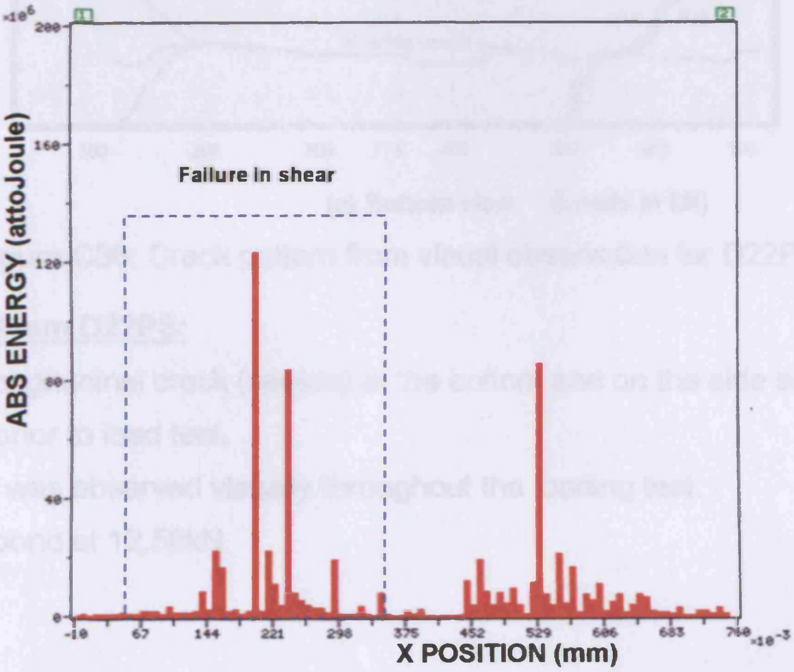

Figure C35: Source location of total emission at failure for A22PS.

6. BEAM D22PS

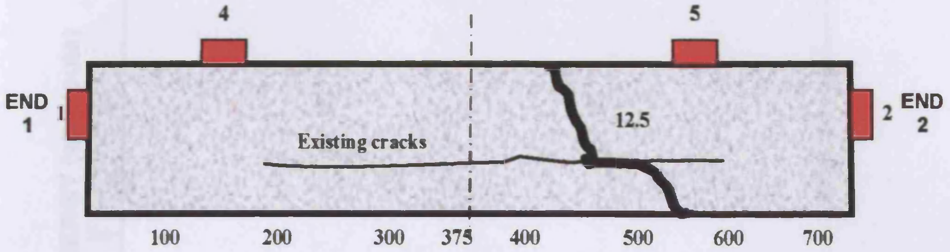

(a) Side view **(Loads in kN)**

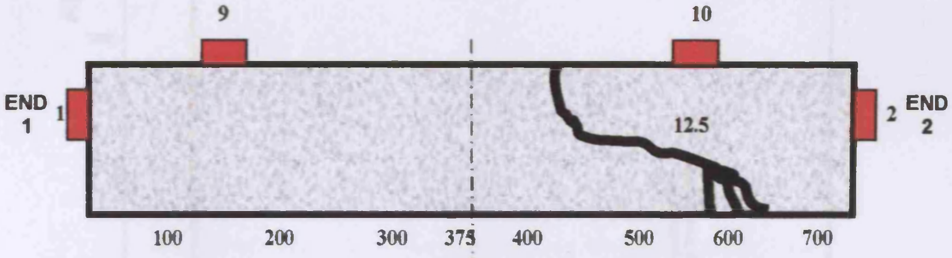

(b) Side view **(Loads in kN)**

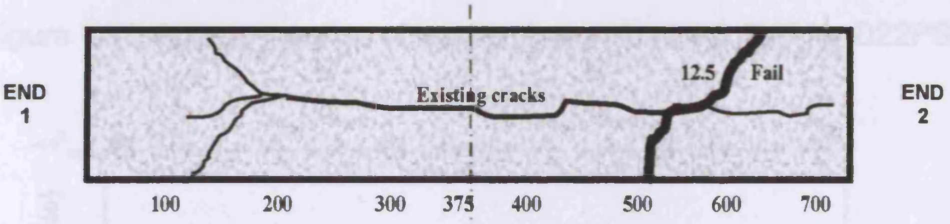

(c) Bottom view **(Loads in kN)**

Figure C36: Crack pattern from visual observation for D22PS

Note for Beam D22PS:

Exhibit a longitudinal crack (severe) at the bottom and on the side surface of the beam prior to load test.

One crack was observed visually throughout the loading test.

Failure in bond at 12.50kN.

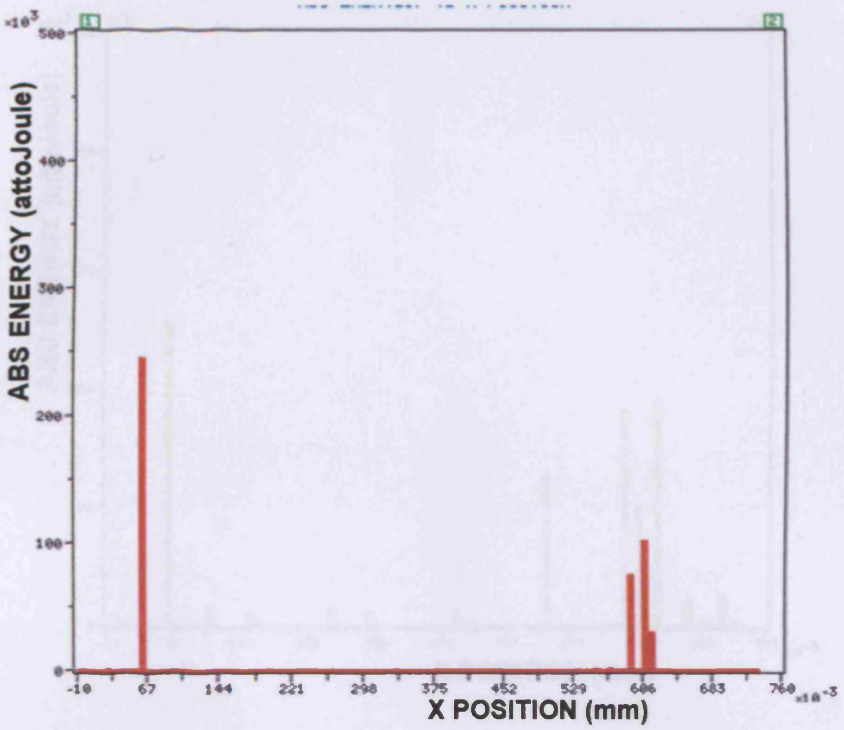

Figure C37: Source location of total emission from 0-2.5kN for D22PS.

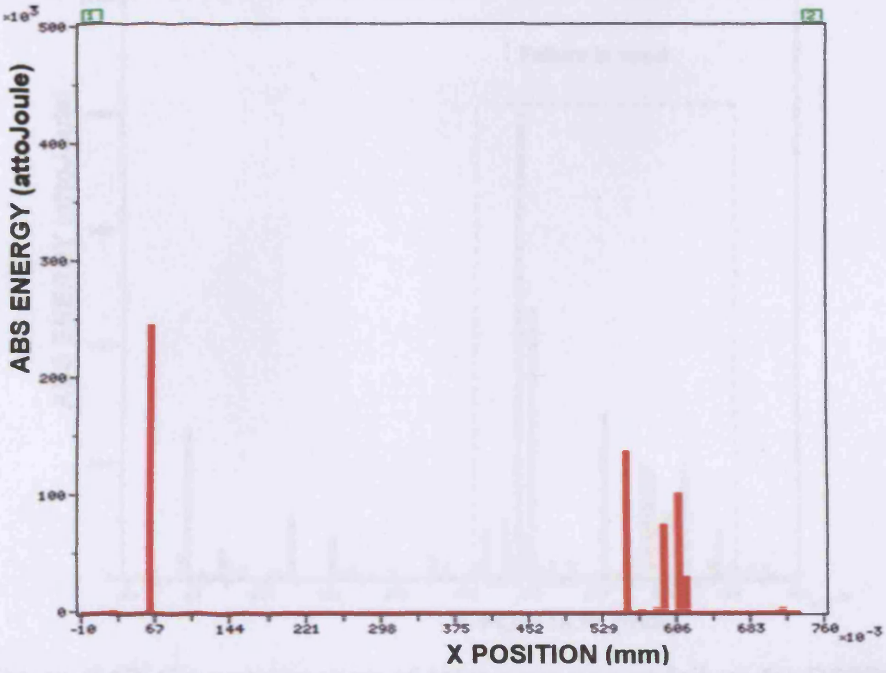

Figure C38: Source location of total emission from 0-5.0kN for D22PS.

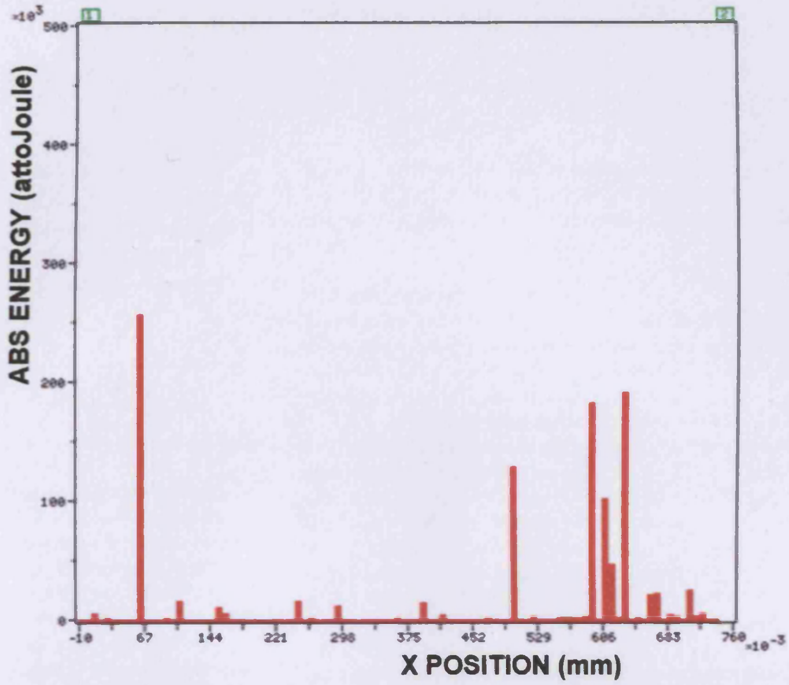

Figure C39: Source location of total emission from 0-10.0kN for D22PS.

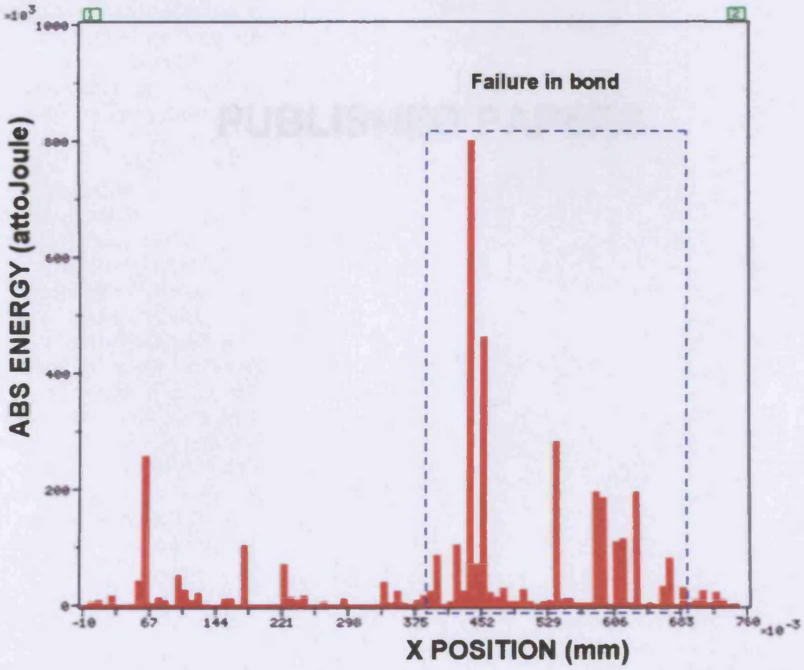

Figure C40: Source location of total emission at failure for D22PS.

APPENDIX D

PUBLISHED PAPERS

Acoustic emission monitoring of concrete structures suffering from reinforcement corrosion

This article describes an experimental programme to investigate the behaviour of reinforced concrete structures subject to deterioration as a consequence of reinforcement corrosion using acoustic emission monitoring.

Norazura Muhamad Bunnori, **Karen Holford** and **Robert Lark**, Cardiff School of Engineering, Cardiff University

Two types of test specimen were used; pre-corroded (PR) specimens in which the cross-sectional area of the reinforcement was reduced but, as they were cleaned before being cast into the concrete, the integrity of the concrete itself and the bond between the steel and the concrete were unaffected by the corrosion; and post-corroded (PS) specimens in which the corrosion products were developed within the specimen. All specimens were tested in four-point bending, monitored using an acoustic emission (AE) sensor system.

The approach used to evaluate the relative AE activity was based on the measurement of parameters such as hits, amplitudes and absolute energy. This method of analysis has been shown to be sensitive to the initiation and growth of cracks within both homogeneous and composite materials and structures(1,2). Also, the application of a linear location, time of arrival method was used to determine the location of the damage in an area between an array of sensors, as well as to monitor the progression of the resultant cracking.

Materials and specimen preparation

In this programme the specimens were cast using a concrete with a target strength of 40MPa using a water/cement ratio of 0.56 and with material proportions of 1:2:2.5 by weight of cement, sand and aggregate. The specimens were 100 × 150 × 750mm with a single, high-yield 12mm-diameter reinforcing bar placed centrally approximately 50mm above the soffit of the beam (i.e. a cover of 44mm). For the pre-corroded specimen, lengths of the 12mm-diameter reinforcement were corroded to three levels of damage using an anodic current before the concrete was cast. In the post-corroded specimen, a middle section of the reinforced concrete beams was encased in an acrylic tank and immersed in a 5% NaCl solution as shown in Figure 1.

The post-corroded specimen exhibited longitudinal cracking on the bottom face of the beams along the line of the reinforcement due to the formation of the extensive corrosion products that were developed inside the concrete.

Acoustic emission technique

Acoustic emission testing is based on the fact that solid materials emit sound when they are mechanically or thermally stressed to the point where deformation or fracture occurs.

Location can be defined as the determination of the spatial position of an acoustic emission source from arrival time measurements using an array of sensors(3). In this case, a linear location technique was used, since the position of the source was known to be somewhere between a pair of transducers attached to the beam. Using a time of arrival approach, a difference in the measured arrival times of the emissions from a source at any two transducers uniquely determines the location of this source. The accuracy of the source location depends on the wave velocity calculation, time difference measurements and good sensor positions(1). In this case the acoustic emission source is the cracking and degradation of the concrete resulting from the application of the load but influenced by the level of corrosion that is present. The sensors for measuring the acoustic emission were attached to the concrete using magnetic

● **Acknowledgement:**
This article is a shortened version of a paper that was originally presented at the 2006 *Concrete Communication* Conference, a joint event held by The Concrete Centre, British Cement Association and The Concrete Society at University College London (UCL).

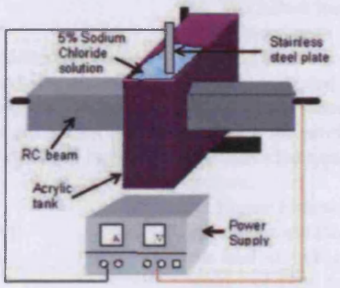

Figure 1: Set-up for the corrosion of the post-corroded specimens.

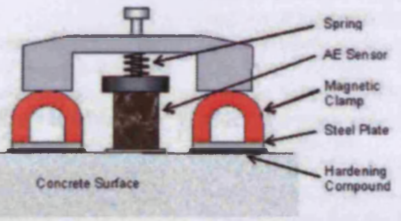

Figure 2: Sensor fixing.

Table 1: Failure loads of pre-corroded specimens.

Specimen (pre-corroded)	Load at point (kN)				
	A	B	C	D	Failure
A11PR (control)	15.0	17.5	45.0	55.0	59.21
B11PR (low corrosion)	15.0	25.0	–	42.5	54.77
C11PR (medium corrosion)	15.0	20.0	–	25.0	34.81
A22PR (control)	15.0	20.0	45.0	55.0	59.54
B22PR (low corrosion)	15.0	20.0	40.0	45.0	47.50
C22PR (medium corrosion)	15.0	20.0	–	25.0	35.08
D22PR (high corrosion)	15.0	20.0	–	20.0	23.46

Figure 3: Load–displacement curve for specimen A22PR.

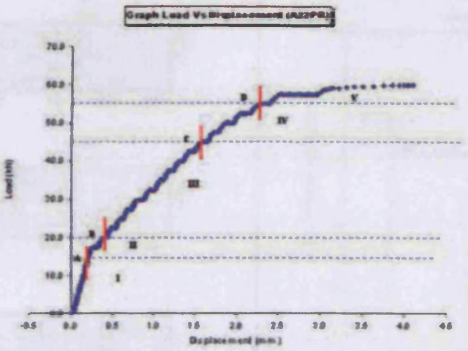

Figure 4: Load–displacement curve for specimen A22PS.

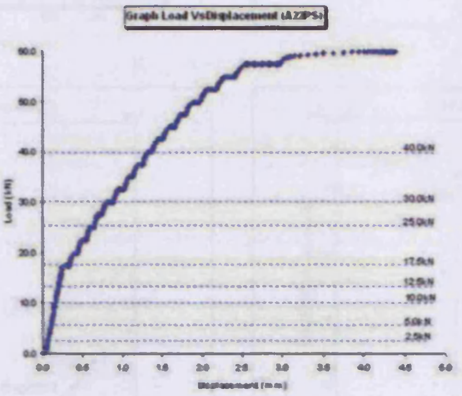

Figures 5a and b above: Beam failed in shear mode and flexural mode.

clamps that hold the sensors against steel plates glued to the surface of the specimen (see Figure 2).

Results and discussion

The behaviour of concrete subjected to different loading conditions is governed by the initiation and propagation of the internal cracks and flaws during loading. Figure 3 shows the load–displacement curve for beam A22PR (pre-corroded) and this can be split into five different regions where there is:

- micro-cracking
- localised crack propagation (point A)
- distributed flexural cracks (point B)
- shear cracking (point C)
- damage localisation (point D).

The load carried by each of the pre-corroded specimens at the above points is given in Table 1. From this it can be seen that although the uncorroded specimens developed flexural cracking in the centre of the beam where the bending moment was a maximum, the ultimate failure mode was one of shear. The specimens in which the steel had been corroded failed in flexure.

Table 2: Failure loads and mode of failure of post-corroded specimens.

Specimen (post-corroded)	Failure load (kN)	Failure mode
A11PS (0%)	54.78	Shear
B11PS (9.60%)	28.40	Flexure
C11PS (17.00%)	14.53	Bond
D11PS (33.45%)	5.98	Bond
A22PS (0%)	60.0	Shear
B22PS (8.90%)	45.92	Flexure
C22PS (14.69%)	18.84	Bond
D22PS (31.30%)	12.50	Bond

Note: The percentage corresponds to the level of the corrosion measured by weight loss of the reinforcement.

The failure loads and mode of failure for the post-corroded specimens are given in Table 2 and a typical load–displacement curve is shown in Figure 4. In this case the heavily corroded specimen exhibited much less flexural cracking and failed in a brittle manner due to a loss of bond between the reinforcing bar and the concrete. Figure 5 illustrates the typical specimen failure modes in shear and flexure.

Figure 6 shows the crack pattern of one of the control specimens and this can be compared with a location plot of the total AE in Figure 7, expressed in terms of the absolute energy of these emissions, obtained throughout the duration of this test. From this it can be seen that the two regions of high emissions are consistent with the location of the primary shear cracks that lead to the failure of this specimen. However, lower energy emissions are also found at the centre of the beam at an earlier stage in the test and these are typical of the flexural cracking which is found in phase III.

A similar AE plot for one of the pre-corroded specimens that failed in flexure is given in Figure 8. In this case, it can be seen that the flexural cracking in Region 1 dominates the output, although it should be noted that the energy of these emissions is generally less than that of the shear cracks. Regions 2, 3 and 4 also correspond to the location of flexural cracks that were observed visually. Generally, AE identified the onset of flexural cracking at a load of approximately 10kN, whereas visually these cracks were not observed until the load reached 15kN.

Figures 9 and 10 present similar data for one of the post-corroded specimens, which failed due to a loss of bond. In this case the flexural cracking was much more localised because of the loss of bond and is characterised by the emissions in Regions 1 and 2, which correspond to the two cracks above and below the existing crack in the bottom view of the beam. It is also noticeable that in this

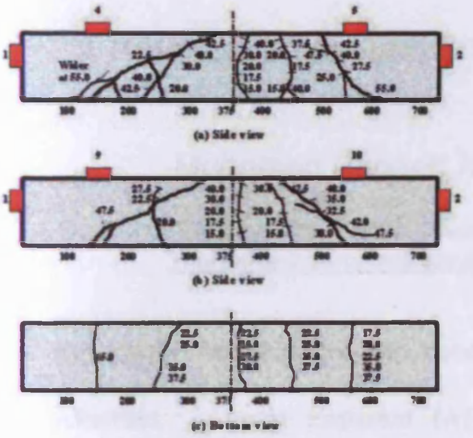

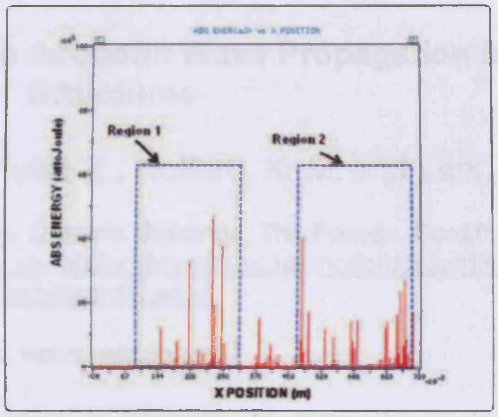

Figure 6 far left: Crack patterns obtained by visual observation of A22PR.

Figure 7 left: Source location of total emission during damage localisation (0–55.0kN) for A22PR.

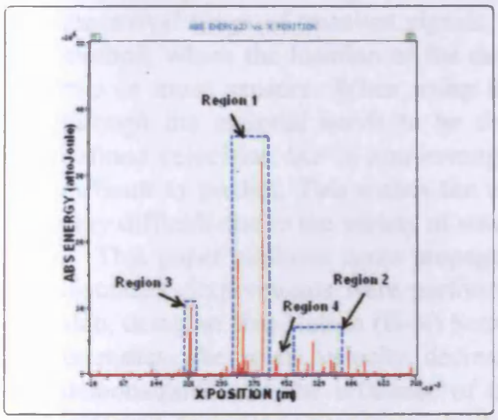

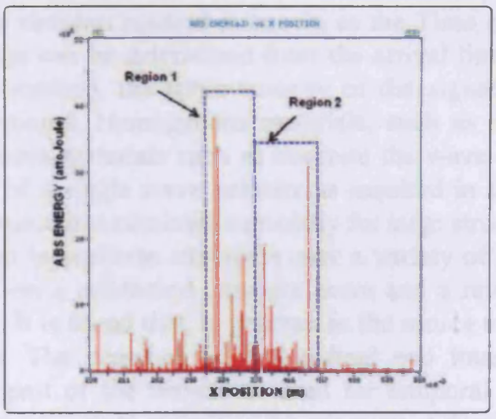

Figure 8 far left: Source location of total emission during damage localisation (0–25.0kN) for C22PR.

Figure 9 left: Source location of total emission from 0kN to 25.0kN for B22PS.

case there are many more low-energy emissions distributed throughout the length of the beam. It is believed that these emissions are due to the breakdown in the bond between the steel and the concrete, and rubbing of the faces of the existing longitudinal crack, both of which are a consequence of the corrosion process.

Concluding remarks

It has been shown that AE can be used to monitor the development of cracking in a simple reinforced concrete section subject to flexure. Flexural cracking can be identified and located prior to it being visible and its development under an increasing load can be tracked. Internal damage due to corrosion of the reinforcement within the concrete is characterised by much lower energy emissions that are distributed throughout the length of the beam, although it is not yet clear whether these emissions are a consequence of the loss of bond or due to rubbing of the faces of cracks initiated by the expansion of the corrosion products. The energy of the emissions generated during the shear failure of the uncorroded specimens was greater than that obtained from those that failed in flexure, although the only evidence of this prior to failure was the increased activity in the regions where shear failure might be anticipated.

Based on the above evidence it can be concluded that AE can be used to identify damage and/or deterioration of reinforced concrete structures due to both load effects and corrosion, but that further work is required to explicitly characterise the different emissions that are obtained. ■

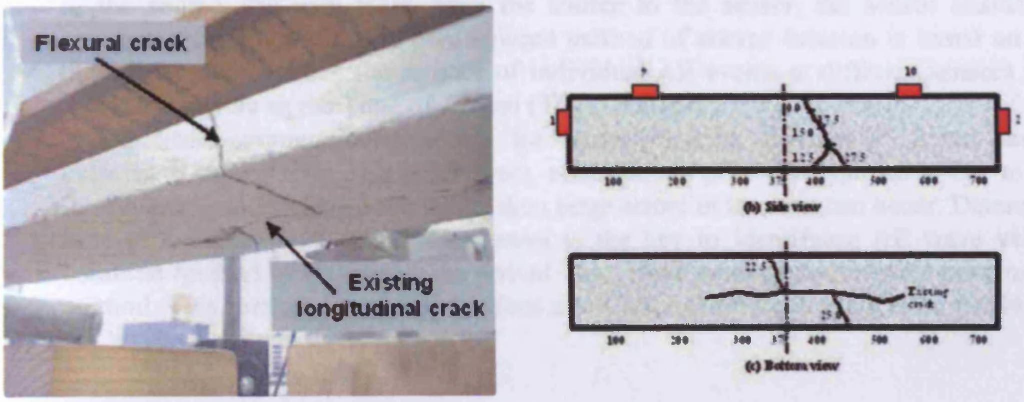

Figures 10a and b: Crack patterns by visual observation at 25.0kN for B22PS.

References:

1. BECK, P. *Quantitative damage assessment of concrete structures using acoustic emission.* Cardiff School of Engineering, University of Wales, Cardiff, UK. 2004.
2. OH, B. and KIM, K. Micro-damage characterisation of concrete structures based on acoustic emission. *In Proceedings of the 2005 International congress Global construction: Ultimate concrete opportunities,* University of Dundee, Scotland. pp.13–28.
3. MILLER, R. and McINTIRE, P. *Nondestructive testing handbook: Acoustic emission testing.* Vol.5, Second Edition, American Society for Nondestructive Testing, p.136. 1987.

Advanced Materials Research Vols. 13-14 (2006) pp. 205-211
online at http://www.scientific.net

A Practical Investigation into Acoustic Wave Propagation in Concrete Structures

Muhamad Bunnori N., Pullin R., Holford, K. M. and Lark, R. J.

School of Engineering, Cardiff University, Queen's Buildings, The Parade, Cardiff, CF24 3AA, UK,
muhamadbunnorin@cardiff.ac.uk, pullinr@cardiff.ac.uk, holford@cardiff.ac.uk
lark@cardiff.ac.uk

Keywords: Acoustic Emission, concrete, wave velocity

Abstract. Acoustic Emission (AE) testing in concrete structures shows great potential for monitoring and assessing the health condition of structures. Source location is normally based on the arrival times of transient signals, the simplest method is known as the Time of Arrival (TOA) method, where the location of the damage can be determined from the arrival time of the event at two or more sensors. When using this method, the wave velocity of the signals that propagate through the material needs to be determined. Homogenous materials, such as steel, have well-defined velocities, but in non-homogeneous materials such as concrete the wave velocity is more difficult to predict. This makes the use of a single wave velocity as required in the TOA method very difficult due to the variety of wave velocities obtained, especially for large structures.

This paper explores wave propagation in concrete structures over a variety of source to sensor distances. Experiments were performed on a reinforced concrete beam and a reinforced concrete slab, using an Hsu-Nelsen (H-N) Source. It is found that, in general, as the source to sensor distance increases, the wave velocity decreases. The presence of longitudinal and transverse waves is demonstrated and the influence of the part of the waveform used for temporal measurement is explored. In order to provide a practical approach to velocity determination, different thresholds are investigated and the results are discussed in relation to the wave modes present.

Introduction

Acoustic Emission (AE) has emerged as a potential non-destructive tool and AE sensors are used to detect stress waves propagating in structures for inspection and monitoring purposes.

There are several approaches to analysing AE data, either by using a parameter-based approach or by analysing the collected waveform. Most use a parameter-based approach and little attention has been paid to the collected waveform. Yet the waveform collected can often contain information on source location especially in analysing the different modes of wave which travel at different velocities.

According to Miller and McIntire (1987), the waveform signal is affected by; the characteristics of the source, the path taken from the source to the sensor, the sensor characteristics and the measuring system itself. The predominant method of source location is based on measurement of time difference between the arrivals of individual AE events at different sensors in an array. This method is known as the Time of Arrival (TOA) method.

The basic computational process for source location assumes a known and constant wave velocity. If the velocity used is incorrect, either due to poor assumptions or due to the triggering of the system by a different wave mode, then large errors in location can occur. Determining the arrival time of a feature in a propagating wave is the key to identifying AE wave velocity. The most common method of estimating the arrival time, used in many commercial systems is the threshold method. This method is used by Holford and Carter (1999) and Ding et al. (2004) to calculate the AE wave velocity in a structure.

There are two major wave modes of stress wave propagation: the bulk wave (longitudinal stress wave (L-wave or P-wave) and shear wave (S-wave)), that travels within the solid and also a surface wave, known as the Rayleigh wave (R-wave) which travels along the surface of the solid. In AE, the arrival time of the P-wave is, among other parameters, of prime importance for indicating the location of the AE event source.

The fundamental difference between AE and Ultrasonics is that AE is generated by the material itself, while in ultrasonics the acoustic wave is generated by an external source and introduced into the material (Beattie, 1983). In recent years, there has been adequate research regarding wave velocities in ultrasonic studies on concrete but less material relating to AE. In Ultrasonic studies, depending on various characteristics, commonly used non-destructive testing methods to measure the wave velocities may include the ultrasonic pulse-velocity method (Wu et al., 2000, Philippidis and Anggelis, 2005), the impact-echo method (Gassman and Tawheed, 2004, Kim et al., 2006) and a spectral analysis of surface wave method (SASW)(Cho, 2003, Kim et al., 2006). Most of these methods use a transmitter and receiver transducer. A number of researchers have reported the relationship between wave velocities and the age of the concrete (Gassman and Tawheed, 2004, Chang et. al., 2006), water to cement ratio (Philippidis and Anggelis , 2005), aggregate to cement content (Philippidis and Anggelis, 2005), concrete strength (Wu et. al., 2000, Cho, 2003), pulse frequency (Philippidis and Anggelis, 2005) and concrete cover thickness and steel bar spacing (Wu et. al, 2000, Kim et. al., 2006). However no previous study in AE has investigated the relationship between wave velocities with sensor distances from the source. Moreover, the chosen pre-set threshold level will also influence the measured wave velocity.

Experimental Procedure

This investigation used a cast in-situ reinforced concrete (RC) beam and an actual RC slab. The water to cement ratio for the RC beam used was 0.56 and the material proportions were 1:1.5:3.1:0.47 by weight of cement, sand, aggregate and water respectively giving a concrete design strength of 40MPa (the actual 28 days compressive strength was 48MPa). The dimension of the RC beam was (100 x 150 x 2000) mm and the RC slab was 2750mm wide by approximately 1000mm thick. Fig. 1 shows the reinforced concrete beam test specimen and Fig. 2 shows the reinforced concrete slab test specimen.

For both concrete samples (RC beam and RC slab), seven resonant frequency sensors (Physical Acoustic R6D) at a spacing of 250mm were attached to the specimen. Seven pairs of steel plates were attached to the specimen surface using a plastic padding and the sensors were held in position using a magnetic clamp; silicon grease was applied as an acoustic couplant. Experiments were performed using a H-N Source, and the source was repeated ten times and recorded simultaneously at all sensors using a Physical Acoustic's DiSP system.

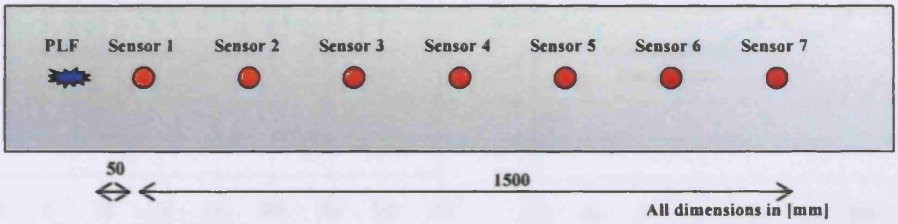

Fig. 1. Reinforced concrete beam test specimen

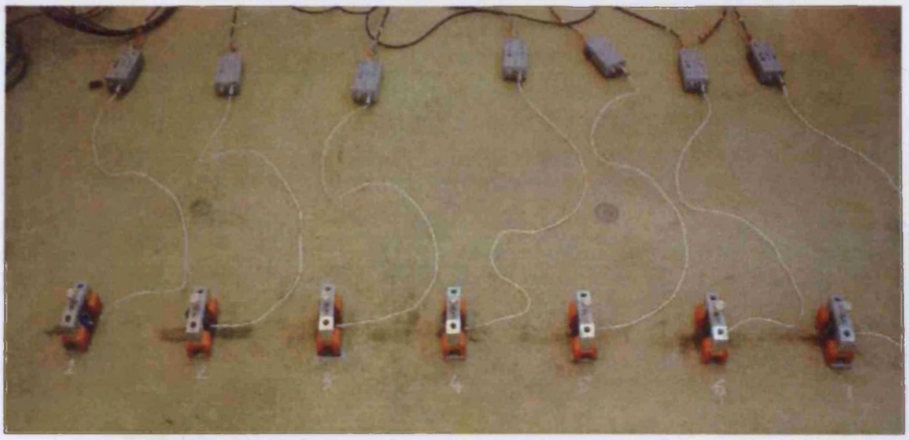

Fig. 2. Reinforced concrete slab test specimen

AE signals were "corrected" in order to ensure that, for a particular threshold, the same temporal position in each waveform was used for velocity calculations. The correction procedure involved normalizing each signal up to a peak value of 10 Volts, i.e., regardless of the amplitude attenuation due to the distance or path traveled by the wave, each signal is corrected to a 10 Volt peak.

Velocity is determined at each position using a synchronous trigger at sensor 1 and by identifying the time of arrival at subsequent sensors.

Results and Discussion

Fig. 3 shows a signal from a single source as recorded at sensor 1 and sensor 3. At further sensor to source distances, the arrival of various wave modes can be more clearly seen, specifically a relatively low amplitude and relatively high amplitude which are known as the longitudinal wave (P-wave) and all other waves (transverse (shear), Rayleigh, etc.) respectively. Fig. 4 shows the different pre-set threshold level of 40dB (0.01V), 50dB (0.0316V) and 60dB (0.1V) at sensor 3 for raw and corrected signals. All the calculated wave velocities are based on this pre-set threshold level. This paper aims to investigate the P-wave velocity of concrete specimen at different pre-set threshold levels and the impact of source to sensor distance on the calculated wave velocity.

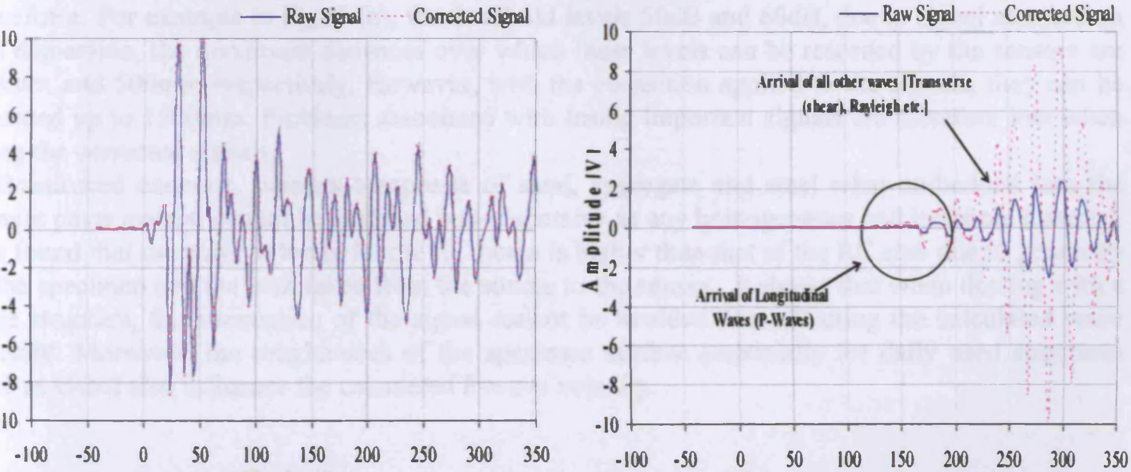

(a) Sensor 1

(b) Sensor 3

Fig. 3. Results of PLF for raw and corrected signal at (a) sensor 1 and (b) sensor 3

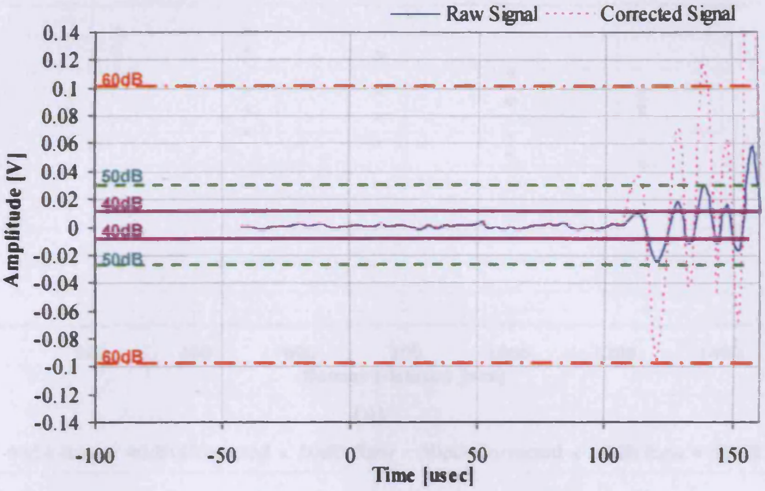

Fig. 4. Arrival of longitudinal waves (P-waves) at different threshold levels at sensor 3

Wave velocity is the main parameter in analysing the source location. Fig. 5 (a) and (b) shows calculated wave velocities at various distances using raw signals and attenuation corrected signals at three different thresholds. It shows that the calculated wave velocity is dependent on the threshold; as the threshold increases, the calculated wave velocity decreases with the same sensor distance. For instance, in Fig. 5(a), by considering only one source to sensor distance of 250mm, with different threshold levels, the calculated wave velocities are in the range 4000m/s to 4500m/s and these velocities decrease as the source to sensor distance increases. Philippidis and Aggelis (2005) found that at a sensor distance of 150mm, the wave velocity of P-waves in concrete ranged from 4100m/s to 4700m/s using a from 15 kHz tone burst. Gassman and Tawheed (2004) and Chang et al. (2006) discovered that the wave velocity in concrete varies from 3500m/s to 4000m/s depending upon concrete composition, age and condition.

The wave velocity of the corrected signals is higher than that of the raw signals. This is because the entire raw signal is adjusted to allow the same part of the signal to be used for each threshold crossing. This method attempts to ensure that the arrival time is taken from the same part of the waveform. For example in Fig. 5 (b), for threshold levels 50dB and 60dB, due to signal attenuation and dispersion, the maximum distances over which these levels can be recorded by the sensors are 750mm and 500mm respectively. However, with the correction applied to the signals, they can be recorded up to 1500mm. Problems associated with losing important signals are therefore low when using the corrected signals.

Reinforced concrete, being a composite of sand, aggregate and steel rebar embedded into the cement paste matrix, cannot be assumed non-dispersive as any homogeneous and isotropic material. It is found that the wave velocity for the RC beam is higher than that of the RC slab due to geometry of the specimen and the path taken from the source to the sensor. It shows that when dealing with a large structure, the attenuation of the signal cannot be avoided thus effecting the calculated wave velocity. Moreover, the roughnesses of the specimen surface (especially for daily used structures such as slabs) also influence the calculated P-wave velocity.

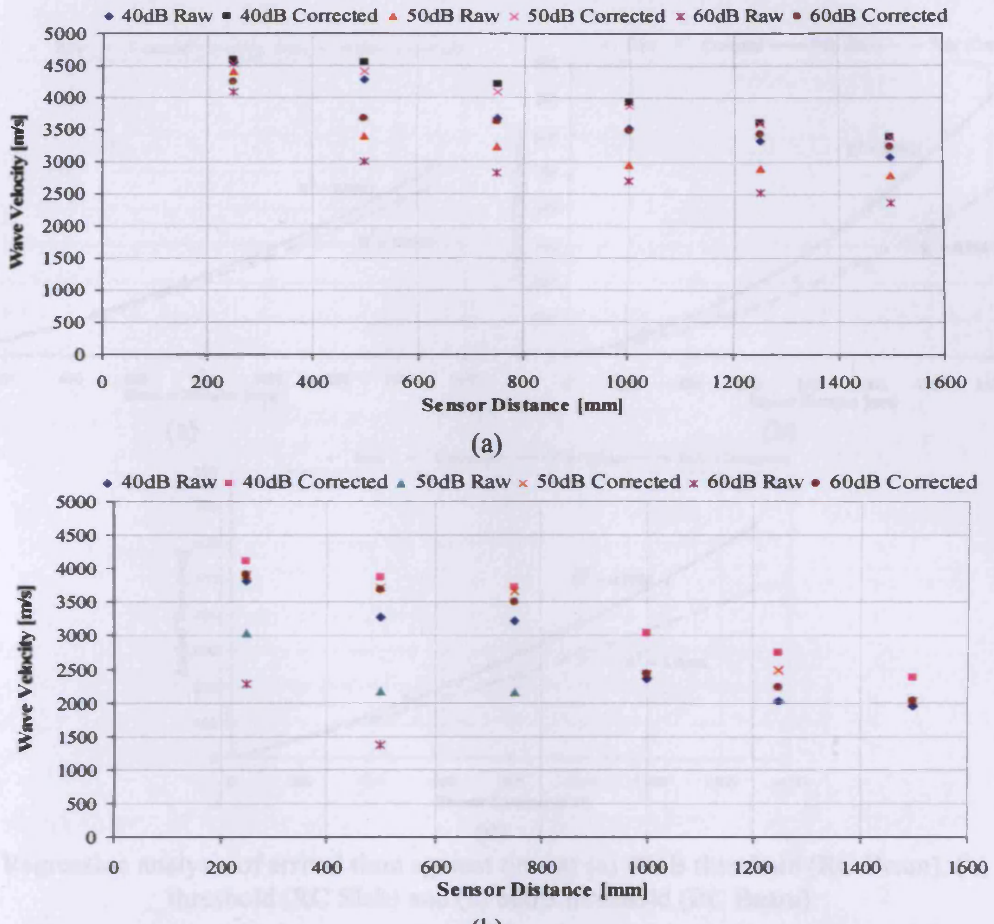

(a)

(b)

Fig. 5. Wave velocity for raw and corrected signal at 40dB, 50dB and 60dB for (a) RC beam (b) RC slab

Philippidis and Aggelis (2005) investigated the effect of water to cement ratio on wave velocity in concrete, where for a range of water to cement ratios between 0.375 and 0.45, the P-wave velocity varied between 3500m/s and 4700m/s. As the water to cement ratio reduced, the velocity of the P-wave increased.

Acoustic waves are modified as they propagate through the material due to scattering, absorption, attenuation and retransmission through the different material (aggregates, cement paste, reinforcement, air gaps due to cracks etc.) and this will affect the wave propagation (Miller and McIntire ,1987). This accounts for the reduction in velocity as distance increases and is an important result as experimentalists often take a velocity measurement at one distance and use it in location studies over the range of distances.

Fig. 6 (a), (b) and (c) shows the regression analysis of the arrival time data plotted against sensor distance. It justifies the use of corrected data. The small difference between the regression analysis values of the raw and corrected data, demonstrates that the time of arrival that has been taken has been correctly assumed to be from the same signal. These results also show that attenuation cannot be avoided when dealing with concrete structures. With a sensor distance of 1.5 metres, the signal amplitude that was recorded was only 40dB, which definitely means that the ability to locate damage in concrete structures is limited.

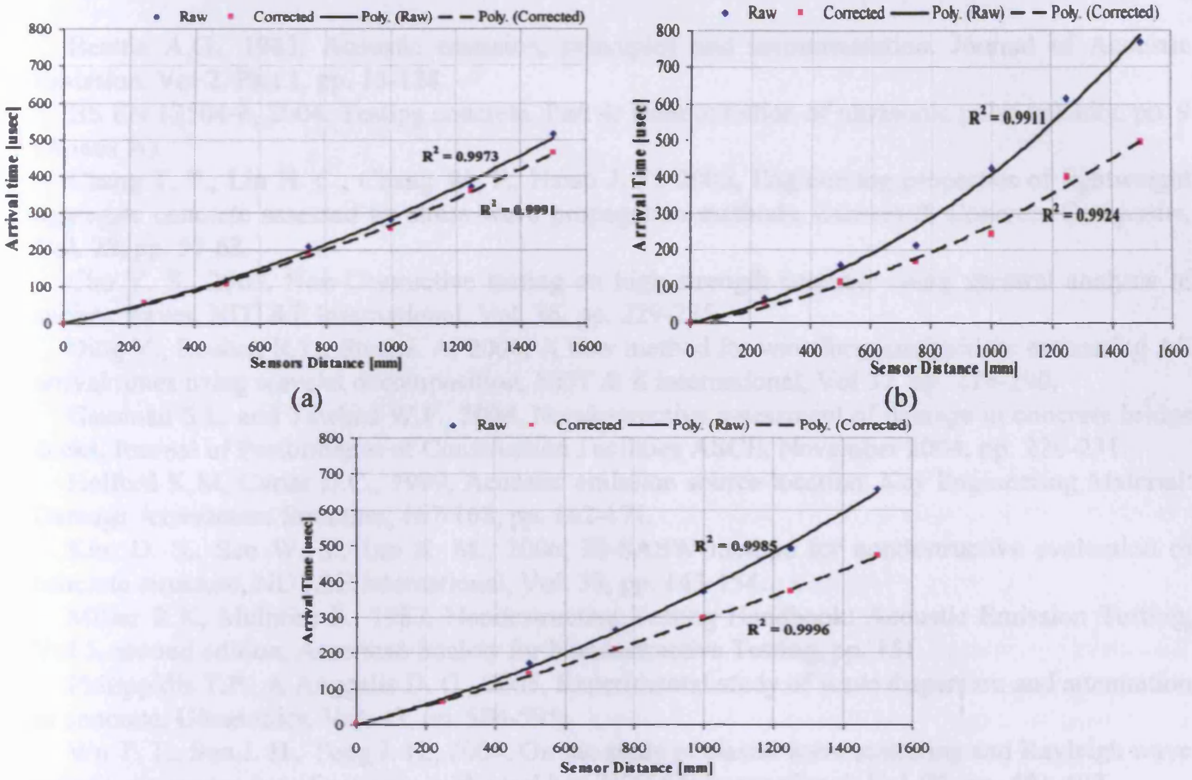

(a) (b)

(c)

Fig. 6: Regression analysis of arrival time against time at (a) 40dB threshold (RC Beam), (b) 40dB threshold (RC Slab) and (c) 60dB threshold (RC Beam)

Moreover, from the regression analysis, it can be seen that the results of this experimental programme do not concur with the hypothesis proposed in BS EN 12504-4 (2004) for the testing of concrete using Ultrasonics. In this standard the determination of the Ultrasonic pulse velocity is obtained by assuming that the relationship between the arrival time data and sensor distance is linear. The slope of the best straight line drawn through the points is measured and recorded as the mean wave velocity along the concrete surface. However, in this work it can be seen that the relationship between the arrival time and sensor distance is not linear. Consequently, the actual wave velocity decreases as the sensor distance increases.

Conclusions

Two wavemodes can be observed in concrete beams and slabs known as the longitudinal wave and shear wave/Rayleigh wave which travel at velocities in the range 2000m/s to 4500m/s. A practical investigation of two concrete structures shows that as the source to sensor distance increases, the calculated wave velocity decreases.

The wave velocity used in automatic TOA should be carefully selected considering both the distance at which measurements will be taken and the threshold used. Propagation of the elastic waves in concrete are affected by; the geometry of the sample, the path taken from the source to sensor and the concrete composition and condition.

References

Beattie A.G., 1983, Acoustic emission, principles and instrumentation. Journal of Acoustic Emission, Vol 2, Part 1, pp. 15-128.

BS EN 12504-4, 2004, Testing concrete, Part 4: Determination of ultrasonic pulse velocity, pp. 9 (Annex A).

Chang T. P., Lin H. C., Chang W. T., Hsiao J. F., 2006, Engineering properties of lightweight aggregate concrete assessed by stress wave propagation methods, Cement & Concrete Composite, Vol. 28, pp. 57-68.

Cho Y. S., 2003, Non-Destructive testing on high strength concrete using spectral analysis of surface waves, NDT&E International, Vol. 36, pp. 229-235.

Ding Y., Reuben R.L., Steel J. A, 2004, A new method for waveform analysis for estimating AE arrival times using wavelet decomposition, NDT & E International, Vol 37, pp. 279-290.

Gassman S.L. and Tawhed W.F., 2004, Nondestructive assessment of damage in concrete bridge decks, Journal of Performance of Construction Facilities ASCE, November 2004, pp. 220-231.

Holford K.M, Carter D.C., 1999, Acoustic emission source location. Key Engineering Material: Damage Assessment Structure, 167-168, pp. 162-171.

Kim D. S., Seo W. S., Lee K. M., 2006, IE-SASW method for nondestructive evaluation of concrete structure, NDT&E International, Vol. 39, pp. 143-154.

Miller R.K, McIntire P., 1987, Nondestructive Testing Handbook: Acoustic Emission Testing, Vol 5, second edition, American Society for Nondestructive Testing, pp. 151.

Philippidis T.P., A Anggelis D. G., 2005, Experimental study of wave dispersion and attenuation in concrete, Ultrasonics, Vol. 43, pp. 584-595.

Wu T. T., Sun J. H., Tong J. H., 2000, On the study of elastic wave scattering and Rayleigh wave velocity measurement of concrete with steel bar, NDT&E International, Vol. 33, pp. 401-407.

THE APPLICATION OF ACOUSTIC EMISSION MONITORING TO THE ASSESSMENT CONCRETE STRUCTURES SUFFERING FROM REINFORCEMENT CORROSION

N. Muhamad Bunnori, K.M. Holford & R.J. Lark
Cardiff School of Engineering, Cardiff University

INTRODUCTION

This paper describes an experimental programme to investigate the behaviour of reinforced concrete structures subject to deterioration as a consequence of reinforcement corrosion using acoustic emission monitoring. Two types of test specimen were used: pre-corroded (PR) specimen in which the cross sectional area of the bar was reduced but, as they were cleaned before being cast into the concrete, the integrity of the concrete itself and the bond between the steel and the concrete were unaffected by the corrosion; and post-corroded (PS) specimen in which the corrosion products were developed within the specimen. All specimens were tested in four-point bending monitored using an Acoustic Emission (AE) sensor system.

A parameter-based approach was used to analyse the data. This approach evaluates relative AE activity based on the measurement of parameters such as hits, amplitudes and absolute energy. This method of analysis has been shown to be sensitive to the initiation and growth of cracks within both homogeneous and composite materials and structures (Oh and Kim (2005), Beck P., (2004)). It is also shown that the application of a linear location, Time of Arrival (TOA) method can be used to determine the location of damage in an area between an array of sensors and to monitor the progression of the resultant cracking.

MATERIALS AND SPECIMEN PREPARATION

In this programme the specimen were cast using a concrete mix with a target strength of 40MPa using a water to cement ratio of 0.56 and with material proportions of 1:2:2.5 by weight of cement, sand and aggregate. The specimen were 100mm x 150mm x 750mm with a single, high-yield 12mm diameter reinforcing bar placed at the centre of the width of the section approximately 50mm above the soffit of the beam (i.e. a cover of 44mm).

For the pre-corroded specimen, lengths of the 12mm diameter reinforcement bar were corroded to three levels of damage using an anodic current before the concrete was cast. In the post-corroded specimen, a middle section of the reinforced concrete beams were encased in an acrylic tank. This section was then immersed in a 5% NaCl solution as shown in Figure 1.

The post-corroded specimen exhibited longitudinal cracking on the bottom face of the beams along the line of the reinforcement. This was clearly due to the formation of the extensive corrosion products that were developed inside the concrete.

ACOUSTIC EMISSION (AE) TECHNIQUE

Acoustic emission testing is based on the fact that solid materials emit sound or acoustic emission in the material itself when they are mechanically or thermally stressed to the point where deformation or fracture occurs.

Location can be defined as the determination of the spatial position of an acoustic emission source from arrival time measurements using an array of sensors (Miller and McIntire, 1987). In this case a linear location technique was used since the position of the source is known to be somewhere along a straight line between a pair of transducers attached to the beam. Using a time of arrival (TOA) approach, a difference in the measured arrival times of the emissions from a source at any two transducers uniquely determines the location of this source. The accuracy of the source location depends on the wave velocity calculation, time difference measurements and good sensor positions (Beck P., 2004). In this case the acoustic emission source is the cracking and degradation of the concrete resulting from the application of the load but influenced by the level of corrosion that is present. The sensors for measuring the acoustic emission were attached to the concrete using magnetic clamps that hold the sensors against steel plates glued to the surface of the specimen (Figure 2).

RESULTS AND DISSCUSSION

The behaviour of concrete subjected to different loading conditions is governed by the initiation and propagation of the internal cracks and flaws during loading. Figure 3 shows the load deflection curve for the beam A22PR (Pre-corroded) and this can be split into five different regions where there is:

I Micro-cracking
II Localised crack propagation (**Point A**)
III Distributed flexural cracks (**Point B**)
IV Shear cracking (**Point C**)
V Damage localization (**Point D**)

The load carried by each of the pre-corroded specimen at the above points is given in Table 1. From this it can be see that although the un-corroded specimen developed flexural cracking in the centre of the beam where the bending moment was a maximum, the ultimate failure mode was one of shear. The specimens in which the steel had been corroded failed in flexure.

The failure loads and mode of failure for the post-corroded specimen are given in Table 2 and a typical load deflection curve is shown in Figure 4. In this case the heavily corroded specimen exhibited much less flexural cracking and failed in a brittle manner due to a loss of bond between the reinforcing bar and the concrete. Figure 5 illustrates the typical specimen failure modes in shear and flexure.

In Figure 6 the crack pattern of one of the control specimen is given and this can be compared with a location plot of a the total AE in Figure 7, expressed in terms of the absolute energy of these emissions, obtained throughout the duration of this test. From this it can be seen that the two regions of high emissions are consistent with the location of the primary shear cracks that lead to the failure of this specimen. However, lower energy emissions are also found at the centre of the beam at an earlier stage in the test and these are typical of the flexural cracking which is found in phase III. A similar AE plot for one of the pre-corroded specimen that failed in flexure is given in Figure 8. In this case it can be seen that the flexural cracking in region 1 dominates the output, although it should be noted that the energy of these emissions is generally less than that of the shear cracks. Regions 2, 3 and 4 also correspond to the location of flexural cracks that were observed visually. Generally AE identified the onset of flexural cracking at a load of approximately 10kN, whereas visually these cracks were not observed until the load reached 15kN.

Figures 9 and 10 present similar data for one of the post-corroded specimen, which failed due to a loss of bond. In this case the flexural cracking was much more localised because of the loss of bond and is characterised by the emissions in regions 1 and 2, which correspond to the two cracks above and below the existing crack in the bottom view of the beam. It is also noticeable that in this case there are many more low energy emissions distributed throughout the length of the beam. It is believed that these emissions are due to the breakdown in the bond between the steel and the concrete and rubbing of the faces of the existing longitudinal crack both of which are a consequence of the corrosion process.

CONCLUSIONS

It has been shown that AE can be used to monitor the development of cracking in a simple reinforced concrete section subject to flexure. Flexural cracking can be identified and located prior to it being visible and its development under an increasing load can be tracked. Internal damage due to corrosion of the reinforcing bar within the concrete is characterised by much lower energy emissions that are distributed throughout the length of the beam, although it is not yet clear whether these emissions are a consequence of the loss of bond or due to rubbing of the faces of cracks initiated by the expansion of the corrosion products. The energy of the emissions generated during the shear failure of the un-corroded specimens was greater than that obtained from those that failed in flexure, although the only evidence of this prior to failure was the increased activity in the regions where shear failure might be anticipated.

Based on the above evidence it can be concluded that AE can be used to identify damage and/or deterioration of reinforced concrete structures due to both load effects and corrosion, but that further work is required to explicitly characterise the different emissions that are obtained.

REFERENCES

1. Beck P., 2004. Quantitative Damage Assessment of Concrete Structures Using Acoustic Emission, Cardiff School of Engineering. University of Wales, Cardiff. UK

2. Miller R.K, McIntire P., 1987. Nondestructive Testing Handbook: Acoustic Emission Testing, Volume 5, Second Edition, American Society for Nondestructive Testing, pp. 136.

3. Oh B. H. and Kim K. S., 2005, Micro-Damage Characterisation of Concrete Structures Based on Acoustic Emission. Proceeding of the International Conference: 2005 International Congress Global Construction: Ultimate Concrete Opportunities, University of Dundee, Scotland, UK, pp. 13-28

Specimen **Pre-corroded**	**Load at point (kN)**				
	A	**B**	**C**	**D**	**Failure**
A11PR (control)	**15.0**	**17.5**	**45.0**	**55.0**	**59.21**
B11PR (low corrosion)	**15.0**	**25.0**	**-**	**42.5**	**54.77**
C11PR (medium corrosion)	**15.0**	**20.0**	**-**	**25.0**	**34.81**
A22PR (control)	**15.0**	**20.0**	**45.0**	**55.0**	**59.54**
B22PR (low corrosion)	**15.0**	**20.0**	**40.0**	**45.0**	**47.50**
C22PR (medium corrosion)	**15.0**	**20.0**	**-**	**25.0**	**35.08**
D22PR (high corrosion)	**15.0**	**20.0**	**-**	**20.0**	**23.46**

Table 1: Failure loads of pre-corroded specimen

Specimen **Post-corroded**	**Failure Load (kN)**	**Failure Mode**
A11PS (0%)	**54.78**	**Shear**
B11PS (9.60%)	**28.40**	**Flexure**
C11PS (17.00%)	**14.53**	**Bond**
D11PS (33.45%)	**5.98**	**Bond**
A22PS (0%)	**60.0**	**Shear**
B22PS (8.90%)	**45.92**	**Flexure**
C22PS (14.69%)	**18.84**	**Bond**
D22PS (31.30%)	**12.50**	**Bond**

Note: The percentage corresponds to the level of the corrosion measured by weight loss of the reinforcing bar

Table 2: Failure loads and mode of failure of post-corroded specimen

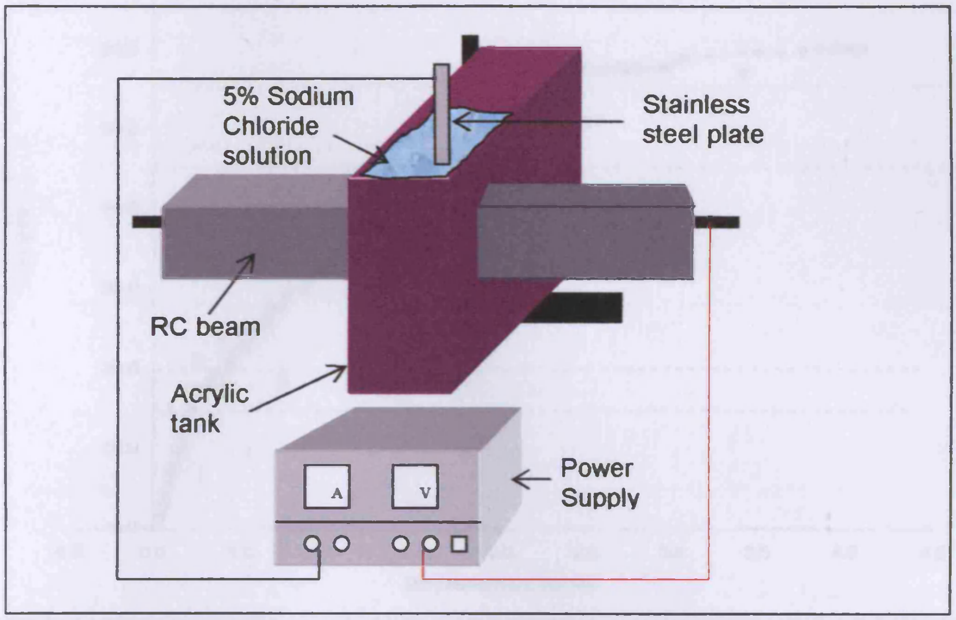

Figure 1: Setup for the corrosion of the post-corroded specimens

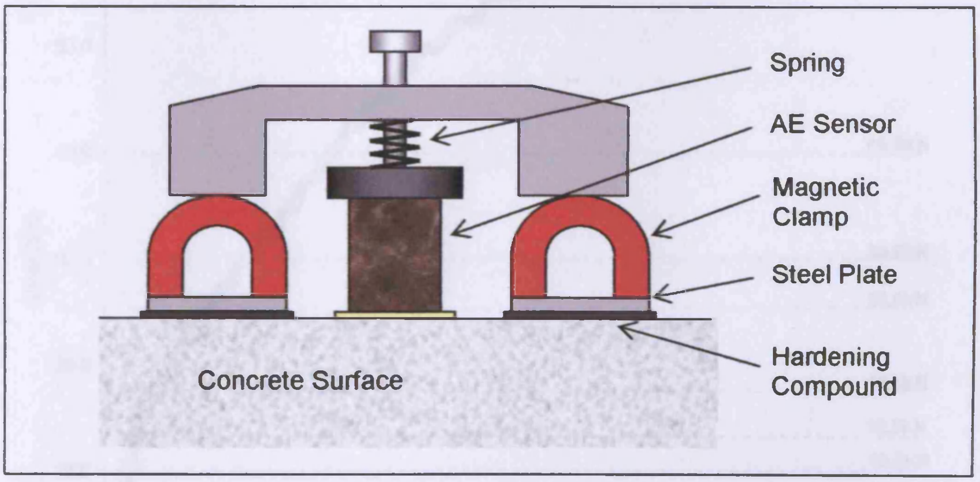

Figure 2: Sensor Fixing

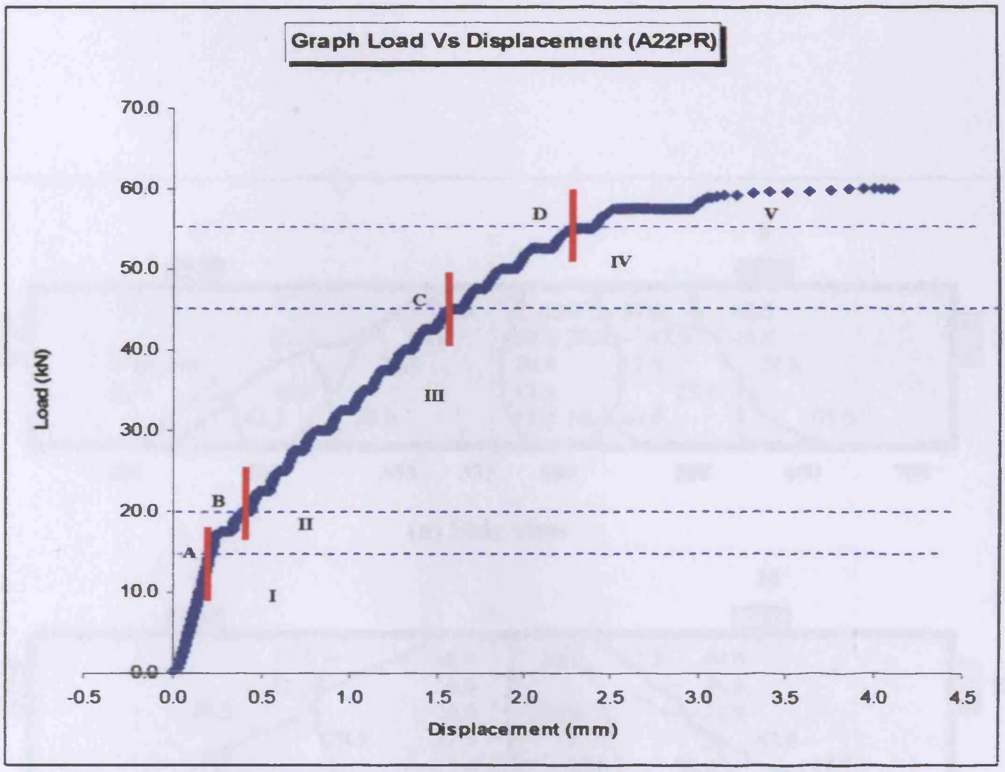

Figure 3: Load / displacement curve for specimen A22PR

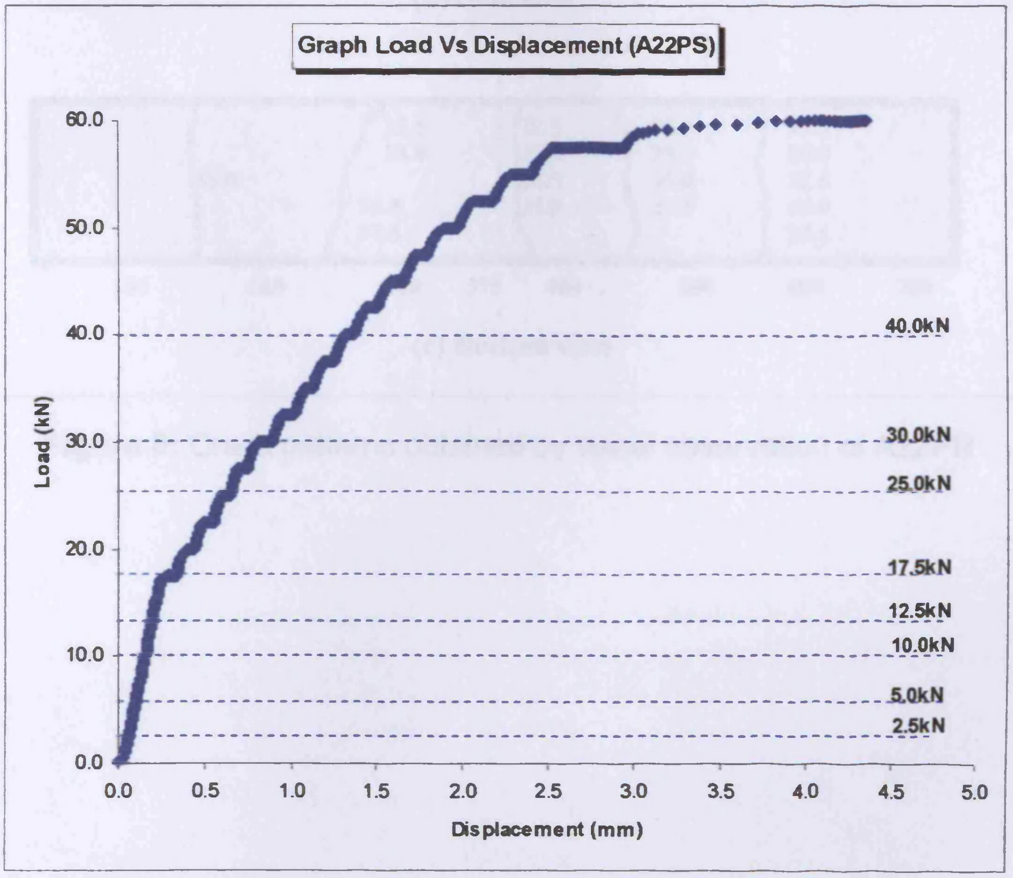

Figure 4: Load / Displacement curve for specimen A22PS

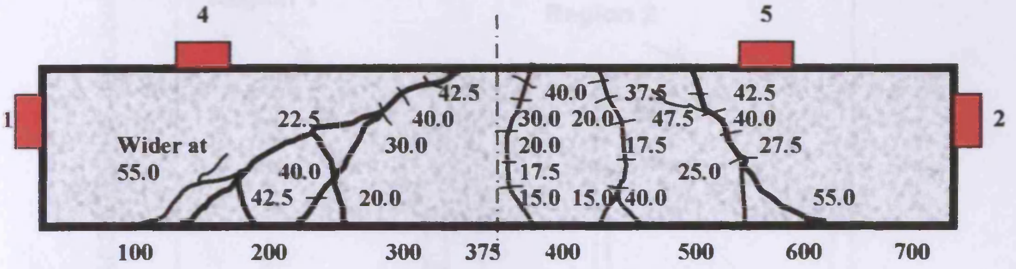

(a) Side view

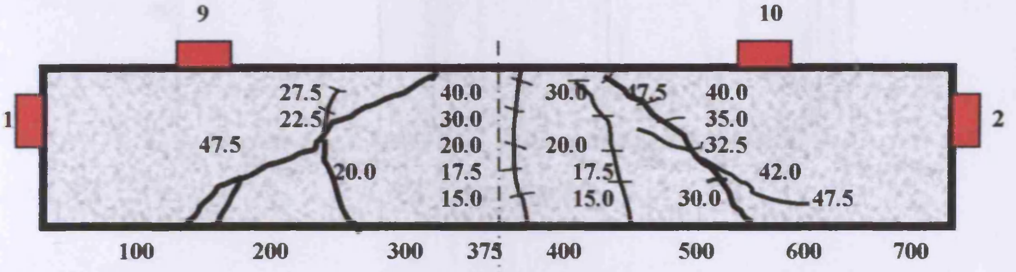

(b) Side view

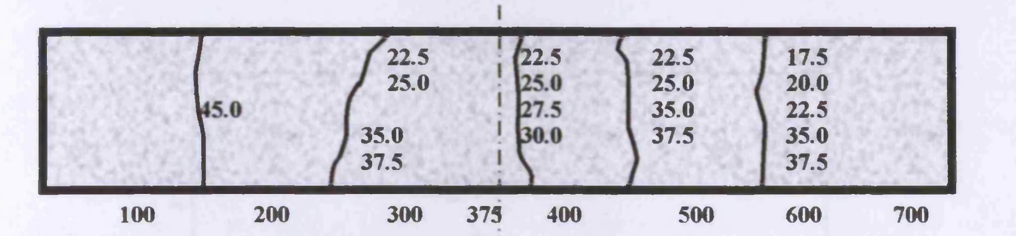

(c) Bottom view

Figure 5: Crack patterns obtained by visual observation of A22PR

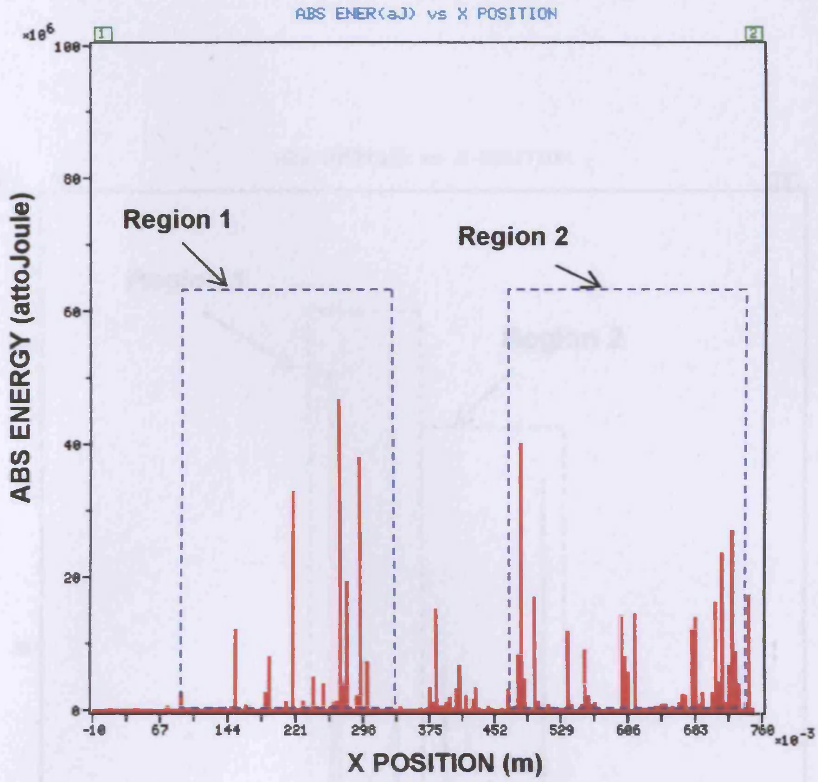

Figure 6: Source location of total emission during damage localization (0-55.0kN) for A22PR

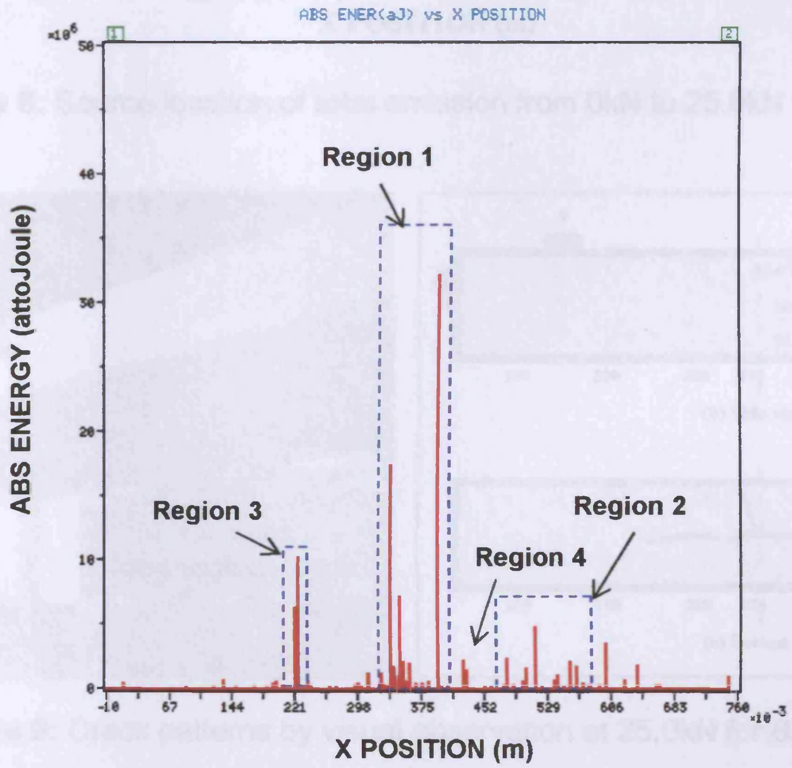

Figure 7: Source location of total emission during damage localization (0-25.0kN) for C22PR

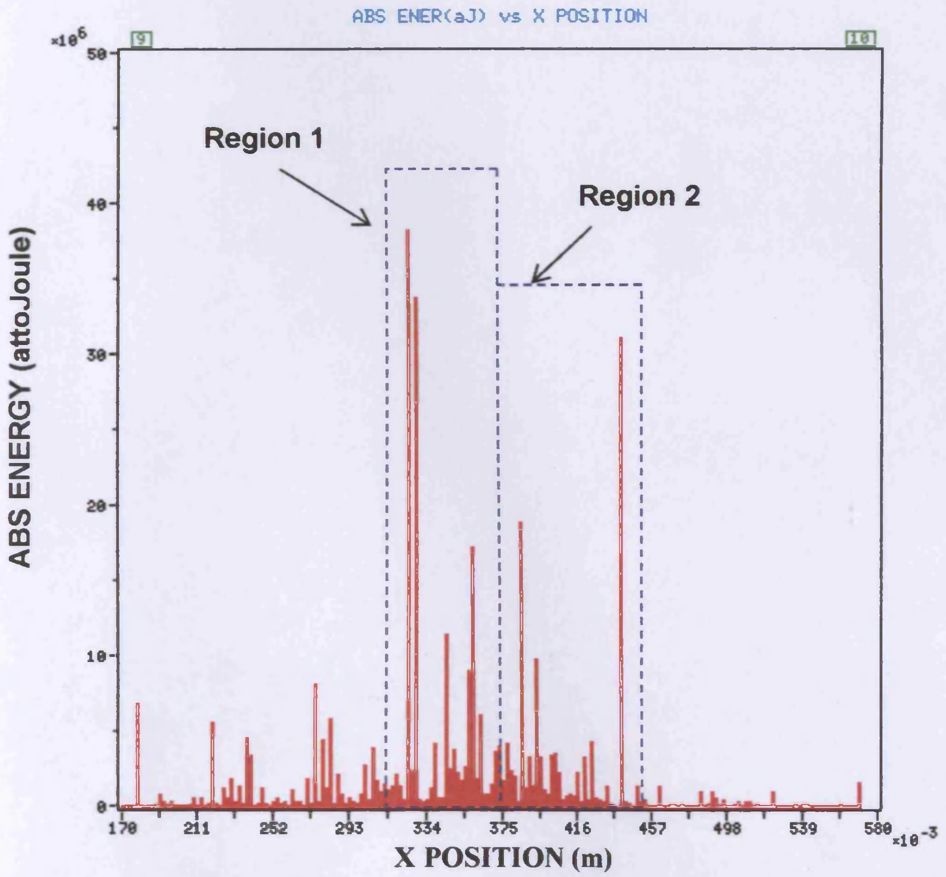

Figure 8: Source location of total emission from 0kN to 25.0kN for B22PS

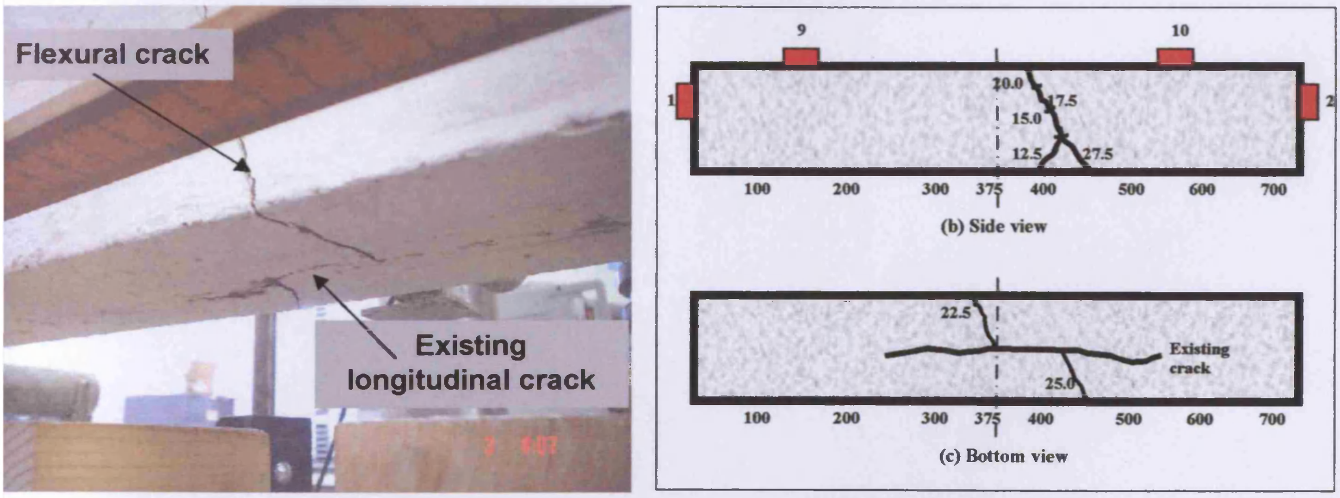

(b) Side view

(c) Bottom view

Figure 9: Crack patterns by visual observation at 25.0kN for B22PS